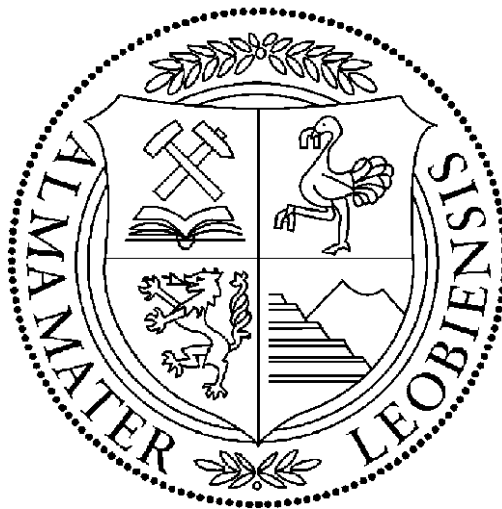


Dissertation

Physically based modelling of creep-fatigue in hot work tool steels

Dipl.-Ing. Friedrich Krumphals

Institute of Metal Forming



A thesis submitted to the Faculty of Product Engineering
in partial fulfillment of the requirements for the degree of
“doctor rerum montanarum”

UNIVERSITY OF LEOBEN

January, 2014

“Nicht alles, was wahr ist, müssen wir sagen, aber was wir sagen, muss wahr sein.”

Peter Rosegger (1843 – 1918), Heimatdichter

“Siehst du einen guten Zug, suche einen besseren.”

Emanuel Lasker (1868 – 1941), 2. Schachweltmeister

“Ich hätte schon früher heiraten können, aber ich hatte keine Zeit.”

Vladimir Kramnik (*1975), 14. Schachweltmeister

For my first mentors, old Aunt Mary and my Grandfather

Affidavit

I declare in lieu of oath, that I wrote this thesis and performed the associated research myself, using only literature cited in this volume.

Leoben, January 2014

Friedrich Krumphals

Acknowledgement

I deeply want to express my thanks to my supervisor Prof. Christof Sommitsch, Head of the Institute of Materials Science and Welding and Dean of the Faculty of Mechanical Engineering for patient and dedicated scientific support. Thanks to my second supervisor Prof. Otmar Kolednik for precise expertising the PhD-thesis.

Sincere thanks are given to the employees at Böhler Edelstahl for scientific guidance, experimental and tool materials support.

Thanks to my chess colleagues, which strongly enriched my life over the last decades on various points of view.

Many thanks to my colleagues and friends at the Institute for Materials Science and Welding and FELMI at Graz University of Technology.

Thanks to my former colleagues at the University of Leoben, who are working at different Institutes and at the MCL, always giving me a warm welcome during a visit in Leoben.

Thanks to my new colleagues and friends around the globe.

Thanks to the one and most important person in my life during almost my whole academical education and my family.

Abstract

Hot work tool steels, which are used for the extrusion of non-ferrous metals, are exposed to high cyclic thermo-mechanical loads. Due to high production costs, a long lifetime is of high importance and, therefore, improvements in the microstructure are demanded. A reliable estimation of the service-lifetime of the tool is also essential. Presently, empirical approaches exist, such as the phenomenological Chaboche model, which is implemented in AbaqusTM. With this model, the inelastic strains in the tools can be calculated after the determination of the cyclic thermo-mechanical loads, which are simulated in DeformTM. The disadvantage of this approach lies in the fact that the parameters, which are required for the model, are only valid for a certain annealing condition of the material and a certain temperature range. Since the elastic-viscoplastic Chaboche model needs a large number of empirical parameters, which must be determined by extensive experimental methods, a simplification would be highly desirable.

Therefore, the ambition in this work is to correlate the characteristics of the tool's microstructure with the macroscopic material response. In order to realise such an idea, a physically based model is introduced, which should allow us to understand the reaction of the microstructure due to a thermo-mechanical load pattern, which occurs during an extrusion process. Three basic parameters are needed in this physical based approach, the conditions of the precipitates, the substructure, as well as the dislocation density. The model is based on a system of coupled differential equations, which calculates the evolution of the dislocation density due to the thermo-mechanical loading with the software MathCadTM. Hereby the initial substructure and the precipitation status are taken into account. The precipitation status is simulated using the thermo-kinetic software MatCalcTM. With this physically based modelling approach, the influence of a specific microstructure onto the material response due to service loads can be estimated. The results of both the phenomenological and the physically based approach can be compared by the inelastic strain value, which is an important output parameter in both approaches. Lifetime calculations were performed for different process conditions, and the service life of different tool steels was compared.

Kurzfassung

Warmarbeitsstähle, die für Strangpressapplikationen von Nichteisenmetallen verwendet werden, sind hohen thermo-mechanischen Belastungen ausgesetzt. Aufgrund der hohen Herstellkosten solcher Werkzeuge ist eine möglichst lange Einsatzzeit von Bedeutung, und daher auch die Frage nach Verbesserungspotentialen in der Mikrostruktur. Auch eine verlässliche Abschätzung der Werkzeuglebensdauer ist von entscheidender Wichtigkeit. Derzeit gibt es dazu empirische Ansätze, wie das phänomenologische Chaboche Modell, das in AbaqusTM implementiert ist. Mit diesem Modell können für die betrachteten Strangpresswerkzeuge die inelastischen Dehnungen mittels zuvor in DeformTM simulierter zyklisch thermo-mechanischer Belastungen berechnet werden. Der Nachteil dieses Ansatzes ist, dass die Parameter des Modells nur für einen bestimmten Wärmebehandlungszustand des Werkstoffes und für einen bestimmten Temperaturbereich gültig sind. Da das elastisch-viskoplastische Chaboche Modell eine Vielzahl von empirischen Parametern benötigt, die nur mit sehr aufwendigen experimentellen Methoden bestimmt werden können, ist hier eine Vereinfachung höchst erstrebenswert.

Daher wird in dieser Arbeit versucht, Charakteristika der Mikrostruktur des Werkzeuges in Zusammenhang mit der makroskopischen Werkstoffantwort zu bringen. Um dieses Vorhaben zu realisieren, ist es notwendig, über ein physikalisch basiertes Modell ein Verständnis zu erlangen, wie sich die Mikrostruktur zufolge thermomechanischer Beanspruchungsmuster, die während eines Strangpressprozesses auftreten, ändert. Für den physikalisch basierten Modellansatz sind die drei Parameter, Ausscheidungszustand, Substruktur und Versetzungsdichte wesentlich. Das Modell basiert auf einem System gekoppelter Differentialgleichungen, das die Versetzungsdichteentwicklung zufolge thermomechanischer Belastungen in MathCadTM berechnet, unter Berücksichtigung der anfänglichen Substruktur, sowie des Ausscheidungszustandes, der mithilfe der thermo-kinetischen Software MatCalcTM simuliert wird und Eingang ins Modell findet. Mit diesem Modellierungsansatz kann der Einfluss der Mikrostruktur auf die inelastische Materialantwort zufolge der Belastungen während des Strangpressprozesses berechnet werden. Die Ergebnisse beider Ansätze, des phänomenologischen und des physikalisch basierten, können über die resultierende inelastische Dehnung, welche in beiden Modellen einen wichtigen Ausgabeparameter darstellt, verglichen werden. Lebensdauerberechnungen wurden zufolge unterschiedlicher Prozessbedingungen durchgeführt, und die Einsatzzeiten von verschiedenen Warmarbeitsstählen verglichen.

Contents

Declaration of Originality	I
Acknowledgements	II
Abstract	III
Kurzfassung	IV
Contents	V
List of Abbreviations	VII
List of Symbols	VIII
1. Introduction	1
2. Literature review.....	5
2.1 Hot work tool steels.....	5
2.2 Microstructure of a complex hot work tool steel.....	7
2.2.1 Precipitates	9
2.2.2 Dislocations and substructure.....	10
2.3 Loading patterns and damage mechanisms during service	16
2.4 Microstructure evolution during cyclic thermo-mechanical loads	22
2.4.1 Hardening processes.....	22
2.4.2 Softening processes	23
2.5 Modelling the lifetime at cyclic high thermo-mechanical loads	24
3. Experimental.....	26
3.1 Material and heat treatment.....	26
3.2 Experimental verification of boundary conditions during a hot extrusion process	28
3.2.1 Pressure and temperature.....	28
3.3 Creep tests	31
3.4 Fatigue tests.....	32
3.5 Creep-fatigue tests.....	32
3.6 Microstructure characterization.....	33

4. Simulation	34
4.1 FE-simulation of the extrusion process	34
4.1.1 Extrusion model and process simulation	34
4.1.2 Inelastic strain evolution and lifetime prediction	36
4.2 Physical based microstructure modelling.....	42
4.2.1 Modelling of the precipitation kinetics.....	42
4.2.2 Modelling the dislocation density evolution	43
5. Results.....	46
5.1 Experimental tests	47
5.1.1 Pressure and temperature evaluation during a copper extrusion process	47
5.1.2 Pressure and temperature evaluation during an aluminium extrusion process	50
5.1.3 Evaluation of friction behaviour.....	53
5.1.4 Creep tests	54
5.1.5 Fatigue tests.....	57
5.1.6 Creep-fatigue tests.....	60
5.2 Microstructure characterization.....	64
5.2.1 Metallographical investigations.....	64
5.2.2 TEM investigations	76
5.2.3 X-ray diffraction.....	87
5.3 Simulation	88
5.3.1 Thermo-mechanical induced stress and strain distribution	88
5.3.2 Damage evolution and lifetime prediction	91
5.3.3 Precipitation kinetics	92
5.3.4 Dislocation density evolution during service	97
6. Discussion.....	100
6.1 Experimental and FE-Simulation of the extrusion process	102
6.2 Microstructure evolution simulation and experimental characterization	103
7. Summary and Outlook.....	113
8. References	115
9. Appendix	120

List of Abbreviations

<i>Abbreviation</i>	<i>Meaning</i>
AC	accumulation of creep damage
bcc	body centered cubic
CCD	charge-coupled device
DCCW	diamond counter clockwise
DCW	diamond clockwise
EBSD	electro back scatter diffraction
EDX	energy dispersive X-ray spectrometry
EELS	electron energy loss spectroscopy
e.g.	example given
Eq.	equation
fcc	face centered cubic
Fig.	figure
GND	geometrically necessary dislocations
i.e.	that is
IMLP	incremental multiaxial life prediction law
IP	in phase
LCF	low cycle fatigue
LEDS	low energy dislocation structure
LOM	light optical microscope
MC	metal carbide
MDA	multiaxial damage accumulation law
NLK	nonlinear kinematic hardening rule
OP	out of phase
SAGB	small angle tilt grain boundary
SEM	scanning electron microscope
SRP	strain rate partitioning
SSD	secondary stored dislocations
STEM	scanning transmission electron microscope
TEM	transmission electron microscope
TME	thermo-mechanical experiments
TVBO	thermoviscoplasticity based on overstress
VMR	vacuum melted and remelted

List of Symbols

<i>Symbol</i>	<i>Meaning</i>	<i>Unit</i>
A	point	[-]
a	lattice parameter	[m]
A_0	constant	[1]
a_r	aspect ratio	[1]
b	Burgers vector	[m]
c	fatigue ductility exponent	[1]
$^{\circ}C$	degree, celsius	[$^{\circ}C$]
c_1, c_2	material parameters	[1]
C_i	damage variables	[1]
c_j^e	concentration of jogs in thermodynamic equilibrium	[m^{-3}]
D	diffusion coefficient	[m^2s^{-1}]
$d_{annihil-c}$	critical distance for spontaneous annihilation	[m]
D_{cr}	creep damage parameter	[1]
D_{gb}	grain boundary diffusion coefficient	[m^2s^{-1}]
d_{lock}	critical distance for spontaneous lock formation	[m]
D_{SD}	self diffusion coefficient	[m^2s^{-1}]
D_{sub}	subgrain diameter	[m]
E	young's modulus	[Pa]
E_0	energy factor	[J]
F	interaction force	[N]
f_v^p	volume fraction of particles	[m^{-3}]
G	shear modulus	[Pa]
g	equilibrium stress vector	[Pa]
h_b	distance between dislocations in the subgrain boundary	[m]
J_i	first/second invariant; $i=1,2$	[1]
k	elastic limit	[m]
K	kinematic hardening parameter	[Pa]
L_{eff}	effective glide distance	[m]
L_i	forest dislocation spacing in the cell interior	[m]
$L_{i, obst}$	obstacle spacing	[m]
L_p	spacing of precipitates	[m]
L_w	forest dislocation spacing in the cell walls	[m]
m_l	stress dependence of the lifetime behaviour	[1]
n_l	time dependence of the lifetime behaviour	[1]
M_{sg}	mobility of subgrain boundary	[$m^3N^{-1}s^{-1}$]
N_f	cycles to failure	[1]
N_s^p	number of precipitates per unit of area	[m^{-2}]
N_v^p	number of precipitates per unit of volume	[m^{-3}]

<i>Symbol</i>	<i>Meaning</i>	<i>Unit</i>
\dot{p}	von Mises equivalent inelastic strain rate	$[s^{-1}]$
p_{sg}	driving force for subgrain growth	$[Nm^{-2}]$
Q	activation energy	$[J]$
Q_{bulk}	activation energy for bulk diffusion	$[J]$
Q_{SD}	activation energy for self diffusion	$[J]$
Q_{Sel}	saturation parameter of the softening of k	$[J]$
r	isotropic hardening variable	$[1]$
R_a	stress field range	$[m]$
$R_{mean, i}$	mean radius of a precipitate class i	$[m]$
r_p	particle/precipitate radius	$[m]$
R_{sub}	subgrain radius	$[m]$
r_v	radius defining the distance between two dislocations	$[m]$
R_v	stress triaxiality	$[-]$
\mathbf{S}	applied stress deviator	$[-]$
s_{el}	related isotropic softening variable of the elastic limit	$[1]$
S_{el}	softening of the initial elastic limit	$[1]$
t	time	$[s]$
T	temperature	$[^{\circ}C]$
t_0	start time, initial time	$[s]$
Δt	time incement	$[s]$
T_m	melting temperature	$[^{\circ}C]$
\mathbf{u}	displacement vector	$[-]$
\mathbf{v}	velocity	$[ms^{-1}]$
V	volume, activation volume	$[m^3]$
v_c^l	climb velocity due to diffusion of vacancies	$[ms^{-1}]$
v_g	glide velocity of mobile dislocations	$[ms^{-1}]$
v_{climb}	dislocation climb velocity	$[ms^{-1}]$
$v_{c,m}$	climb velocity of mobile dislocations	$[ms^{-1}]$
$v_{c,m}^l$	climb velocity of mobile dislocations due to lattice diffusion	$[ms^{-1}]$
$v_{c,m}^p$	climb velocity of mobile dislocations due to pipe diffusion	$[ms^{-1}]$
$v_{c,s}$	climb velocity of static dislocations	$[ms^{-1}]$
$v_{c,s}^l$	climb velocity of static dislocations due to lattice diffusion	$[ms^{-1}]$
$v_{c,s}^p$	climb velocity of static dislocations due to pipe diffusion	$[ms^{-1}]$
v_{sg}	subgrain boundary migration velocity	$[ms^{-1}]$
\mathbf{X}	internal back stress	$[-]$
\mathbf{Z}	matrix	$[-]$

<i>Symbol</i>	<i>Meaning</i>	<i>Unit</i>
α	slip system	[-]
α_i	related kinematic hardening variable (in Chaboche Model)	[-]
α_m	Taylor factor	[1]
β_i	factor related to the internal spacing of dislocations i	[1]
β_w	factor related to the spacing of dislocations in cell walls	[1]
$\dot{\gamma}$	shear rate	[s ⁻¹]
γ'	phase, commonly Ni ₃ (Al, Ti, Nb)	[-]
γ_{gb}	grain boundary energy	[J m ⁻²]
γ_{SFE}	stacking fault energy	[J m ⁻²]
γ_{sg}	interface energy of a small angle grain boundary	[J m ⁻²]
δ	subgrain size	[m]
δ_{gb}	grain boundary thickness	[m]
ε	strain	[-]
$\dot{\varepsilon}$	strain rate	[s ⁻¹]
$\Delta\varepsilon$	strain increment	[-]
ε_e	elastic strain	[-]
ε_{ij}	macroscopic strain tensor	[-]
ε_{ij}^e	elastic, reversible macroscopic strain including thermal strain	[-]
ε_{ij}^p	plastic, irreversible macroscopic strain including thermal strain	[-]
ε_{in}	inelastic (plastic) strain	[-]
ε_{th}	thermal strain	[-]
θ	misorientation angle	[rad, °]
κ	ageing variable	[-]
λ_m	distance between mobile dislocations	[m]
λ_p	distance between particle centres	[m]
λ_s	effective distance between particles	[m]
ν	frequency	[s ⁻¹]
ν_{debye}	Debye frequency	[s ⁻¹]
π	number pi, constant	[1]
ρ	dislocation density	[m ⁻²]
$\dot{\rho}$	dislocation density evolution	[s ⁻¹]
ρ_b	boundary dislocation density	[m ⁻²]
ρ_m	mobile dislocation density	[m ⁻²]
ρ_s	static dislocation density	[m ⁻²]
σ	stress	[Pa]
σ_{d_eq}	damage equivalent stress	[Pa]
σ_{eq}	von Mises equivalent stress	[Pa]
σ_H	hydrostatic stress	[Pa]
σ_V	volumetric stress	[Pa]
τ	shear stress	[Pa]
τ_α	acting shear stress on a slip system α	[Pa]

<i>Symbol</i>	<i>Meaning</i>	<i>Unit</i>
τ_{eff}	effective shear stress	[Pa]
$\tau_{eff,i}$	effective shear stress in the cell interiors	[Pa]
$\tau_{eff,w}$	effective shear stress in the cell walls	[Pa]
τ_i^j	sum of internal stresses	[Pa]
τ_i^m	backstress due to mobile dislocations	[Pa]
τ_{loop}	line tension of a dislocation loop	[Pa]
τ_{or}	Orowan stress	[Pa]
τ_p	Peierls stress	[Pa]
τ_{th}	threshold stress	[Pa]
Ω	atomic volume	[m ⁻³]

1. Introduction

“Nicht weil es schwer ist, wagen wir es nicht, sondern weil wir es nicht wagen, ist es schwer.”

Seneca (4 vChr – 65)

Main parts of the present work were carried out in the years 2007-2011 during my research work at the Christian Doppler Laboratory for Materials Modelling and Simulation at the Institute of Metal Forming, University of Leoben as well as at the Institute for Materials Science and Welding at Graz University of Technology, from 2009 on. The work was finalized in 2013.

Rods and long products with simple and complex profiles are applied in automotive, aerospace, building industry and construction in general. Wires, pipes, frames for windows, doors or balustrades, reinforcing profile components with complex geometry in cars and airplanes are only a few examples to mention.

Due to a high demand for such products, the extrusion industry tries to accelerate the manufacturing processes. Hence to increase the efficiency, the extrusion press experiences elevated loads during service, especially the tools, which stay in direct contact with the hot metal. Tools applied for hot forming processes are continuously in service under extreme conditions. They have to withstand cyclic thermal and mechanical loads. Cyclic loading patterns require specific non-trivial model approaches for an overall well performed simulation.

Efforts for maintenance and replacement of damaged tools are costly. During an extrusion process, tools are exposed to thermal and mechanical loading conditions, which can cause creep-fatigue. Such cyclic thermal and mechanical loads and their interaction, respectively, are the main reasons for local damage initiation and finally component failure at critical regions, see Fig. 1.1.



Figure 1.1: Damage observed in a W400 extrusion die. The cracks are marked with white lines.

The considered tool materials in this work are Böhler W300 and W400, both X38CrMoV5-1, 1.2343, as well as the austenitic hot work tool steel Böhler W750, X6NiCrTi26-15, 1.2779. Copper and aluminium extrusion experiments were performed at the Institute of Metal

Forming, University of Leoben, to experimentally evaluate the process boundary conditions. The main focus of the physical test program to validate the microstructure model was put on the description of the W300 tool material. A few single test conditions, i.e. creep, fatigue and creep-fatigue tests were also performed with W400 specimen for comparative reasons, while the W750 results are pure numerical in this work. The experimental test program to evaluate the phenomenological Chaboche model parameters for W300, W400 and W750 was performed at the Bundesanstalt für Materialprüfung (BAM) in Berlin.

The specimens were heat treated at the Materials Center Leoben to fully martensitic as well as bainitic matrix state and afterwards tested in the creep laboratory and physical testing laboratory, both at the Institute of Materials Science and Welding at Graz University of Technology. The light optical microscope analyses of selected specimens were also performed at the Institute of Materials Science and Welding, the TEM investigations and XRD dislocation measurements were carried out at FELMI and TU Vienna, respectively.

The FE-simulation of the extrusion process was established in DEFORM-2D with an axisymmetrical model. The obtained pressure and temperature boundary conditions were transmitted to ABAQUS to calculate the inelastic strains in the tools with the aim of ZMat, where the phenomenological elastic-viscoplastic Chaboche model was implemented to calculate the resulting inelastic strains in the tools. The damage calculation was related to the accumulation of the inelastic strain and subsequently a lifetime rule was added to estimate the number of extrusion cycles to failure. In Fig. 1.2 the whole phenomenologically based approach is described schematically.

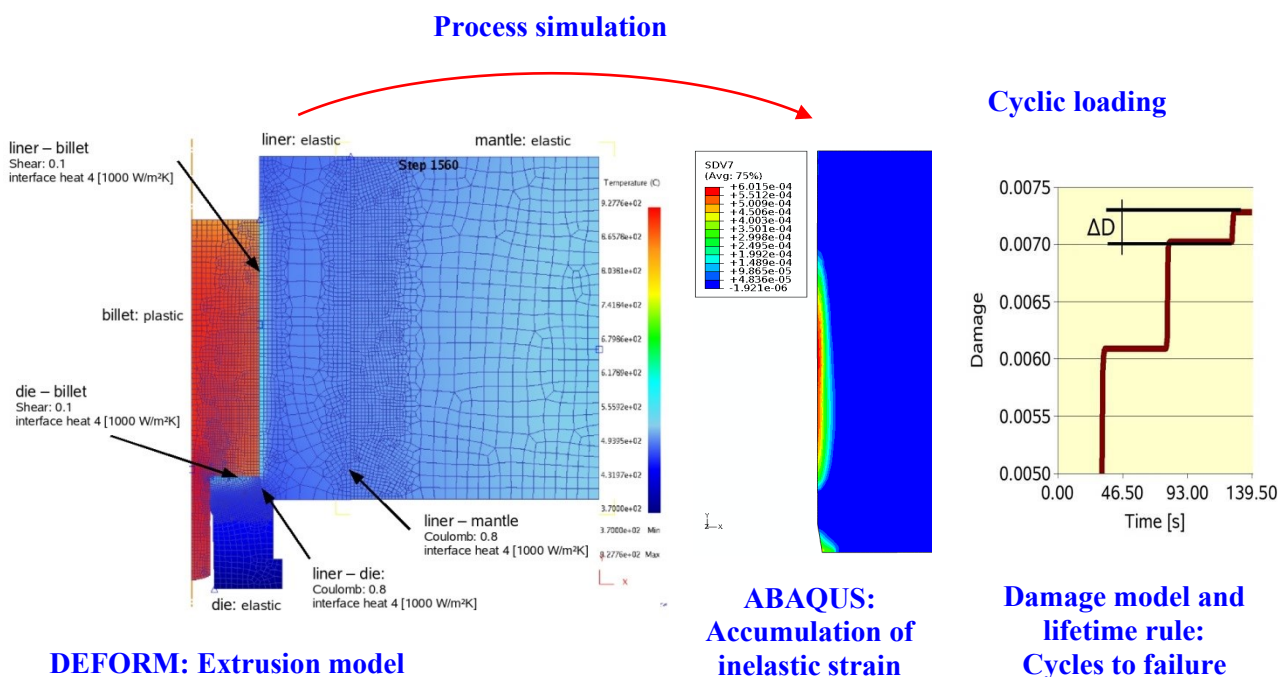


Figure 1.2: Schematic drawing of the established phenomenologically based modelling workflow.

Since a large number of empirical parameters, which must be determined by extensive experimental methods are needed for the elastic-viscoplastic Chaboche model, a simplification would be highly desirable. Therefore, the aim of this work is to correlate the characteristics of the tool's microstructure with the macroscopic material response. In order to realise such an idea, a physically based model is introduced, which allows to understand the reaction of the microstructure due to a thermo-mechanical load pattern, which occurs during an extrusion process. Hence the main challenge is to describe the microstructure evolution, i.e. the precipitation kinetics as well as the substructure and dislocation density evolution, to integrate a physically based approach characterizing the material behaviour under thermo-mechanical cyclic loading conditions, causing creep- and fatigue-influenced damage mechanisms. In Fig. 1.3 the physically based modelling workflow is presented.

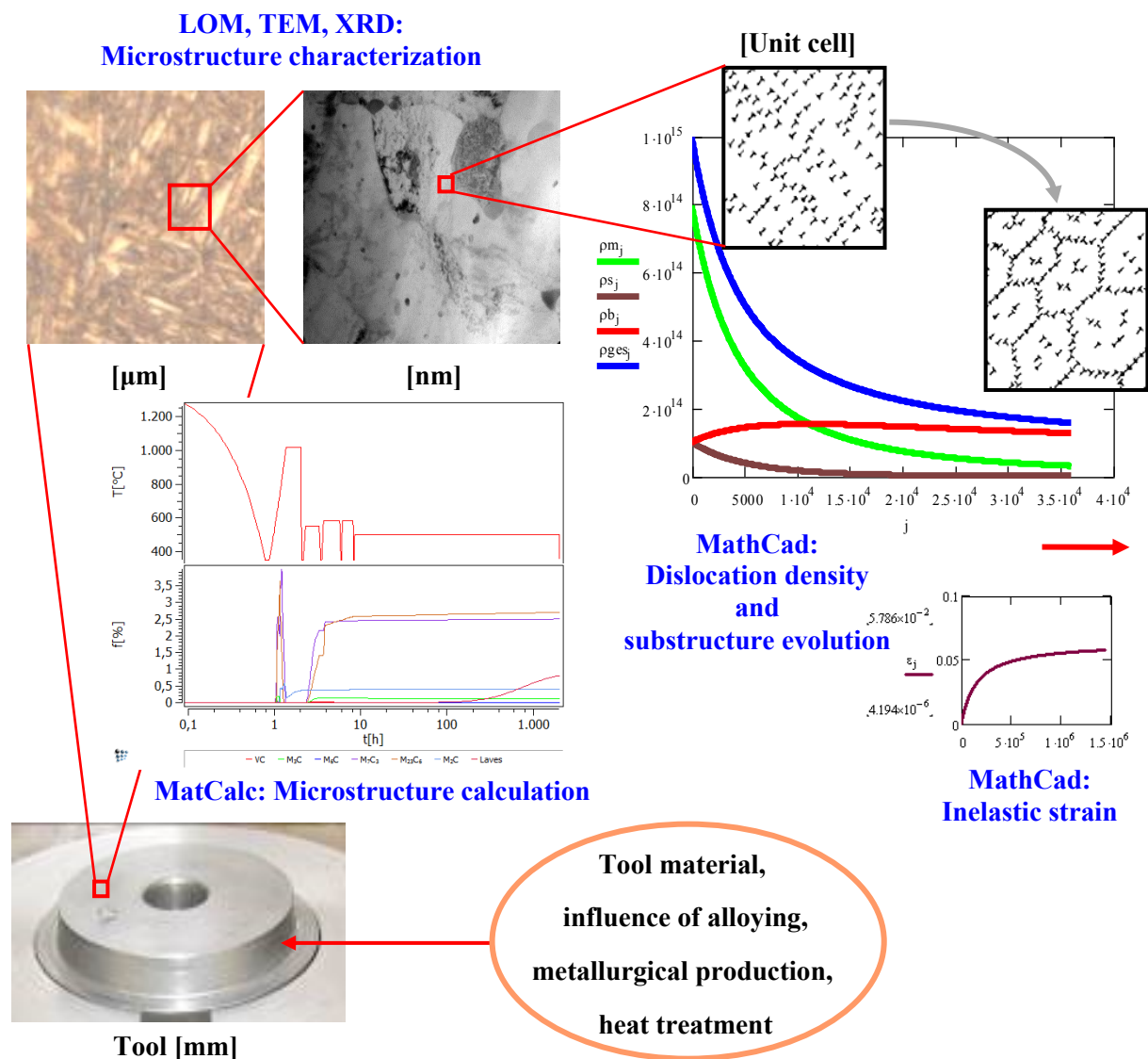


Figure 1.3: Schematic drawing of the physically based microstructure modelling workflow, which was developed in this work.

To describe the microstructure evolution, a dislocation density evolution model based on creep application was adapted in MathCad. It represents one volume element in which a certain substructure evolves due to thermo-mechanical loading conditions. To account for obstacles, which inhibit dislocation glide and subboundary migration, respectively, the precipitation state was simulated by means of the thermo-kinetic software MatCalc. The precipitation size and -density was transmitted into the MathCad model. Besides the prediction of the evolving dislocation density, an additional output parameter of the dislocation density evolution model is the inelastic strain value, which is a result according to dislocation glide. The inelastic strain output of both the dislocation density evolution model and the phenomenological elastic-viscoplastic Chaboche model can be compared and validated.

The lifetime of the tools can subsequently be optimised through adjusting optimum initial tool conditions before service application. The initial microstructural configuration can be adjusted with an adequate heat treatment, as found with MatCalc simulations.

The final target is to be able to estimate the lifetime according to a certain thermo-mechanical load for a whole group of alloys with variable heat treatments. Therefore, the developed approach incorporates several physically based modelling approaches to account for alterations in material, i.e. allowed variabilities within the norm, as well as process boundary conditions.

The work starts with a literature review about hot work tool steels and theoretical basics about microstructure, heat treatment and modelling.

Subsequently, in chapter 3, the investigated materials and considered heat treatment conditions are described as well as the whole experimental program.

In chapter 4, both the two stage FE-modelling of the extrusion process in DEFORM and ABAQUS and the microstructure modelling; which consists of two main parts, namely the precipitation and the dislocation density evolution calculations is explained.

Chapter 5 contains all experimental creep, fatigue and creep-fatigue test results (5.1) as well as the microstructure characterization (5.2). In chapter 5.3 the FE-simulation results of the extrusion process, damage evolution and lifetime prediction are mentioned. Furthermore the outcome of the precipitation calculations in MatCalc and the results of the dislocation density evolution calculations in MathCad are stated.

In chapter 6 the opportunities and challenges of the thesis are discussed and the work is summarized in chapter 7.

2. Literature review

In the following chapter, the tool material alloying concept, the typical industrial service process applications as well as the required microstructure characteristics of the tool to sustain the service loads are described. The developed microstructure shows high temperature strength and therefore it is suitable for hot working processes. Several attempts on describing the microstructure evolution during service have been accomplished. However the basic aim is to account for a reliable lifetime prediction, which can be provided through phenomenological models as well as physical approaches, which are not only valid for one single materials state. A comprehensive literature study on that topic was already done in a Masters Thesis [1] with the novel approach to couple a physical based methodology to account for lifetime during several service conditions.

2.1 Hot work tool steels

Dies for metal forming require a special type of steel, namely cold or hot work tool steels. Materials used as steels for hot forming processes belong to a special type of tool steels, which have to sustain mechanical loads at elevated temperatures as well as abrasive wear. Suchlike steels are classified as hot work tool steels, AISI type H. The development of the tool steel history is generally regarded to the evolution of steels in general, but the beginning of tool steel history is generally regarded to the year 1740 [2]. Much has happened in the development since then and today there exist numerous types of tool steels, but the desire to increase the performance of the tool steels still remains. The most important demands on the tool material are advanced hot strength, toughness, creep resistance, thermal conductivity and low thermal expansion as well as temper resistance and microstructural stability [3].

Hot work tool steels are commonly used in a quenched and tempered condition. An appropriate strength can be achieved after tempering at around 550-650°C, depending on the alloy composition, which causes a hardening reaction, involving the precipitation of secondary hardening carbides [4]. To maintain the properties at elevated temperatures, an increased temper resistance is required.

Strong carbide forming elements such as vanadium, chromium, tungsten and molybdenum are responsible for an effective secondary hardening peak. When the tool material is subjected to elevated temperatures, these elements play an important role, since they precipitated as fine alloy carbides, which are not only decelerating the softening processes with ongoing service time, but also increase the tool's hardness.

The service temperature of such tools lies permanently above 200°C. Billet material with temperatures of about 400 to 1200°C can be formed through such a process. The time, where the hot billet material stays in contact with the tool can last from milliseconds up to

minutes and the longer the contact lasts, the higher the tool's surface area gets where high temperature time dependent phenomena such as creep can occur in addition to the cyclic time independent fatigue loads. To account for suchlike loading patterns during service, a hot work tool material has to exhibit four main properties [5], firstly a high tempering resistance to avoid a decrease in hardness due to thermal loads during use, which is maintained by a deceleration of martensite dissolution by alloying elements, precipitation of secondary carbides (Cr, W, Mo, V) and special heat treatment, secondly a demanding hot strength, hardness and wear resistance at high temperatures to ensure deformation and wear resistance, which can be achieved at tempering temperatures around 600°C by solid solution strengthening and precipitation of intermetallic compounds, third a demanding toughness to prevent brittle fractures in zones with high concentrated stresses where also homogeneity and purity are required and fourth thermo-shock resistance to avoid cracks caused by thermal fluctuations can be improved by a good thermal conductivity and low thermal expansion, high toughness, homogeneity and hot strength.

There are several categories of hot work tool steels involving a great diversity, which makes a classification not easy. According to service conditions, different hot and high strength heat treatable steels with or without secondary hardening peak are in use. For service temperatures above 650°C, high strength as well as corrosion resistible Ni-based austenitic hot work tool steels are applied, which show a lower tendency to diffusion creep mechanisms due to their higher atomic packing density. On the one hand, according to their properties, hot work tool steels can be generally classified into following three categories, namely impact resistant hot work tool steels, wear resistant ductile steels and high temperature strength steels and alloys and on the other hand, they can be classified by their main alloying element. The AISI type H hot work tool steel is divided into three subgroups according to the dominant alloying element, which are in that case chromium, tungsten or molybdenum hot work tool steels.

2.2 Microstructure of a complex hot work tool steel

The as-received condition is generally soft-annealed with spheroidal carbide fractions embedded in a ferritic matrix. The chromium alloyed AISI H11 tool steel, also found among the material number 1.2343 or X38CrMoV5-1 or Böhler trade mark “W300” is the major investigated material in the work and also compared to the “W400”, which has a similar alloying concept but a more extensive metallurgical production route guaranteeing a finer and higher homogeneity of the microstructure.

To achieve the required mechanical properties, the as-received tool material undergoes a complex heat treatment procedure after the final tool profiling, which varies according to the alloy composition. In Fig. 2.2 a common heat treatment for AISI H11 tool steels is demonstrated. For low alloyed steels, austenitization temperatures around 830 to 900°C and 1000 to 1080°C for high alloyed tool steels are usual.

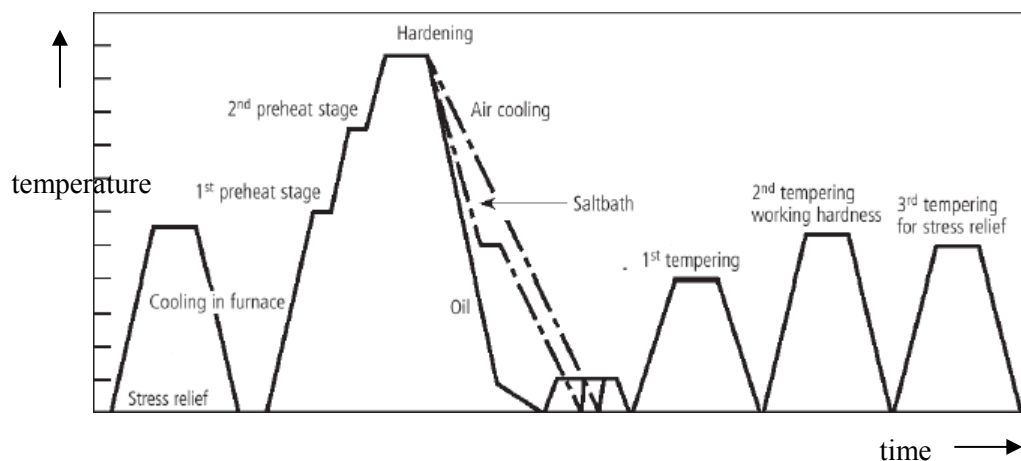


Figure 2.2: Schematic time-temperature guidance for the heat treatment of an AISI H11 tool steel [6].

Adequate preheating steps reduce thermal stresses in cross sectional variations and between edge and core of the component. Lower hardening temperatures are adjusted for tools with high required toughness, complex geometries and small section thicknesses, higher hardening temperatures are common for massive components [6].

The quenching medium, e.g. air, oil, warm bath, salt bath or nitrogen for vacuum hardening or cryogenic treatment, is dependent on the steel grade. Too low quenching rates cause pre-eutectoid carbide precipitates or lead to high amounts of bainite, whereas too rapid quenching causes distortion and stress induced cracks. The tempering temperatures are around 550 to 650°C, usually in two or three separate steps each lasting for one to two hours. The higher the tempering temperature, the higher is the decrease in hardness due to the decomposition of martensite and the tougher the material becomes. The considered W300 tool steel shows a distinct secondary hardening maximum due to precipitation of so called secondary carbides and the transformation of retained austenite into martensite [6]. The most

stable carbide in this steel is the vanadium carbide, hence also playing an important role in the heat treatment, because they are responsible for pinning grain boundaries in order to inhibit grains from growing and due to their high temperature stability, they allow elevated austenitization temperatures avoiding the negative effect of too much grain growth. It has been shown that V:C ratios close to stoichiometry gives a better secondary hardening effect as well, simply because the amount of VC available for precipitation is greater [4]. Studies have shown that decreasing the chromium and increasing the molybdenum content will generate more stable carbides, because the chromium rich carbides M_7C_3 and $M_{23}C_6$ can easily coalesce and coarsen, which has negative influences onto the mechanical properties.

To minimise the wear rupture of dies, high quality hot work tool steels are in use and in addition, several surface treatments, such as nitriding, are introduced to increase wear resistance of the tools. Nitriding consists of introducing nitrogen into metallic materials to improve their surface hardness, wear and corrosion resistance, as well as fatigue life. During nitriding of steels, two different structures are formed from surface to core, known as the compound layer and diffusion region. The compound layer consists of iron nitrides of the phase (ϵ - $Fe_{2-3}N$), gamma phase (γ' - Fe_4N) or of a mixed phase ($\epsilon + \gamma'$) developed at the surface. Wear characteristics of the compound layer depend on many factors such as compound layer composition (epsilon/gamma), compound layer thickness, mode of mechanical loading, etc. [6]. On the other hand, the diffusion region causes an improvement of fatigue strength when compared to an untreated material. In the material, nitrogen atoms are also dissolved interstitially in excess in the ferritic lattice, which provides the formation of nitride precipitates [7].

The microstructure can be described with respect to several parameters, which influence the mechanical properties of the material in specific manner. The considered microstructure parameters are listed as follows:

- precipitation state for the evolved precipitate's volume fraction, f_v^p , particle size, r_p and number density N_v^p
- grain size
- subgrain radius r_{sub}
- subboundary misorientation angle θ
- dislocation density ρ_{tot}
 - mobile dislocation density ρ_m
 - subboundary dislocation density ρ_b
 - static dislocation density ρ_s

The meaning of each microstructure parameter related to the physically based dislocation density evolution model will be explained in the following.

2.2.1 Precipitates

A basic mechanism in hot work tool steels to achieve advanced mechanical properties is precipitation hardening. The nature of interfaces is important for the estimation of the interaction behaviour of dislocations with precipitates. Commercial alloys are commonly heterogeneous, i.e., comprise second phases in a solid solution matrix. Dislocation motion in such systems has to take into account solid solution hardening and precipitation hardening. Shearable precipitates essentially affect the yield stress only, while the hardening behaviour of the respective alloy is akin to that of the pure matrix materials or its solid solution. Non-shearable particles affect plastic flow mainly in two ways. First, they increase the yield stress by the Orowan stress, τ_{or} :

$$\tau_{or} = \frac{Gb\sqrt{f_v^p}}{r_p} \quad (2.1)$$

with G denoting the shear modulus, b the burgers vector. Second, they drastically increase the hardening rate due to the plastic zone (geometrically necessary dislocations) in the surrounding area of the particles. The dislocation concept introduced here does not lend itself easily to accommodate these physical processes, but they can be accounted for qualitatively by the basic equations derived so far. A higher yield stress can be represented by a larger glide resistance as expressed by a larger activation energy Q for glide [8]. The increased hardening rate is influenced by a modification of the slip length, i.e., by incorporating the precipitate spacing, λ_p :

$$\lambda_p = \frac{r_p}{f_v^p} \quad (2.2)$$

in the effective slip length. In particular, for elevated temperature deformation, λ_p may depend on time, since precipitation and Ostwald ripening may occur during deformation. A concept proposed by Estrin and co-workers [9] is used in order to account for microstructure changes regarding the evolution of precipitates.

2.2.1.1 Secondary hardening precipitates

Secondary hardening precipitates, which are responsible for the hardness peak evolving during tempering, are mostly carbides formed at temperatures above 500°C. The highest volume fractions of carbides and other precipitated phases in the X38CrMoV5-1 hot work tool steel are

- MX (V(C,N)),
- M_3C (Fe_3C),
- M_6C (Cr_6C),
- M_7C_3 (Cr_7C_3),
- $M_{23}C_6$, ($Cr_{23}C_6$),
- M_2C (Mo_2C) and
- Laves phase.

In general, on the one hand chromium is partly substituted by molybdenum in the Cr_xC -carbides, and on the other hand, the molybdenum is partly substituted in the Mo_xC -carbides by chromium elements. Subsequent TEM investigations with EDX scans showed that there is at least a small percentage in each carbide, in which the dominant carbide forming element is being substituted by another one.

2.2.2 Dislocations and substructure

Dislocations are a main microstructure constituent and it is necessary to know how they react and which mechanisms are operating when loads are applied. In a bcc-Fe lattice dislocation glide occurs in the direction of the closed packed direction $\langle 111 \rangle$. Closed packed layers in bcc-metals are from the type $\{110\}$. $\{123\}$ planes and non-crystallographic planes $\{hkl\}$ have been found in addition to the dominant gliding planes $\{110\}$, $\{112\}$. With increasing temperature and/or decreasing strain rate, the dominated sliding plane changes (according to Smoluchowsky and Opinsky, in [10]) as follows: $\{110\}$, $\{112\}$, $\{123\}$ and non crystallographic glide, $\{hkl\}$ as shown in Tab. 2.2.

Table 2.2: Gliding plane families in bcc-metals at different temperatures [9].

Metal/Alloy	Gliding plane at		
	RT	low T	High T or low ϵ
Fe	$\{112\}$ $\{110\}$	$\{110\}$ $\{112\}$	$\{123\}$ $\{hkl\}$
Fe-3Si	$\{112\}$ $\{110\}$	$\{110\}$ $\{112\}$	$\{123\}$ $\{hkl\}$

The non-crystallographic glide (hkl) at elevated temperatures and/or low strain rates can be explained by cross-slip of screw dislocations. Precipitates can inhibit dislocation gliding, i.e. the dislocation has to climb or cut the precipitation. The only way to pass incoherent, non-shearable particles is to form an Orowan loop or climb. Climb of dislocations can occur through local or general climb (Fig. 2.3).

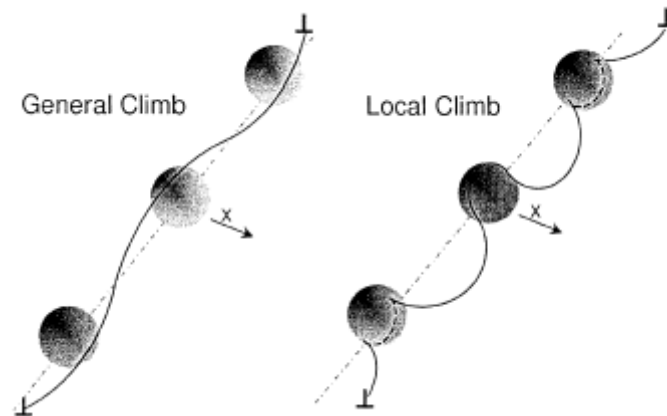


Figure 2.3: Imagination of passing particles by climbing, x denotes the dislocation glide direction [11].

The high stacking fault energy in Fe and bcc Fe-alloys is a reason that stacking faults cannot be observed in these materials. However, atomistic calculations found out that screw-dislocations under passive state split up marginally. This is also a characteristic caused by the high Peierls stress. The approaches dealing with the movement of a splitted, non-planar screw dislocation are related to crystallographic glide, where the core structure changes before overpowering the Peierls barrier [12]. Coherent particles can be passed by both mechanisms, namely through cutting or the Orowan mechanism, depending on the particle size. The energy for cutting small particles is much less than for cutting bigger ones, which are passed by forming an Orowan ring, which is energetically more favourable.

The microstructure of the investigated hot work tool steel at service-ready conditions consists of tempered martensite with martensitic lath structure, fractions of bainite and homogeneously distributed precipitates within the substructure as well as heterogeneous ones formed at lath- and prior austenitic grain boundaries. The development of the substructure for metals with high affinity to the formation of subgrains is schematically demonstrated in Fig. 2.4.

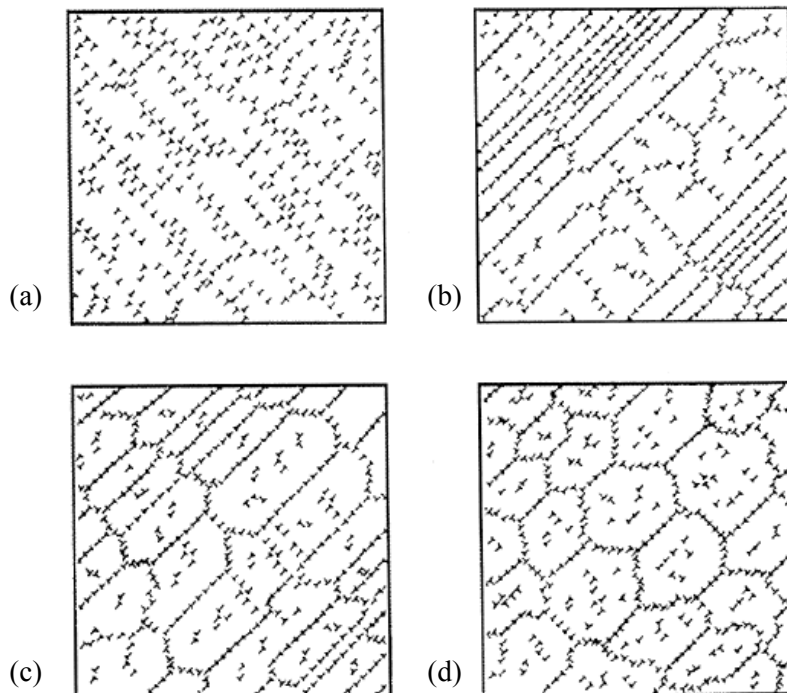


Figure 2.4: Schematical evolution of the substructure during a primary and secondary creep. Loading (a), early range (b) and late range (c) of primary creep and accumulated subgrain structure (d) in the secondary creep range [13].

Due to recovery during creep, the cellular structure is transformed into a substructure. In contrary to perfect LED-structures (low energy dislocation structures) such as subgrain boundaries, the cell walls are an accumulation of dislocations, which do not all take an LED-position. Cell borders or cell walls consist of dislocation dipoles which annihilate during creep.

Basically the following mechanisms are responsible for subgrain growth [14]:

- Subgrain growth due to reduction of the whole interface energy, at varying specific interface energy by recovery and knitting processes in the subgrain boundary or regions close to the boundary, nucleation of subgrains by transition of a critical dislocation density in the inner subgrain,
- recovery of dislocations at the subgrain boundary, and
- knitting processes: knitting out and knitting in of dislocations

For a movement of subgrain boundaries, it is necessary that the dislocations in the subgrain boundary are able to glide and climb. Climbing of dislocations is the slower and determining step that limits the subgrain boundary mobility. In general it is known that the subgrain structure in metals with a high stacking fault energy γ_{SFE} , at homologous temperatures of about $0.3-0.4T_m$ is formed due to energetical factors. The character of this two-dimensional dislocation structure reaches from ideal conceptions of a low energy dislocation structure (LEDS) to clews of dislocations, which can be associated with cell walls. Following general statements can be formulated [15]:

- In metals with a low stacking fault energy γ_{SFE} , which have no tendency to form subgrains, recrystallisation can occur.
- The propability of a cell or network formation decreases with decreasing stacking fault energy, which is a reason of advanced split-up of dislocations, which impedes a cross sliding of screw dislocations. Solid solution generation decreases the stacking fault energy and minimizes the affinity to cell creation.
- Generally the size of the cell expands in relation to the steady state with increasing stacking fault energy.
- The subgrain size in Fe-based alloys is independent of the grain size.

The velocity of a subgrain boundary v_{sg} can be described by the attempt of Einstein [16]

$$v_{sg} = M_{sg} p_{sg} \quad (2.3)$$

with M_{sg} standing for the mobility ($[M_{sg}] = [m^3/Ns]$) of the subgrain boundary and p_{sg} depicting the force ($[p_{sg}] = [N/m^2]$) of the subgrain growth. Several models are related to different formulations of the driving force p_{sg} due to energy minimisation by subgrain growth. The specific interface energy γ_{sg} , according to Read and Shockley [17], of a small angle grain boundary is a function of the misfit θ

$$\gamma_{sg} = -E_0\theta(A + \ln(\theta)) \quad (2.4)$$

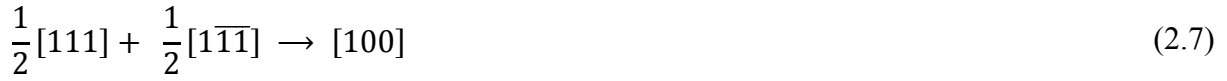
with

$$E_0 = \frac{Gb}{4\pi(1-\nu)} \quad (2.5)$$

and

$$A = 1 + \ln\left(\frac{b}{2\pi r_0}\right) \quad (2.6)$$

as a function of the cut-off radius. Where ν denotes the Poisson ratio and r_0 the subgrain radius. The approaches by Sandström, Humphreys and Saetre [16, 18] can be adapted in the case of creep by implication of the kinetics of the dislocation density in the subgrain boundaries ρ_b and therefore with a inconstant specific interface energy γ_{sg} . The amount of the misfit θ , see Eq. 2.4., is caused by the dislocations in the subgrain boundary with the dislocation density ρ_b . According to Orlova et al. [19], subgrains in α -Fe contain of a tilt as well as of a torsion part. Besides dislocations of type $\frac{a}{2}\langle 111 \rangle$, also dislocations with the Burgers vector $\langle 001 \rangle$ can be found. The formation of these dislocations is established by the reaction



If two interacting dislocations are of screw type, a pure screw dislocation with the Burgers vector $[001]$ is the result.

The plane of the investigated sheet lies parallel to the plane of the network. Dingley et al. [20] found out that the percentage of $[100]$ dislocations is about 20. Investigations of the dislocation structure of subgrain boundaries at deformed and recovered α -Fe by thin-sheet experiments are already published manifold [10]. It was possible to explicate and correlate the form of subgrain boundaries and networks by $a\langle 111 \rangle$ -edge-dislocations. Total concordance with the theory of Frank is given for some observed networks only for the account that $a\langle 110 \rangle$ -dislocations are formed by cutting $a\langle 100 \rangle$ -dislocations. In the case of only rotary boundaries, the fractions of dislocations, which imply an acute angle, react by the energy law. The sections of dislocations, which imply an obtuse angle would react to an $[110]$ dislocation. If the interbreeding dislocations do not lie in the rotary plane, both reactions can occur [21, 22]. The density of interface dislocations is defined as length per unit of area or break-through points per unit of length. According to Gottstein and Argon [23], the density reads

$$\rho_b^l = \frac{\theta}{b} = \frac{1}{h_b} \quad (2.8)$$

with $[\rho_b^l] = [\text{m}^{-1}]$ as a function of the misfit-angle θ and the distance between the dislocations in the subgrain boundary h_b . Therefore $\theta \sim \sin \theta$ and $\theta \ll 1$ is assumed. If the volume-density ρ_b of the subgrain boundary dislocations is considered, then

$$\rho_b^l = \rho_b D_{sub} \quad (2.9)$$

with D_{sub} as the subgrain diameter, is obtained. Introducing ρ_b^l results for the factor ρ_b by

$$\rho_b = \frac{1}{h_b D_{sub}} \quad (2.10).$$

The assumption that the subgrain boundary generally only consists of two dislocation families with distances of the same amount, the distance in the subgrain boundary, finally results in

$$h_b = \frac{2}{\rho_b D_{sub}} = \frac{1}{\rho_b r_{sub}} \quad (2.11).$$

Additionally to intrinsic dislocations, there is also an accumulation of dislocations at the interface. Such dislocations, which are immobilised after a gliding process, are defined as static dislocations, which do not adopt an LED-position and are comparable to dislocation dipoles in cell walls. Due to the density of these static dislocations ρ_s , it is possible to describe the change of nature of the substructure-interfaces during creep of cell walls to subgrain boundaries.

The qualitative developing of misorientation with increasing deformation for various materials is known from literature facts. According to investigations of cubic metals, the misorientation among subgrain boundaries increases with advanced strain, whereas in the investigation of pure iron, the distance between the dislocations h_b and the angle between subgrain boundaries from a distinctive strain on, remains constant and embraces significant smaller values 1.5° instead of $> 3^\circ$. Initiating at small values ($\sim 10'..20'$), the devolution of θ as a function of time or strain shows a comparative linear rising in the primary and partly in the secondary creep range until a saturation value is approached. The kinetics of misorientation is similar to, or dependent on several kinetic distributions of other microstructure parameters such as the dimensions of subgrains or the dislocation density [22, 24].

2.3 Loading patterns and damage mechanisms during service

Hot work tool steels are thermally and mechanically loaded during complex load cases. Depending on the load type, the tool will exhibit a certain service lifetime. High cyclic thermal loads cause time dependent creep, cyclic mechanical loads cause time independent fatigue mechanisms. One cycle can last splits of a second to minutes, depending on the process and lifetime is commonly defined as number of cycles to failure. The interaction of these load cases can generate creep-fatigue, which causes an earlier component failure than only creep or fatigue. Hot work tool steels are applied in a temperature field over 200°C to 500°C. In extrusion industry, the thermal load occurring during service depends on the processing of specific metals and alloys, see Fig. 2.5.

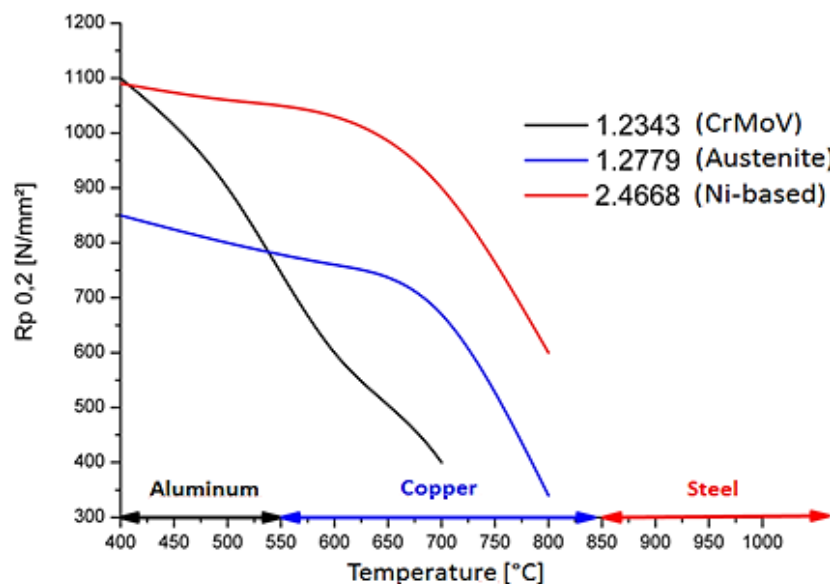


Figure 2.5: Thermal loading onto the hot work tool material in relation to the processed metal.

If the material is exposed to temperatures higher than $0.3 T_m$, which actually means temperatures above 350°C to 400°C, the tool steel will additionally show creep deformation phenomena (Fig. 2.6).

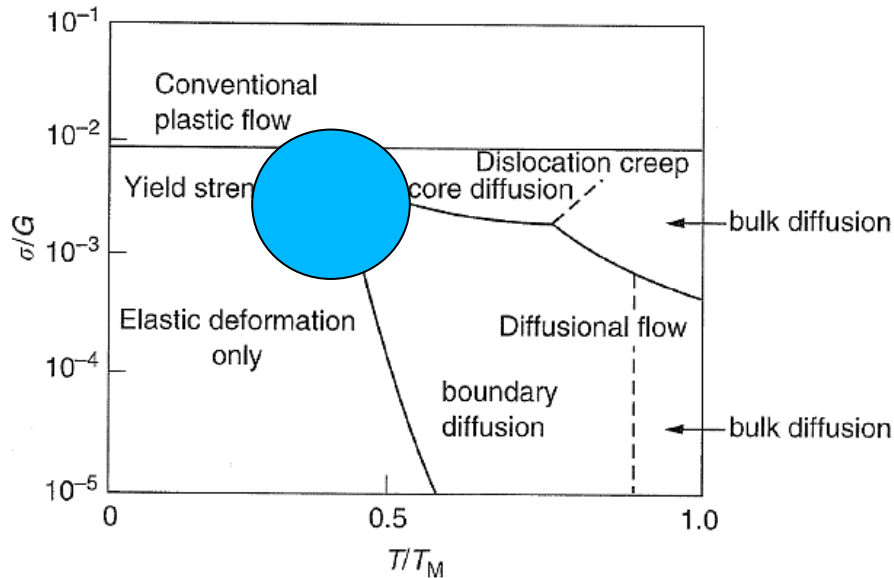


Figure 2.6: Deformation mechanisms at different stresses and temperatures [25]. The occurring critical thermo-mechanical load range is marked.

The creep mechanism is naturally determined by the temperature, stresses and strain rates, respectively. At high stresses and strain rates, dislocation creep and core diffusion is expected. At lower stresses and high homologous temperatures, diffusion creep (Coble creep via grain boundaries, and at even higher temperatures Nabarro-Herring creep via the lattice) occurs (Fig. 2.7). According to calculations of Sommitsch et al. [26, 27], dislocation creep can be considered as the dominant creep mechanism in hot work tool steels during use.

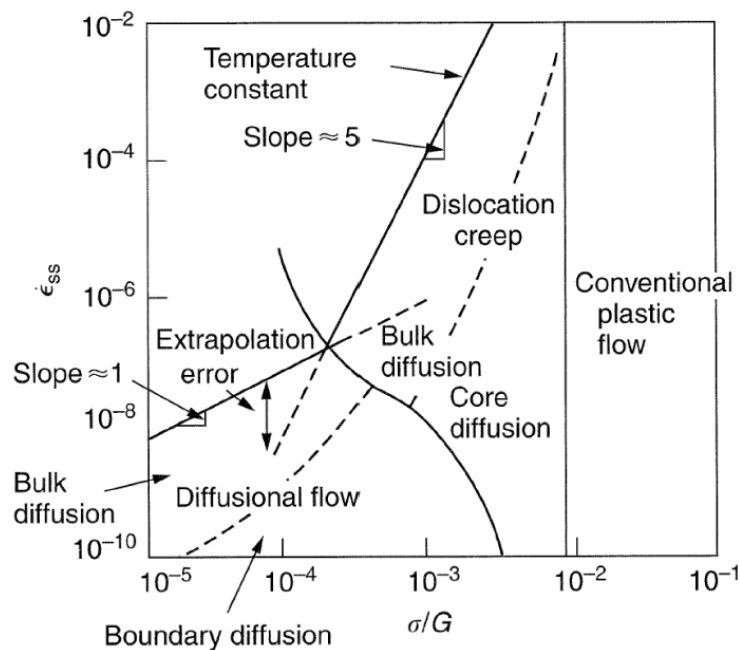


Figure 2.7: Deformation mechanisms at different strain rates and stresses [24].

Hot work tool steels for extrusion processes are supposed to carry cyclic mechanical loads, which peaks are above the elastic limit and high thermal loads, which enable time dependent creep phenomena. Due to these cyclic loads, which generate plastic deformations, the component is not able to sustain more than 10^3 to 10^5 cycles, which lies in the range of low cycle fatigue and creep. Creep-fatigue occurs due to overlapping of high thermal loads causing creep and cyclic mechanical loads, which cause fatigue. Creep can produce large strain deformation, stress relaxation, and crack initiation and growth (Fig. 2.8). For materials under fatigue and creep loading, the interaction of creep and fatigue has been observed to have different effects on the creep-fatigue life of different materials.

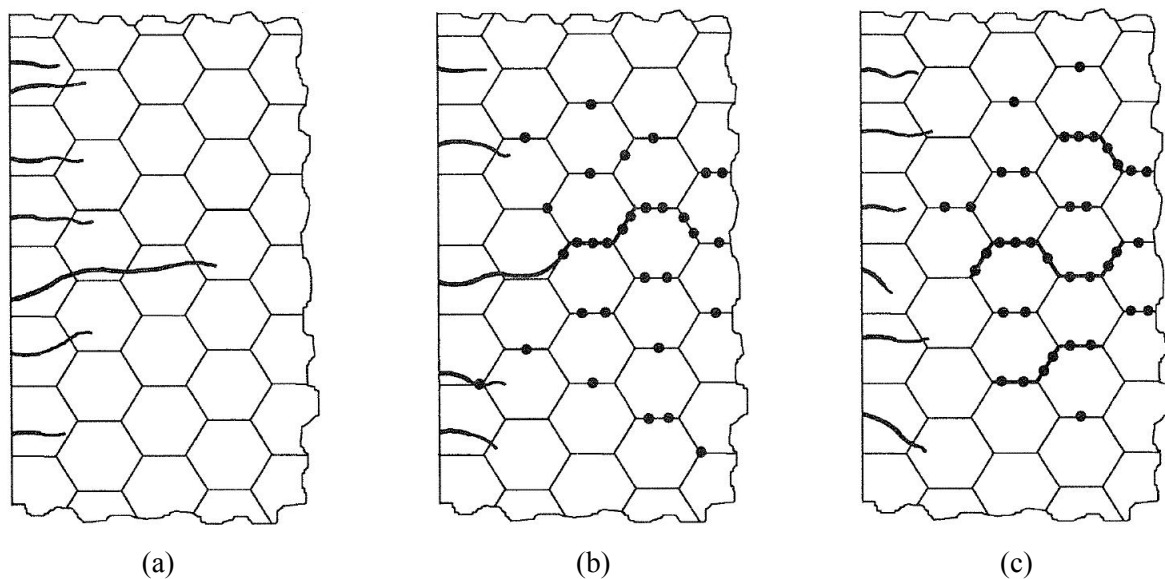


Figure 2.8: Influence of several damage mechanisms on crack propagation at high temperature alternating deformation, in which fatigue damage (a), creep-fatigue alternation (b) or creep damage (c) dominates [28].

Creep-fatigue interactions can be observed in high temperature components in energy- and propulsion technology and industrial hot working processes. The components, which are mainly affected are blades in airplane or gas turbines, hot forging, extrusion or casting dies.

In laboratory experiments it is tried to investigate the effects of the coexistent time independent and dependent loads during practical application of these high temperature materials with the aim of thermal and thermo-mechanical fatigue experiments. Due to a three dimensional inhomogeneous temperature distribution and resulting thermal strains, a thermo-mechanical loaded specimen is regulated strain controlled in the experiment [26]. Several experiments were performed for the hot work tool steel W400, see [27].

In thermal fatigue experiments, one volume fraction of a real component with specific temperature and load distribution is considered. In common such experiments are conducted on specimens with cylindrical or rectangular cross sections in a servo-hydraulic test device, operating in a closed regulator circuit [28]. A constant level of the plastic strain amplitude is advantageous for the interpretation of the measured cycles to fracture, because the plastic strain amplitude determines the lifetime in the LCF-range decisively. In principal, user defined load distributions and phase shifts between mechanical and thermal cycles are possible. However in practical experiments, triangular in-phase (IP) and out-of-phase (OP)

specified values for strain and temperature can be applied, which simulate the worst load cases in real components and are defined as basic types of thermo-mechanical fatigue experiments. TME experiments with a phase shift of $\pm 90^\circ$ between load and temperature distribution can be realised, which are known as *diamond – clockwise* (DCW) and *diamond – counterclockwise* (DCCW), Fig. 2.9 [29].

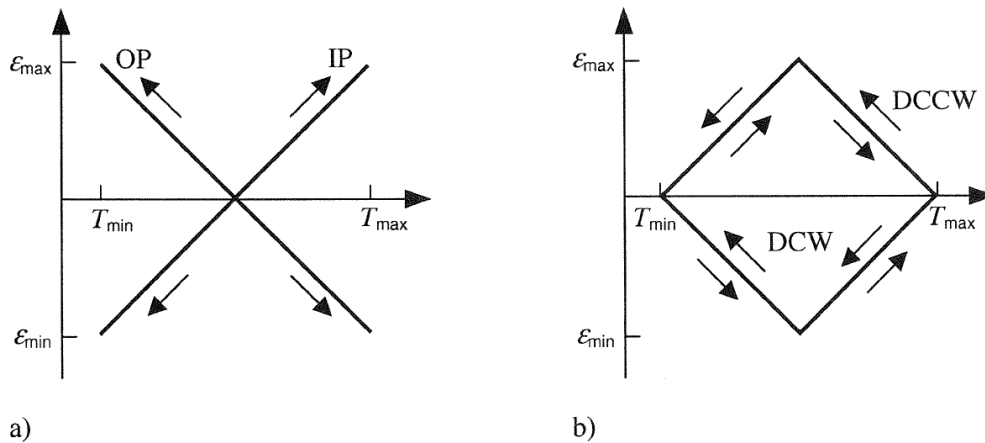


Figure 2.9: Schematical phase distribution between temperature and strain at TME-load for an IP and OP experimental guidance (a) and a DCW and DCCW load (b) [29].

According to a fracture mechanical consideration, creep-fatigue exists, if the crack propagation rate is higher than the linear summation of the time dependent fatigue and time dependent creep induced crack propagation rate [30]. Besides the alteration in the damage mechanisms, characteristic growth mechanisms are working, depending on the load cases and material conditions, which are systematically shown in several *Void Growth Mechanism Maps*. By considering growth models for intergranular pores, Riedel [31] calculated the growth rates of different mechanisms and generated a void growth map.

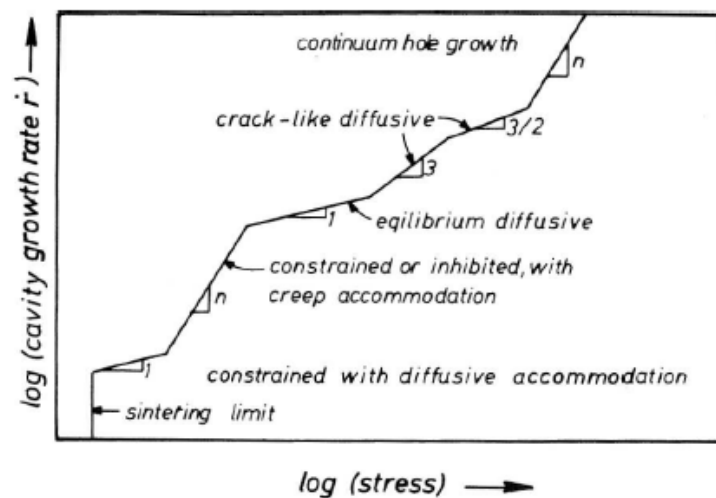


Figure 2.10: Calculated cavity growth rates, schematically [31].

Fig. 2.10 gives a simplified picture of the cavity growth rates calculated from various models and it schematically shows the ranges in which different mechanisms predominate. Of course,

real materials do not necessarily exhibit all of the mechanisms indicated there, it depends on material parameters and on the cavity size and spacing. If, for example the surface diffusion coefficient is large, crack-like cavity growth may have no range of validity between equilibrium diffusive growth and plastic hole growth. Fig. 2.11 summarises the times to cavity coalescence calculated for instantaneous cavity nucleation at the beginning of a test. In many cases, the time to cavity coalescence is approximately equal to the time to rupture, but in the case of constrained growth, this relation is questionable.

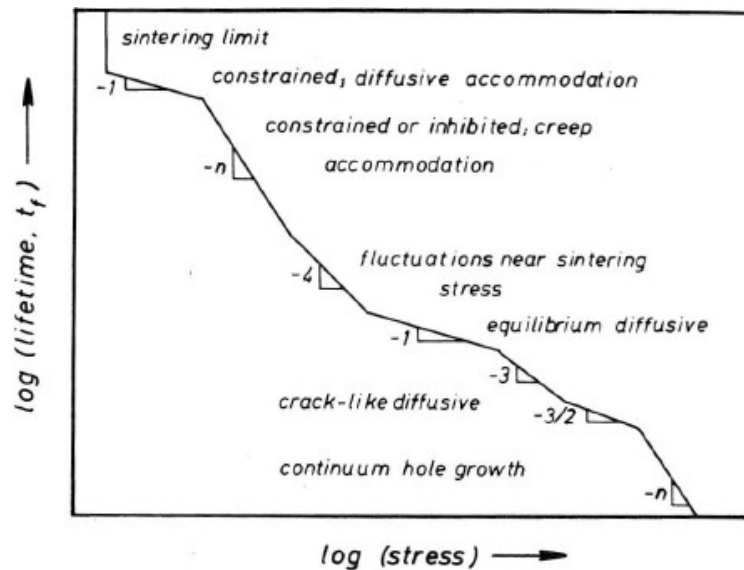


Figure 2.11: Calculated lifetimes for instantaneous nucleation, schematically [31].

To make a precise prediction for the point in time when failure occurs, an indicator is required. This indicator has to be described by the parameters such as pore radius, pore density and distance of pores for both, intra- and transgranular pores. The coagulation of pores to cracks (see Fig. 2.12) is not considered in that way, but as an increase of the stress due to reduction of area, which leads to the changeover to fracture mechanical theory [22].

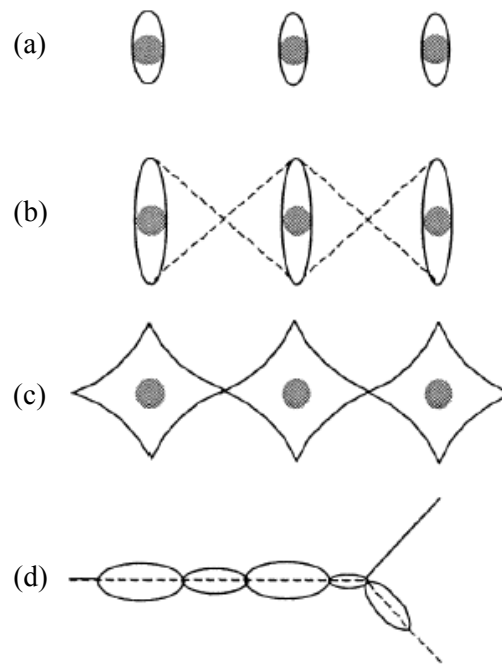


Figure 2.12: Coagulation of trans- and intragranular pores. (a), (b) and (c) illustrate the growth and coalescence of transgranular pores, whereas in (d) the critical state of coagulation of intragranular pores at a grain boundary is depicted [32].

If given parameters are applied, three different failure criteria can be implemented:

- reaching a critical stress,
- exceeding a critical damage parameter D_{crit} and
- coagulation of pores, if $2r \geq \lambda$.

Polycrystalline metals exhibit a variety of intrinsic stress concentrated areas, such as grain boundaries, triple junctions and inclusions, which can rapidly initiate a crack under an applied cyclic load. Therefore, even with a highly polished surface, cracks can still initiate in these regions as long as the resolved shear stresses in the vicinity of these inherent microstructural defects are sufficiently high and aligned favourably along preferential slip systems of the material crystal structure (e.g. $\langle 111 \rangle \{110\}$ systems in face centered cubic (fcc), $\langle 110 \rangle \{111\}$ in body centered cubic (bcc) metals). If considered at the sub-micron level, lattice defects such as dislocations and the evolving dislocation structure ultimately controls the damage initiation process [33, 34].

2.4 Microstructure evolution during cyclic thermo-mechanical loads

Cyclic thermo-mechanical loads stress the material in various ways. The main phenomena, which determine the material's strength at a certain point in time during service are the counteracting hardening and softening processes. Both mechanisms are influenced by the homogeneity in the material, by the grain size, precipitation state as well as the initial dislocation distribution and density as well as the cell- or subgrain size.

2.4.1 Hardening processes

Hardening takes place due to the dislocations produced by the plastic deformation of a metallic material. Point defects such as vacancies and interstitial atoms, which are also generated by inelastic deformation, are highly mobile and too few in number to play an important role to account for the hardening effect. Dislocations introduced into a crystal can harden it in two ways: Firstly they increase the internal stresses and which can hinder the development of loops from active sources by elastic interactions. Secondly the increase of the forest dislocation density, which penetrates slip planes and hence inhibiting the dislocations, which are associated to the affected slip planes, from gliding. Thus the development of the loops requires that proportionally more jogs are formed. When the elastic limit, σ_y , which is meant to be the stress at the start of plastic deformation, does not go back to zero, a few Frank-Read sources will start emitting loops [35]. Three types of Frank-Read sources are known, which depend on the orientation of the burgers vector of the dislocation pairs to one another [36, 37], see Fig. 2.13.

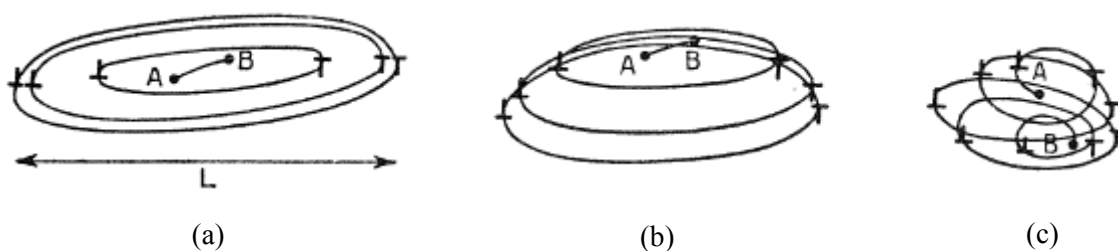


Figure 2.13: The three types of Frank-Read sources: (a) flat; (b) spatial; (c) spiral [34].

Commonly, the macroscopic strength σ can be directly connected with the dislocation density ρ through following relation:

$$\sigma \propto \sqrt{\rho}$$

That means that with increasing dislocation density the strength increases proportionally, with each different material having its specific factor.

2.4.2 Softening processes

The material's state during loading is basically unstable, because the produced dislocation structure does not lie in a thermodynamic equilibrium. At comparatively low temperatures, the plastic deformation maintains due to mechanical stability, because the dislocations remain in a mechanical equilibrium of forces after load retraction. At higher temperatures, such a mechanical stability can be overpowered by thermal activated processes, when dislocations are able to circumvent their inhibition by cross slip of screw dislocations or climbing of edge dislocations. Thereby dislocations can switch to other gliding planes and adopt energetic advantageous positions, which are able to annihilate one another or leave the crystal. This procedure is known as recovery and causes a decrease of dislocation density and produces specific dislocation structures, consisting a network of small-angle grain boundaries, which is defined as polygonisation. The recovery is based onto the interaction of dislocations due to their wide ranged stress field. The interaction force F of an edge dislocation with the Burgers vector b_1 upon a parallel dislocation with the Burgers vector b_2 yields to

$$F = \tau b_2 = \frac{Gb_1 b_2}{2\pi r_v (1 - \nu)} \cos\Phi \cos 2\Phi \quad (2.12)$$

with r_v and Φ determining the position of one dislocation in relation to another, and ν denotes the poisson ratio. If both dislocations have the same sign and maintain on the same gliding plane, i.e. $\Phi = 90^\circ$, the force is positive and they repel. If both dislocations have antipodal signs, the force is negative, they attract, fuse and annihilate one another. This process is responsible for a decrease of the dislocation density. If the dislocations with antipodal signs do not have the same gliding plane, but one in-between, a dislocation dipole is formed, which corresponds to a chain of vacancies and has a significant lower energy than both single dislocations, where annihilation can result due to climbing by the distance of one atomic layer. This annihilation also occurs by attraction and manifold climbing over a couple of layer distances. If the gliding planes are far away, so that $\Phi > 45^\circ$, the sign changes according to Eq. 2.12 and anti-parallel dislocations repel, whereas parallel dislocations attract each other. The equilibrium position of two parallel dislocations is reached when they are lying upon each other, then $\Phi = 90^\circ$ and $F = 0$, see Eq. 2.12. Every deflection out of this position finally ends up in the idle state. If many dislocations arrange one upon the other, a significant minimisation of dislocation energy is caused. Such a periodic arrangement of edge dislocations causes a dislocation interaction, which reduces the range R_a of the stress field to the magnitude of the dislocation distance r_v . If there are ρ_b^l dislocations per cm in such an arrangement, the energy per unit of area amounts to

$$\gamma_{sg} = \rho_b^l \left[\frac{Gb^2}{4\pi(1 - \nu)} \ln \frac{r_D}{2b} + E_C \right] \quad (2.13),$$

where E_C denotes the energy of the dislocation core. The described arrangement approximates a small angle tilt grain boundary (SAGB) and γ_{sg} denotes the specific grain boundary energy. The formulations considering the orientation influence of the adjacent subgrains can be found in detailed literature [38]. A complete regional network can be built up by several small angle grain boundaries consisting of screw, edge and hybrid dislocations, which has a much lower energy than randomly distributed dislocations.

2.5 Modelling the lifetime at cyclic thermo-mechanical loads

To account for the complex interaction of pure fatigue, creep and environmental conditions at practical relevant dimensioning of high temperature components, several methods and approaches exist. According to Danzer [39], lifetime prediction methods can be classified into four main groups:

- empiric models
- damage mechanism methods
- physical models
- fracture mechanical methods

An incremental multiaxial lifetime prediction law (IMLP), which consists of the three-dimensional thermo-viscoplasticity theory based on overstress (TVBO) combined with a multiaxial damage accumulation law (MDA) to compute the lifetime or cycles to crack initiation is considered [37]. This theory developed by Yeh and Krempl is for infinitesimal strain and orthotropy. It is of unified type and does not use a yield criterion and loading/unloading conditions. The elastic strain is formulated to be independent of thermo-mechanical path and the inelastic strain rate is a function of overstress, the difference between the stress σ , and the equilibrium stress g . The long-term asymptotic values of stress, equilibrium stress, and kinematic stress rates, which can be obtained for a constant mechanical strain rate and ultimately constant temperature, are assumed to be independent of the thermal history as well as the ultimate levels of the rate dependent overstress and the rate independent contribution to the stress. Therefore, the material functions and constants can be obtained from isothermal tests within the temperature range of interest. All material constants can be functions of the temperature. This dependence is not explicitly displayed. The temperature dependence can be an usual Arrhenius relation or can deviate from that approach [38]. The precisest results for complex load cases should be obtained by physical models, which means models describing the damage evolution on the basis of movement of atoms, vacancies and dislocations, because these models describe the damage evolution by taking into account physically based functions. Physical methods to describe high temperature deformation were developed to model the pore growth during creep [24]. Although they have no free fitting parameters, they describe the growth rate of pores in their applicable range

quite well. The occurring parameters in these models can be determined metallographically (over distance between pores or grain size) or they are common physical parameters such as diffusion coefficient and atomic volume.

For technical alloys, the damage mechanisms during application conditions are not often known exactly. In general it is not known in advance, at which load which damage mechanisms occurs and which physical model is appropriate to calculate the lifetime. But in some single cases it could be shown that some empiric and damage mechanic models conform to physical models. Thus the meaning of physical models for lifetime prediction at this time is to show the physical background for the empiric and damage mechanic models. This can be useful to determine the load ranges, which are described by empiric models, and to define the limits of these methods [28].

3. Experimental

To ensure for a reliable confirmation of simulated microstructure evolution predictions of tools in service, i.e. dislocation density evolution, precipitation size and volume fraction evolution as well as adjusted thermo-mechanical boundary conditions of the process itself, a comprehensive experimental program was performed, which can be subdivided into two main objectives to achieve. On the one hand, experimental hot extrusion tests were performed to evaluate thermal and mechanical loads the tool has to withstand during service, see chapter 5.1.1 and on the other hand, physical simulations, see chapters 5.1.2 - 5.1.4, to consider the behaviour of the tool steel itself according to the prior evaluated boundary conditions and industrial process-near loading conditions, to reproduce the process related microstructure evolution conditions.

To ascertain for all the phenomena, i.e. multiple material responses, which can occur in that loading regime, creep as well as fatigue loading influences onto the microstructure and damage evolution, both load cases were considered in addition to the performed process-near creep-fatigue loading pattern.

3.1 Material and heat treatment

The investigated materials were W300 ISODISC and W400 VMR grade (vacuum melted and remelted), which guarantees a higher homogeneity of the microstructure. The austenitic hot work tool steel W750 was also considered for phenomenological material modelling and lifetime prediction for service temperatures above 600°C, whereas the application of W300 and W400 is limited to temperatures below the last annealing step, which lied at 585°C. The chemical composition of the considered hot work tool steels is shown in Tab. 3.1.

Table 3.1: Chemical composition of the ferritic hot work tool steels W300 and W400 as well as the composition of the austenitic tool steel W750.

Grade	C	Si	Mn	Cr	Mo	Ni	V	Ti	Al	B
W300	0.38	1.10	0.40	5.00	1.30	-	0.40	-	-	-
W400	0.37	0.20	0.30	5.00	1.30	-	0.50	-	-	-
W750	0.02	0.20	1.40	15.0	1.30	25.0	0.30	2.70	0.25	0.005

The heat treatment was applied to a final hardness of 48-50 HRC as usual for industrial service conditions for that specific tool material. The detailed plan is given in Tab. 3.2.

Table 3.2: Heat treatment sequence of the specimens, which were subsequently tested.

Material	Austenitization temperature [°C]	Austenitization time [min]	Quenching rate λ [s ⁻²]	Annealing temperatures [°C]	Annealing times [h]	Hardness [HRC]	Matrix structure
W300	1020	40	0.6	550/585/585	1 / 2 / 2	49	martensitic
W300	1020	40	15	550/585/590	1 / 2 / 2	48.5-49	bainitic
W400	990	40	0.6	550/585/585	1 / 2 / 2	49-49.5	martensitic

In Figs. 3.1 and 3.2 the geometries of the tested creep and fatigue as wells as creep-fatigue specimens are shown.

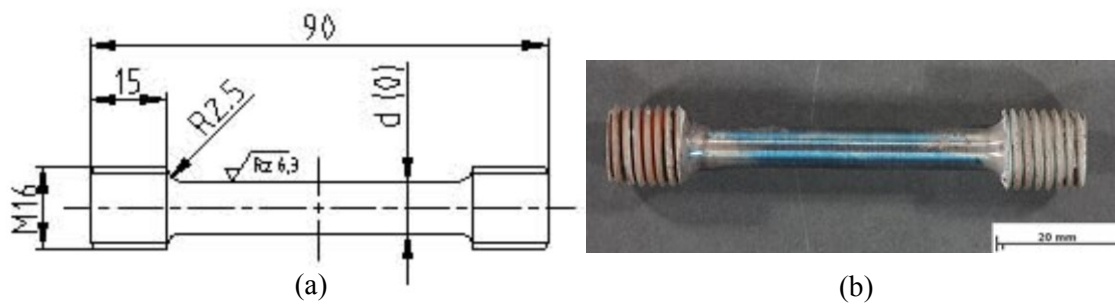


Figure 3.1: Schematic drawing (a) of a short term creep specimen and (b) after in situ testing.

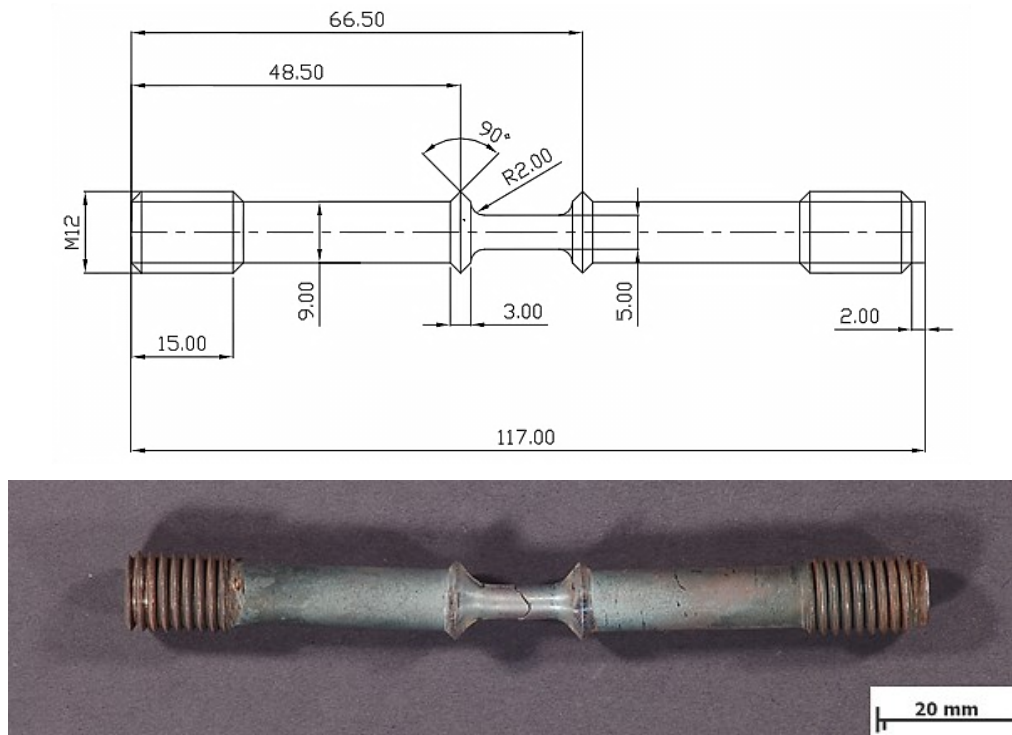


Figure 3.2: Schematic drawing of a fatigue test specimen (above) and after rupture.

The fatigue and creep-fatigue specimens sharp edges for measuring and control of the applied strain, are clearly visible in Fig. 3.2.

3.2 Experimental verification of boundary conditions during a hot extrusion process

An accurate simulation as well as a reliable experimental validation of the boundary conditions during a hot extrusion process is mandatory. The magnitude of the occurring thermo-mechanical loads, i.e. pressure and temperature as well as friction conditions, strongly influence the tool's lifetime.

3.2.1 Pressure and temperature

To experimentally determine boundary conditions for copper and aluminium extrusion processes, respectively, and to compare them with the values used for finite element simulations, an experimental extruding plant was constructed to perform miniature extrusion tests to obtain temperature and pressure distributions in the container via a special constructed measurement system (Fig. 3.3). A hydraulic 100t press, which could ensure a ram speed of 7mm/s at an extrusion ratio of 1:14, was adapted to small scale extrusion experiments (Fig. 3.4). These experimental outcomes were considered to validate cyclic temperature and pressure behaviour during the extrusion process.

The dimensions of the experimental extruding plant were as follows: The length L , inner diameter D_i and outer diameter D_o of the liner, mantle and billet, respectively, are as follows:

Liner: $L = 115$ mm; $D_i = 45$ mm; $D_o = 105$ mm,

Mantle: $L = 115$ mm; $D_i = 105$ mm; $D_o = 270$ mm,

Billet: $L = 100$ mm; $D = 45$ mm.

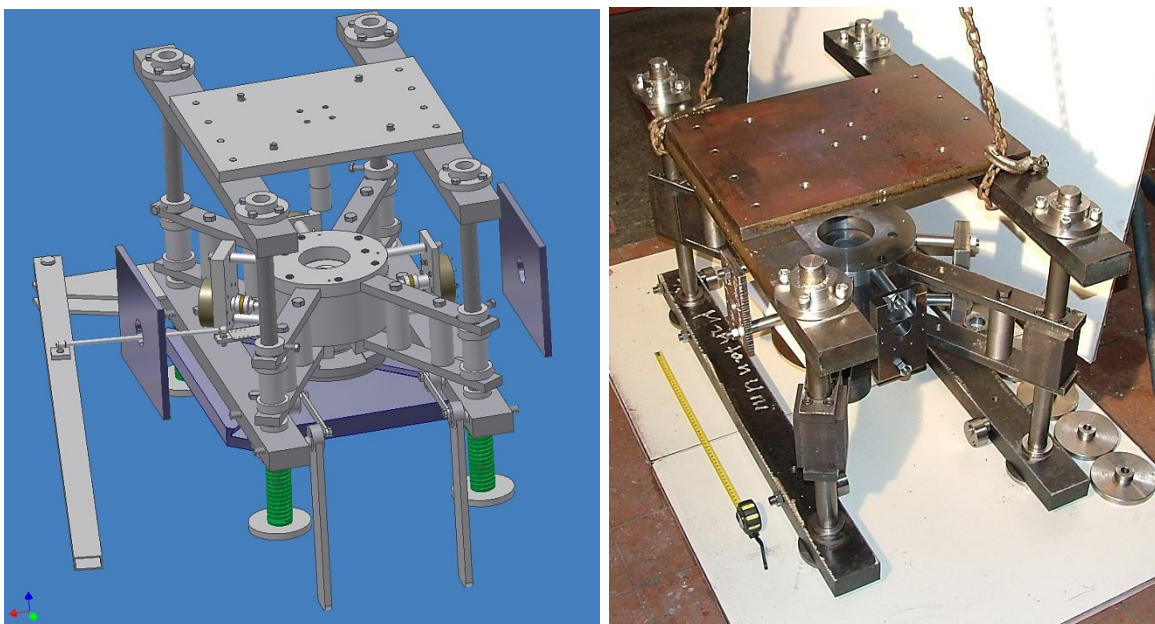


Figure 3.3: Schematical drawing (left) and constructed experimental extrusion plant (right).



Figure 3.4: Experimental extruding plant during application: Remarkable is the heating sleeve (light grey colour, in the centre) around the mantle. The maximum press speed of the adapted hydraulic 100 ton press is 7 mm/s.

The shrink-fitting of the mantle onto the liner was calculated by a misfit of 0.8%. The measuring system for the evaluation of both compressive stresses reacting at the liner and temperature distribution in the container is demonstrated in Fig. 3.5. To obtain a pressure distribution in the liner, three holes at different levels (L1, L2, L3) were drilled into the container, with only a thin container wall thickness left. The pressure force is transmitted through a plug gauge with a ceramic temperature isolator to a load cell (Fig. 3.5(b)). The system plug gauge / load cell sustains the liner wall against damage. The same drilled holes are also used for temperature measurements (Fig. 3.5b). Measurement points were positioned near the inner wall of the liner (T1, T2, T3) and in the centre of the container (T4, T5). Measurement point T2 was also used for heat control, see Fig. 3.5(c).

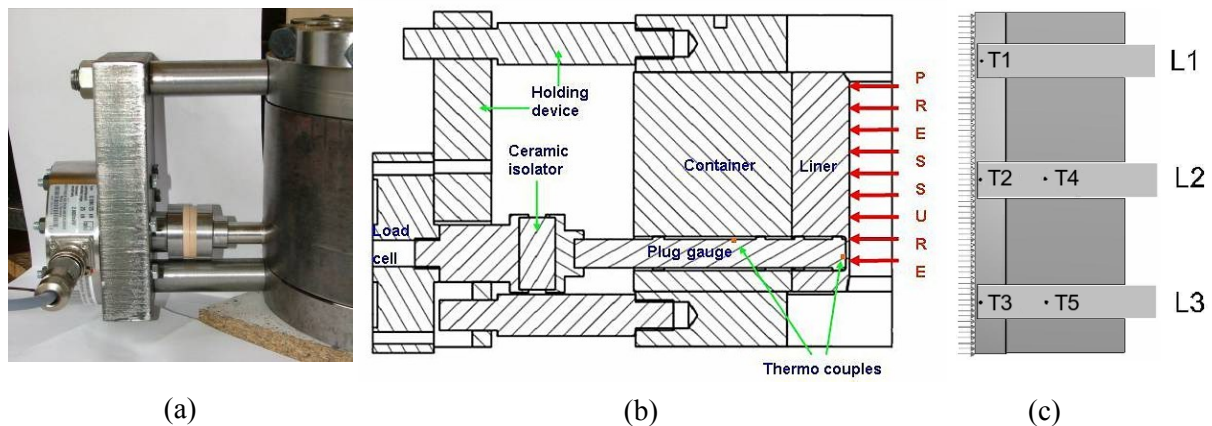


Figure 3.5: Measurement system to obtain both the pressure and temperature distribution at the inner liner wall for copper and aluminium extrusion: (a) Image of the lower measurement point, (b) in detail and (c) definition of pressure measurement levels (L1-L3) and temperature measurement points (T1-T5), schematically. T1, T2 and T3 are positioned about 2.5 mm behind the inner wall of the liner and fixed at the plug-gauge. The extrusion direction is top-bottom.

A possible influence of the tool's surface condition, i.e. a nitrided tool surface or no surface treatment, became a matter of interest when taking into account the friction behaviour. Subsequently, spike tests were performed and simulated with FORGETM in the framework of a project thesis [40], see Fig. 3.6.



Figure 3.6: Experimental set-up to perform the spike test series. In the centre, upper and lower die with the aluminium billet and thermocouples are apparent. The heating sleeve in the left was used to heat up the tools to working temperature, the aluminium billet was preheated in a furnace.

3.3 Creep tests

According to the experimentally validated loads acting onto the tool during service, related creep tests were performed to characterize the pure creep behaviour of the material. The experimental tests were performed at four different temperatures, 500, 540, 580 and 590°C, respectively, with three defined loads, namely 400, 600 and 800 MPa to cover several possible process-related critical thermo-mechanical loading conditions. Therefore a standard creep furnace with constant load was used (Fig. 3.7).



Figure 3.7: Creep furnace used for short term creep tests at constant load.

The disadvantage of short term creep tests at constant load is that soon after the beginning of the reduction of area the specimen fails, which means a short secondary creep range followed by an extremely short tertiary creep range.

3.4 Fatigue tests

To evaluate the cyclic behaviour of the material, pure fatigue tests were performed at the same temperatures as for the creep tests, namely 500, 540 and 580°C, respectively, with a cyclic strain amplitude $\Delta\varepsilon = 1.2\%$ with $R = -1$ and a strain rate $\dot{\varepsilon} = 10^{-3}$. The tests were performed on a hydraulic 100kN compression-tension testing unit with adapted heating, see Fig. 3.8.



Figure 3.8: Testing device for cyclic loading conditions, which was used to perform the experimental fatigue as well as the creep-fatigue test series.

3.5 Creep-fatigue tests

To simulate the material behaviour during process-near service conditions, creep-fatigue tests near the critical temperatures, which were the same as in the creep and fatigue tests for the purpose of reasonable comparison, and also the same cyclic strain amplitude $\Delta\varepsilon = 1.2\%$ with $R = -1$ and a strain rate $\dot{\varepsilon} = 10^{-3}$ with a holding time in compression of 300 seconds (5 minutes) to simulate near process conditions, were performed to evaluate both, lifetime as well as damage evolution and to characterize the microstructure evolution.

3.6 Microstructure characterization

Selected creep, fatigue and creep-fatigue specimen were characterized via light optical microscopy (LOM), hardness tests (HV 10), scanning electron microscopy (SEM) [41], TEM analysis on a Philips CM20/STEM equipped with a GATAN imaging filter [42]. The FEI microscope was operated at 200kV with a LaB₆ cathode. The spectra and images were recorded with a slow scan CCD camera integrated in the GIF [43]. EELS and EDX spectra were recorded in STEM mode, with a probe diameter of about 7 nm, using a Noran HPGe detector with an ultrathin window. The images and spectra recorded with the slow scan CCD camera have been processed with *Gatan's Digital Micrograph*, and were corrected for dark current and ratio variations. For quantitative analysis of STEM images the “three window” and “two window” method can be applied. An adequate study of quantitative analysis of EFTEM elemental distribution images is given by Hofer et al. [44]. When quantitatively analyzing the precipitate parameters, their radii, number densities and volume fractions cannot be observed directly in the distribution maps, but have to be evaluated by stereological methods. The precipitation state can be calculated with the new method developed by Sonderegger [45]. The proposed new correction method is not using one single correction factor, but calculating factors for each precipitate separately. Evidently, this procedure is applicable to any size distribution and varying sample thickness, because systematic deviations are avoided for each single precipitate.

To account for the dislocation density, X-ray diffraction peak profile analyses were performed [46].

4. Simulation

The modelling and simulation workflow, which is described in the following chapter, is split into two main parts, namely the FE-simulation of the extrusion process in ABAQUS/ZMat with the implemented phenomenological Chaboche model to obtain the inelastic strain response of the material with subsequent lifetime prediction calculations according to the approach of Yeh and Krempl [47] and the microstructure modelling by means of physically based equations taking into account the precipitation kinetics as well as dislocation density and substructure evolution [14].

4.1 FE-simulation of the extrusion process

Extrusion tools exhibit a complex strain-time pattern under a variety of cyclic loading conditions and thus are prone to failure by creep-fatigue interactions. Elevated temperature failure by creep-fatigue processes is time dependent and often involves deformation path dependent interactions of cracks with grain boundary cavities. The extrusion industry tries to accelerate the manufacturing process by increasing the billet temperature and/or by accelerating the press speed that raise the loading of the tools. Additionally the tool steel producers develop enhanced more homogeneous and cleaner materials in order to increase the tools lifetime [48]. Finite element simulations of the extrusion process to get the temperature and stress evolution in the container, coupled with constitutive equations as well as lifetime consumption models in order to calculate both the inelastic strains and the tools lifetime, help to optimise the extrusion process and to compare the operating times of different hot work tool steels.

4.1.1 Extrusion model and process simulation

In general the most interesting and investigated areas are the most critical ones. During extrusion, the equivalent stress and temperature maxima are not located at exactly the same place in the tool, however, the largest accumulated damage occurs in regions that exhibit maximum overlapping temperature and equivalent stress loading. According to that reason the critical regions of the tools are generally edges, diminutions and areas under high thermal and/or mechanical loads, respectively.

The miniature extrusion tests were simulated in DEFORMTM2D. The temperature distribution and friction and heat transfer coefficients in the axis-symmetrical model are shown in Fig. 4.1. The temperature increase at the interface of the billet and tools is clearly recognizable.

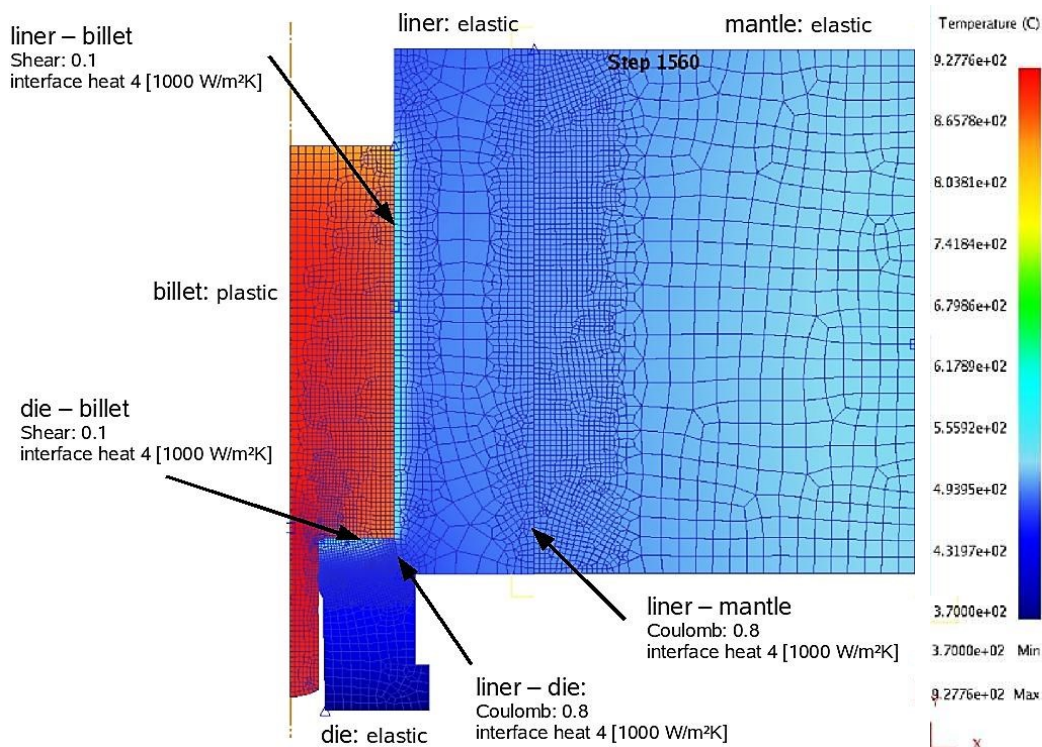


Figure 4.1: Axis-symmetrical FE-model with temperature distribution during the extrusion of a copper billet in DEFORMTM2D with friction and heat transfer boundary conditions (marked by arrows). The mantle and die are made from Böhler W300, the liner from Böhler W750 and the billet is copper with 99.99% purity.

The boundary and contact data were taken from literature as well as compared with experimental results. To perform a realistic simulation, the whole loading history, i.e. the shrink-fitting of the mantle onto the liner, the preheating of the container to working temperature, the pressing on the container against the die and the forward extrusion of the billet, was taken into account.

4.1.2 Inelastic strain evolution and lifetime prediction

To predict damage, the accurate knowledge of the unsteady local thermal and mechanical loading of the die within each cycle is of particular importance. In the following a model to calculate the inelastic strain caused by the complex loading pattern in a W750 tool material is avowed and it is further explained how to proceed with the calculated data applying an appropriate lifetime rule.

With respect to the calibration of the constitutive model it has to be said in particular, that strong attention must be paid to the attribution of the terms in the constitutive equations to the individual phenomena of the hardening or softening behavior observed in the experiments in order to determine the corresponding material parameters, especially with respect to the hardening phenomena (e.g., isotropic and kinematic hardening appearing, respectively, in the diameter and the midpoint of the elastic range within the quasi-linear ranges in the hysteresis loops at unloading). For the elaboration of the determination of the material parameters of the time dependencies, i.e. primary rate dependence (n, K_0), static recovery (d_i, m_i, f, s) and ageing (g, z, K_ω), it is referred to Sommitsch et al. [49].

At 750 and 800°C the hot work steel W750 shows a decrease of the flow stress after initial hardening at a strain rate of 10^{-3}s^{-1} , see Eqs. (4.14) and (4.15). This can be related to the kinetic of the metastable intermetallic γ' -phase. This phase transforms into the stable η -phase after longtime annealing between 750 and 850°C. The transformation is enhanced by mechanical loading. The solid solution temperature of γ' -phase was found to be at 855°C.

The constitution of the constitutive model is as follows: In a Cartesian reference configuration, the strain $\boldsymbol{\varepsilon}_{ij}$ is taken to be composed of elastic $\boldsymbol{\varepsilon}_{ij}^e$ (reversible, includes thermal strain), inelastic or plastic $\boldsymbol{\varepsilon}_{ij}^p$ (irreversible) parts such that

$$\boldsymbol{\varepsilon}_{ij} = \boldsymbol{\varepsilon}_{ij}^e + \boldsymbol{\varepsilon}_{ij}^p \quad (4.1).$$

Inelastic strain does not exist in the stress-free virgin state and when the reversible elastic part and thermal strain is considered separately, the equation is a little different. The total strain $\boldsymbol{\varepsilon}$ of the constitutive model is decomposed into the thermal strain $\boldsymbol{\varepsilon}_{th}$, the elastic strain $\boldsymbol{\varepsilon}_e$, which is connected with the stress $\boldsymbol{\sigma}$ by Hooke's law, and into the inelastic strain $\boldsymbol{\varepsilon}_{in}$:

$$\boldsymbol{\varepsilon} = \boldsymbol{\varepsilon}_e(\boldsymbol{\sigma}) + \boldsymbol{\varepsilon}_{in} + \boldsymbol{\varepsilon}_{th}(T) \quad , \quad \boldsymbol{\varepsilon}_{th}(T) = \boldsymbol{\varepsilon}_{th}(T) \mathbf{1} \quad (4.2).$$

where $\mathbf{1}$ denotes the unit tensor. The viscoplastic potential and the hardening variables are developed in the framework of unified viscoplasticity, considering only one inelastic strain. The existence of a viscoplastic potential in the stress space is assumed. Its position, shape, and size is dependend on the various hardening variables. It is limited to the case where the potential is a given function of the viscous stress or overstress.

The Hooke's law is given by

$$\boldsymbol{\sigma} = 2G\boldsymbol{\varepsilon}'_e + \frac{E}{3(1-2\nu)} \text{tr} \boldsymbol{\varepsilon}_e \mathbf{1} \quad (4.3),$$

where G denotes the shear modulus, E the Young's modulus, ν the Poisson's ratio and the deviator of the elastic strain tensor $\boldsymbol{\varepsilon}_e$

$$\boldsymbol{\varepsilon}'_e := \boldsymbol{\varepsilon}_e - \frac{1}{3} \text{tr} \boldsymbol{\varepsilon}_e \mathbf{1} \quad , \quad \text{tr} \boldsymbol{\varepsilon}_e := \varepsilon_{e,1} + \varepsilon_{e,2} + \varepsilon_{e,3} \quad (4.4).$$

For the lifetime prediction of highly stressed extrusion tools during service, taking into account the inelastic strain rate during a cycle, it was necessary to be able to assess the inelastic stress-strain response of the material. The influence of the thermo-mechanical history on the current stress-strain behaviour was described with internal (non-measurable) variables, beside the measurable (external) variables of deformation, time, temperature and stress.

In a viscoplastic, i.e. unified inelastic, model, creep and plasticity are covered within a single inelastic strain variable, as hardening as well as time-dependent recovery effects take place with the same dislocations, this causes the creep-plasticity interaction. According to the viscoplastic model of Chaboche the flow rule for the single inelastic strain $\boldsymbol{\varepsilon}_{in}$ reads:

$$\dot{\boldsymbol{\varepsilon}}_{in} = \frac{3}{2} \left\langle \frac{J_2(\mathbf{S} - \mathbf{X}) - (k - S_{el} + R)}{K} \right\rangle^n \frac{\mathbf{S} - \mathbf{X}}{J_2(\mathbf{S} - \mathbf{X})} \quad , \quad \langle y \rangle := \begin{cases} y, & \text{if } y > 0 \\ 0, & \text{otherwise} \end{cases} \quad (4.5)$$

$$\mathbf{S} := \boldsymbol{\sigma} - \frac{1}{3} \text{tr} \boldsymbol{\sigma} \mathbf{1} \quad , \quad J_2(\mathbf{A}) := \sqrt{\frac{3}{2}} \|\mathbf{A}\| \quad (4.6),$$

where $\boldsymbol{\sigma}$ denotes the external applied stress, R the increase of the initial elastic limit k , \mathbf{X} the internal backstress, n a material parameter and S_{el} is the softening of the initial elastic limit. The Chaboche model is based on the concept of threshold stress: if the applied stress deviator \mathbf{S} exceeds the threshold stress (with k as the initial threshold stress), inelastic flow occurs to the extent of this overstepping.

A softening that also occurs at higher strain rates (in the range of 10^{-3}s^{-1}) is likely influenced by the deformation because there would be not enough time for a solely time dependent softening. The decrease of the flow stress is predominantly related to the decrease of the elastic limit, i.e. to the lowering of the area of elastic behaviour with no plastic flow. In Eq. 4.7, the softening of the initial elastic limit S_{el} is introduced:

$$S_{el} = Q_{S_{el}}(T) s_{el} \quad (4.7)$$

with $Q_{S_{el}}$ as the saturation parameter of the softening of k ($0 \leq Q_{S_{el}} \leq k$) and s_{el} as the related isotropic softening variable of the elastic limit $k - S_{el} + R$

$$\dot{s}_{el} = b_{Sel} (1 - s_{el}) \dot{p}, \quad s_{el}(t=0) = 0, \quad \dot{p} = \sqrt{\frac{3}{2}} \|\dot{\boldsymbol{\varepsilon}}_{in}\| \quad (4.8),$$

where b_{Sel} is a material parameter and \dot{p} the von Mises equivalent inelastic strain rate. Due to inelastic straining two kinds of hardening, denoted by the scalar R and by the tensor \mathbf{X} , arise. The increase R of the initial elastic limit k describes the expansion of the elastic range, the so-called isotropic hardening. As originally indicated by Olschewski et al. for non-isothermal loading and discussed in the following finite state function is proposed for the isotropic hardening variable, in the sense of the concept of Chaboche for thermo-mechanical hardening:

$$R = Q_R(T) r \quad (4.9)$$

with $Q_R(T)$ as the saturation parameter of R at isothermal loading, T denotes the actual temperature, and r is the related isotropic hardening variable with the evolution equation

$$\dot{r} = b_R \left(1 - \frac{R}{Q_R}\right) \dot{p} - \frac{f}{Q_R} \left(\frac{R}{Q_R}\right)^s, \quad r(t=0) = 0 \quad (4.10),$$

where b_R , f and s are material parameters. b_R characterises the rate of isotropic hardening with the accumulated inelastic strain p . f and s describe the time dependent, so-called static, recovery of the deformation induced hardening: f denotes the rate of the static recovery in the fully hardened state ($R \approx Q_R$) and s the transition to the fully recovered state by the time. The parameters b_R and b_{Sel} as well as the saturation parameters Q_R and Q_{Sel} of the deformation induced softening of the elastic limit describe the increase as well as the decrease of the radius of the elastic area with preceding accumulating inelastic deformation p .

The development of the internal back stress tensor \mathbf{X} depends on the direction of deformation, i.e. it represents a strain-induced anisotropy. The evolution of \mathbf{X} is related to the Bauschinger effect via the displacement of the midpoint of the elastic range, the so-called kinematic hardening (see, e.g., Lemaitre and Chaboche [50]). The internal backstress \mathbf{X} is decomposed into two parts

$$\mathbf{X} = \mathbf{X}_1 + \mathbf{X}_2 \quad (4.11),$$

where \mathbf{X}_1 characterises the fast nonlinear kinematic hardening with inelastic strain present already at small deformation and \mathbf{X}_2 describes the slower hardening with inelastic strain at larger deformation ($|\boldsymbol{\varepsilon}_{in}| > 0.1\%$). For both of them a finite state function is applied:

$$\mathbf{X}_i = \frac{2}{3} a_i(T) \boldsymbol{\alpha}_i, \quad i=1,2 \quad (4.12),$$

where $a_i(T)$ are saturation parameters of the internal backstresses \mathbf{X}_i at isothermal loading and $\boldsymbol{\alpha}_i$ are related kinematic hardening variables:

$$\dot{\boldsymbol{\alpha}}_1 = c_1 \phi(p) \left(\dot{\boldsymbol{\epsilon}}_{in} - \frac{3}{2} \frac{\mathbf{X}_1}{a_1} \dot{p} \right) - \frac{3}{2} \frac{d_1}{a_1} \left(\frac{J_2(\mathbf{X}_1)}{a_1} \right)^{m_1} \frac{\mathbf{X}_1}{J_2(\mathbf{X}_1)}, \quad \boldsymbol{\alpha}_1(t=0) = \mathbf{0} \quad (4.13a)$$

$$\phi(p) = \phi_\infty + (1 - \phi_\infty) \exp(-\omega p) \quad (4.13b)$$

$$\dot{\boldsymbol{\alpha}}_2 = c_2 \left(\dot{\boldsymbol{\epsilon}}_{in} - \frac{3}{2} \frac{\mathbf{X}_2}{a_2} \dot{p} \right) - \frac{3}{2} \frac{d_2}{a_2} \left(\frac{J_2(\mathbf{X}_2)}{a_2} \right)^{m_2} \frac{\mathbf{X}_2}{J_2(\mathbf{X}_2)}, \quad \boldsymbol{\alpha}_2(t=0) = \mathbf{0} \quad (4.13c)$$

with c_i , d_i and m_i as material parameters: c_i denotes the rate of kinematic hardening with inelastic straining, d_i describes the rate of static recovery in the fully hardened state ($J_2(\mathbf{X}_i) \approx a_i$) with time and m_i the transition to the fully recovered state with time. The function $\phi(p)$ [51] represents the hardening as well as softening of the coefficient $c_1 \phi$ of the kinematic hardening, and ω denotes the rate of this softening with inelastic straining.

The related hardening variables r and $\boldsymbol{\alpha}_i$ describe the degree of hardening, which corresponds to the accumulation of immobile dislocations in the material structure and that causes subsequently certain internal backstresses \mathbf{X}_i , at a specific temperatures.

Ageing of strength, i.e. a time-dependent decrease of an initial present flow resistance at high temperatures can be described according to Chaboche by a time-dependent decrease of the viscosity coefficient K :

$$K = K_0(T) \kappa \quad (4.14)$$

with $K_0(T)$ denoting the initial viscosity parameter and κ is the related ageing variable with the evolution equation

$$\dot{\kappa} = -\frac{b_K}{K_0} \langle K - K_{\infty 1} \rangle \dot{p} - \frac{g}{K_0} \left(\frac{\langle K - K_{\infty 2} \rangle}{K_0 - K_{\infty 2}} \right)^z, \quad \kappa(t=0) = 1 \quad (4.15),$$

where g , z , b_K , $K_{\infty 1}$ and $K_{\infty 2}$ are material parameters: g characterises the rate of ageing at the beginning of loading ($K = K_0$), z describes the transition to the fully aged material state and $K_{\infty 2}$ is the viscosity in this state. b_K and the saturation parameter $K_{\infty 1}$ of the deformation induced softening of the viscosity K describes the decrease of the viscous stress with advanced accumulating inelastic deformation p and hence partly also the drop of the extend of the stress decrease at the initial relaxation in different cycles of a reversal strain experiment. The thermodynamic consistency of this description of softening is given corresponding to the proof of Chaboche and Cailletaud et al. [52]. The related ageing variable κ describes the degree of ageing, which can be caused, e.g., by a coarsening of second phase particles, due to a long time exposure at high temperatures.

4.1.2.1 Lifetime rule for complex processes

Cyclically loaded structures suffer a fatigue failure. Fatigue lifetime means in a macroscopic model the initiation of a macrocrack (typically a fraction of a millimetre). Fatigue lifetime rules are usually formulated on the basis of mean quantities of a cycle, such as stress or strain ranges. In contrast, time incremental lifetime rules evaluate the total damage in each time increment and, thus, can be also applied to complex multiaxial loading paths, for which the definition of a single loading parameter describing the entire cycle could be difficult. Furthermore, a time incremental lifetime rule can easily be implemented in a material subroutine for finite element analysis of structures just as an evolution equation for an additional internal variable, the lifetime consumption D , $0 \leq D \leq 1$. The following lifetime rule is used:

$$\frac{dD}{dt} = \left(\frac{\sigma_{d_eq}}{A} \right)^{m_l} \left(\frac{\dot{p}}{\dot{p}_0} \right)^{n_l} \dot{p}_0 \quad (4.16),$$

where σ_{eq} is the Von Mises equivalent stress, \dot{p} the inelastic Mises equivalent strain rate as defined in Eq. (4.16) and \dot{p}_0 is a normalisation constant. The material parameters A and m_l describe the stress-dependence of the lifetime behaviour. An influence of the mean stress of a cycle was taken into account automatically by the fact that a stress process, which is non-symmetric to the zero-point in the stress space during a cycle, moves for the same stress range as in a symmetric process at higher stress magnitudes, nevertheless. The parameter n_l describes the time-dependence of the lifetime: for rate-independent behaviour n_l is equal to 1, n_l equal to zero means that a fully time-dependent lifetime behaviour is present. n_l was found to be positive but significantly lower than 1 for the investigated high temperature loading. The parameters A and m_l were determined from LCF tests with strain rates of 10^{-3} s^{-1} with and without hold-times. The parameter n_l was identified by the influence of hold times in LCF tests on the lifetime behaviour [53].

To consider the influence of the stress triaxiality R_v , the damage equivalent stress σ_{d_eq} was used, which is a one-dimensional stress. For a certain value of the damage, the damage equivalent stress yields the same value of the elastic strain energy density as that of a three-dimensional state:

$$\sigma_{d_eq} = \sigma_{eq} \sqrt{R_v} \quad , \quad \sigma_{eq} := \sqrt{\frac{3}{2} \|\sigma'\|} \quad (4.17)$$

and

$$R_v = \frac{2}{3}(1 + \nu) + 3(1 - 2\nu) \left(\frac{\sigma_H}{\sigma_{eq}} \right)^2 \quad (4.18),$$

where σ_H denotes the hydrostatic stress. The numbers of cycles to failure N_f were calculated for the seek of simplicity by

$$N_f \approx 1/(\Delta D)_3 \quad (4.19),$$

where $(\Delta D)_3$ is the lifetime consumption within a stabilized cycle where steady state can be assumed. At the investigated high temperatures, subsequent cyclic softening appears without any saturation of the hysteresis loops, but integration of the time-incremental lifetime rule over all cycles up to the fatigue failure ($D = 1$) would be too costly for a real component. Nevertheless, the damage rate takes into account the whole loading complexity within one cycle.

The parameter values for the elastic-viscoplastic Chaboche model for W300 in the temperature range from 470-590°C can be found in Appendix C, Tab. 9.1 and for W750 in the temperature range 650-850 in Tab. 9.2. All the parameter values were determined by the Bundesanstalt für Materialprüfung (BAM) in Berlin.

4.2 Physical based microstructure modelling

An adequate scientific method to describe the material behaviour at complex loads, occurring during service, can be achieved by physical approaches. To take into account microstructural evolution processes, it is necessary to observe the microstructure on micro- as well as on nanoscale, where the precipitation state, the grain size, in that case the prior austenitic grain size, as well as the substructure and dislocation density are important parameters defining the material's state. The initial structure, which means in the context here, the material's microstructure after the complete heat treatment, is accurately characterized to further investigate the structure evolution due to low cycle creep-fatigue as well as pure creep and fatigue, i.e. overlapping of precipitation coarsening with dislocation density evolution and subgrain formation, i.e. in general competing hardening and softening processes. The loads acting on the tools during service are calculated by FE simulations to obtain stress and temperature as input data for the physical based microstructure model. Representative thermal and mechanical load types are taken into account, which react on a defined unit cell with predefined initial structure, which is characterized and validated by experimental microstructure investigations. Such a unit cell is modelled continuum mechanically as a grain with a substructure evolution described by physical based dislocation density evolution functions. To experimentally validate those predictive calculations, adequate LCF experiments are performed and a detailed investigation of the resulting microstructure due to various experimental parameters is carried out.

4.2.1 Modelling of the precipitation kinetics

To provide a global description of the phenomena occurring in the tool material during application, it is unavoidable to characterize the microstructural changes due to multiple load patterns. The microstructure evolution of bcc-lattice structured hot work tool steels during thermo-mechanical loads, such as fatigue at elevated temperatures, creep and creep-fatigue loads, is described by means of thermodynamic precipitation calculations performed with the software MatCalcTM [54]. The precipitation state of the specimens is characterized after the last annealing step, i.e. the final state before starting the experimental program as well as after rupture.

4.2.2 Modelling the dislocation density evolution

In consideration of the precipitation state, initial grain and subgrain size, dislocation density evolution calculations are carried out to account for the inelastic strain quantity on a physical basis. The precipitation state after the heat treatment, the thermal and mechanical loading conditions, the initial dislocation density as well as the subgrain size are key parameters in the used physically based dislocation density evolution model according to Ghoniem et al. [14], which is capable of describing the recovery processes in the material. Since the applied thermal loads during service have to be generally lower than the last annealing step of the heat treatment procedure, a constant precipitation state as initial condition is assumed, which is an input parameter for the model and the focus lies on the investigation of the dislocation structure. The dislocation density calculations were performed with MathCad™ to describe the dislocation density and subgrain structure evolution during the creep and fatigue load range at elevated temperatures based on the above mentioned model for thermal creep using the rate theory. To evaluate the predicted results, the dislocation density was evaluated with X-ray diffraction peak profile analysis method [46].

4.2.2.1 Concept of the dislocation density evolution model

The basis of the model is to describe the dislocation structure evolution through:

- the generation and immobilization of dislocations at subgrain boundaries, i.e. multiplication as well as annihilation of dislocations due to interaction processes,
- the recovery of the static dislocations at the boundaries as well as the absorption of mobile dislocations in the cell wall,
- the generation of dislocations by emission from the cell wall,
- the dynamics of nucleation and growth of subgrains from dislocations within the cells as well as
- the subgrain growth due to coalescence driven by the subboundary energy.

Hence the total dislocation density ρ_{tot} , is separated into three categories of dislocations, namely mobile (ρ_m), static (ρ_s), and boundary (ρ_b) dislocations to consider all the specific dislocation dynamics mentioned above. The temporal evolution of the mobile dislocation density ρ_m is given in Eq. 4.20 with v_g denoting the glide velocity of the dislocations, β as a parameter for the dislocation emission, R_{sub} is the subgrain radius, h_{sg} the distance between two dislocations in the subgrain boundary, v_c^m the climb velocity of mobile dislocations and δ determines the dynamic annihilation distance:

$$\frac{d\rho_m}{dt} = \underbrace{v_g \rho_m^{3/2}}_{\text{Frank-Read-sources}} + \underbrace{\frac{\beta R_{sub}}{h_{sg}^2} v_g}_{\text{Emission from cell walls}} - \frac{\rho_m}{2R_{sub}} v_g - \underbrace{8v_c^m \rho_m^{3/2}}_{\text{Static recovery}} - \underbrace{\delta \rho_m (\rho_m + \rho_s) v_g}_{\text{Dynamic recovery}} \quad (4.20).$$

The evolution equation for describing the static dislocation density is given in Eq. 4.21, where v_c^s denotes the climb velocity of static dislocations:

$$\frac{d\rho_s}{dt} = \underbrace{\frac{\rho_m}{2R_{sub}} v_g}_{\text{Immobilization}} - \underbrace{8 \frac{\rho_s}{h_{sg}} v_c^s}_{\text{Static recovery}} - \underbrace{\delta \cdot \rho_s \rho_m v_g}_{\text{Dynamic recovery}} \quad (4.21).$$

The glide velocity is defined as follows (Eq. 4.22):

$$v_g = c_1 \exp\left\{\frac{-Q}{kT}\right\} \tau \frac{\Omega}{kT} \quad (4.22),$$

with c_1 denoting a constant in the order of unity, Q the activation energy, k the Boltzmann constant, T the temperature, τ the acting shear stress and Ω represents the atomic volume.

The principle, which is valid for all three dislocation categories are

dislocation generation by:

- Frank-Read sources and emission of dislocations at cell walls (ρ_m),
- immobilization (ρ_s),
- absorption and static recovery (ρ_b), as well as

the decrease of dislocation density due to:

- static and dynamic recovery (ρ_m, ρ_s),
- coalescence and growth (ρ_b).

A further important parameter, which is included in the formula of the glide velocity v_g , is the space length λ between forest dislocations. When the static dislocation density decreases, λ increases, which means easier gliding and resulting faster annihilation of mobile dislocations. The effects of solutes and precipitates, which strengthen the material, are considered in the evolution of the boundary dislocation density, which is mentioned in Eq. 4.23. The input parameters from the kinetic precipitation calculations $R_{\text{mean}, i}$ and N_i , for arbitrary different types ($i = 1..n$) of precipitates, are introduced into the model:

$$\frac{d\rho_b}{dt} = \underbrace{8(1-2\zeta) \frac{\rho_s}{h_{sg}} v_c^s}_{\text{Absorption of dislocation and static recovery}} - \underbrace{\frac{\rho_b}{R_{sub}} M_{sg} \left[p_{sg} - 2\pi \cdot \left(\sum_{i=1}^7 R_{\text{mean}, i}^2 \cdot N_{v,i} \right) \cdot \gamma_{sg} \right]}_{\text{Coalescence and growth of subgrains}} \quad (4.23),$$

with the parameter ζ describing the annihilation at the subgrain boundary, M_{sg} the mobility of subgrains, p_{sg} the driving force of the subgrain boundary, $R_{v,\text{mean}, i}$ the radius of a precipitate

class i , N_i the related number of particles per volume and γ_{sg} the surface energy of the subgrain boundary. The subgrain size evolution subsequently follows Eq. 4.24:

$$\frac{dR_{sub}}{dt} = M_{sg} \left[p_{sg} - 2\pi r_p^2 N_v^p \gamma_{sg} \right] - \mu \eta_v K_c R \left[(\rho_m + \rho_s)^{0.5} - \frac{K_c}{2R} \right] \frac{\Omega D_s}{k_B T} \quad (4.24),$$

with R_{sub} as the subgrain radius, M_{sg} denoting the mobility of the subgrain boundary, N_v^p the number of precipitates per unit volume, μ , η_v and K_c are constants in the order of unity, D_s is the coefficient for self diffusion and k_B the Boltzmann constant.

The calculations were compared with FE-simulations and experiments via the resulting true inelastic strain rate $d\varepsilon/dt$, calculated by Eq. 4.25, which is an additional output of the model:

$$\frac{d\varepsilon}{dt} = \frac{1}{M} \rho_m c_1 \exp \left\{ \frac{-Q}{kT} \right\} \tau \frac{\Omega}{kT} b = \frac{1}{M} \rho_m v_g b \quad (4.25),$$

where $M = 3$ is the Taylor factor for the bcc lattice structure and b the burgers vector.

To run the model, the start values for the microstructure variables ρ_m , ρ_s , ρ_b and R_{sub} , which were determined via TEM and X-ray diffraction, have to be typed into the program code. Furthermore the precipitate size classes, the considered service temperature and mechanical loading pattern as well as several energy terms are essential input parameters. The most relevant output parameters are the dislocation density evolution curves, the subgrain size evolution as well as the inelastic strain. Further details with the whole program code in MathCad can be found in Appendix B, page 120.

5. Results

The following chapter, in which the experimental and calculated results are shown, is subdivided into three sections. In section 5.1 the thermo-mechanical boundary conditions during an extrusion process were simulated and experimentally validated. The aim was to ensure for reliable temperature and pressure boundary conditions for the numerical FE-simulation of the extrusion processes with variable process guidance. The friction conditions were also considered to account for a complete view on possible influencing parameters. Creep, fatigue and creep-fatigue tests were performed to simulate process near service conditions, which have an influence onto the tool's microstructure evolution and material properties. An application limit for the tool steel regarding thermo-mechanical loads was found by means of these experimental test programs. The characterization of the tested specimens of the experimental program, considered in section 5.1 is shown in section 5.2, starting from metallographic investigations and hardness tests to get an overview and finally applying TEM investigations, which provided a detailed characterization of the precipitate state as well as X-ray diffraction peak profile analysis to account for the dislocation density evolution at several stages during service. In section 5.3 precipitation kinetic simulations with MatCalc as well as dislocation density evolution calculations with the aim of a physical model based on rate equations are presented. Copper and aluminium extrusion process simulations with the afore validated boundary conditions and results for the lifetime prediction of the tool component are finally stated. The decisive factor of approximately the same chemical composition but different metallurgical production route onto the service life of the material will be exemplified by experimental tests and numerical simulations in subsequent chapters. Since the common tool material production route is casting and further profiling to bars, plates or rods for commercial selling, the microstructure can exhibit small segregations and texture, which can influence the local material properties as shown in Fig. 5.1.

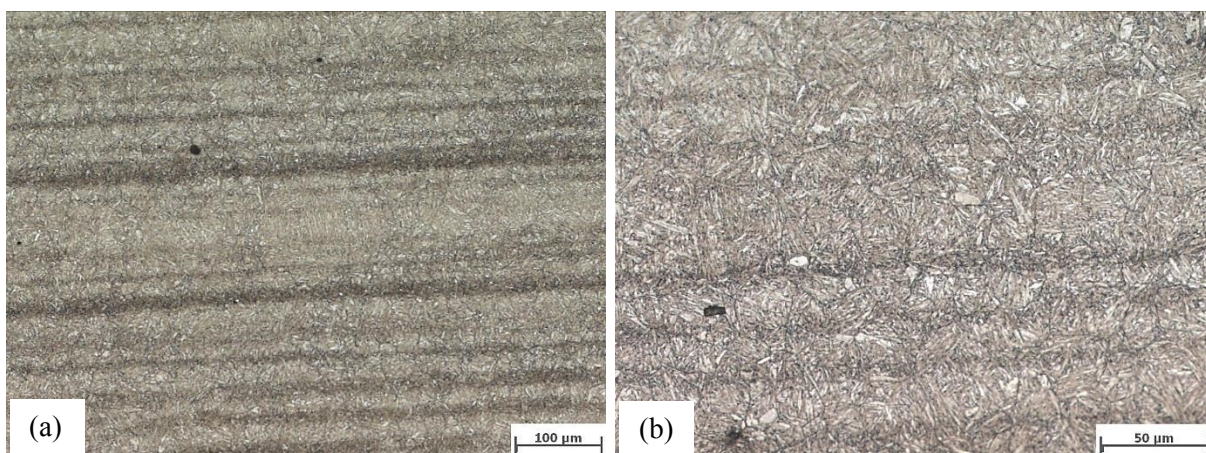


Figure 5.1: Microstructure investigation parallel to the horizontal axis direction of a W300 rod, where the specimens for thermo-mechanical testing were taken from. The chemical texture resulting from the production history is clearly visible through the local different attack of the etchant.

5.1 Experimental tests

In the following subchapter the performed experimental extrusion test results as well as the results of the mechanical test series, i.e. fatigue, creep and creep-fatigue tests are shown. In the mechanical test series the two types of tool steels, namely Böhler W300 and W400, known as X38CrMoV5-1 were tested. The influence of different heat treatment conditions was investigated on W300, where the effect of bainitic as well as martensitic matrix structure on creep, fatigue and creep-fatigue resistance was evaluated.

5.1.1 Pressure and temperature evaluation during a copper extrusion process

The thermo-mechanical boundary conditions, i.e. temperature and pressure during copper extrusion were evaluated using an experimental extruding plant, which was implemented into a hydraulic 100t press. To consider variable process conditions and their influence onto the quantity of the thermo-mechanical loading of the tools, the temperature guidance was varied. The process parameters during copper extrusion are depicted in Tab. 5.1, tool as well as billet temperature and the related peak stress and temperature values of the pressure measurement level L2 and thermocouple T2 are stated. The ram speed was held constant at 7mm/s with an extrusion ratio of 14. In Fig. 5.2 the temporal pressure evolution is demonstrated.

Table 5.1: Variation of experimental copper extrusion process parameters and their impact on the mechanical and thermal tool loading. The inverse relation of tool and forming temperature to the occurring mechanical stresses is recognizable.

Temperature guidance		Induced tool loading	
Tool temperature [°C]	Billet temperature [°C]	Peak liner temperature [°C]	Peak pressure [MPa]
450	850	525	1050
450	900	547	780
450	950	579	636
500	850	549	755
500	930	551	598
500	950	582	621

In Fig. 5.2 the first 15 - 20 seconds indicate the loading period of the billet, where only small mechanical loads can be detected. The extrusion starts at that point in time, when the pressure values begin to raise up immediately.

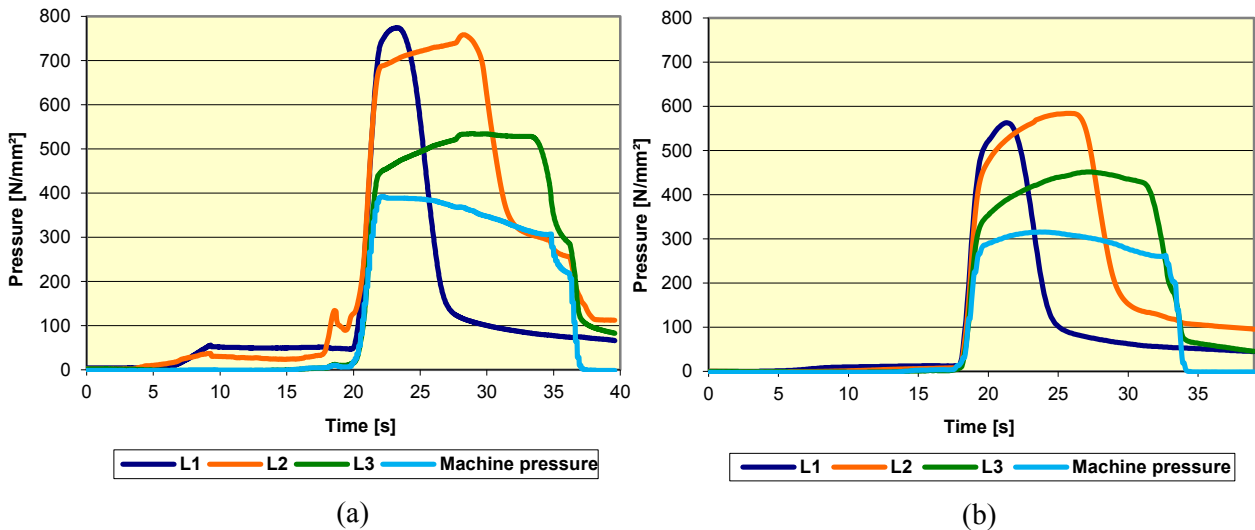


Figure 5.2: Mechanical load distribution on the liner during a copper extrusion process. The influence of different forming temperatures onto the forging force, i.e. the mechanical loads at (a) comparatively lower (850°C) and (b) higher billet temperature (930°C), both at 500°C liner temperature at cycle 1, are demonstrated.

Regarding the thermal loading during the process, the peak temperature in the tool in case of copper extrusion can increase to values of more than 90°C above the initial tool temperature, see Fig. 5.3.

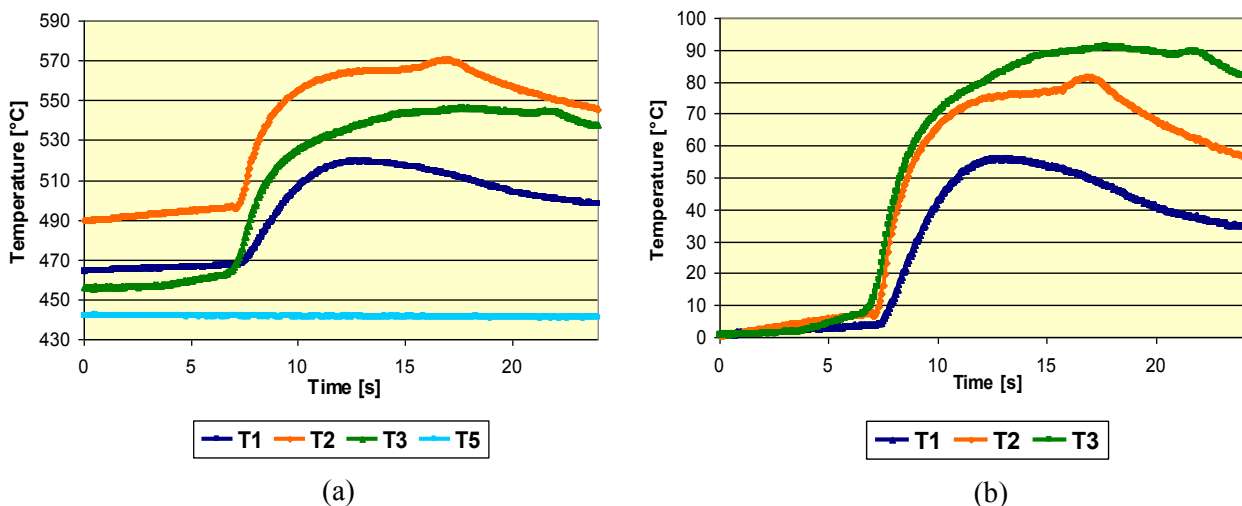


Figure 5.3: (a) Temperature evolution during the process and (b) absolute temperature increase at process parameters of 450°C liner and 950°C billet temperature during the first extrusion cycle. The area, which stays longest in contact with the hot copper billet is located at the bottom of the liner near T3, which shows the highest temperature increase during an extrusion cycle. It should also be remarked that the thermocouple is placed about 2.5 mm behind the inner surface of the liner.

During billet to billet extrusion, the mechanical load distribution can change in a way, that at the beginning of the adjacent cycle, the remainder of the prior billet is going to be advanced, which requires higher forces and that causes higher mechanical load peaks, see Fig. 5.4.

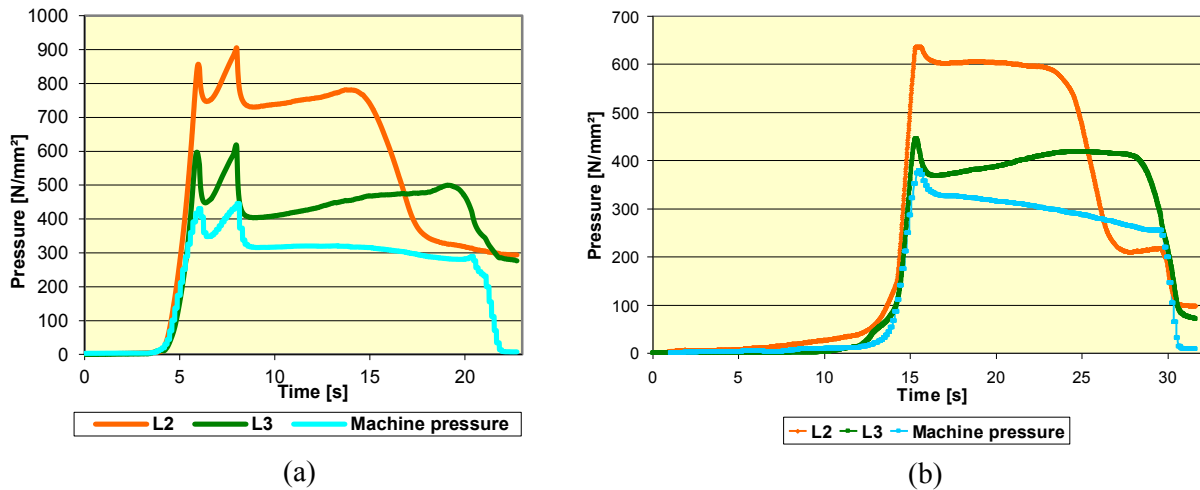


Figure 5.4: Example for mechanical load distribution for billet to billet copper extrusion at (a) 900°C, cycle 2, and (b) 950°C initial billet temperature, cycle 3, at 450°C liner temperature. The peaks at the beginning of the extrusion process indicate the advancing of the remainder, which seems to be an unsteady process.

The aim of the experimental test-setup was to compare and validate the FE-simulations of the extrusion process. In Fig. 5.5 the thermal history during an extrusion process was measured and simulated. T4 in Fig. 5.5 (a) represents the temperature in the mantle, which was also used for heat control.

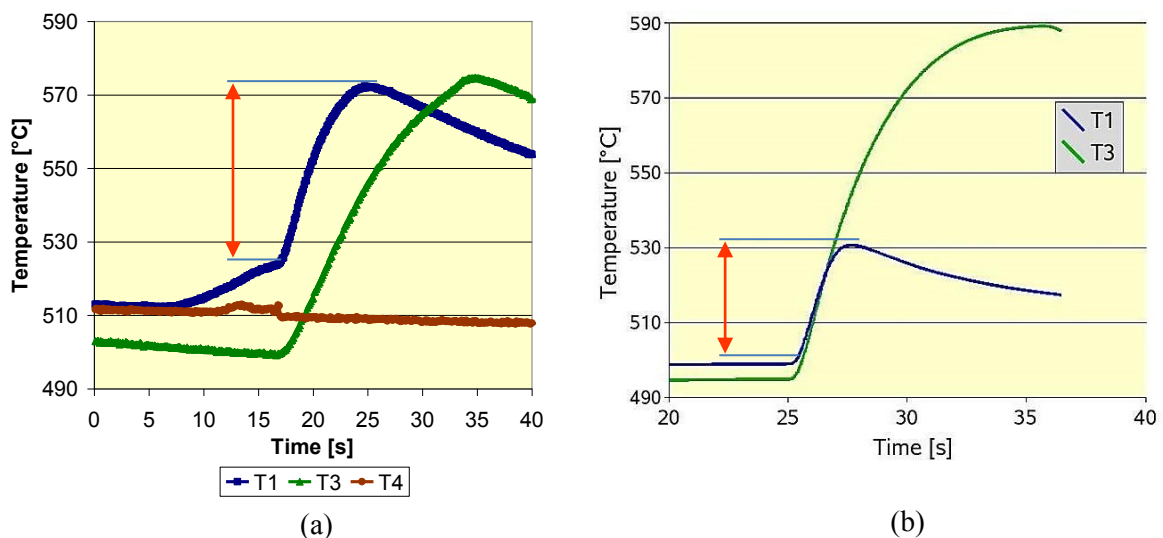


Figure 5.5: (a) Measured temperature evolution for T1 and T3 at process conditions of 930°C initial billet temperature and (b) simulated. The absolute difference according to the real copper extrusion process time is marked with arrows for T1 in (a) experiment and (b) FEM simulation.

The difference in the quantitative temperature result can be explained by the lower initial start temperature in the simulation as well as in the temperature measurement system itself, since the thermocouple is fixed at the plug gage and the value is a mixture of ambient liner and gage temperature, respectively. The validation of the mechanical load distribution in the liner showed some differences, especially for the peak values of L1 in comparison to L2 and L3, however the trend in the increase during the advancing of the extrusion cycle for every measurement point was verified as shown in Fig. 5.6.

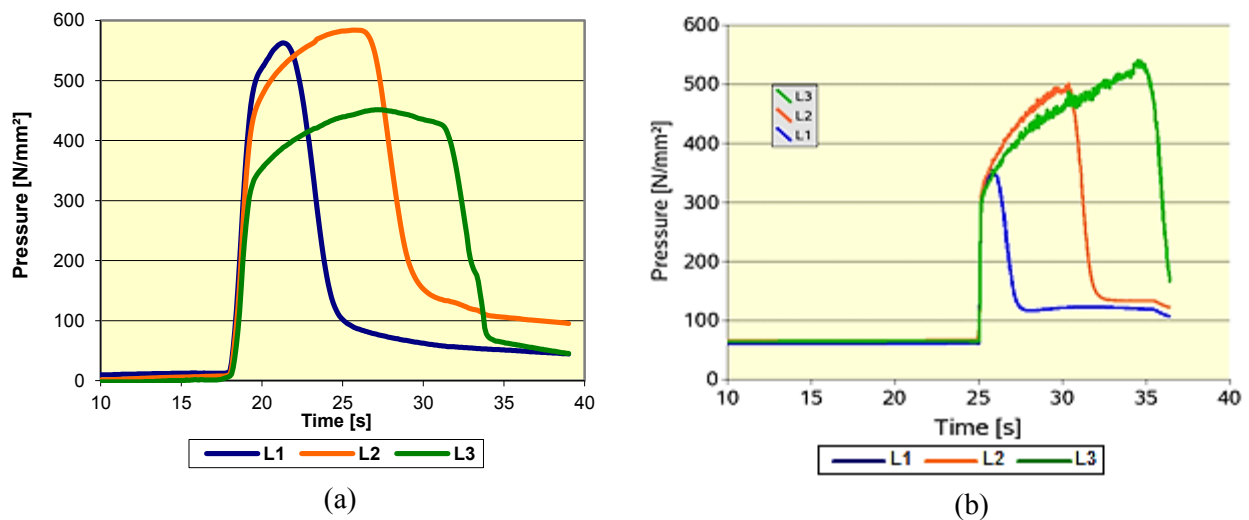


Figure 5.6: (a) Measured pressure evolution at process conditions of 900°C initial copper billet temperature and (b) FEM simulated. During the billet loading process, small mechanical loads could be detected (a). The sudden increase marks the start of the extrusion process.

The bottom areas of the liner experience higher thermal loads. The reason is attributed to both the longer billet-tool contact as well as the deformation heat during the extrusion process, which occurs at the bottom liner region and the die, see Figs 5.3 and 5.5.

5.1.2 Pressure and temperature evaluation during an aluminium extrusion process

The process parameters during aluminium extrusion are depicted in Tab. 5.2, tool as well as billet temperature and the related peak stress and temperature values of the pressure measurement level L2 and thermocouple T2 are stated, which can be directly compared with the copper extrusion values. Additionally, to account for the thermo-mechanical loading of the bottom die, the normal pressure on the die surface as well as the die temperature distribution was evaluated, see Figs. 5.7 and 5.8.

Table 5.2: Variation of experimental aluminium extrusion process parameters and their impact on the mechanical and thermal tool loading. The normal stress onto the die was measured with a special constructed measurement system with a ring-shaped mechanical load cell.

Temperature guidance		Induced tool loading		
Tool temperature [°C]	Billet temperature [°C]	Peak liner temperature [°C]	Peak pressure [MPa]	Pressure on die [MPa]
350	450	371	230	202
350	500	383	216	223
400	550	409	187	214

During aluminium extrusion, the thermal load in the liner increased much less, which means not more than 30-40°C due to the lower temperature gradient of the aluminium billet to the liner. An instrumented die was used to evaluate the thermo-mechanical loading during aluminium extrusion and it was also tried to evaluate the temperature of the extruded rod immediately after extrusion, see Fig 5.7. Therefore an additional hole was drilled into the die to reach the extrudate with a thermocouple.

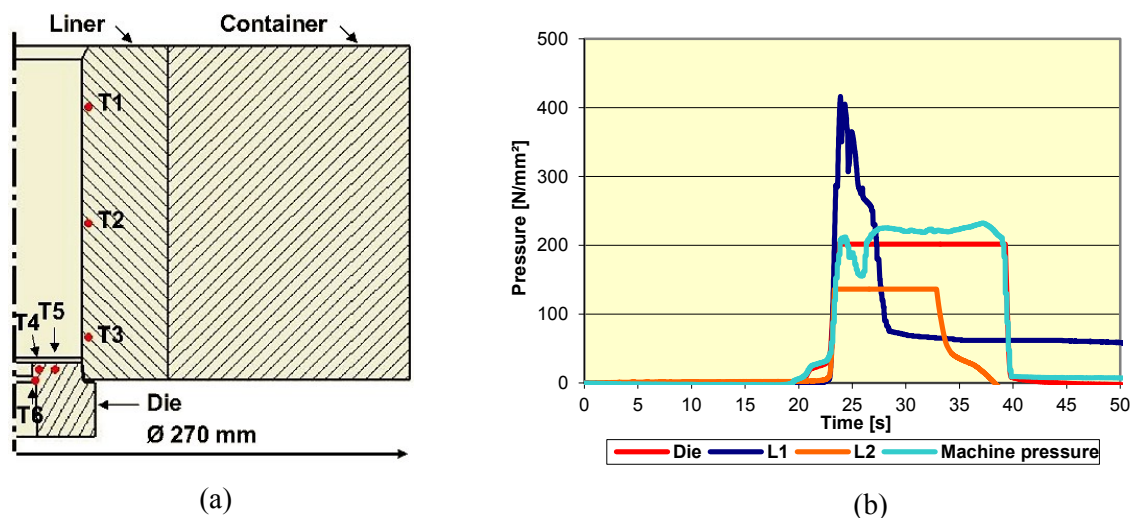


Figure 5.7: (a) Schematic drawing and nomenclature of the measurement points during aluminium extrusion and (b) mechanical load distribution on the liner as well as measured average normal pressure (red line) acting on the die during an aluminium extrusion process at 350°C liner and 450°C billet temperature during cycle 2.

To obtain a temperature distribution along the radius of the die, two thermocouples were introduced below the die surface, see Fig 5.7 (a). To evaluate the normal pressure on the die surface during an extrusion process, a ring-shaped load cell with ceramic heat barrier was placed below the die. In Fig. 5.8 the temperature distribution in the liner, T1-T3, as well as the temperature near the die hole, T4 and further away, T5, during aluminium extrusion is shown. The attempt to measure the temperature of the extrudate, T6, is also demonstrated.

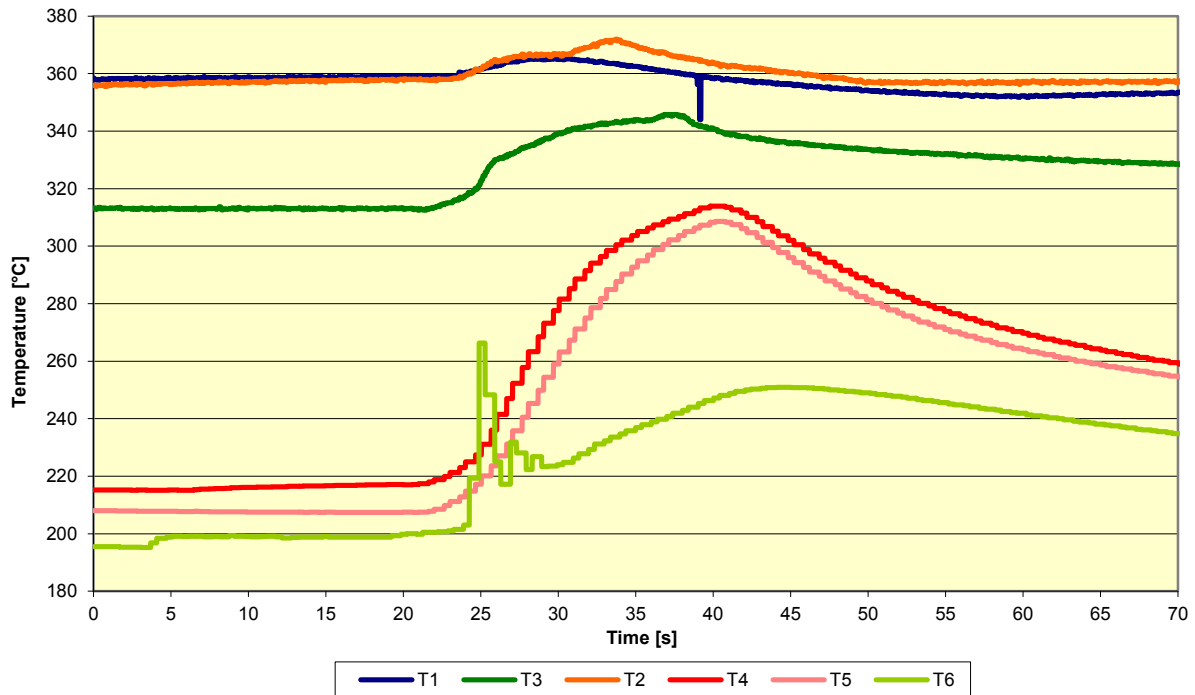


Figure 5.8: Temperature evolution during an aluminium extrusion process with 450°C initial billet and 350°C container temperature, cycle 2. The measurement points follow the description of the thermocouples in Fig 5.7 (a).

The thermo-mechanical loading, which is caused during copper extrusion is much higher than during aluminium extrusion, therefore the appropriate tool material for the liner at copper extrusion applications is the higher thermal stable fcc-structured W750 or further austenitic hot work tool steels, whereas for aluminium extrusion, the bcc-structured hot work tool steels W300, W400 and variations of their alloys are adequate.

5.1.3 Evaluation of friction behaviour

The spike test series resulted in no significant difference in friction behaviour due to the different surface condition according to the laboratory testing conditions, see Fig. 5.9. However in industrial application, a nitrided surface is often used to avoid sticking of the billet material on the tool's surface [40].

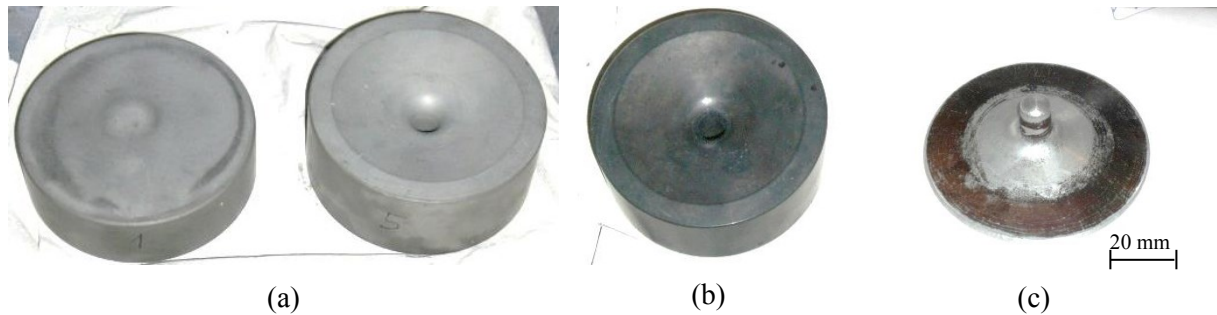


Figure 5.9: The tools: (a) nitrided upper and lower die, (b) lower die without surface treatment and (c) final geometry of the formed aluminium billet.

Depending on the friction coefficient, the final geometry varies. In Fig. 5.10 the evaluation of the friction coefficient in accordance to the resulted geometry achieved in the experiment is shown. The characteristics, which determine the friction coefficient can be found in the relation between the radius of the formed plate to the height of the pin. A friction coefficient $\mu \sim 0.2$ was ascertained from the test series.

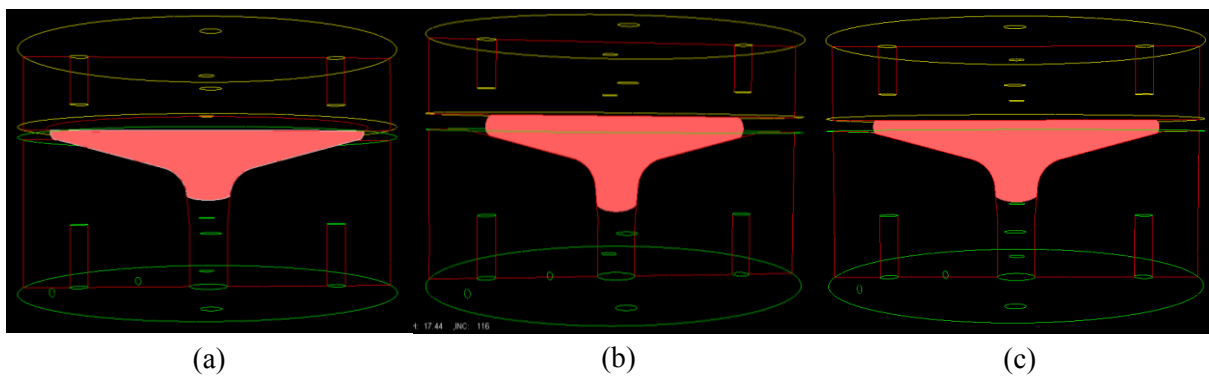


Figure 5.10: Evaluation of the friction coefficient. Resulting geometry according to the assumption (a) $\mu = 0$, (b) $\mu = 1$ and (c) $\mu = 0.2$, the latter fits best to the experimental geometry.

According to literature [27] as well as the results for thermal and mechanical boundary conditions during extrusion, which were obtained by the afore presented experimental program, the further experimental approach was performed to investigate the influence of process parameters such as temperature and forming forces, i.e. mechanical loads, which are caused during service, onto the microstructure evolution and service life of the tool.

5.1.4 Creep tests

Short term creep tests were performed to evaluate the process near creep behaviour of the tool material and to investigate the microstructure and dislocation density evolution as well as to observe microstructure influenced locations for the crack initiation. The results for the temperature intervals, reaching from 500 to 590°C with load intervals from 400 to 800 MPa for W300 with martensitic and bainitic matrix structure are shown in Tab. 5.3 and Tab. 5.4, respectively.

Table 5.3: Short term creep test results of W300 specimens with martensitic matrix.

Specimen	T [°C]	σ^+ [MPa]	t_{break} [h]	L_0 [mm]	L [mm]	D_0 [mm]	D [mm]	A [%]	Z [%]	t_{total} [h]	comments
A31	500	600	949	90	90.8	8.16	-	0.98	-	1074	in situ
A41	500	800	186	90	97.6	7.07	3.76	8.47	71.7	234	break
A42	500	800	181	90	98.1	7.07	3.76	8.97	71.7	227	break
A43	500	800	91	90	90.5	7.07		0.57		91	in situ
A44	540	800	7	90		7.07	3.56		74.6	11	break
A24	540	400	325	90		7.07				376	in situ
A32	540	600	77	90		8.16	4.54		69.0	84	break
A23	580	400	26	90		7.07	3.54		87.5	46	break
A21	590	400	9	90	103.4	10.00		14.9		26	in situ
A22	590	400	9	90	110.5	10.00	3.32	22.7	89.0	26	break

Table 5.4: Short term creep test results of W300 specimens with bainitic matrix.

Specimen	T [°C]	σ^+ [MPa]	t_{break} [h]	L_0 [mm]	L [mm]	D_0 [mm]	D [mm]	A [%]	Z [%]	t_{total} [h]	comments
B31	500	600	949	90	98.5	8.16	6.28	9.47	40.8	1071	break
B41	500	800	113	90	95.1	7.07	5.18	5.63	46.3	141	break
B42	500	800	108	90	97.2	7.07	4.68	8.04	56.2	119	break
B32	500	600	734	90	91.1	8.16		1.23		878	in situ
B43	540	800	5	90		7.07	3.98		68.3	6	break
B44	540	800	6	90		7.07	3.94		68.9	7	break
B33	540	600	55	90		8.16				62	break
B23	540	400	324	90		10.00	6.08		63.0	375	break
B24	580	400	25	90		10.00	4.50		79.8	42	break
B21	590	400	9	90	110.8	10.00	3.50	23.11	87.8	25	break
B22	590	400	9	90	109.9	10.00	3.64	22.12	86.8	23	break

The variables are as follows: T denotes the temperature at which the creep test was performed, σ^+ the applied creep stress, t_{break} the time to rupture, L_0 the initial specimen length, L the length after rupture, D_0 the initial diameter of the measurement length, D the constricted diameter at the fracture zone, A and Z define the percentage of elongation and constriction,

respectively, and t_{total} the time the specimen was exposed to higher thermal loads in total, including prior holding periods. A significant higher creep resistance of W400 was observed, see Tab 5.5.

Table 5.5: Short term creep results of W400 specimens with martensitic structure.

Specimen	T [°C]	σ^+ [MPa]	t_{break} [h]	L_0 [mm]	L [mm]	D_0 [mm]	D [mm]	A [%]	Z [%]	t_{total} [h]	comments
F31	500	800	733	90	97.4	7.07	4.82	8.21	53.5	833	break
F21	540	600	182	90		8.16	4.28		72.5	211	break
F32	540	600	7	90		8.16				11	in situ
F13	580	400	57	90		10.00	4.26		81.9	92	break
F11	590	400	20	90	96.5	10.00		7.17		39	in situ

To estimate the influence of different thermo-mechanical loading onto the microstructure evolution, hardness tests were performed to draw conclusions about the material's softening during service. Worth mentioning is the relation of the measured hardness to measured dislocation densities. The specimens' initial hardness before starting the experimental tests was around 49 HRC, which equals to 490 - 505 HV10. The softening related to different time intervals and temperatures can be clearly seen in Tab. 5.6.

Table 5.6: Hardness measurements of selected creep specimens.

Specimen	T [°C]	σ^+ [MPa]	t_{break} [h]	t_{total} [h]	HV 10	Dislocation density [m ⁻²]	comments
A42	500	800	181	227	421	2.1*10 ¹⁵	break
A43	500	800	91	91	456		in situ
A21	590	400	9	26	327		in situ
B31	500	600	949	1071	380	2.4*10 ¹⁵	break
B32	500	600	734	878	402		in situ
B42	500	800	108	119	429		break
B21	590	400	9	25	334	2.4*10 ¹⁵	break
F31	500	800	733	833	419		break
F11	590	400	20	39	313		in situ

In the following, the creep test results are schematically depicted in a diagram. The characteristic parameter is the time to rupture, which is typical for a defined material condition at constant temperature and load, see Fig. 5.11.

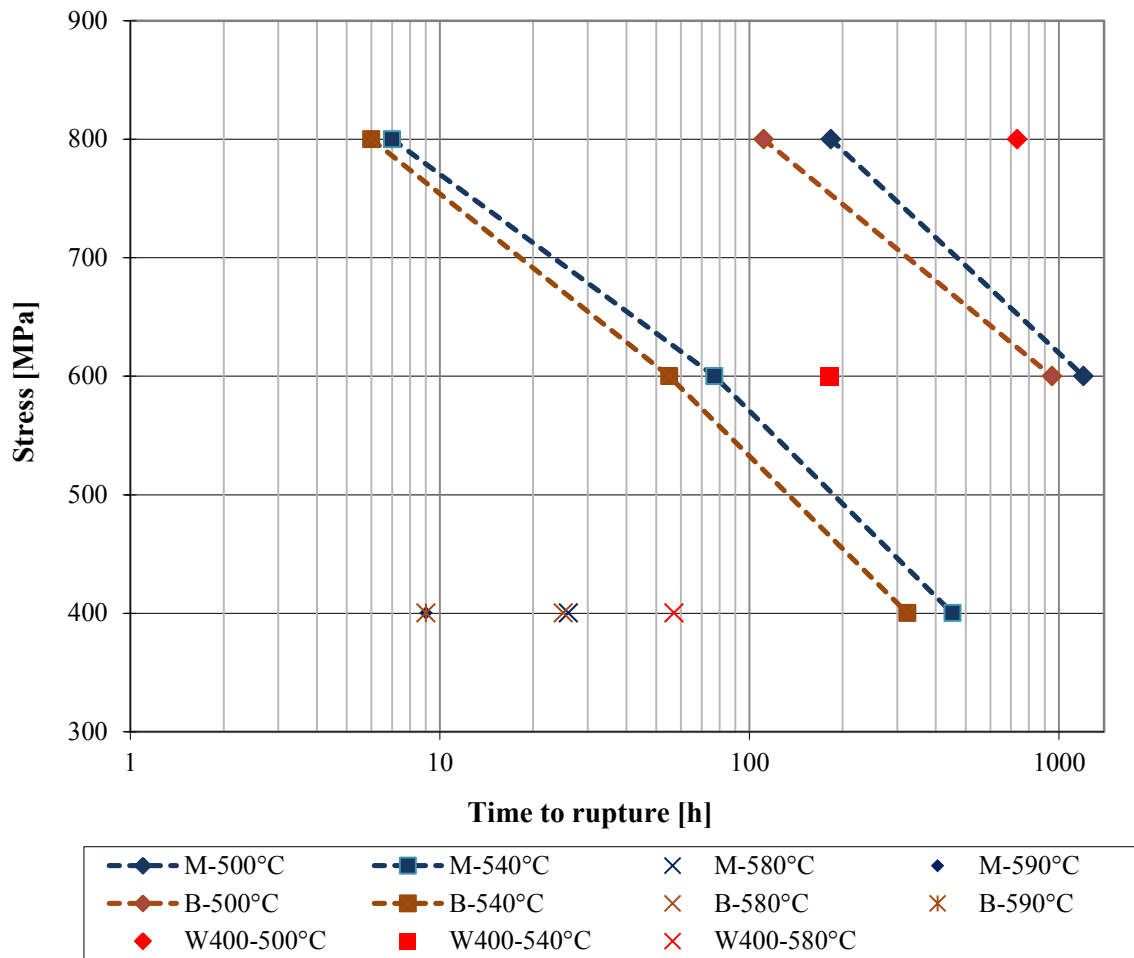


Figure 5.11: Summary of the obtained creep test results. “M” denotes martensitic W300, “B” bainitic W300 and W400 was also tested with martensitic matrix structure.

Remarkable, as shown in Fig. 5.11, is the significant higher creep resistance of W400, which is clearly visible, whereas only a narrow margin in the creep resistivity lies between martensitic W300 in comparison to bainitic W300.

The capital letters with additional numbers in brackets at the very end of each figure description (e.g. B12 in Fig 5.13) in the following chapters refer to the recorded tested specimens. The detailed description of the testing parameters, if not explicitly mentioned can be found in Tabs. 5.3 - 5.12, e.g. the thermo-mechanical loading description as well as the duration and cycles to failure of specimen B12 is described in Tab. 5.8.

5.1.5 Fatigue tests

Fatigue tests were performed to account for the influence of pure fatigue onto the specimens' lifetime. The temperatures were the same as in the creep experiments, namely 500, 540 and 580°C, respectively, with a cyclic strain amplitude $\Delta\varepsilon = 1.2\%$ with $R = -1$ and a strain rate $\dot{\varepsilon} = 10^{-3}$. The results for martensitic W300 (Tab. 5.7), bainitic W300 (Tab. 5.8) and martensitic W400 (Tab. 5.9) are shown in the following.

Table 5.7: Fatigue test results of W300 specimens with martensitic structure.

Specimen	T [°C]	N_c [-]	σ^+ [MPa]	σ^- [MPa]	t_{start} [s]	t_{total} [s]	t_{total} [h]	comments
A9	500	2523	789.67	904.95	6000	61510	17.1	break
A15	500	2000	853.08	893.43	6020	47540	13.2	break
A12	500	100	786.79	835.79	6300	8400	2.3	in situ
A10	540	970	815.61	858.64	6000	60200	16.7	break
A11	580	347	789.67	783.91	6100	13900	3.9	break

Table 5.8: Fatigue test results of W300 specimens with bainitic structure.

Specimen	T [°C]	N_c [-]	σ^+ [MPa]	σ^- [MPa]	t_{start} [s]	t_{total} [s]	t_{total} [h]	comments
B7	500	1284	835.79	893.43	6000	64860	18.0	break
B12	500	3380	749.33	893.43	8600	98400	27.3	break
B13	500	100	847.31	922.25	6798	8800	2.4	in situ
B10	540	1000	835.79	835.79	12500	29660	8.2	break
B11	580	410	806.97	720.51	10626	81566	22.7	break

Table 5.9: Fatigue test results of W400 specimens with martensitic structure.

Specimen	T [°C]	N_c [-]	σ^+ [MPa]	σ^- [MPa]	t_{start} [s]	t_{total} [s]	t_{total} [h]	comments
F2	500	7523	893.43	864.61	9500	164300	45.6	break
F4	540	1710	806.97	432.30	9200	544300	151.2	break

The variables define following: N_c denotes the number of cycles to fracture, σ^+ the cyclic tensile stress peak, σ^- the cyclic compressive peak stress value, t_{start} the starting time, which includes the heating time to the required test temperature. In Fig. 5.12 the cycles to failure for the three material conditions (martensitic W300, bainitic W300 as well as martensitic W400) at three different temperatures are shown. Again, similar as in the creep tests, the more homogeneous W400 shows a significant higher fatigue life. Recognizable is the slightly better behaviour of W300 with bainitic matrix structure in comparison to the martensitic one. During creep testing, also a marginal difference existed between these two material states, but

the other way round, which seems logical. The more ductile bainite shows better fatigue and the harder martensite better creep resistance.

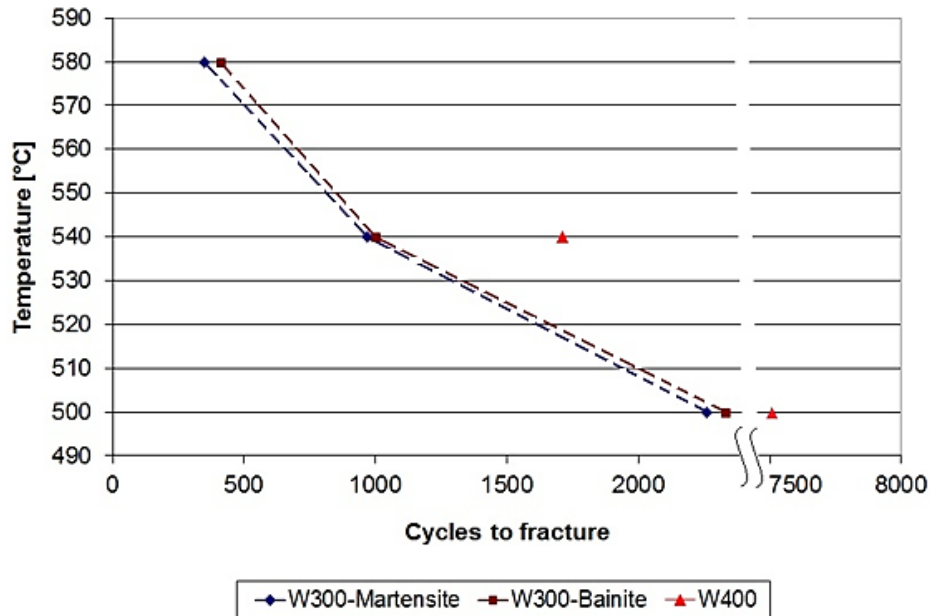


Figure 5.12: Summary of the obtained fatigue test results. The advanced fatigue life of W400 is again clearly visible. Similar to the creep behaviour, again a narrow margin lies between martensitic W300 in comparison to bainitic W300 specimen, but considering fatigue, the more ductile bainitic structure is favourable.

In the following, the stress reactions over the whole cycles to failure, which were recorded during the experiments are shown for three load cases at 500, 540 and 580°C, respectively.

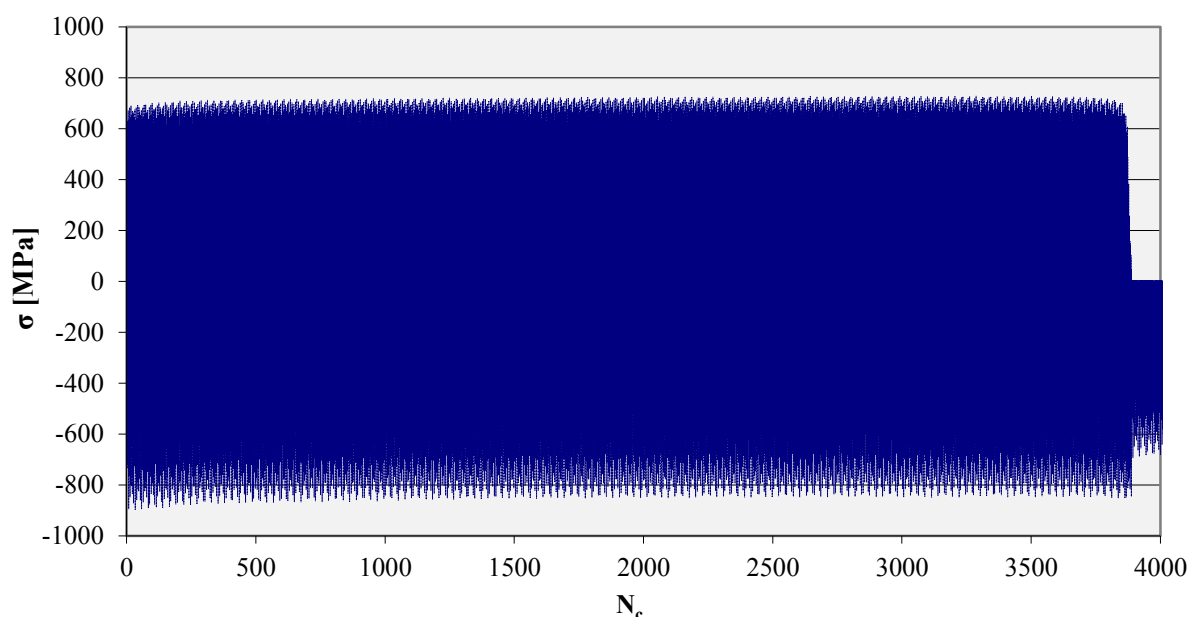


Figure 5.13: Fatigue loaded W300 specimen with bainitic matrix according to $\Delta\varepsilon = 1.2$, $R = -1$ at 500°C (B12).

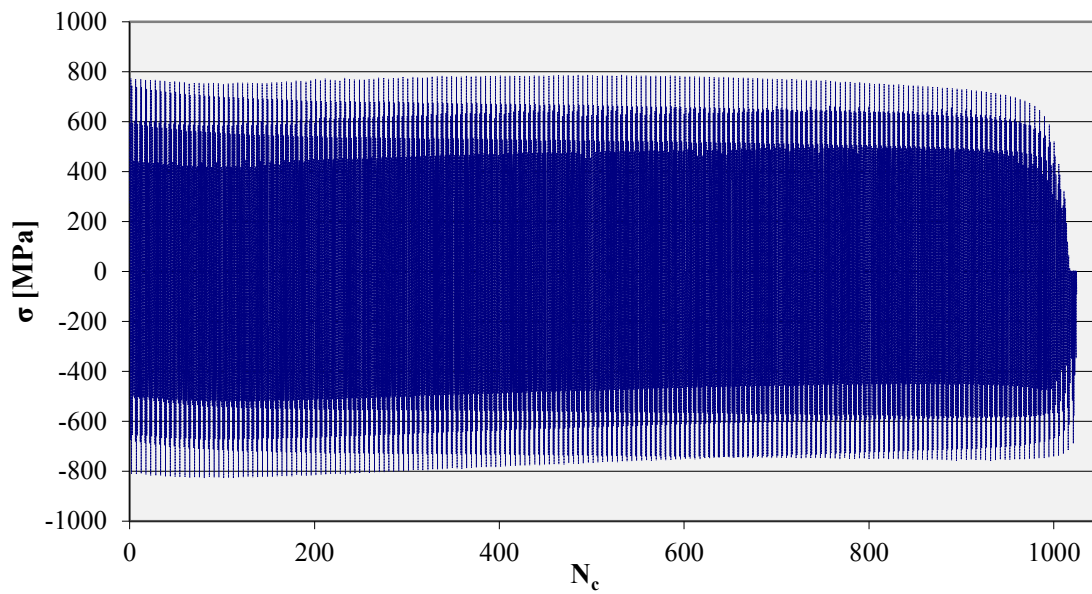


Figure 5.14: Fatigue loaded W300 specimen with martensitic matrix according to $\Delta\varepsilon = 1.2$, $R = -1$ at 540°C (A10).

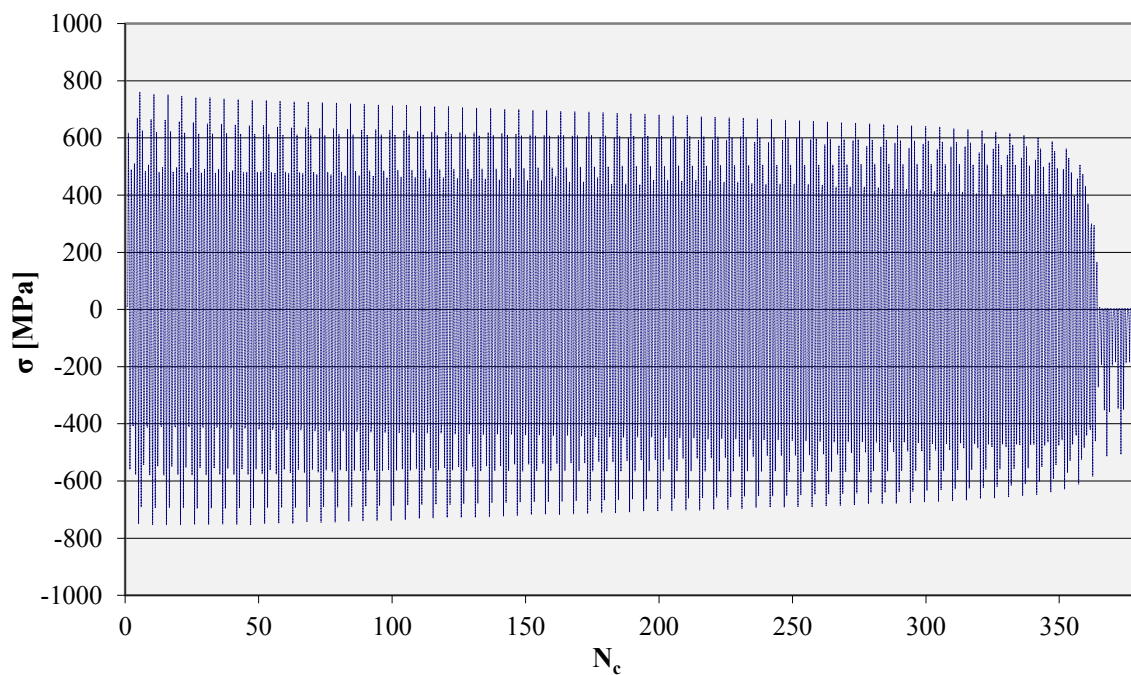


Figure 5.15: Fatigue loaded W300 specimen with martensitic matrix according to $\Delta\varepsilon = 1.2$, $R = -1$ at 580°C (A11).

The cyclic softening at 540°C and 580°C can be clearly seen in all the experiments. At the end of the lifetime, micro-cracks as well as softening are responsible for the lower stress amplitude.

5.1.6 Creep-fatigue tests

In real industrial extrusion processes, a combination of creep and fatigue loading patterns occur. The test temperatures were the same, namely 500, 540 and 580°C as afore applied and a cyclic strain amplitude $\Delta\varepsilon = 1.2\%$ with $R = -1$ and a strain rate $\dot{\varepsilon} = 10^{-3}$ with a holding time in compression of 300 seconds (5 minutes) to simulate near process conditions, were performed to evaluate both, lifetime as well as damage evolution and to characterize the microstructure evolution using in situ as well as broken specimens. The parameters and results of the creep-fatigue tests are shown in Tabs. 5.10 - 5.12.

Table 5.10: Creep-fatigue test results of W300 specimens with martensitic structure.

Specimen	T [°C]	N_c [-]	σ^+ [MPa]	σ^- [MPa]	t_{start} [s]	t_{total} [s]	t_{total} [h]	comments
A13	500	776	922.25	835.79	5500	260170	72.3	break
A17	500	640	951.07	720.51	6200	258200	71.7	break
A18	540	257	922.25	691.69	6000	90555	25.2	break
A14	580	111	835.79	749.33	6000	54200	15.1	break

Table 5.11: Creep-fatigue test results of W300 specimens with bainitic structure.

Specimen	T [°C]	N_c [-]	σ^+ [MPa]	σ^- [MPa]	t_{start} [s]	t_{total} [s]	t_{total} [h]	comments
B3	500	553	951.07	720.51	6620	240300	66.8	break
B15	500	857	720.51	864.61	14000	290000	80.6	break
B2	540	226	864.61	749.33	6000	74400	20.7	break
B16	580	100	806.97	749.33	15400	82200	22.8	break

Table 5.12: Creep-fatigue test results of W400 specimens with martensitic structure.

Specimen	T [°C]	N_c [-]	σ^+ [MPa]	σ^- [MPa]	t_{start} [s]	t_{total} [s]	t_{total} [h]	comments
F3	500	1656	749.33	979.89	6000	585000	162.5	break
F4	540	1710	806,97	432,30	9200	544300	151.5	break
F1	580	470	720.51	489.94	7000	159000	44.2	break

When observing the precipitation state and dislocation density, both the temporal thermal process and the mechanical loading cycle process influence the microstructure evolution. In Fig. 5.16 the results are shown graphically. The creep-fatigue lifetime of the more homogeneous W400 is significantly higher. Martensitic and bainitic W300 show similar lifetime, with a little lifetime enhancement of the more ductile bainitic structures at lower temperature (500°C) and vice versa at elevated temperatures of 540 and 580°C. However, one

clear tendency was observed: At increasing service temperature, both the W300 and W400 loose significant resistivity against thermo-mechanical induced failure mechanisms.

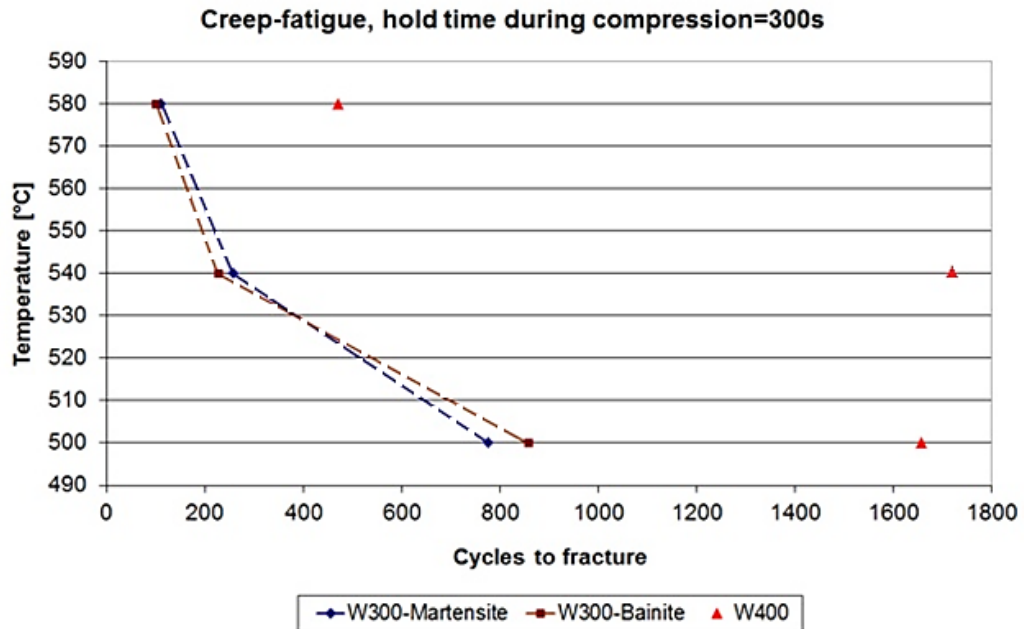


Figure 5.16: Summary of the obtained creep-fatigue test results. The higher creep-fatigue resistance of W400 is clearly visible.

The recorded stress reaction to the applied strain is shown in Figs. 5.17 - 5.20.

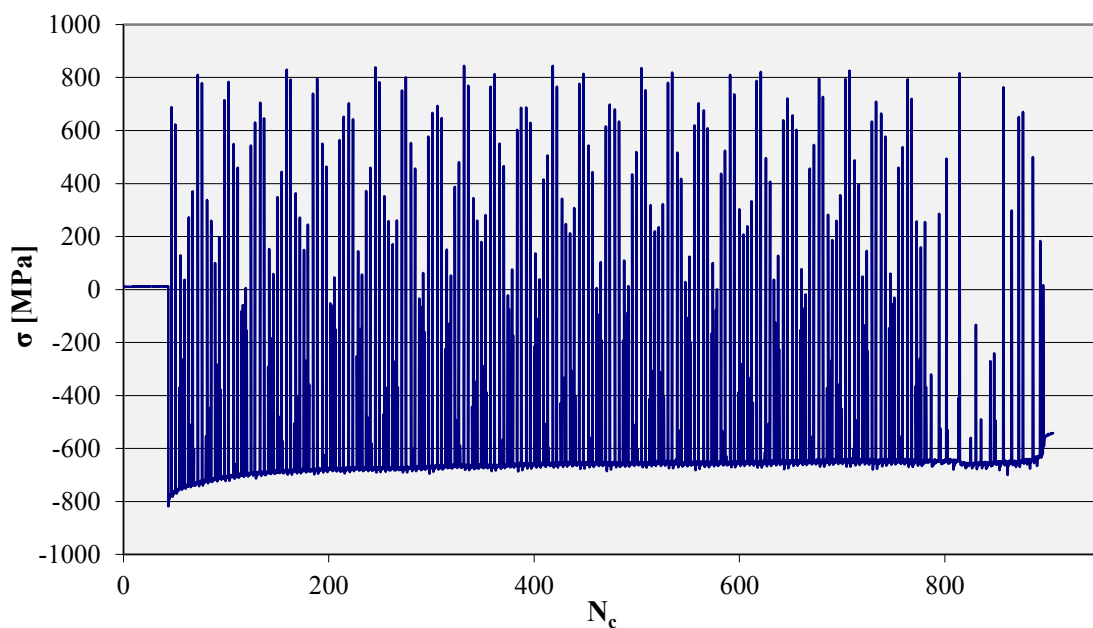


Figure 5.17: Creep-fatigue loaded W300 specimen with bainitic matrix according to $\Delta\varepsilon = 1.2$, $R = -1$ at 500°C with a holding time in compression of 300s (B15).

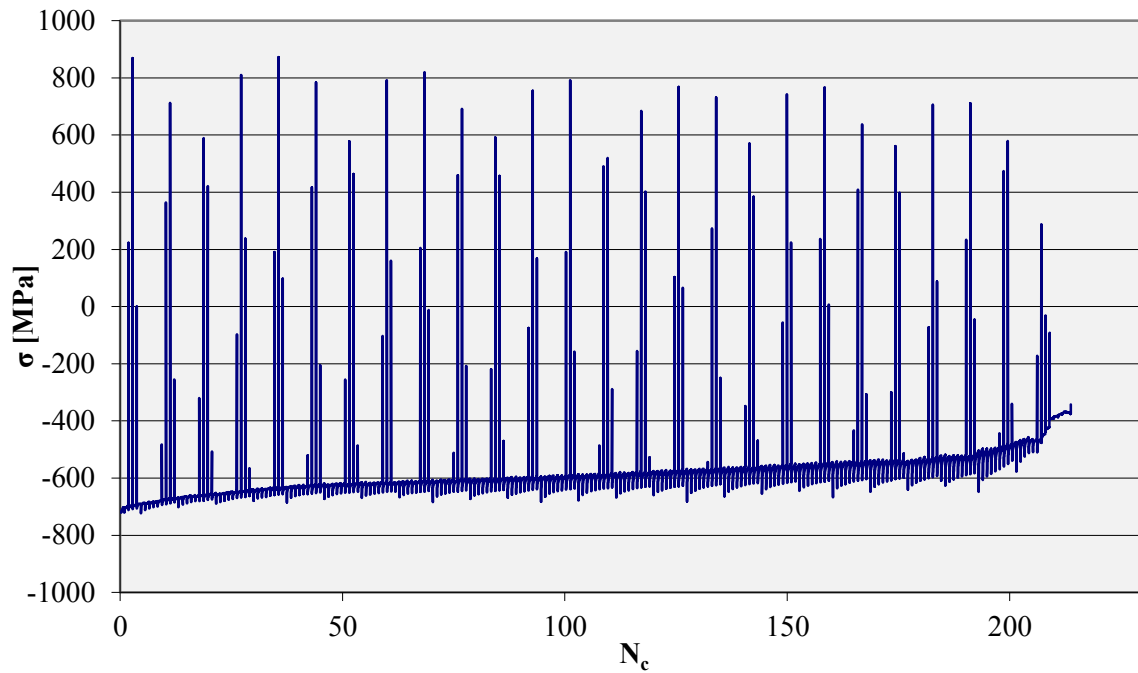


Figure 5.18: Creep-fatigue loaded W300 specimen with bainitic matrix according to $\Delta\varepsilon = 1.2$, $R = -1$ at 540°C with a holding time in compression of 300s (B2).

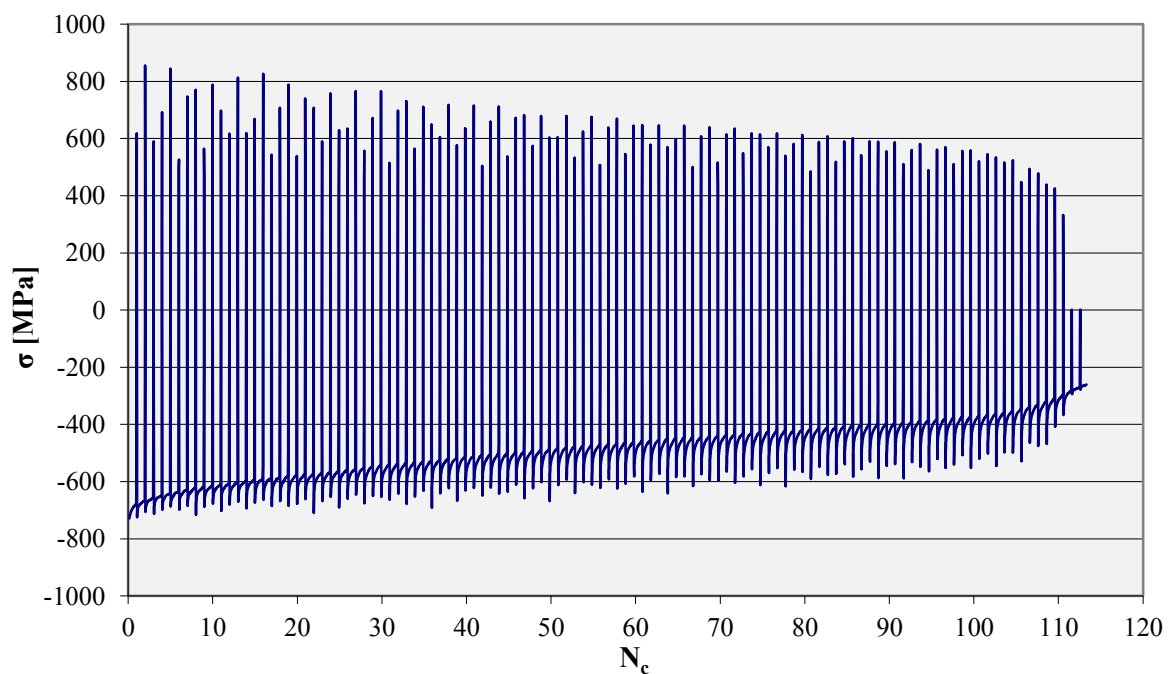


Figure 5.19: Creep-fatigue loaded W300 specimen with martensitic matrix according to $\Delta\varepsilon = 1.2$, $R = -1$ at 580°C with a holding time in compression of 300s (A14).

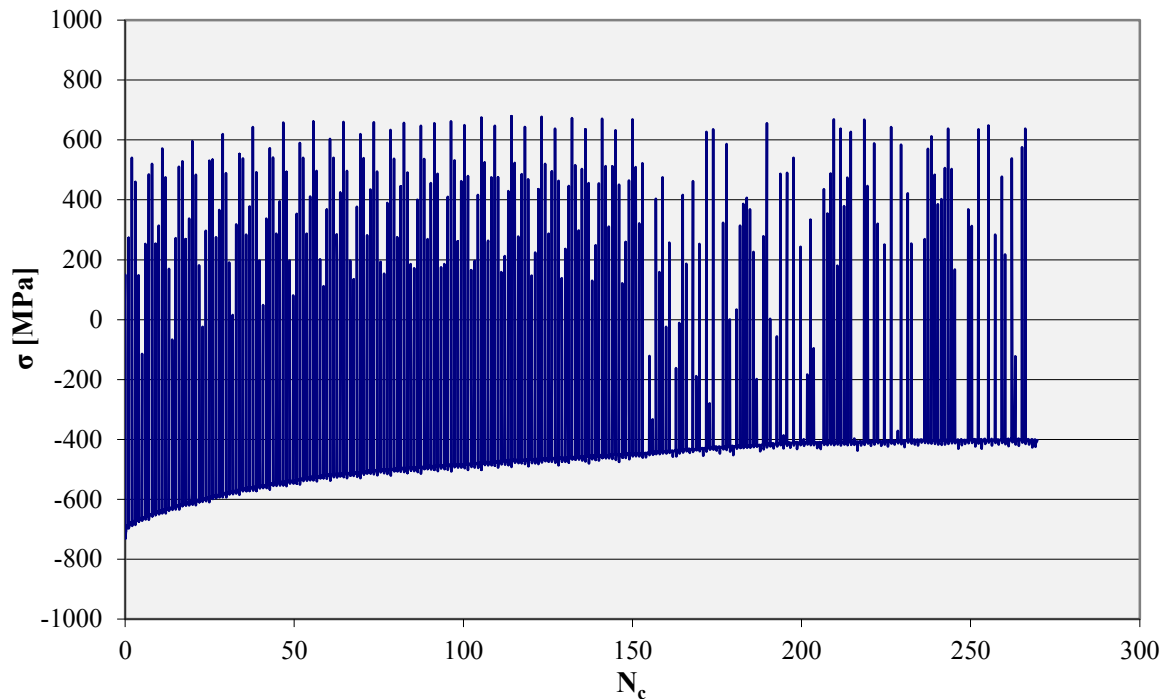


Figure 5.20: Creep-fatigue loaded W400 specimen with martensitic matrix according to $\Delta\varepsilon = 1.2$, $R = -1$ at 580°C with a holding time in compression of 300s (F1).

In Fig. 5.17, at 500°C test temperature, no significant cyclic softening rate was observed until rupture occurred. In Fig. 5.18, where the thermo-mechanical test was carried out at 540°C , a small cyclic softening is recognizable. At 580°C a clear cyclic softening rate was observed, see Figs. 5.19 and 5.20. The cyclic stress range at 500 and 540°C amounts to $\pm 800\text{-}900$ MPa, whereas at 580°C , plasticity occurs earlier. Thus the stress amplitude is reduced and amounts to $\pm 600\text{-}700$ MPa, which is consecutively decreasing, depending on the progressional softening process.

5.2 Microstructure characterization

Most of the specimens were tested until rupture occurred due to the specific loading conditions but some were removed during the experiment before break to investigate the microstructure in situ. To characterize the initial state after completed heat treatment, the material was also investigated in detail. The light optical microscope investigations were followed by selective TEM investigations to characterize the precipitate size evolution during thermo-mechanical loading, to validate the MatCalc calculations. Subsequently to validate the dislocation density model, X-ray diffraction peak profile analysis was applied on selected specimens.

5.2.1 Metallographical investigations

A comparison of the microstructure of two different heat treatments on the same alloy, i.e. W300 with martensitic and bainitic matrix structure as well as of a similar chemical composition, W400, which is produced by a different metallurgical production route is subsequently shown in its initial state, i.e. after completed heat treatment, see Figs. 5.22 - 5.27, as well as after the afore described loading conditions, namely fatigue, creep-fatigue and creep. Figs. 5.28 - 5.32 show the investigations for W300 with martensitic matrix structure, Figs. 5.33 - 5.38 for W300 with bainitic matrix structure and Figs. 5.39 - 5.41 for W400 with martensitic matrix structure. Depending on the cooling rate from austenitization temperature, which was specified as $\lambda = 0.6$ for producing a fully martensitic matrix structure, small differences in the microstructure can develop regarding surface or inner regions of the specimens. The specimens were cut for the metallographic investigation as demonstrated in Fig. 5.21.

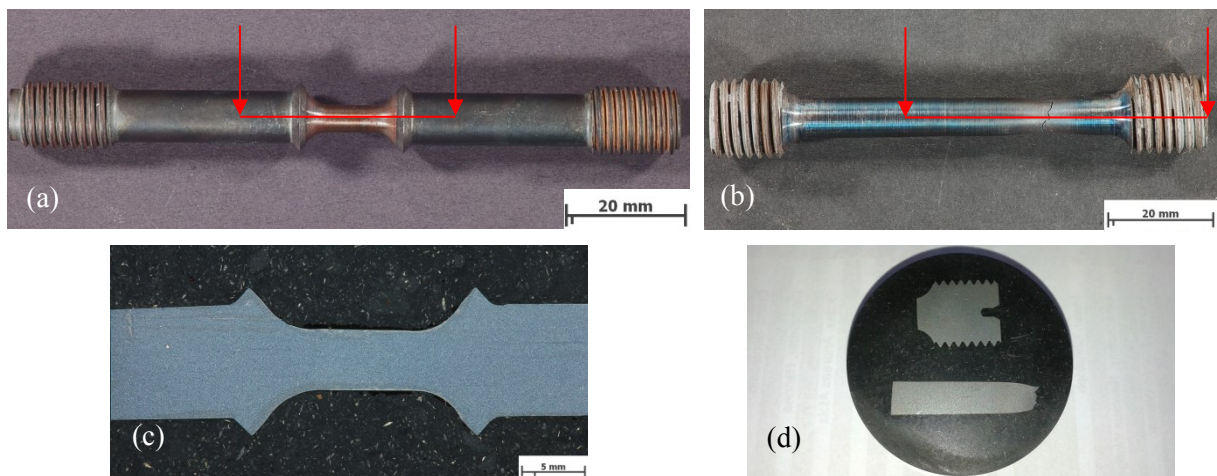


Figure 5.21: Preparation for the metallographic investigation of the (a) fatigue / creep-fatigue and (b) creep specimen and (c, d) related metallographic specimen.

Since the specimen geometry is small compared to massive extrusion tools, the microstructure shows no detectable differences from surface to inner regions, as shown in Figs. 5.22 - 5.27.

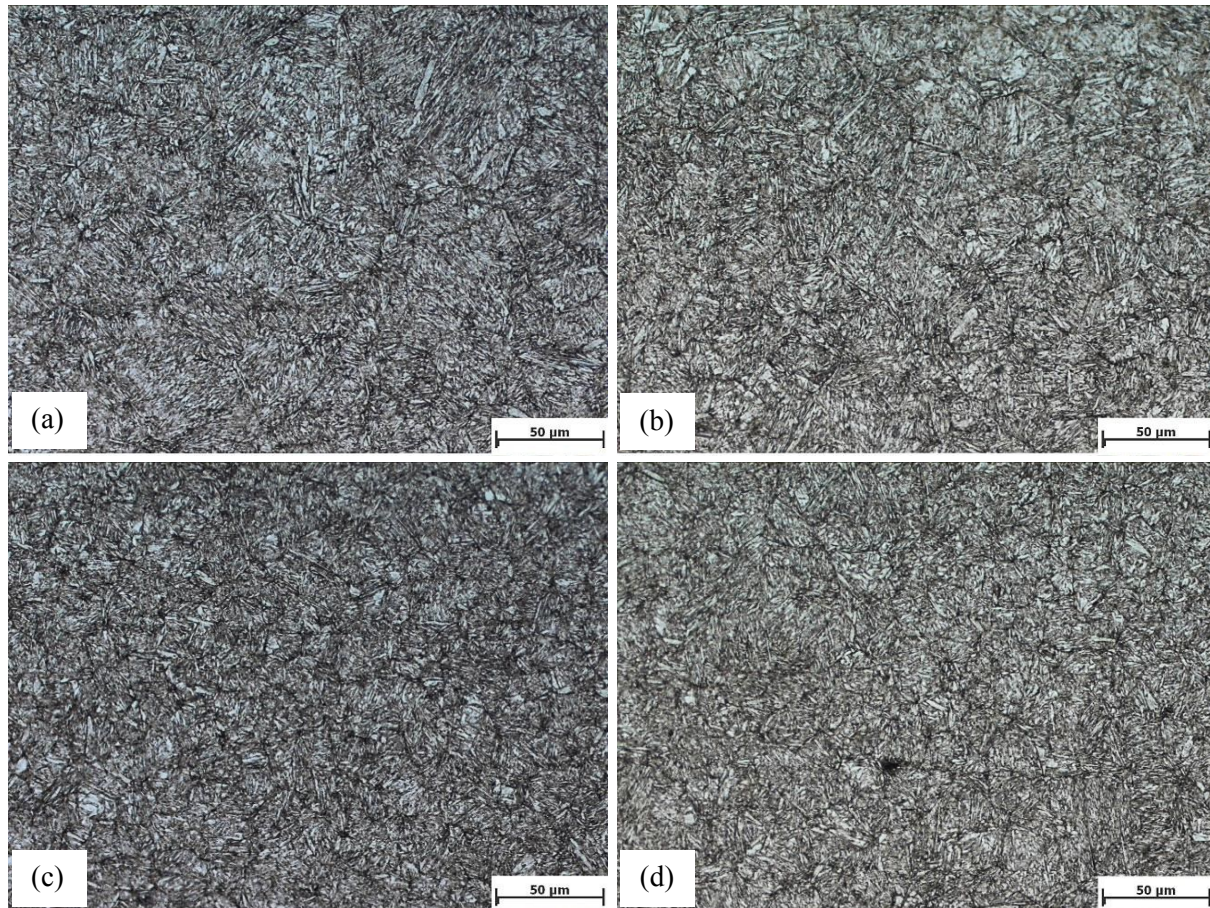


Figure 5.22: W300 with martensitic matrix structure. (a,b) inner region and (c,d) surface near region of the specimen, Nital etchant.

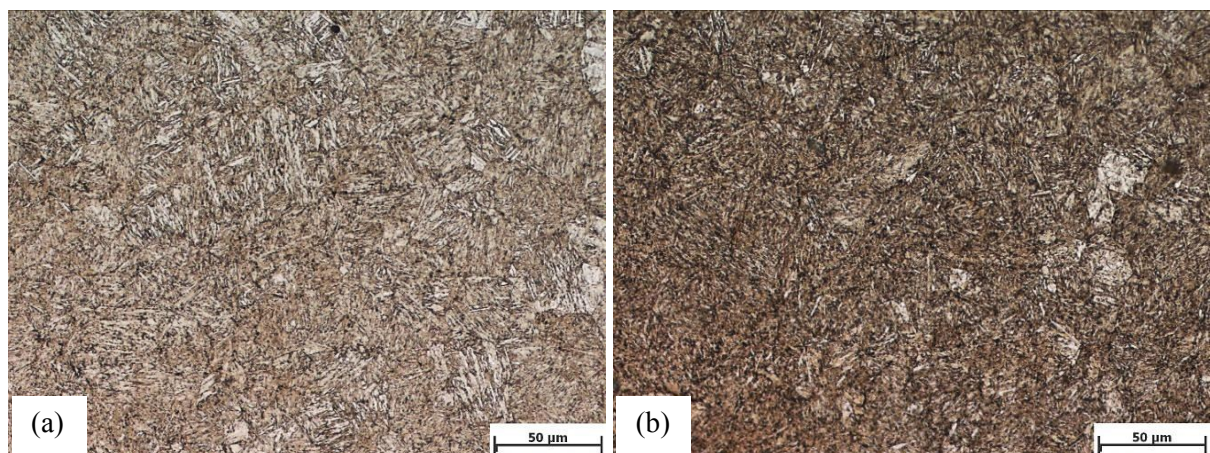


Figure 5.23: W300 with martensitic matrix structure. (a) inner region and (b) surface near region of the specimen, V2A etchant.

A cooling rate of $\lambda = 15$ from austenitization temperature resulted mainly in a bainitic matrix structure with smaller fractions of martensite, see Figs. 5.24 - 5.25. Again, no detectable difference in the microstructure from surface to inner regions was observed.

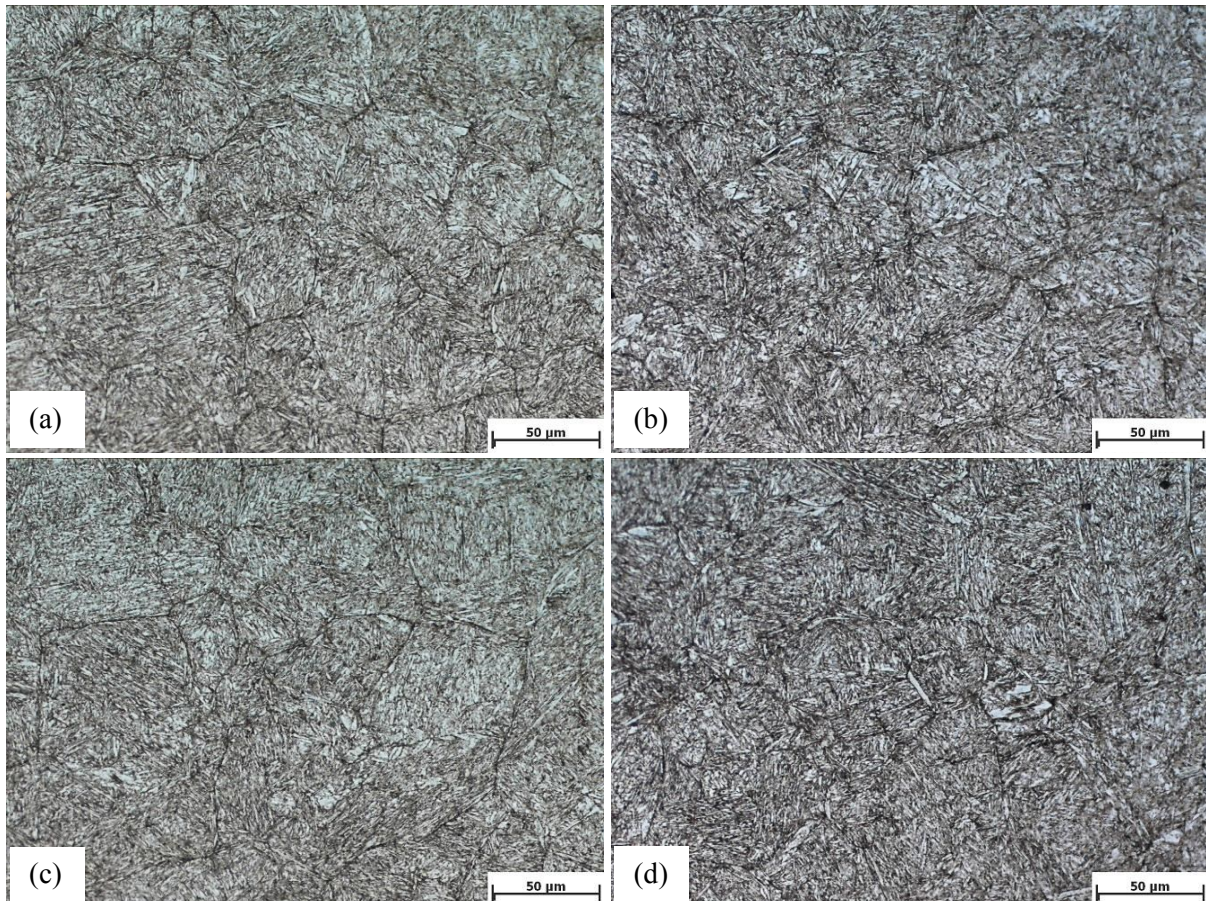


Figure 5.24: W300 with bainitic matrix structure. (a,b) inner region and (c,d) surface near region of the specimen, Nital etchant.

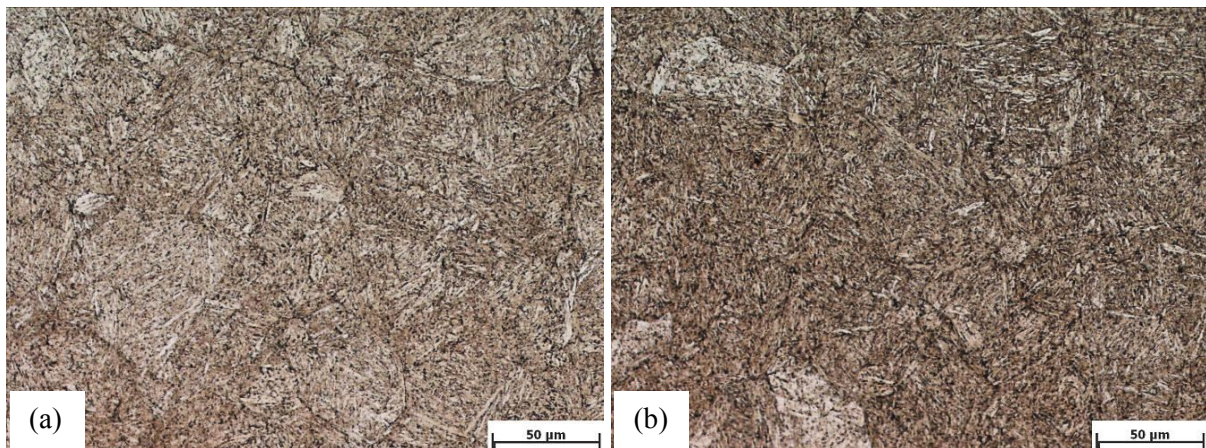


Figure 5.25: W300 with bainitic matrix structure. (a) inner region and (b) surface near region of the specimen, V2A etchant.

In Figs. 5.26 - 5.27 the homogeneously and fine distributed microstructure of W400 is shown via Nital and V2A etchant.

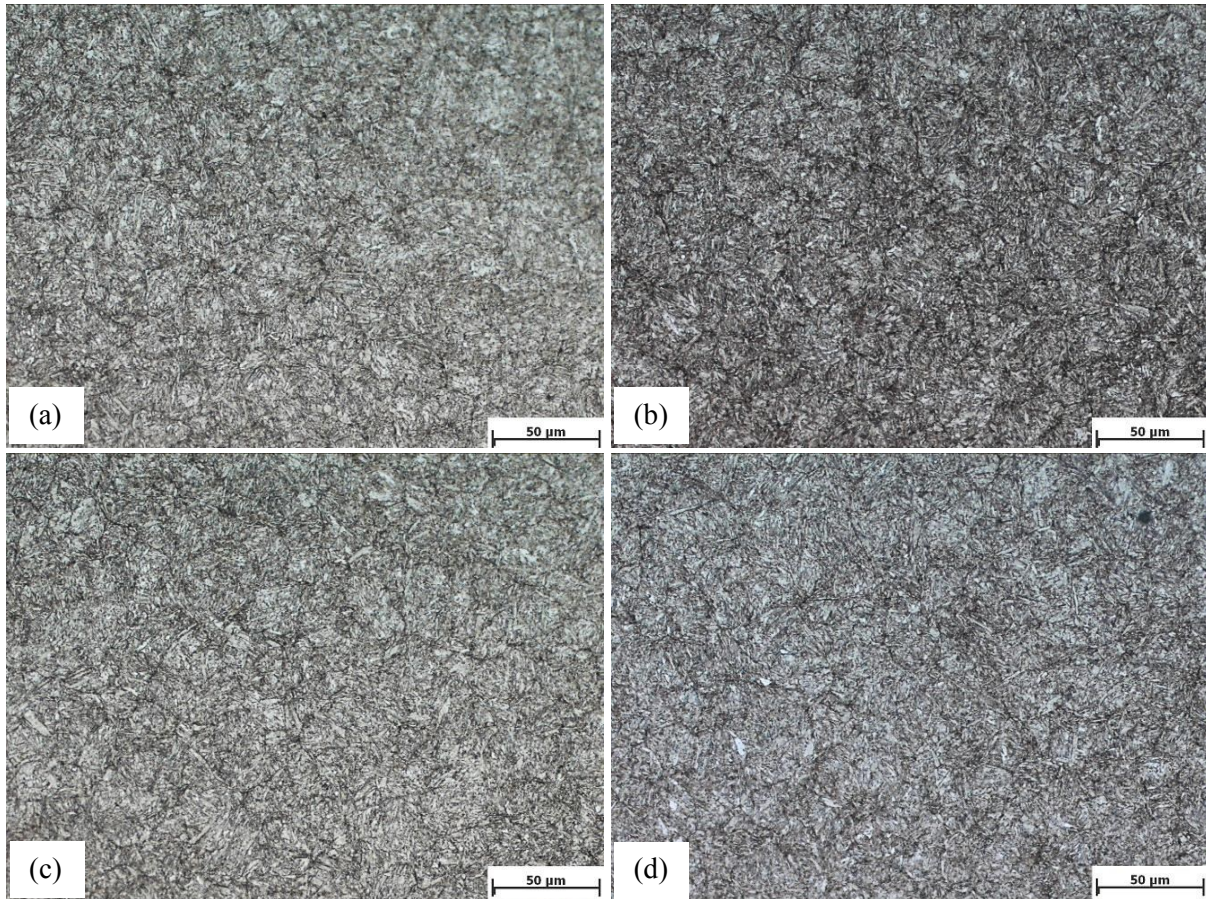


Figure 5.26: W400 with martensitic matrix structure. (a,b) inner region and (c,d) surface near region of the specimen, Nital etchant.

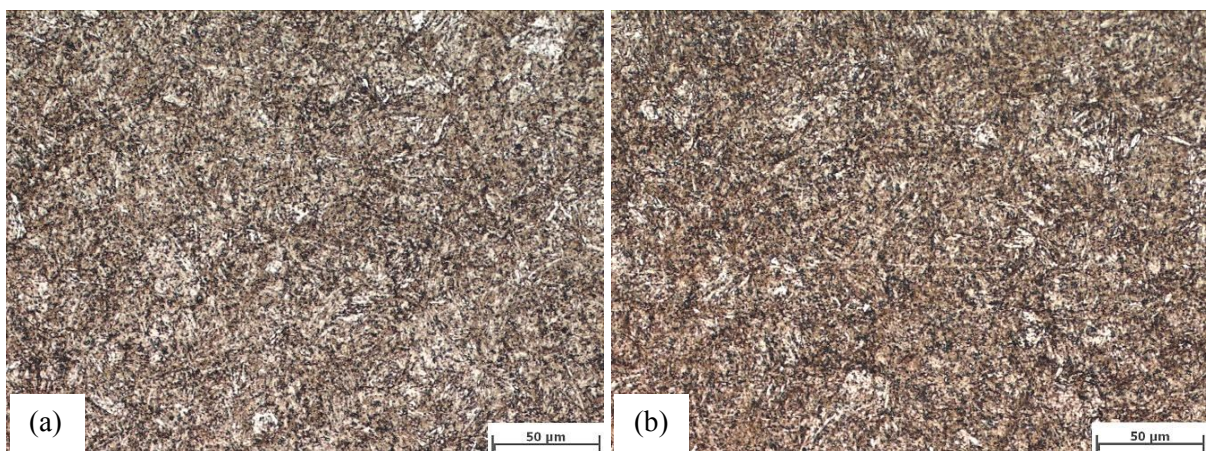


Figure 5.27: W400 with martensitic matrix structure. (a) inner region and (b) surface near region of the specimen, V2A etchant.

When metallographically investigating the specimens in situ or after rupture, the microstructure seems still unchanged, except the prior austenitic grain boundaries become slightly visible, the higher the thermal load the more intensively, compare Figs. 5.28 and 5.29.

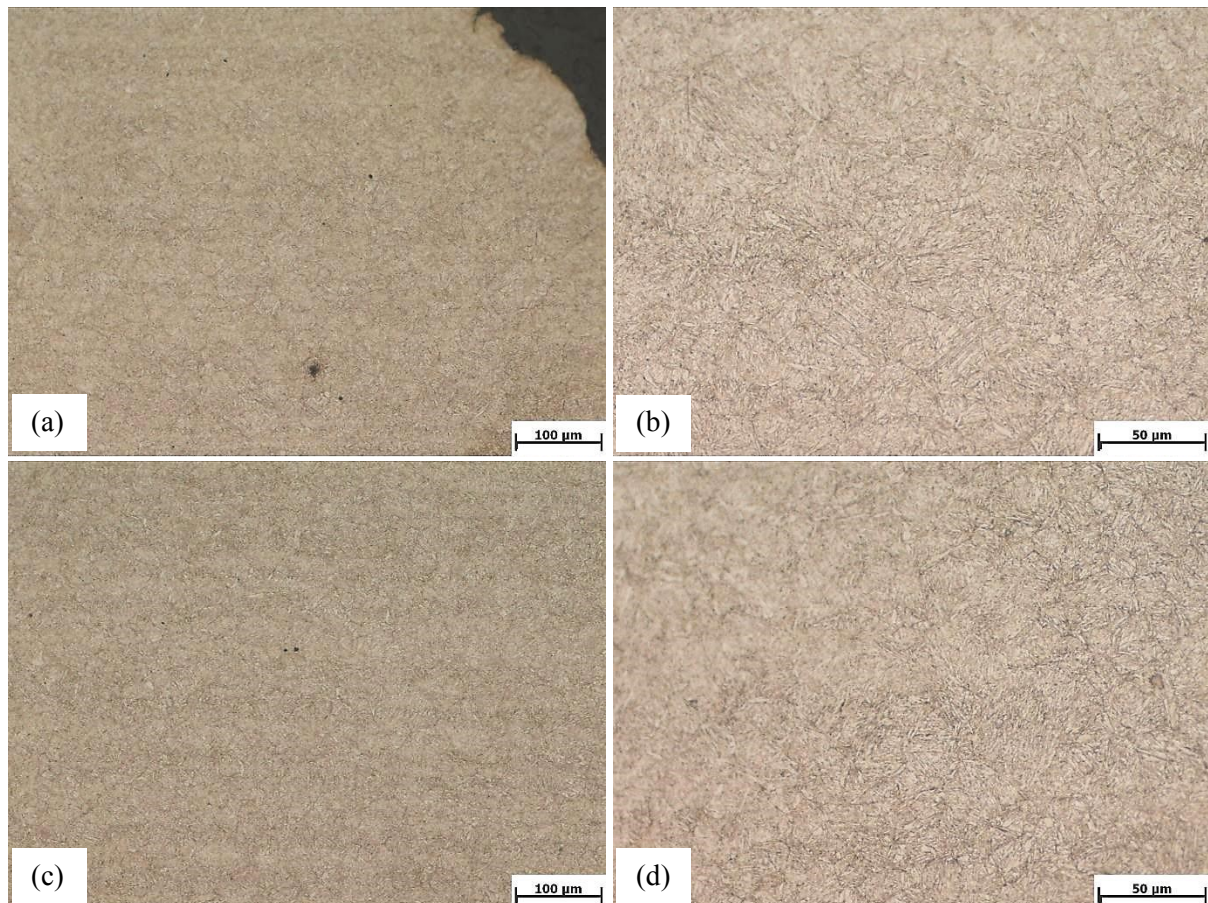


Figure 5.28: W300 with martensitic matrix structure. Fracture near area after fatigue testing at (a,b) 500°C and 2523 cycles and (c,d) at 580°C and 347 cycles to rupture, both $R = -1$ and $\Delta\epsilon = 1.2\%$, V2A etchant (A11).

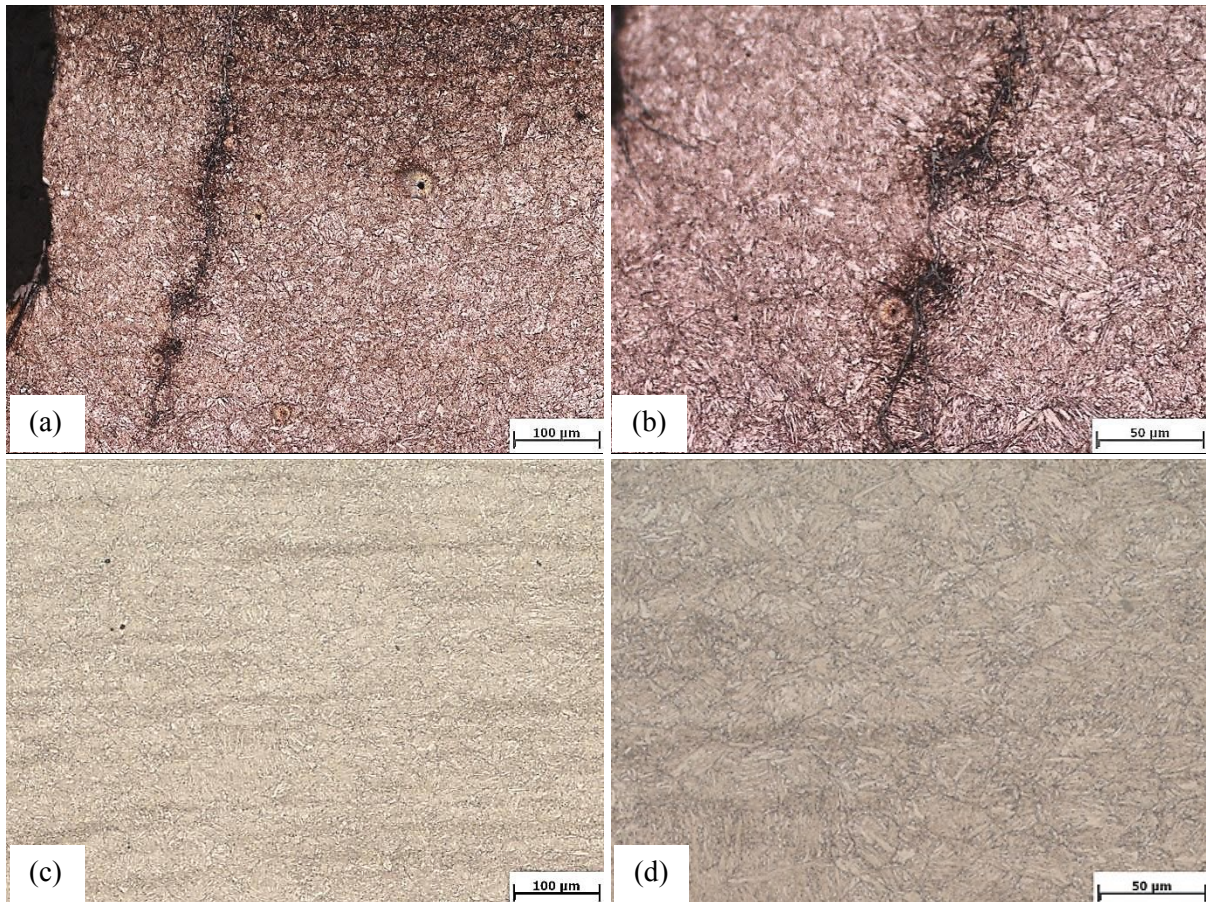


Figure 5.29: W300 with martensitic matrix structure. Fracture near area after creep-fatigue testing at (a,b) 500°C and 776 cycles (A13) and (c,d) at 580°C and 111 cycles (A14) to rupture, both $R = -1$, $\Delta\epsilon = 1.2\%$ and a hold time during compression of 300s, V2A etchant.

Since the strain amplitude is held constant, the fatigue and creep-fatigue experiments do not show global strains as they occur in the constricted area of broken short term creep tests, where the prior austenitic grains as well as the lath structure is already deformed in load direction, which produces elongated texture-like formations of martensitic laths, see Figs. 5.30 - 5.32.

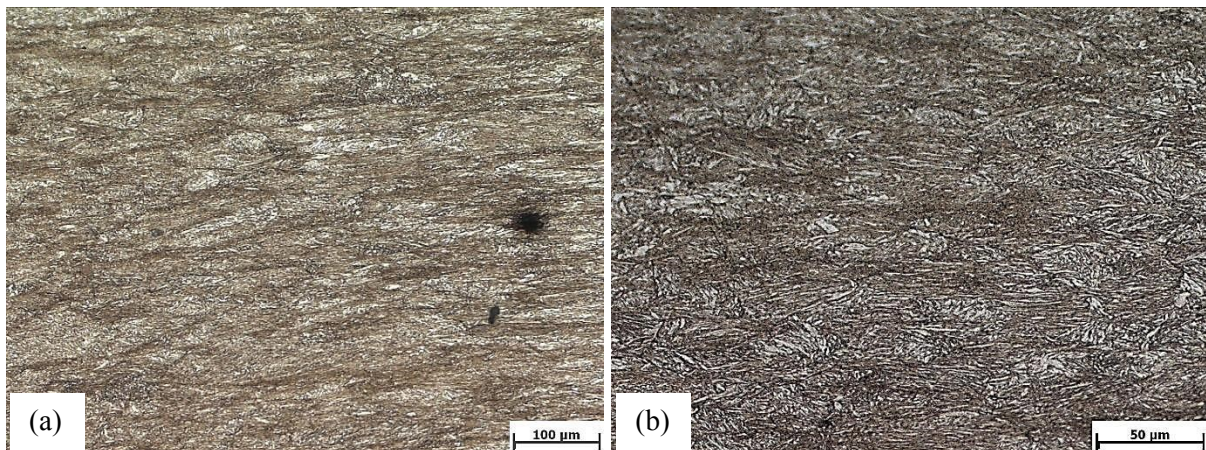


Figure 5.30: W300 with martensitic matrix structure. Fracture near area after creep testing at 500°C and 800MPa (A42).

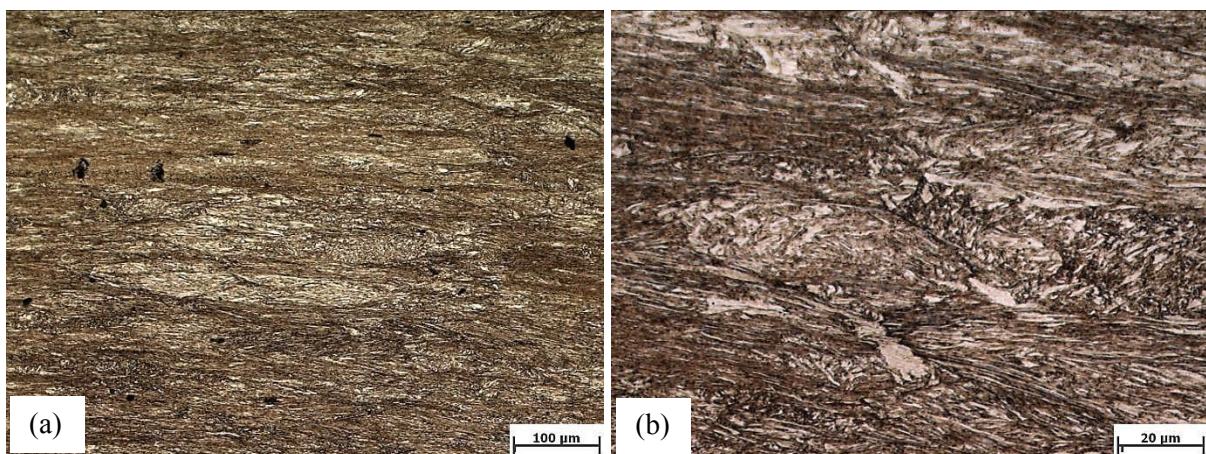


Figure 5.31: W300 with martensitic matrix structure. Fracture near area after creep testing at 540°C and 800MPa (A44).

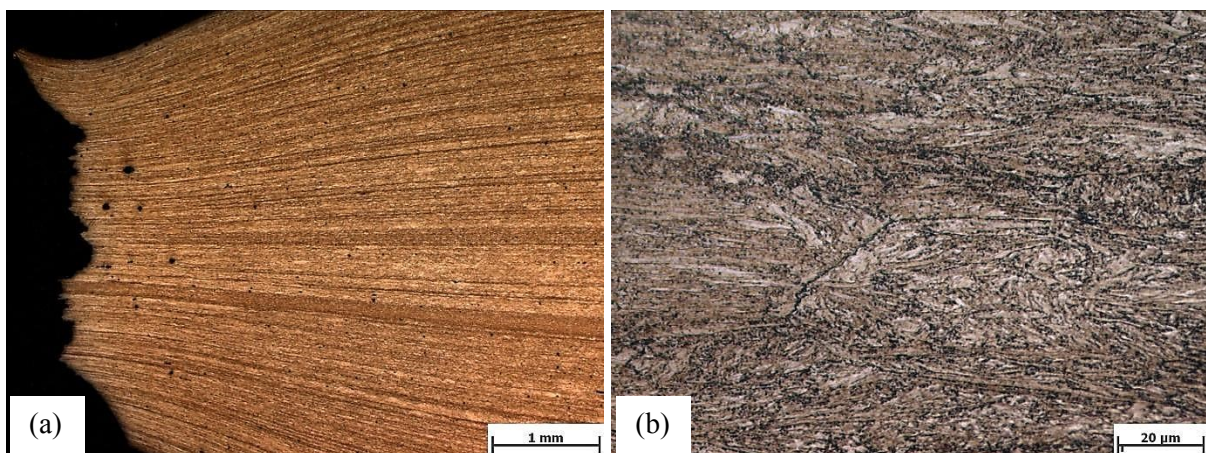


Figure 5.32: W300 with martensitic matrix structure. Fracture near area after creep testing at 580°C and 400MPa (A23).

Fatigue and creep-fatigue ruptured bainitic W300 with clearly visible prior austenitic grain boundaries, are depicted in Fig. 5.33 and 5.34.

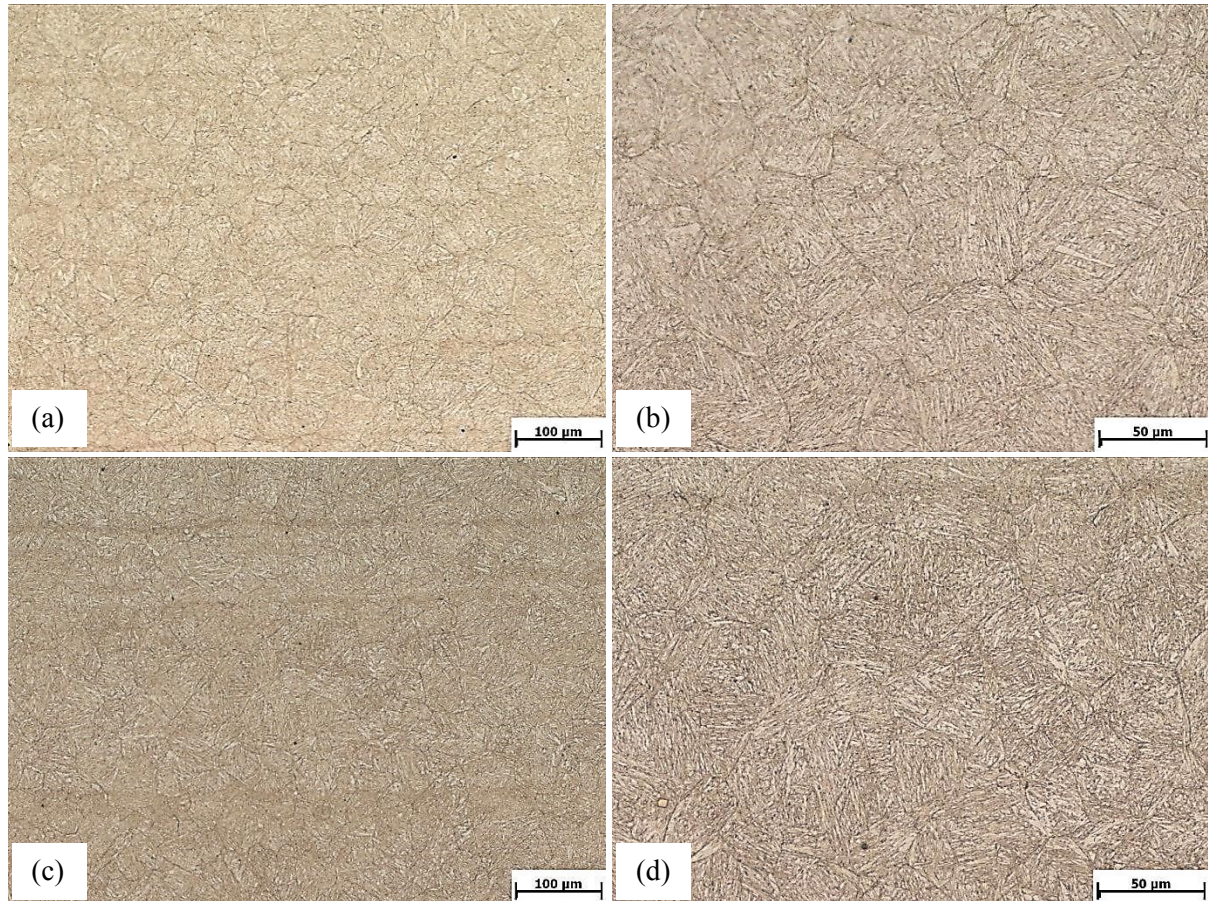


Figure 5.33: W300 with bainitic matrix structure. Fracture near area after fatigue testing at (a,b) 500°C and 1284 cycles (B7) and (c,d) at 580°C and 410 cycles (B11) to rupture, both $R = -1$ and $\Delta\varepsilon = 1.2\%$, V2A etchant.

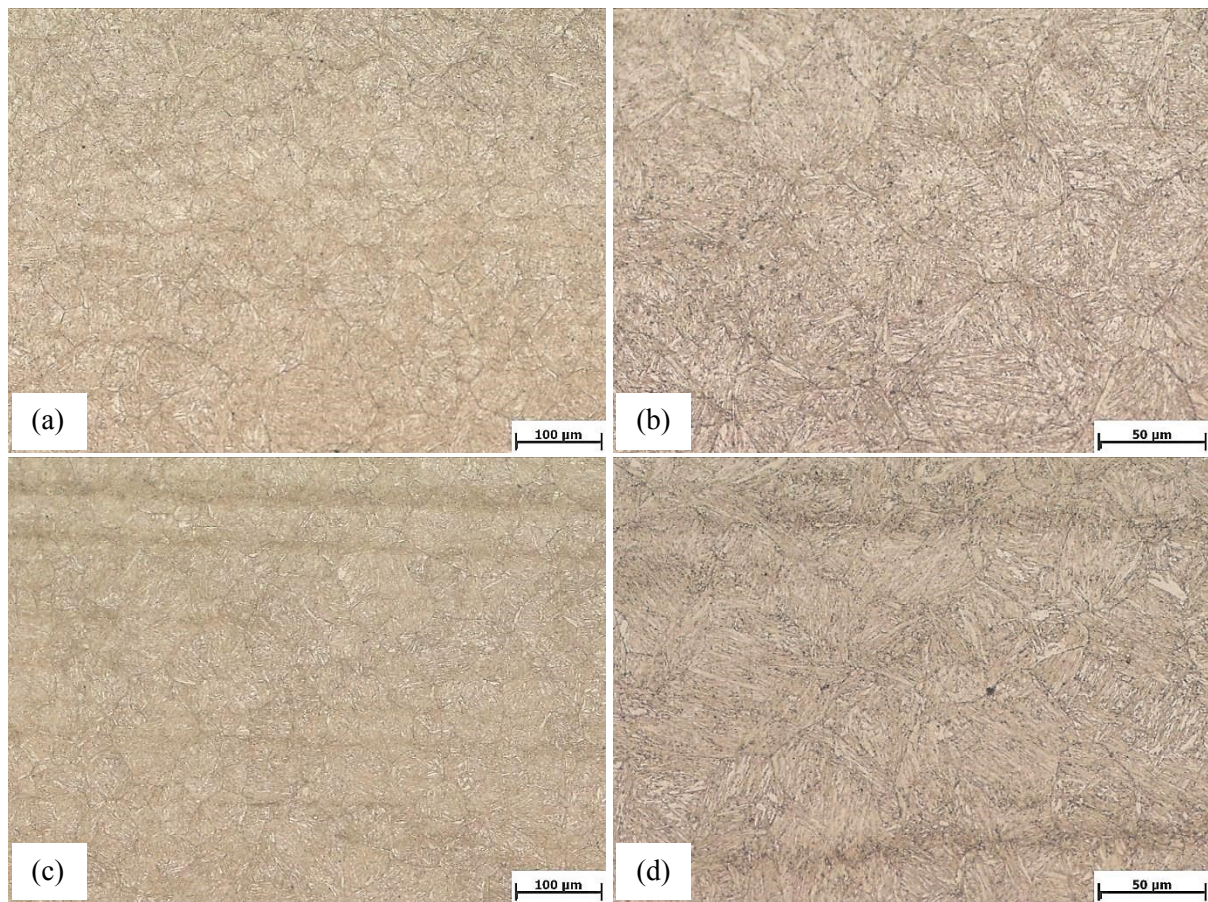


Figure 5.34: W300 with bainitic matrix structure. Fracture near area after creep-fatigue testing at (a,b) 500°C and 857 cycles (B15) and (c,d) at 580°C and 100 (B16) cycles to rupture, both $R = -1$, $\Delta\varepsilon = 1.2\%$ and 300s hold time during compression, V2A etchant.

Crack initiation during creep mainly takes place at triple points of prior austenitic grain boundaries, see Fig. 5.35 (a).

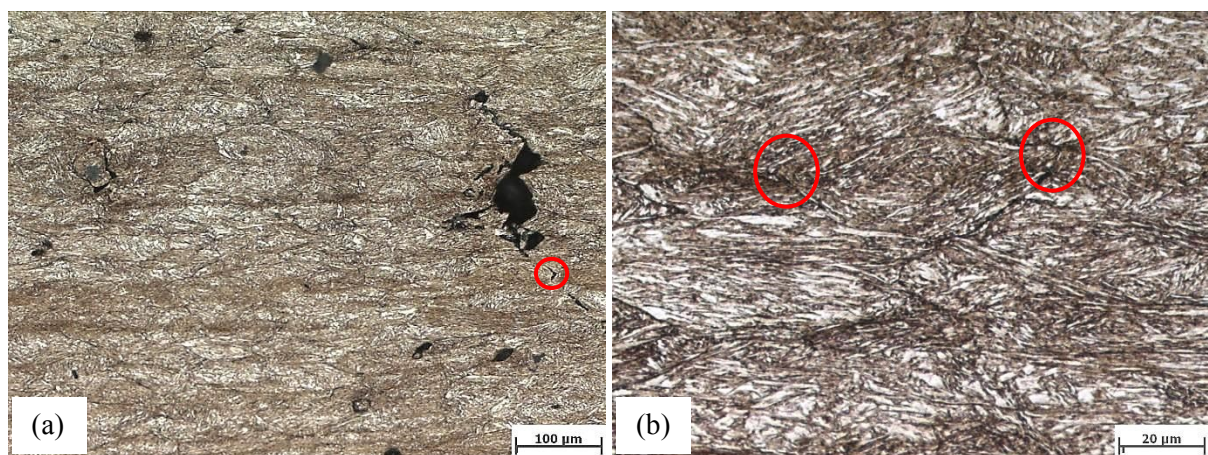


Figure 5.35: W300 with bainitic matrix structure. Fracture near area after creep testing at 500°C and 800MPa. (a) Crack initiation at triple points was found, (b) another detail (B42).

Crack initiation at triple points and propagation at prior austenitic grain boundaries was observed. The differences in the local chemical composition due to the production route are clearly visible when observing different local chemical resistivity during etching, see Fig. 5.36.

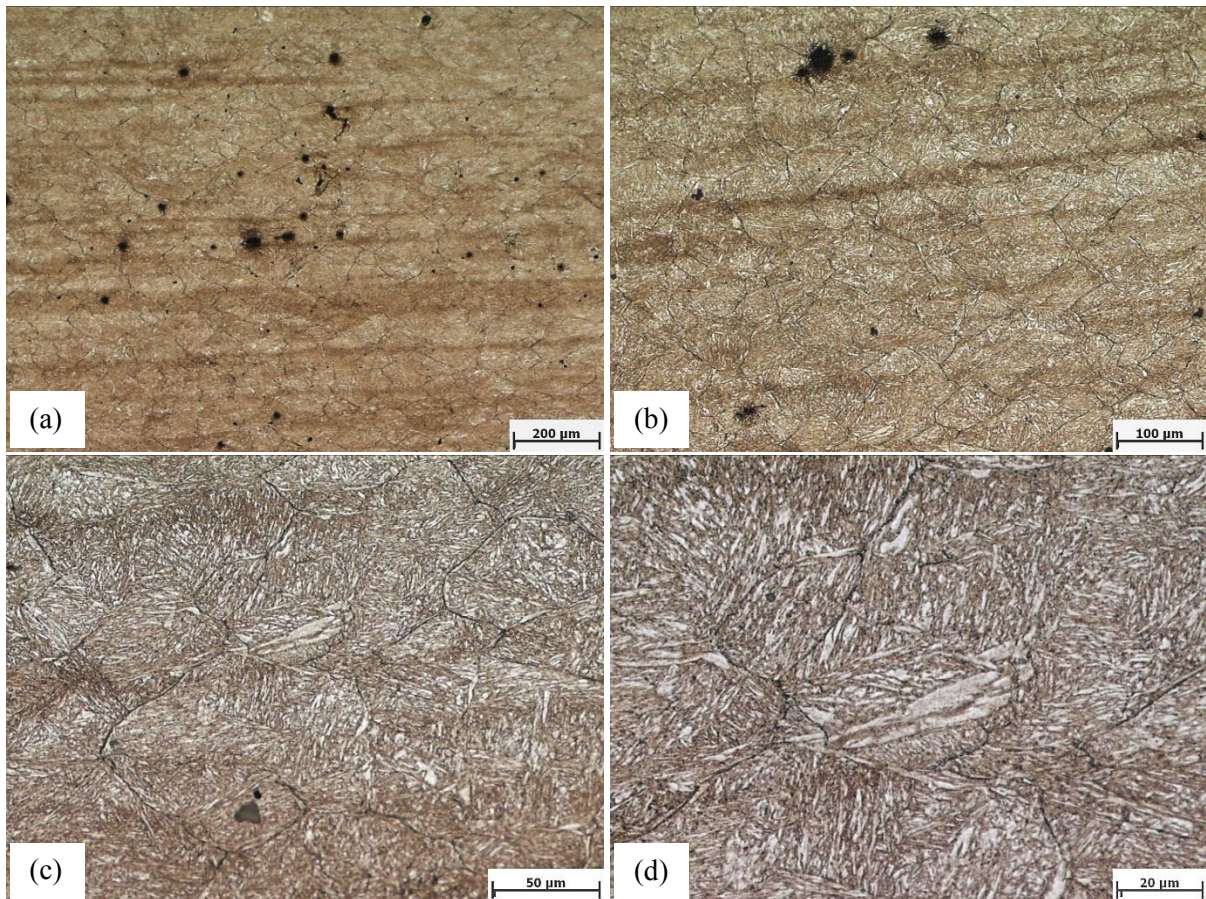


Figure 5.36: W300 with bainitic matrix structure. Fracture near area after creep testing at 500°C and 600MPa. The magnification increases from (a) to (d). The dark dots are etching phenomena, no pores (B31).

At higher temperatures and respectively high stresses, the structure becomes highly unstable, grain boundary sliding with initiation of pores and plastic material flow cause rapid damage and failure. Reasonable temperature-stress load combinations were trespassed, which lies beyond the limit of the tool material's application range, see Figs. 5.37 - 5.38 and 5.40 - 5.41.

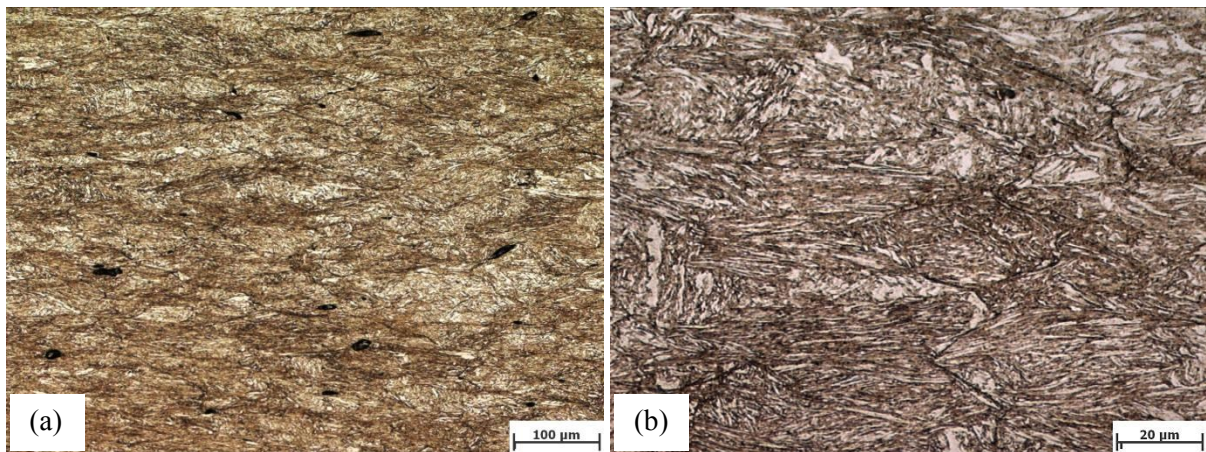


Figure 5.37: W300 with bainitic matrix structure. Fracture near area after creep testing at 540°C and 800MPa (B44).

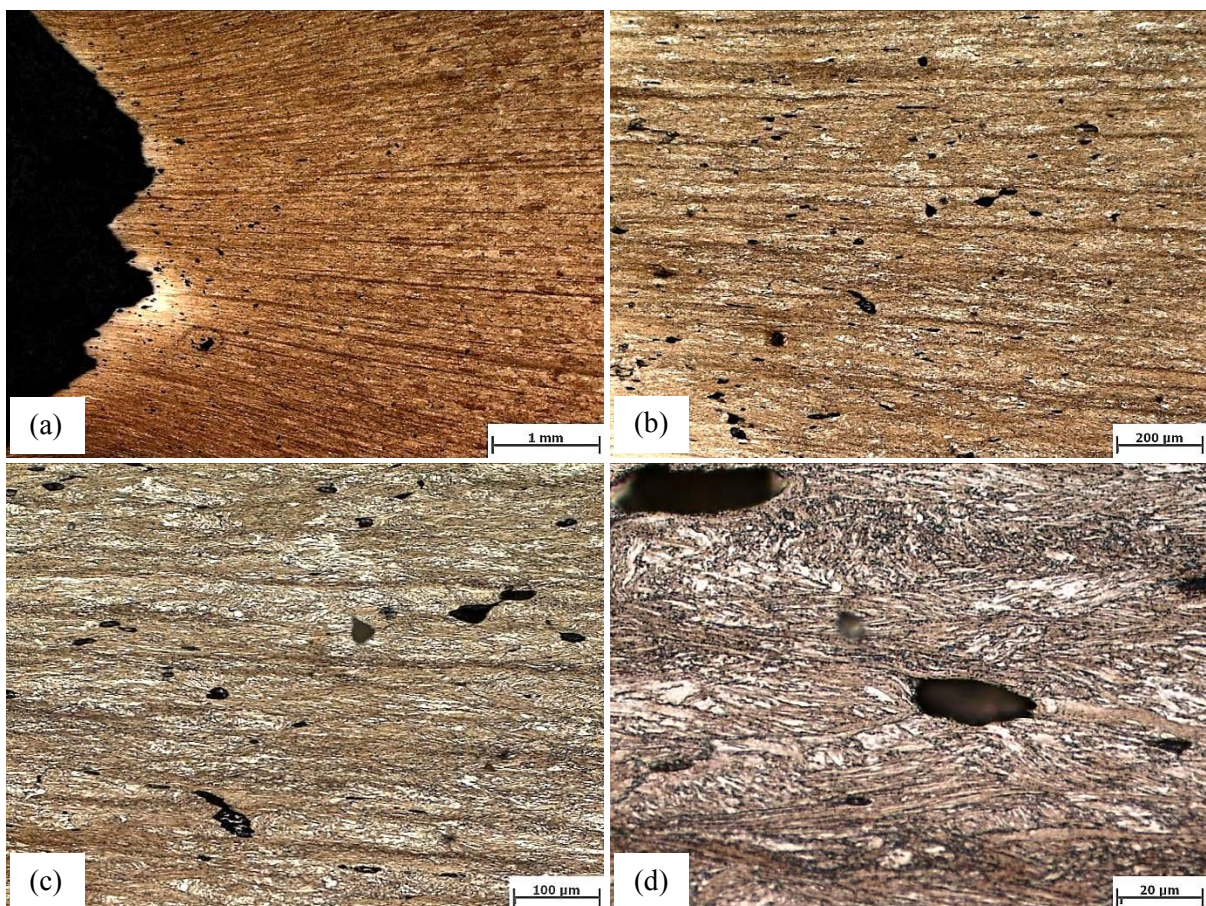


Figure 5.38: W300 with bainitic matrix structure. Fracture near area after creep testing at 580°C and 400MPa with increasing magnification from (a) to (d) (B24).

The reason for the advanced performance of the W400 in comparison to W300 can be mainly explained by the higher homogeneity and finer microstructure, see Fig. 5.39.

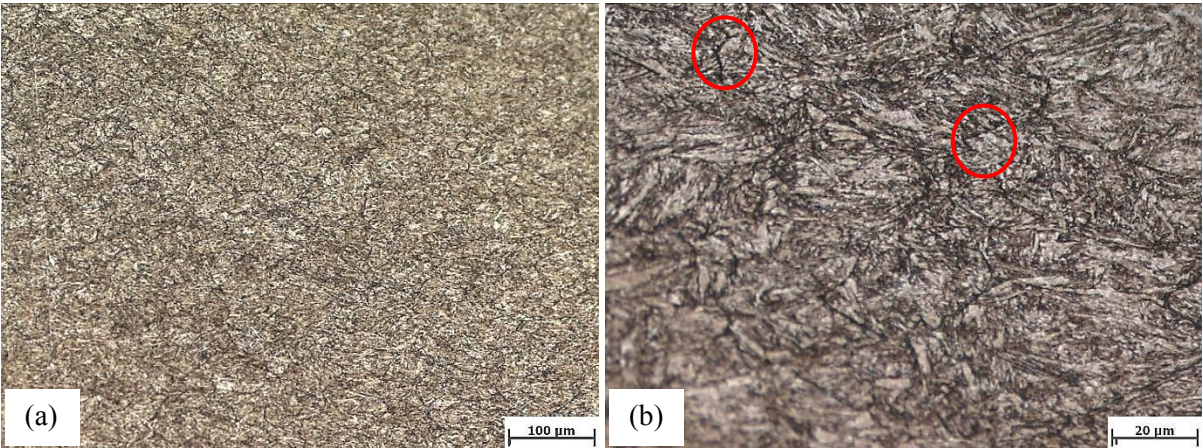


Figure 5.39: W400 with martensitic matrix structure. Fracture near area after creep testing at 500°C and 800MPa (a) Overview of the comparatively finer structure and (b) detail of initiated cracks (F31).

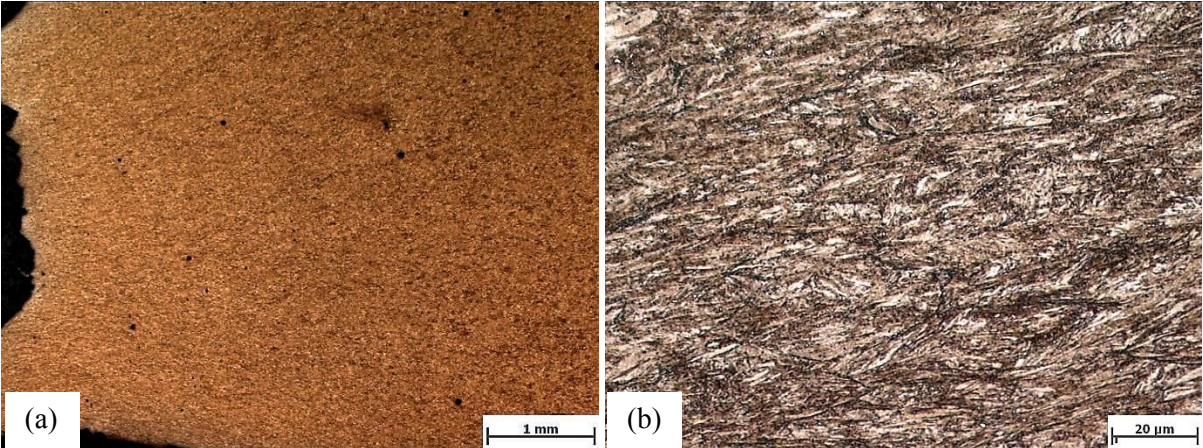


Figure 5.40: W400 with martensitic matrix structure. Fracture near area after creep testing at 540°C and 600MPa (F21).

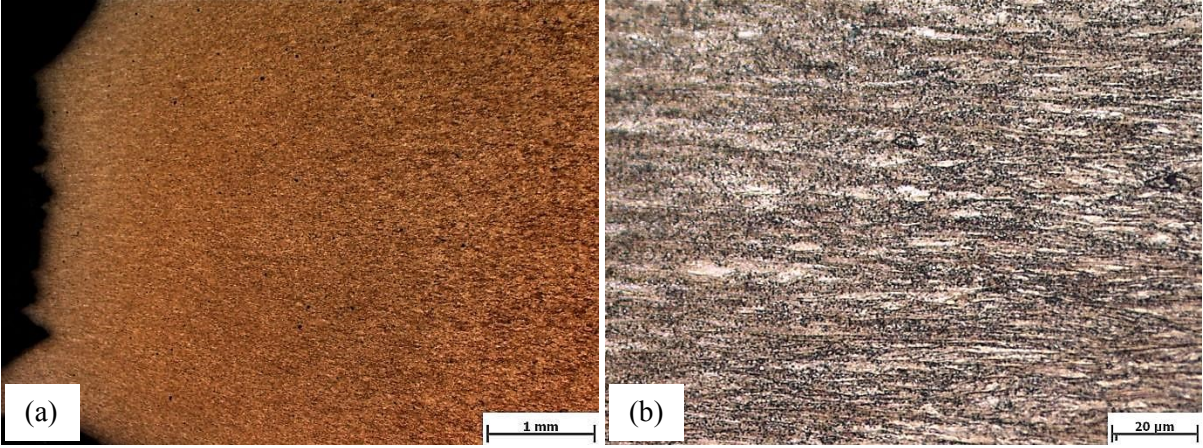


Figure 5.41: W400 with martensitic matrix structure. Fracture near area after creep testing at 580°C and 400MPa (F21).

5.2.2 TEM investigations

To validate the precipitation calculations, performed with the thermo-kinetic software MatCalc, five specimens were investigated in detail by TEM-measurements, see Tab. 5.13.

Table 5.13: Overview of the investigated TEM specimens

Material	Matrix	Load σ^+/σ^- [MPa]	Cycles to rupture [-]	T [°C]	Duration [h]	Dislocation density [10^{15}m^{-2}]	Comments
W300	martensitic	-	-	-	--	2.3	A5, heat treatment only
W300	martensitic	922/836	776	500	72.72	2.1	A13
W300	martensitic	836/749	111	580	15.06	2.8	A14
W300	bainitic	721/865	857	500	80.06	2.5	B15
W400	martensitic	749/980	1656	500	162.5	-	F3

In the light-optical microstructure images, the resolution limit is ca. half of a micron, see Fig. 5.42. Since the secondary hardening precipitates are smaller sized, in the maximum range of 100 - 150 microns, it was necessary to use fine structure investigations.

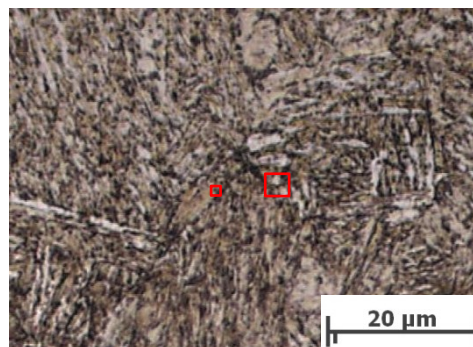


Figure 5.42: Maximum possible resolution of a light-optical micrograph image. The two applied sizes of TEM images, which are around 1 and 3.5 microns in edge length, respectively, are schematically implemented into the image.

The initial state after heat treatment (specimen A5) and before applying any thermal or mechanical load is shown in Fig. 5.43. That can be directly compared with the longest creep-fatigue loaded specimen (A13) of the same material's state, see Fig. 5.44. However, the most detrimental influence onto the tool's microstructure occurs at a service temperature in the range of the tempering temperature. Significant larger sized precipitates were found when the tool material had to sustain a creep-fatigue loading at 580°C. The highest dislocation density was also detected in that specimen. In Figs. 5.43 - 5.48 the left image is the elastic TEM image with the EELS images for the related elements such as Fe, Cr, Mo, V, C and N, respectively, following on the right. Since the microstructure contains numerous and very fine distributed precipitates, five series on each considered parameter variation in temperature and load case were performed. The dominant precipitates are chromium rich carbides. In Fig. 5.44

the precipitates' state is not significantly coarsened in comparison with the initial state in Fig. 5.43.

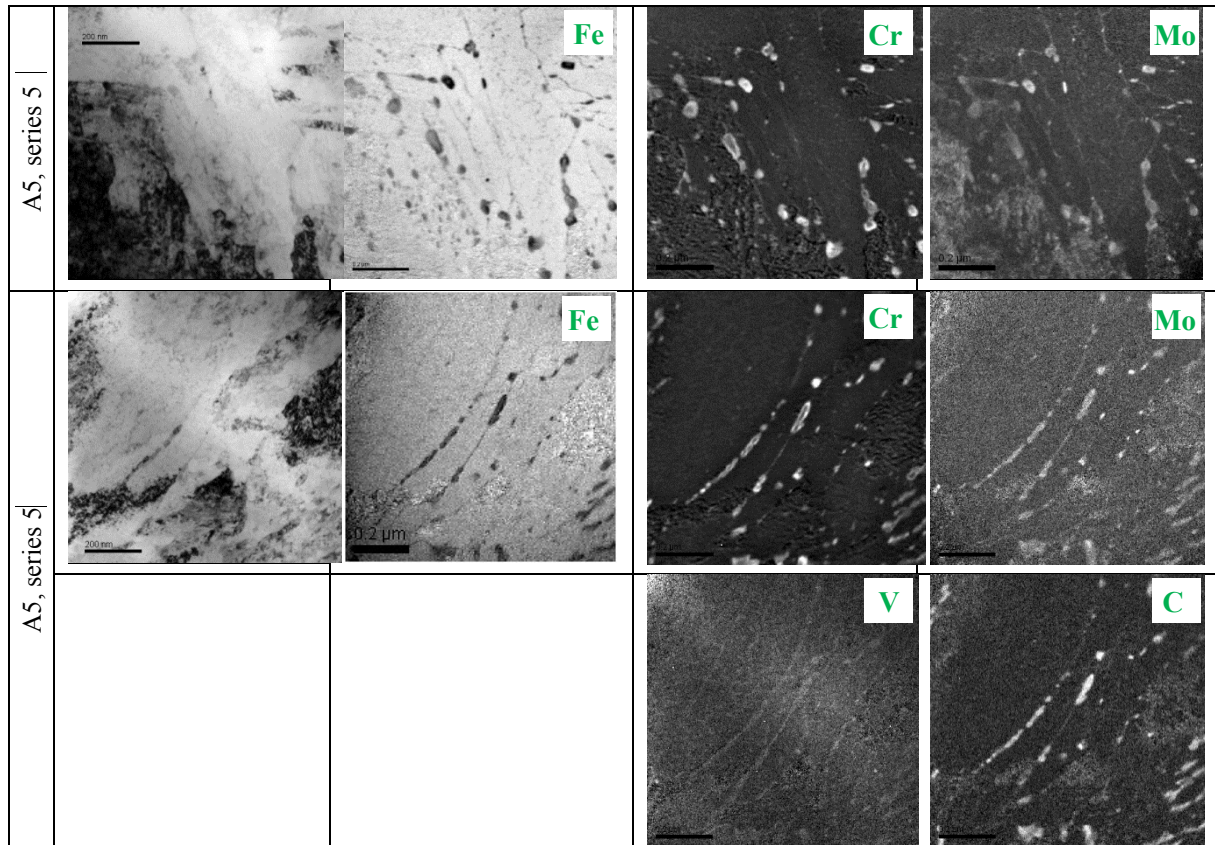


Figure 5.43: TEM investigation of heat treated W300. A tempered martensitic matrix structure with high amounts of small chromium rich carbides was observed. See also Fig. 9.1 in Appendix A.

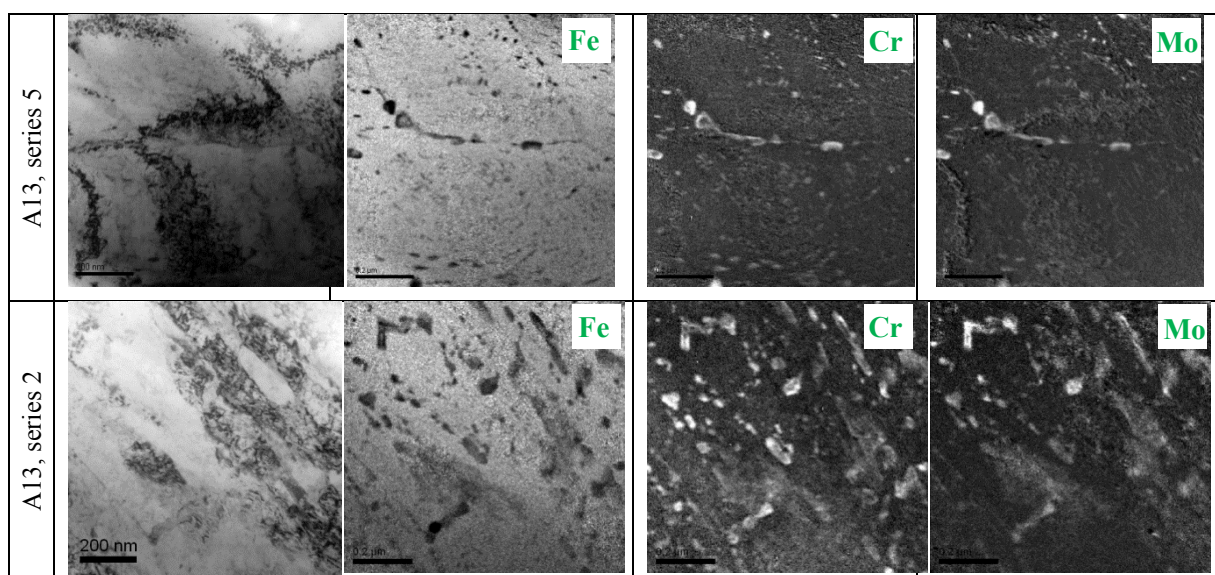


Figure 5.44: TEM investigation of a tempered W300 martensitic matrix structure, creep-fatigue loaded for 72.3 h at 500°C. See also Fig. 9.2 in Appendix A.

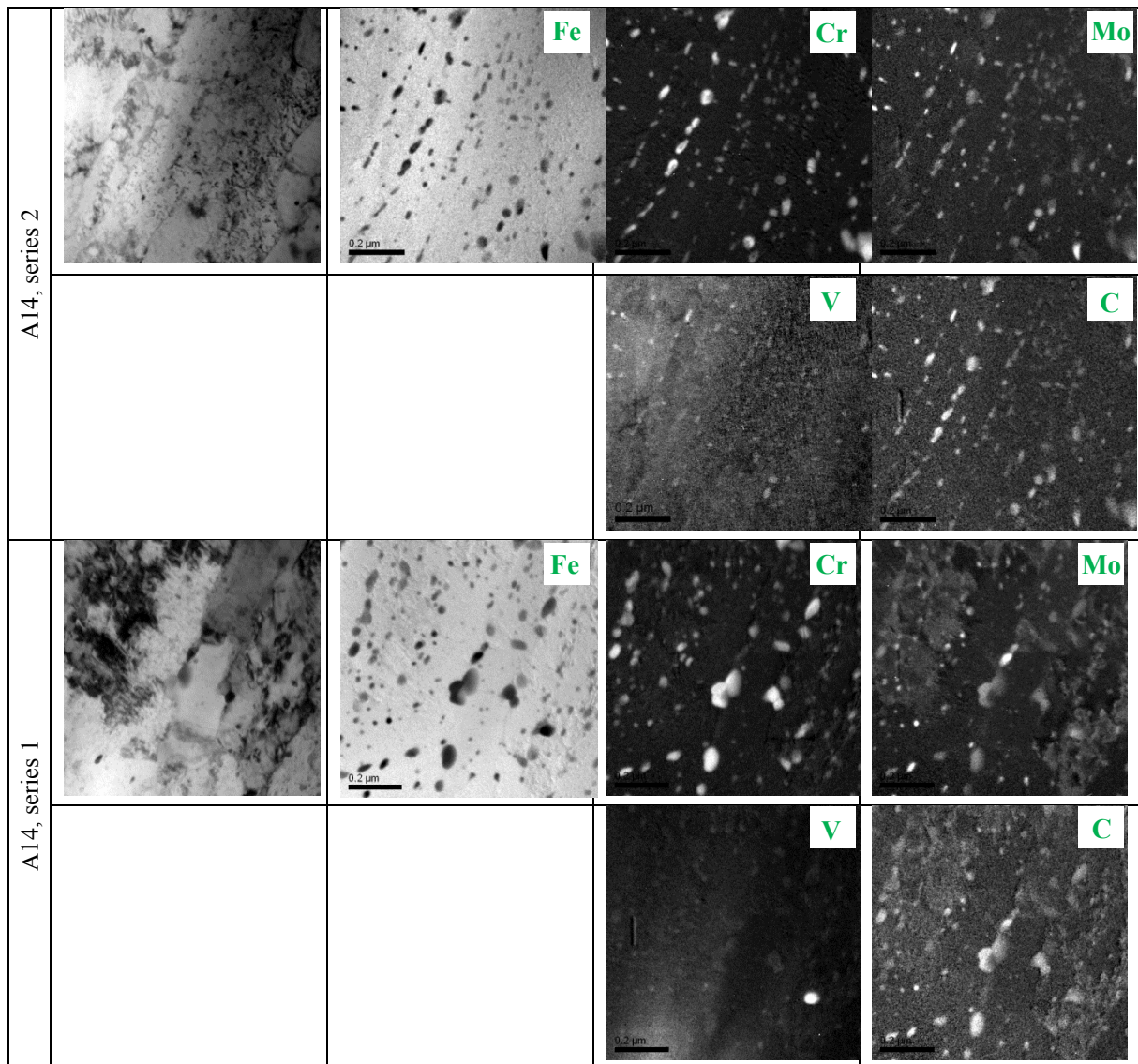


Figure 5.45: TEM investigation of a tempered W300 martensitic matrix structure, creep-fatigue loaded for 15.1 h at 580°C. Again the dominant precipitates are chromium rich carbides. Due to the thermal loading in the range of the highest annealing temperature, the microstructure coarsened significantly. See also Fig. 9.3 in Appendix A.

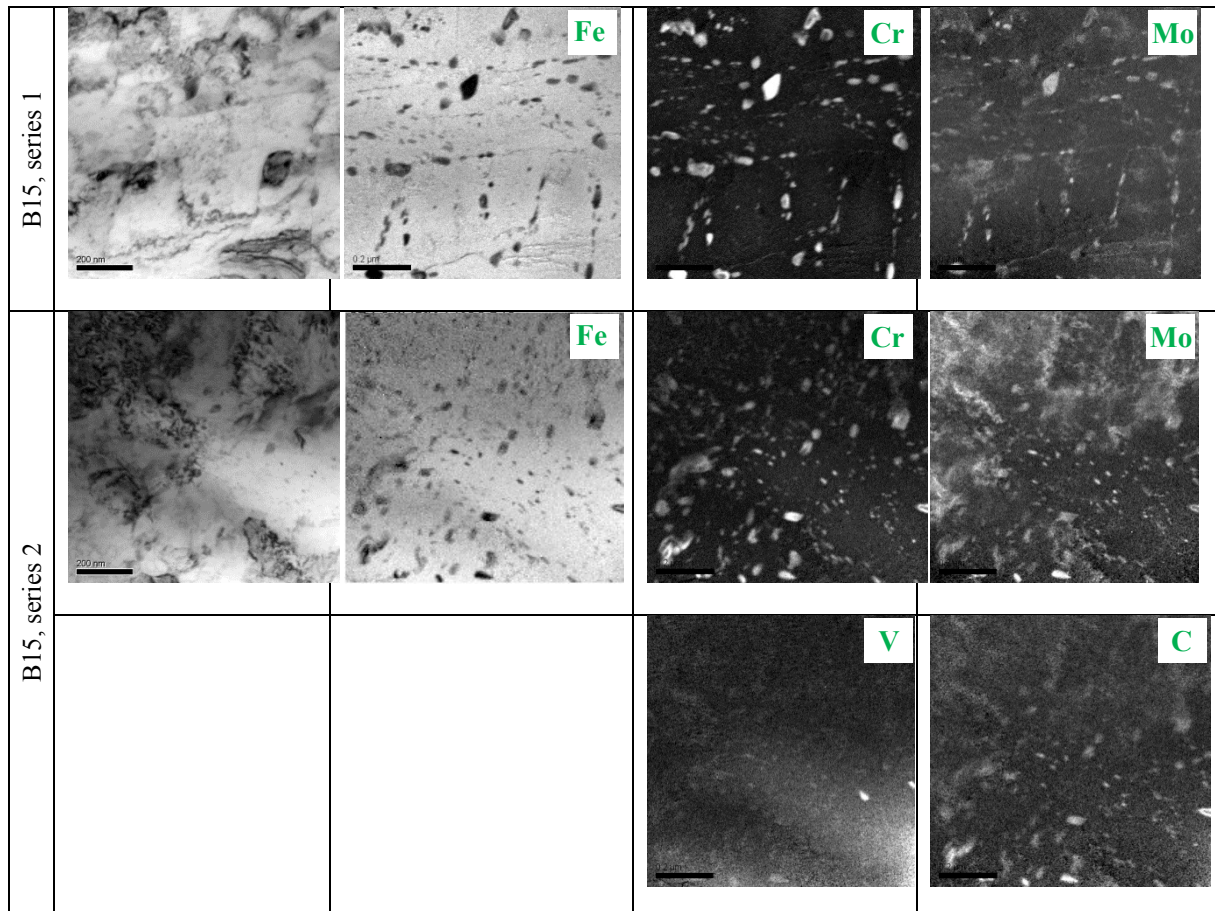


Figure 5.46: TEM investigation of a tempered bainitic matrix structure, creep-fatigue loaded for 15.1 h at 500°C. The dominant precipitates are chromium rich carbides with traces of molybdenum. See also Fig. 9.4 in Appendix A.

A creep-fatigue loaded W400, which was subjected for 162.5 hours at 500°C was also investigated, see Fig. 5.47. When considering series 1 and 3, precipitation of molybdenum enriched carbides at the lath boundaries occurred, in series 5 the small lath size in the centre of the TEM-images is visible due to the afore mentioned molybdenum precipitation. Additionally in series 3, a large CrC-precipitate as well as an (Mo,V)C-precipitate could be detected.

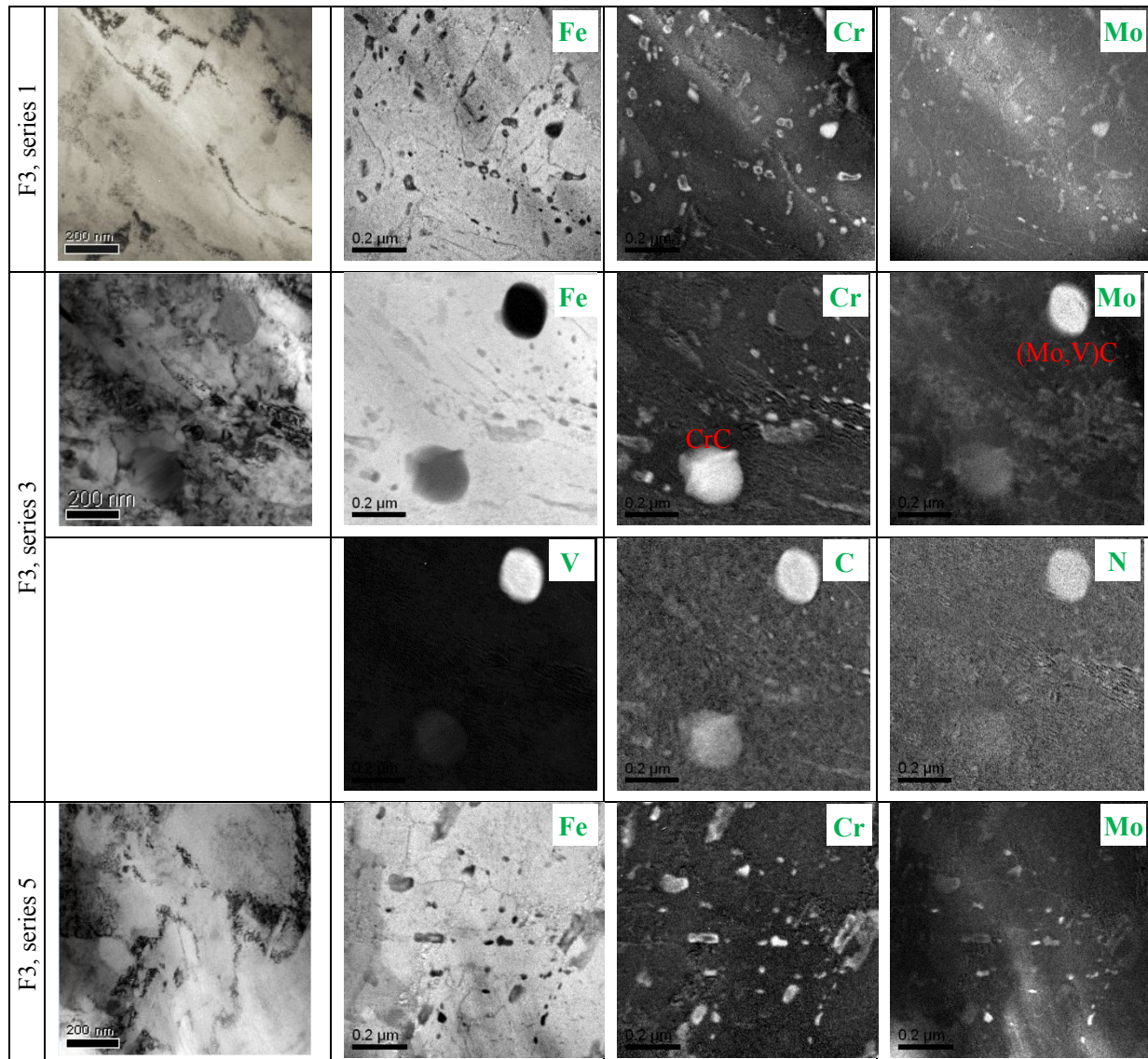


Figure 5.47: TEM investigation of a tempered W400 martensitic matrix structure, creep-fatigue loaded for 162.5 h at 500°C.

For a guarantee of reliable statistics, namely parameter evaluation of precipitate's size distribution as well as volume fraction and number density, the locations of the TEM images was taken randomly. Selecting "good" TEM images on purpose was not required and neither desired. However, 5 out of 25 images showed a pattern-like structure, which is worth

mentioning. Preferred growing directions of $(\text{Cr, Mo, Fe})_x\text{C}$ -precipitates were observed, see Fig. 5.48.

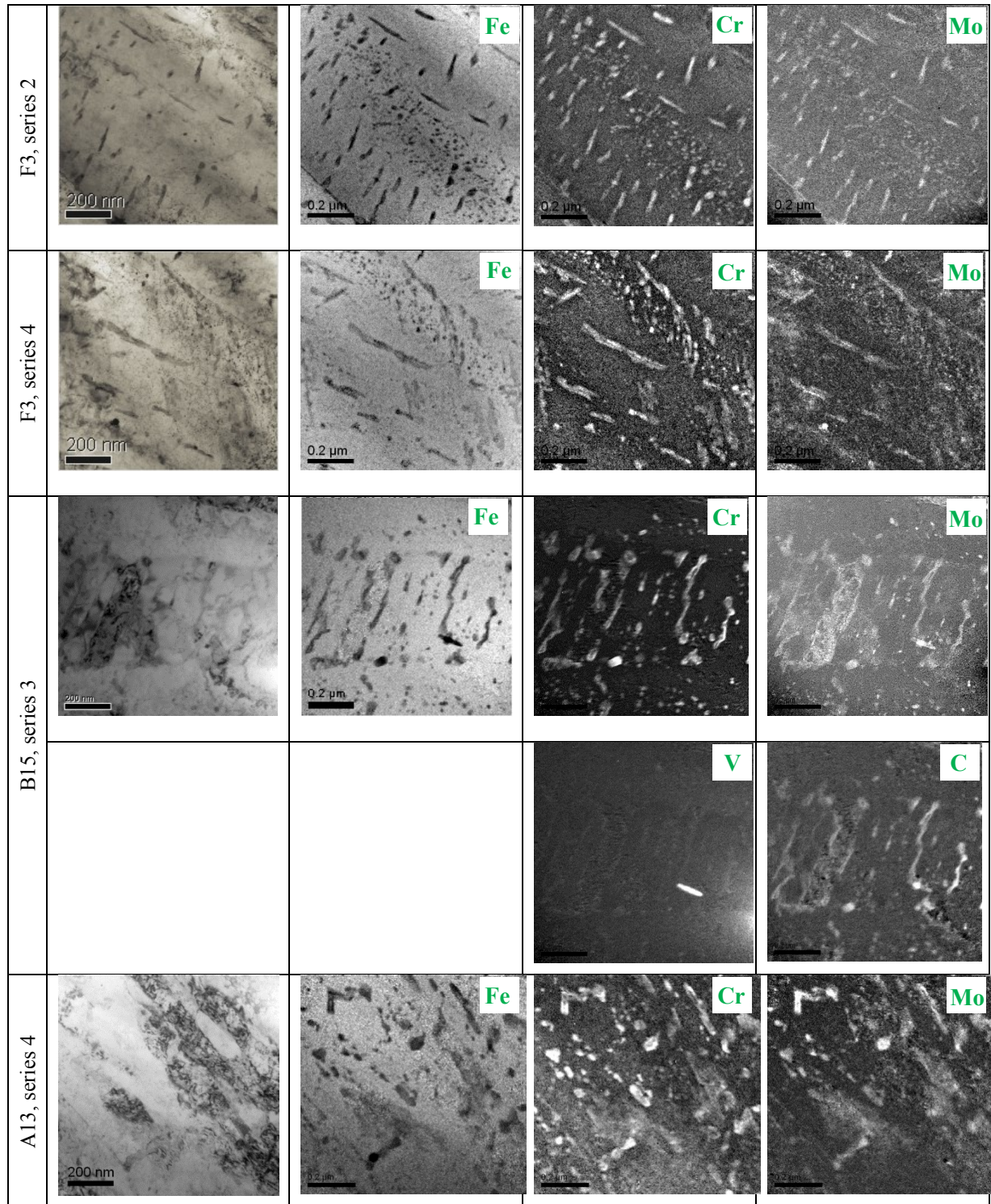


Figure 5.48: Observed preferred orientations of $(\text{Cr, Mo, Fe})_x\text{C}$ precipitates.

Suchlike precipitate structure is mainly the result of a regular ordered lath structure, i.e. locations, where the precipitates can easily form.

In general, the tool material is applied under appropriate service conditions, which means that recrystallization and grain growth must not take place during service. However, the lath- and sublath structure can coarsen with increasing service life, compare Fig. 5.49.

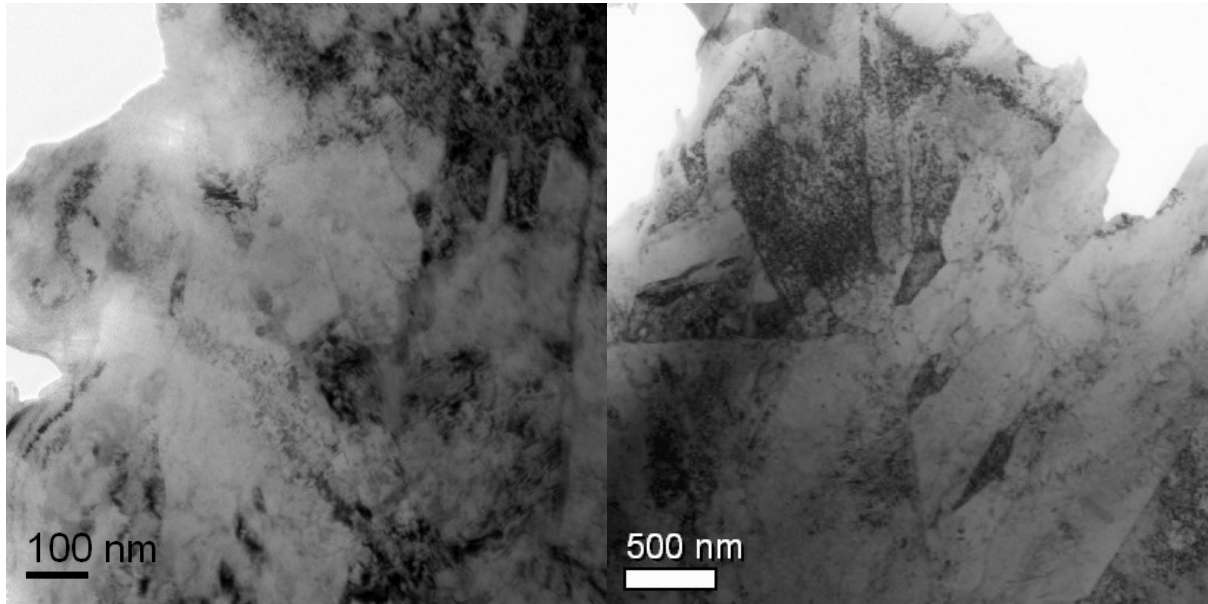


Figure 5.49: Elastic TEM image (a) virgin state after heat treatment and (b) creep-fatigue loaded for 72.3h at 500°C. Remarkable is the coarsening of the lath structure in (b).

A more detailed investigation was achieved when characterizing single precipitates via EDX spot scans. The characterization of the initial condition after heat treatment is shown in Fig. 5.50. Spot scans to identify single precipitates as well as the statistical recording of each considered precipitate via GATAN imaging software is demonstrated.

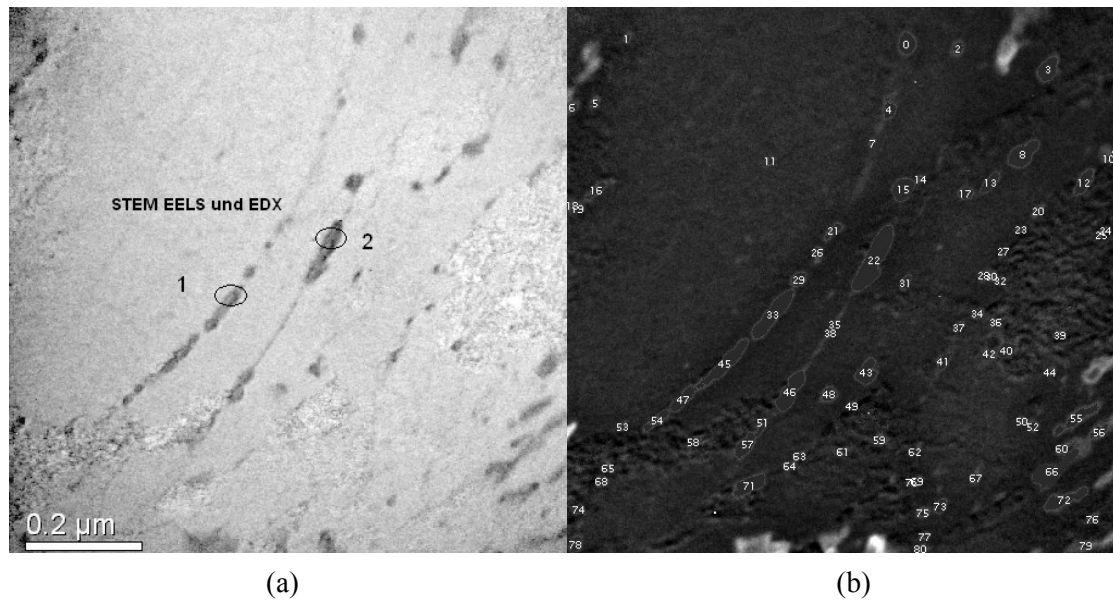


Figure 5.50: (a) STEM EELS spectra with two EDX spots to identify the precipitates via chemical composition and (b) precipitate quantification showing 80 identified precipitates at the initial condition after completed heat treatment.

The EDX scan is shown subsequently. Both precipitates of Fig. 5.50 (a) are chromium rich, where the first one additionally contains higher amounts of vanadium, see Fig. 5.51.

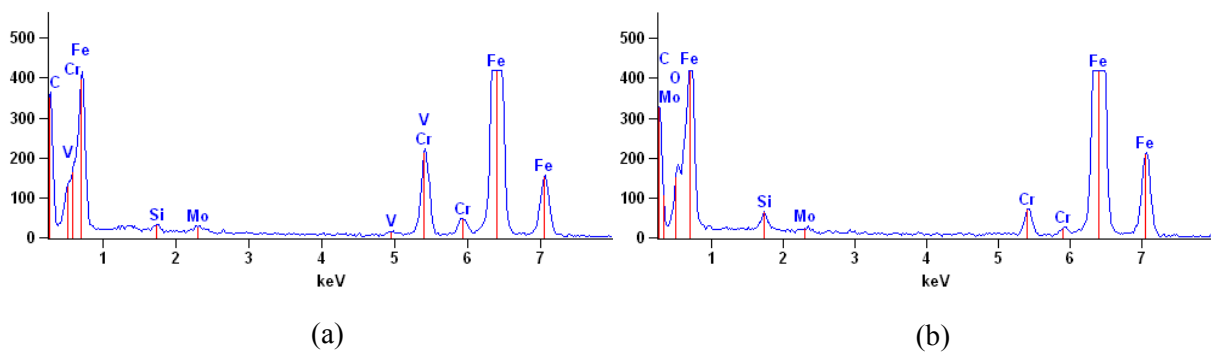


Figure 5.51: (a) Point 1 in Fig. 5.50 (a) shows high Cr and Fe contents with V, and (b) shows similar composition, both indicating an $M_{23}C_6 / M_7C_3$ precipitate.

In Fig. 5.52 and Fig. 5.53, investigations of a creep-fatigue loaded W300 specimen with martensitic matrix structure, which had to sustain 580°C for 15.1 hours are shown. The coarsening of the microstructure is noticeable. The exact composition in weight% is depicted in Tab. 5.14 and Tab. 5.15 below each referring investigation.

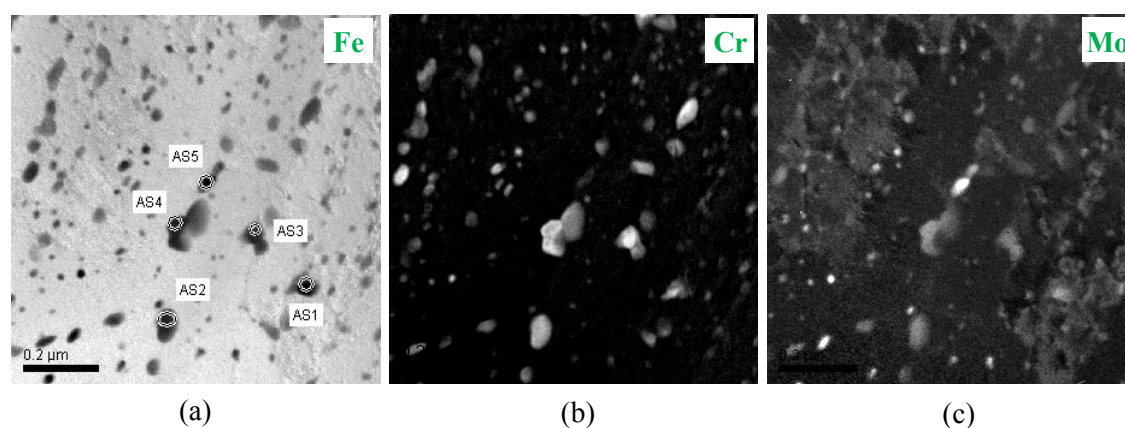


Figure 5.52: STEM EELS spectra in a (a) Fe-map with five EDX spots to identify the exact chemical composition of the precipitates as well as (b) Cr- and (c) Mo-map.

Table 5.14: Identified chemical composition of the single spot scans as shown in Fig. 5.52.

Specimen	Spot	Si	V	Cr	Fe	Mo
A14	matrix	1.22	-	3.97	94.81	-
	AS1	0.82	15.09	4.97	76.11	3.01
	AS2	0.81	-	6.52	92.67	-
	AS3	0.85	0.45	11.26	87.44	-
	AS4	-	2.79	50.42	41.32	3.13
	AS5	2.53	1.06	6.30	72.13	17.70

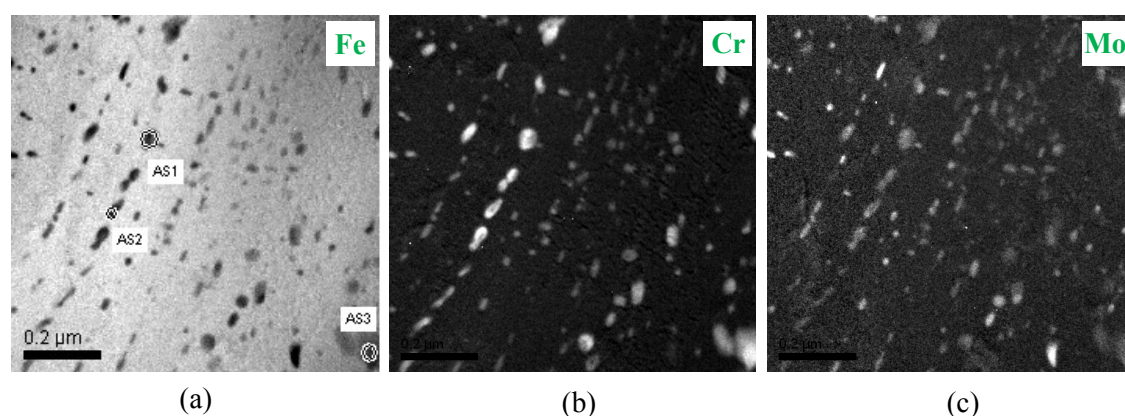


Figure 5.53: (a) STEM EELS spectra in a Fe-map with three EDX spots to identify the exact chemical composition of the precipitates as well as (b) Cr- and (c) Mo-map.

Table 5.15: Identified chemical composition of the single spot scans as shown in Fig. 5.53.

Specimen	Spot	Si	V	Cr	Fe	Cu	Mo
A14	AS1	0.26	1.37	37.32	55.99	-	5.06
	AS2	0.61	0.95	16.57	78.90	0.27	2.69
	AS3	0.51	1.69	34.34	60.21	-	3.25

In Fig. 5.54 an investigation of a creep-fatigue loaded W300 specimen with bainitic matrix structure, which had to sustain 500°C for 80.6 hours is shown. A vanadium rich precipitate was identified, see EDX scan AS5.

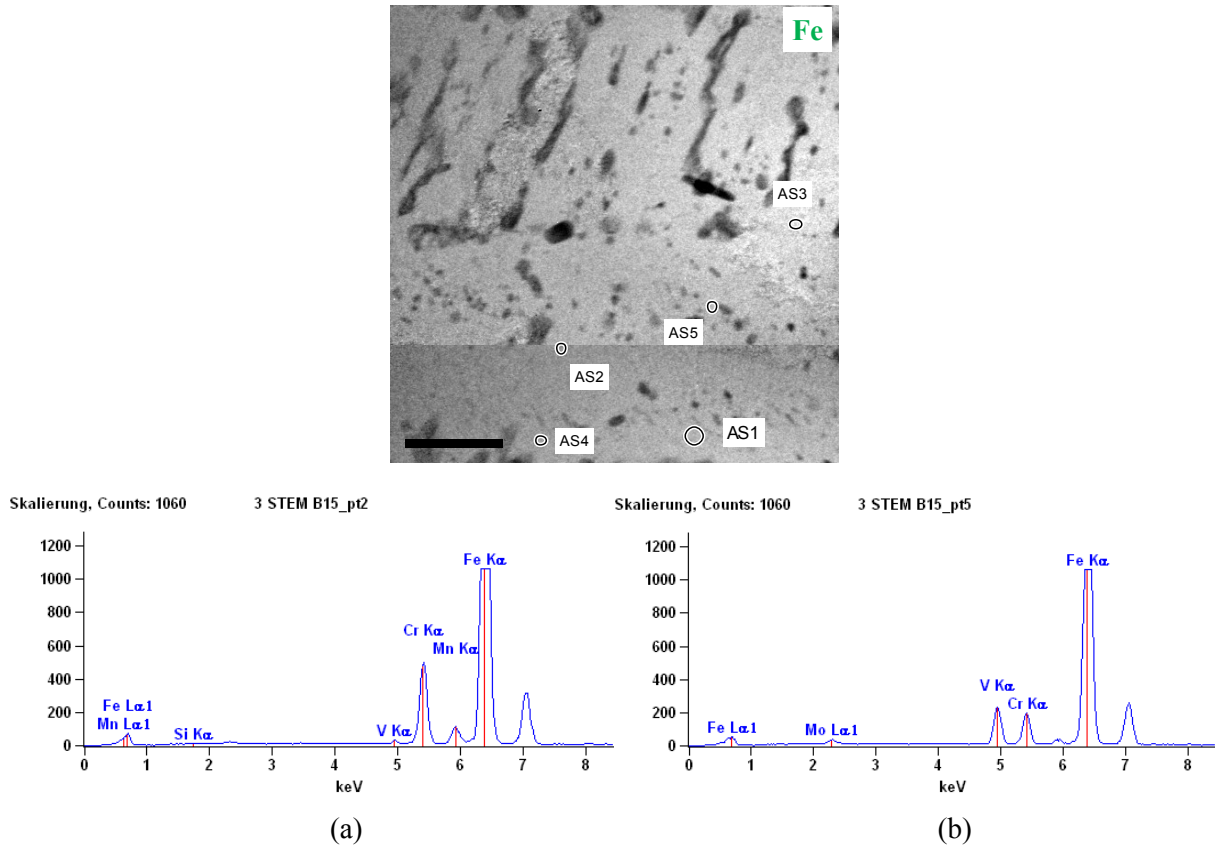


Figure 5.54: (a) EDX scan 2 shows high Cr and Fe contents, indicating an $M_{23}C_6/M_7C_3$ precipitate and (b) EDX scan 5 shows high V contents.

Tab. 5.16 shows the quantities of each element detected by EDX.

Table 5.16: Identified chemical composition of all five single spot scans as shown in Fig. 5.54.

Specimen	Spot	Si	V	Cr	Mn	Fe	Mo
B15	AS1	0.25	0.59	12.49	-	85.41	1.26
	AS2	0.18	0.64	15.11	1.31	82.10	0.65
	AS3	0.23	0.36	11.38	-	87.12	0.91
	AS4	-	0.52	11.87	-	87.00	0.61
	AS5	-	9.12	6.65	-	82.32	1.91

Fig. 5.55 shows an investigation of a creep-fatigue loaded W400 specimen with martensitic matrix structure, which had to sustain 500°C for 162.5 hours. Two spot scans in which chromium-molybdenum rich precipitates were ascertained, are demonstrated in Tab. 5.17.

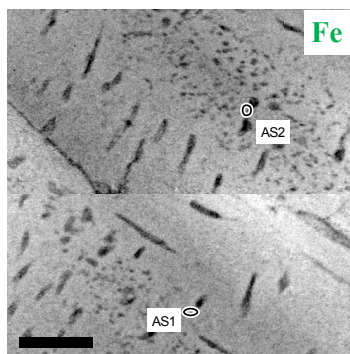


Figure 5.55: STEM EELS spectra with two EDX spot scans.

Table 5.17: Identified chemical composition of the single spot scans as shown in Fig. 5.55.

Specimen	Spot	V	Cr	Fe	Mo
F3	AS1	0.49	8.27	89.04	2.21
	AS2	0.51	7.55	89.93	2.00

Fig. 5.56 shows the same material and service condition as in the previous figure. Two spot scans identified a relatively huge vanadium as well as a chromium rich precipitate, compare Tab. 5.18.

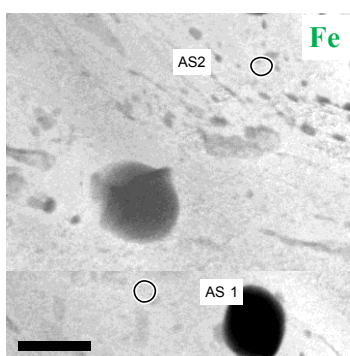


Figure 5.56: (a) STEM EELS spectra with two EDX spots to identify the exact chemical composition of the precipitates.

Table 5.18: Identified chemical composition of the single spot scans as shown in Fig. 5.56.

Specimen	Spot	Si	V	Cr	Fe	Mo
F3	AS1		7.10	52.36	36.36	4.18
	AS2	1.27	66.85	7.91	10.10	13.87

5.2.3 X-ray diffraction

To generate reliable dislocation density data, X-ray diffraction peak profile analysis were performed on seven, mostly creep-fatigue loaded specimens. First attempts were made by considering advanced TEM investigations, which need a special etching to make dislocations visible. Due to a high expected inaccuracy, it was decided to perform X-ray diffraction analysis, where the main principle lies in the detection of the lattice misorientation and the calculation of the amount of dislocations in-between causing the afore detected quantity of misorientation. In Fig. 5.57, the set of specimens prepared for the X-ray diffraction investigation is shown.



Figure 5.57: Creep as well as fatigue and creep-fatigue specimens prepared for dislocation density measurements with X-ray diffraction peak profile analysis.

An overview of the thermo-mechanical loading history with the related dislocation densities can be found in Tab. 5.19.

Table 5.19: Experimental data of the investigated X-ray diffraction specimens.

Material	Matrix	Load σ^+/σ^- [MPa]	Cycles to rupture [-]	T [°C]	Duration [h]	Dislocation density [10^{15}m^{-2}]	Comments
W300	martensitic	-	-	-	--	2.3	A5, heat treatment only
	martensitic	922/836	776	500	72.72	2.1	A13
	martensitic	836/749	111	580	15.06	2.8	A14
	bainitic	721/865	857	500	80.06	2.5	B15
	martensitic	787/836	100	500	2.3	2.5	A12, in situ
	martensitic	800	-	500	181	2.1	A42, creep
	bainitic	800	-	500	108	2.4	B42, creep

5.3 Simulation

The results of the simulation workflow are presented in the following in dependence on the content structure of chapter 4. The extrusion process simulation results in DEFORMTM2D were performed to compute temperatures and stresses in the tools. The obtained thermo-mechanical loads in DEFORMTM2D were transmitted to ABAQUS with an implemented phenomenological material model to calculate the stresses and occurring inelastic strains in the tool, see chapter 5.3.1. Subsequently, in chapter 5.3.2, it was accounted for the damage and service lifetime of the tool dependent on variable process conditions.

The physical based simulation part, which takes into account the occurring microstructure state and its evolution during service is described subsequently. With the thermo-kinetic software MatCalcTM, precipitation kinetics simulations were performed to study and describe the precipitates state after completed heat treatment as well as to account for the ongoing precipitation evolution during service, see chapter 5.3.3. The results obtained from the precipitation calculations were taken into account for subsequent dislocation density evolution calculations, where a set of rate equations was implemented into a MathCad code as described in chapter 4.2.2 and *Appendix B*. The physical based dislocation density evolution calculations, which are presented in chapter 5.3.4, also provide an inelastic strain output, which can be directly linked and compared with the inelastic strain obtained from the phenomenological approach.

5.3.1 Thermo-mechanical induced stress and strain distribution

The pressure distribution in the billet in radial as well as in axial direction is non-uniform, which is demonstrated in the simulation in Fig. 5.58 (a). The highest mechanical loads occur in the top area of the billet where the ram meets the liner. Friction forces at the interface billet-liner will also affect that occurrence.

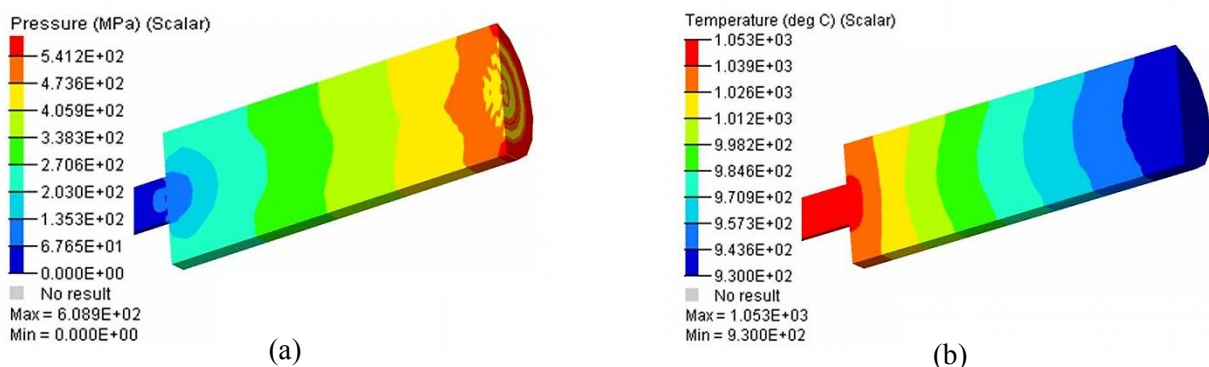


Figure 5.58: (a) Simulated pressure and (b) temperature distribution in a copper billet at process conditions of 930°C initial billet temperature. The heat transfer was set to zero to better visualize the (b) temperature increase during the forming process.

Fig. 5.59 shows a snapshot of the temperature distribution as well as of the accumulated viscoplastic strain in the container during the third extrusion cycle. The non-uniform stress distribution is a result of the complex load cases.

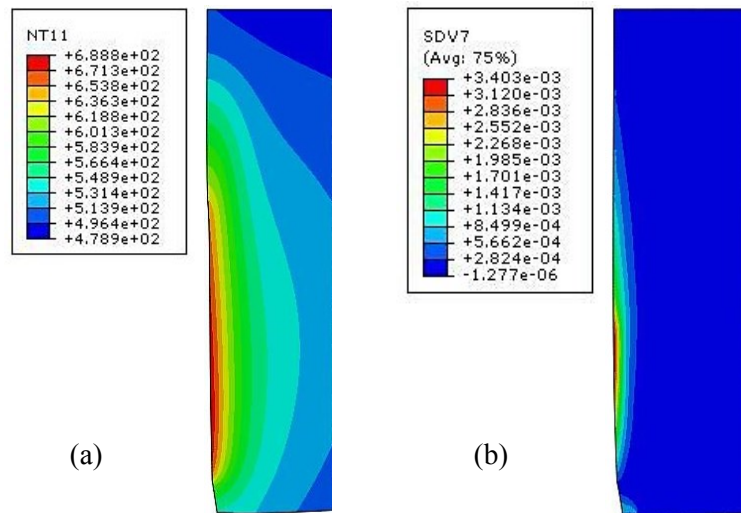


Figure 5.59: (a) Temperature [$^{\circ}\text{C}$] distribution in the liner during the third extrusion cycle and (b) accumulated inelastic strain after the third cycle with a billet temperature of 950°C ; ABAQUS StandardTM v.6.8-3.

In the following, the hysteresis loop of an experimental test performed at the Bundesanstalt für Materialprüfung Berlin (BAM) was simulated in Abaqus/ZMat with the boundary conditions of $\Delta\varepsilon = 0.7\%$, a holding time in compression for 300s and a temperature of 590°C , which lies at or even over the limit of the appropriate service temperature of W400. The simulated stress reaction according to the strain fits with the measured stress values. A further clear outcome of the test, which is reported in Fig. 5.60, is the cyclic increasing amount of tensile stress values. This is related to the holding time in compression, where the material has time to relax, which makes the specimen a little shorter. When applying the same strain amplitude on the shortened length, the stress values are higher in comparison to the previous step. A holding time in tension would provide opposite reactions, namely higher compressive stresses and smaller positive stresses. Since the main cause for damage is simple material separation, i.e. cracks, the specimens which are tested with a holding time in compression, fail earlier. Comparing the service lifetime through the amount of cycles to failure of W300 in relation to W400, the creep-fatigue tests resulted in a doubled or higher performance for the W400. Same conclusions were drawn from an investigation comparing the lifetime of these two hot work tool steels during aluminium extrusion.

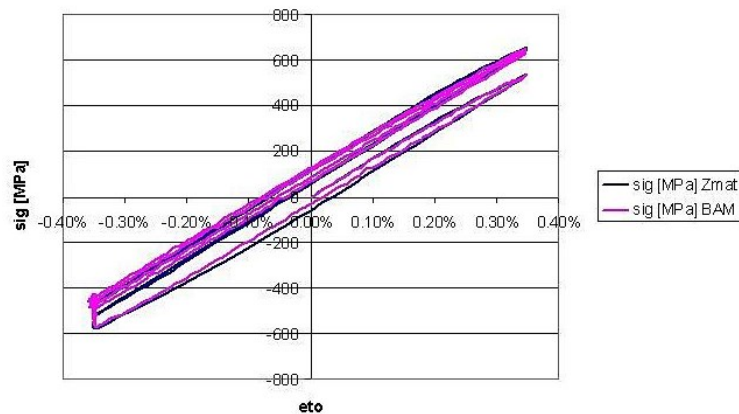


Figure 5.60: Experimental and simulated LCF-test with W400 at conditions of $R = -1$, $\Delta\epsilon = 0.7\%$, holding time = 300s for three cycles at 590°C. The simulation can validate the stress-reaction very well.

The extended Chaboche model for fcc-lattice tools was applied on a W750 austenitic hot work tool steel, Fig. 5.61. Such austenitic tool steels are applied under elevated service temperatures due to their advanced microstructural stability, which is achieved by the formation of the $\text{Ni}_3\text{Al}-\gamma''$ phase. For the W750 liner material, the constitutive elastic-viscoplastic Chaboche model was implemented explicitly by means of Z-Mat package. The uncoupled lifetime consumption model was added as well.

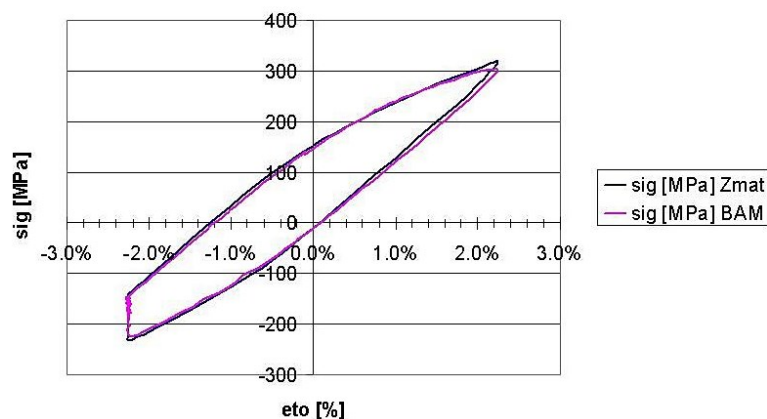


Figure 5.61: Experimental and simulated LCF-test with W750 at conditions of $R = -1$, $\Delta\epsilon = 4.2\%$, holding time = 300s for one cycle at 800°C.

5.3.2 Damage evolution and lifetime prediction

The configuration, which is depicted in Fig. 5.59, was used to predict the damage evolution for a selected point at the area of maximum lifetime consumption at the inner liner wall during the copper extrusion process with different billet temperatures. The lifetime consumption of the third cycle (see ΔD in Fig. 5.62 (b)) was chosen representatively to calculate the lifetime to failure, which is 1050 and 750 cycles until failure occurs according to the initial billet temperatures of 900 and 950°C. Fig. 5.62 (a) depicts the damage distribution after the third extrusion cycle for the hot work tool steel W750.

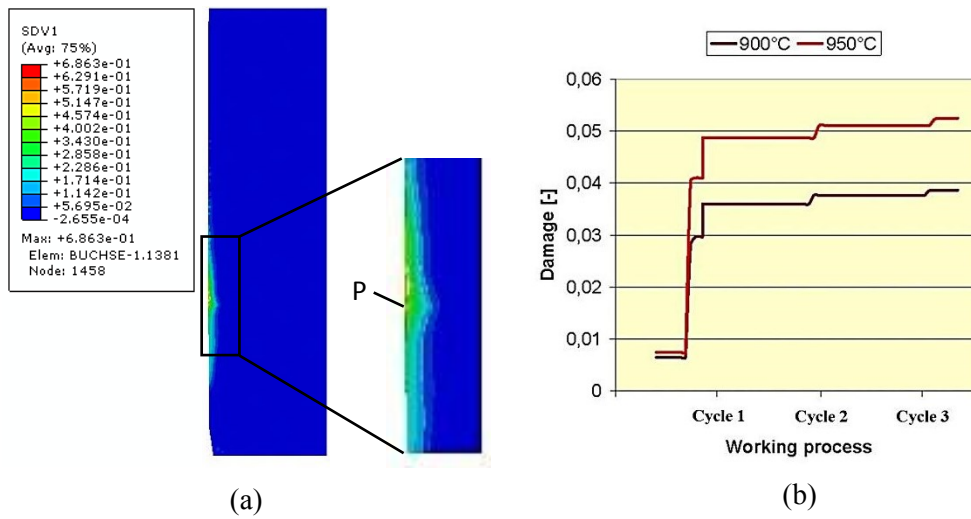


Figure 5.62: (a) Resulting creep-fatigue damage according to 950°C billet temperature as well as (b) the lifetime consumption for two different process conditions, namely 900 and 950°C billet temperature during three cycles of one point of maximum damage (P) at the inner wall of the liner (see Fig. 2); ABAQUS StandardTM v.6.8-3 in conjunction with Z-Mat.

The largest accumulated damage occurs in regions that exhibit maximum accumulated inelastic strain and damage equivalent stress loading (compare Figs. 5.59 and 5.62 (a)). To account for the meaning of each parameter onto the final calculated inelastic strain output, a sensitivity analysis was performed [55]. One parameter after the other was changed in the range of $\pm 10\%$ of literature values [56].

The sensitivity $\Delta \varepsilon$ of the displacement ε according to each variation of a parameter x_i was calculated as follows:

$$\Delta \varepsilon(x_j) = \frac{\partial \varepsilon}{\partial x_j}(x_{i,0}) \cdot \Delta x_j \quad (6),$$

where

$$\varepsilon = f(x_i) \quad (7).$$

The most influencing parameters are shown in Tab. 5.21.

Table 5.21: Results of the sensitivity analysis: The sensitivity of the displacement ε according to a variation of $\pm 10\%$ of the most influencing parameters is shown [55].

	elastic	isotropic	viscous properties		kinematic non linear			
					a1		a2	
x_i	E	k	K	n	M	m	M	m
$\hat{\partial} \varepsilon / \hat{\partial} x_i$	0,1690	0,0250	0,0015	0,0040	0,0015	0,0025	0,0010	0,0042

As observed, small variations in the output displacement prediction were achieved by the model parameters modification. However, even if on the basis of small differences, some general conclusions can be drawn. The parameters that led to highest variations of the percentage error were: the elastic modulus (E), the value of the initial elastic limit (k), the viscous parameters (K, n) and the static recovery constants of the first two kinematic hardening terms (M, m), see Tab. 5.21. In particular, the peak sensibility of the model output corresponded to the variation of the elastic modulus and of the initial elastic limit [55].

5.3.3 Precipitation kinetics

The precipitation kinetics were simulated with the software MatCalcTM, the phase fractions f of the precipitates, which are mainly occurring in the considered alloying concept, are MX (V(C,N)), M₃C (Fe₃C), M₆C (Cr₆C), M₇C₃ (Cr₇C₃), M₂₃C₆, (Cr₂₃C₆), M₂C (Mo₂C) and Laves phase, the particle number N per volume and the related mean radius of the particles, $R_{v_{mean}}$, are the main output parameters. N and $R_{v_{mean}}$ are subsequently important input parameters for the dislocation density evolution model. The evolution of f , $R_{v_{mean}}$ and N as a function of the thermal history is depicted in Fig. 5.63 due to 500°C service condition.

The MatCalcTM simulation compared with the experimental investigation came to a similar correlation that the Cr₇C₃ and Cr₂₃C₆ precipitation volume fractions exhibit the highest amounts among the others. The microstructure during 500°C service temperature seems more stable in volume fraction and mean diameter than at 580°C, compare Figs. 5.63 and 5.64. This unstable microstructure, where the softening processes are predominant, is also an explanation for the fast decreasing lifetime when testing the samples near the annealing temperatures.

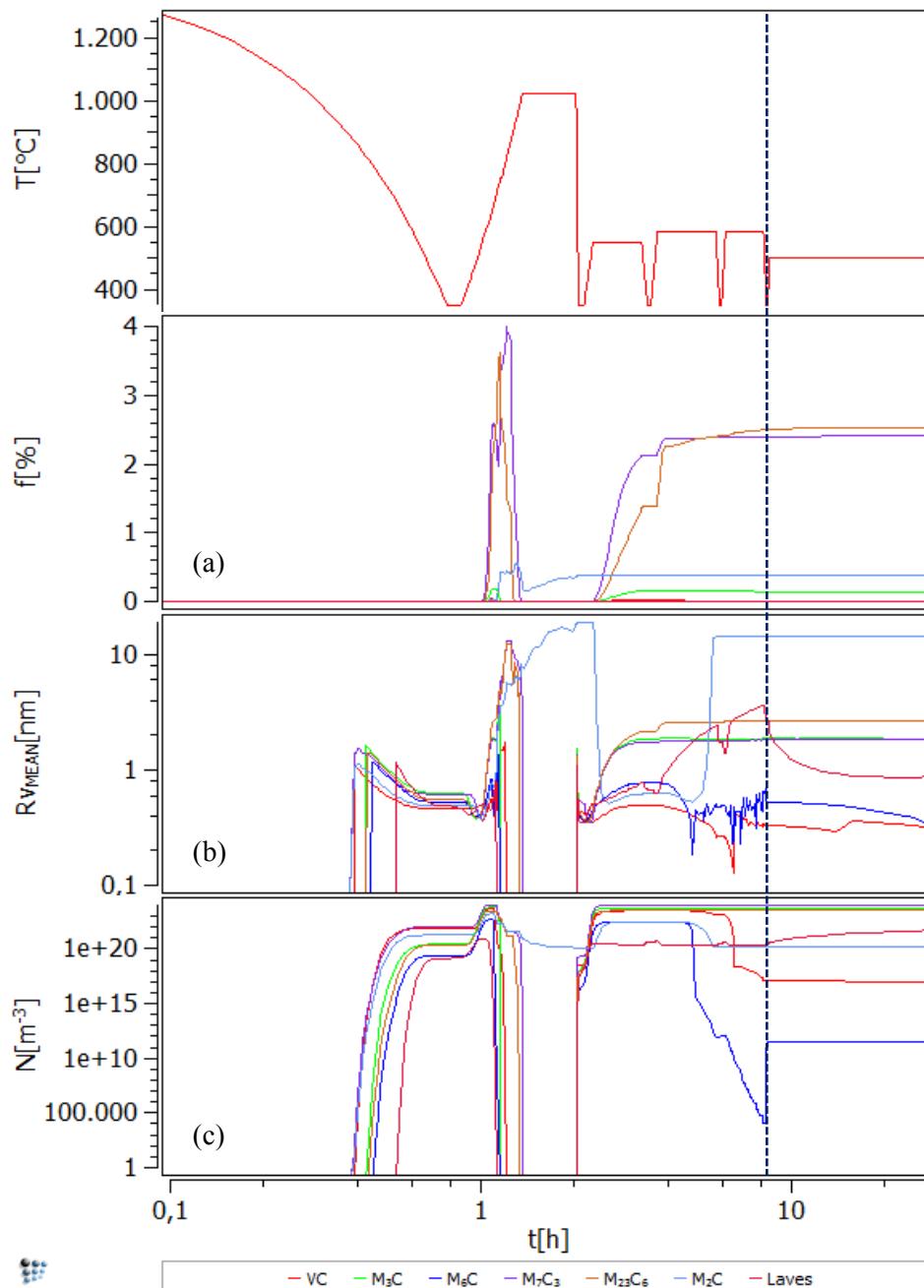


Figure 5.63: (a) Related temporal evolution of volume fractions of the precipitates, (b) corresponding precipitate size evolution and (c) the evolution of the particle number N per volume according to the top shown thermal history with service temperature of 500°C .

At a service load of 500°C , Fig. 5.63, the particle radii as well as the number densities appear more stable than at 580°C , where the structure coarsens more significantly, as shown in Fig. 5.64. The dashed line marks the state at the end of the heat treatment.

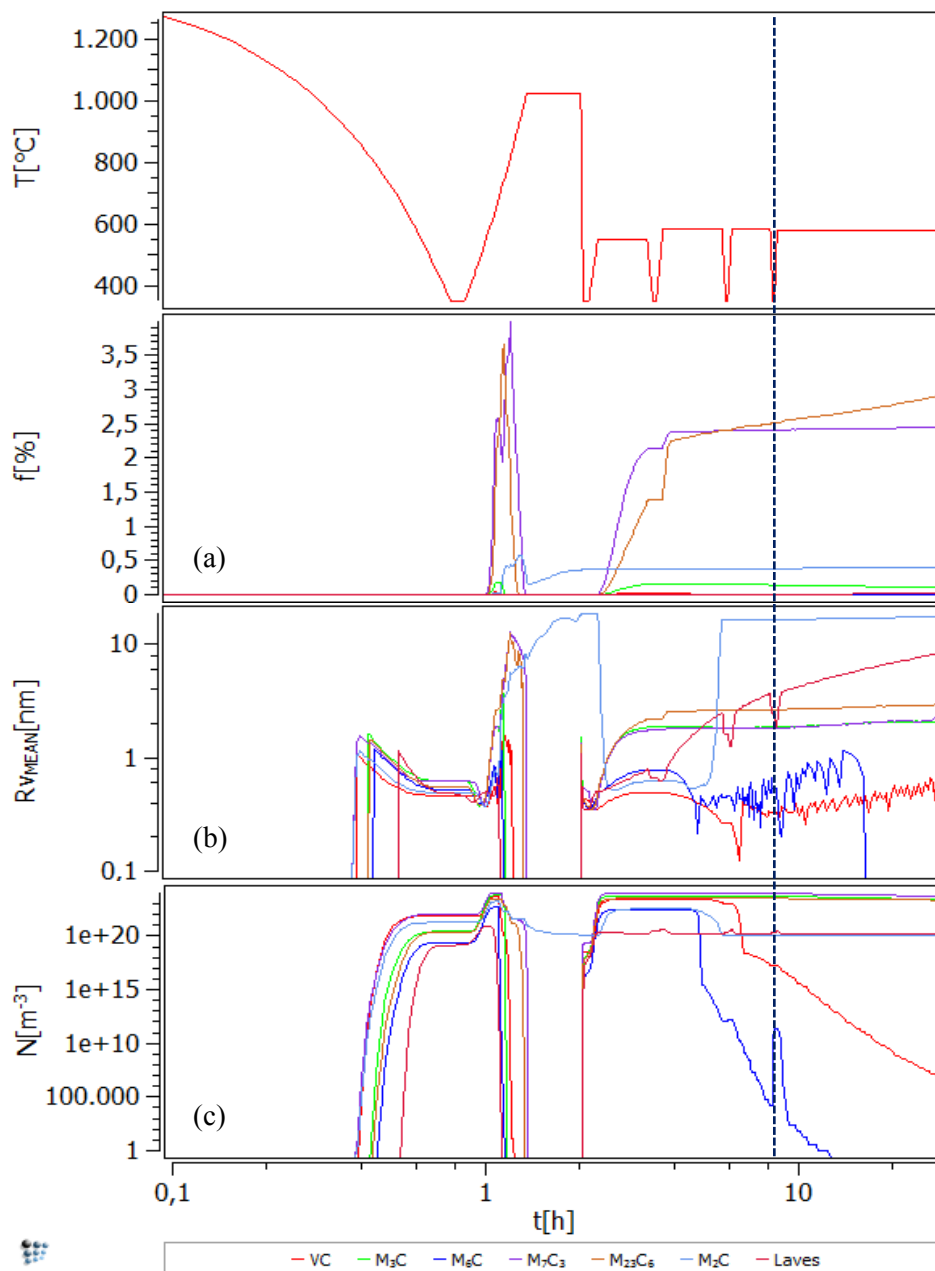


Figure 5.64: (a) Related temporal evolution of volume fractions of the, (b) corresponding precipitate size evolution and (c) the evolution of the particle number N per volume according to the top depicted thermal history with service temperature of 580°C .

The long-term microstructure evolution is decisive for the material's strength, damage evolution and finally resulting lifetime behaviour. In Figs. 5.65 and 5.66 the precipitation kinetics are demonstrated according to a simulated service duration of 2000 hours at 500 and 580°C , respectively.

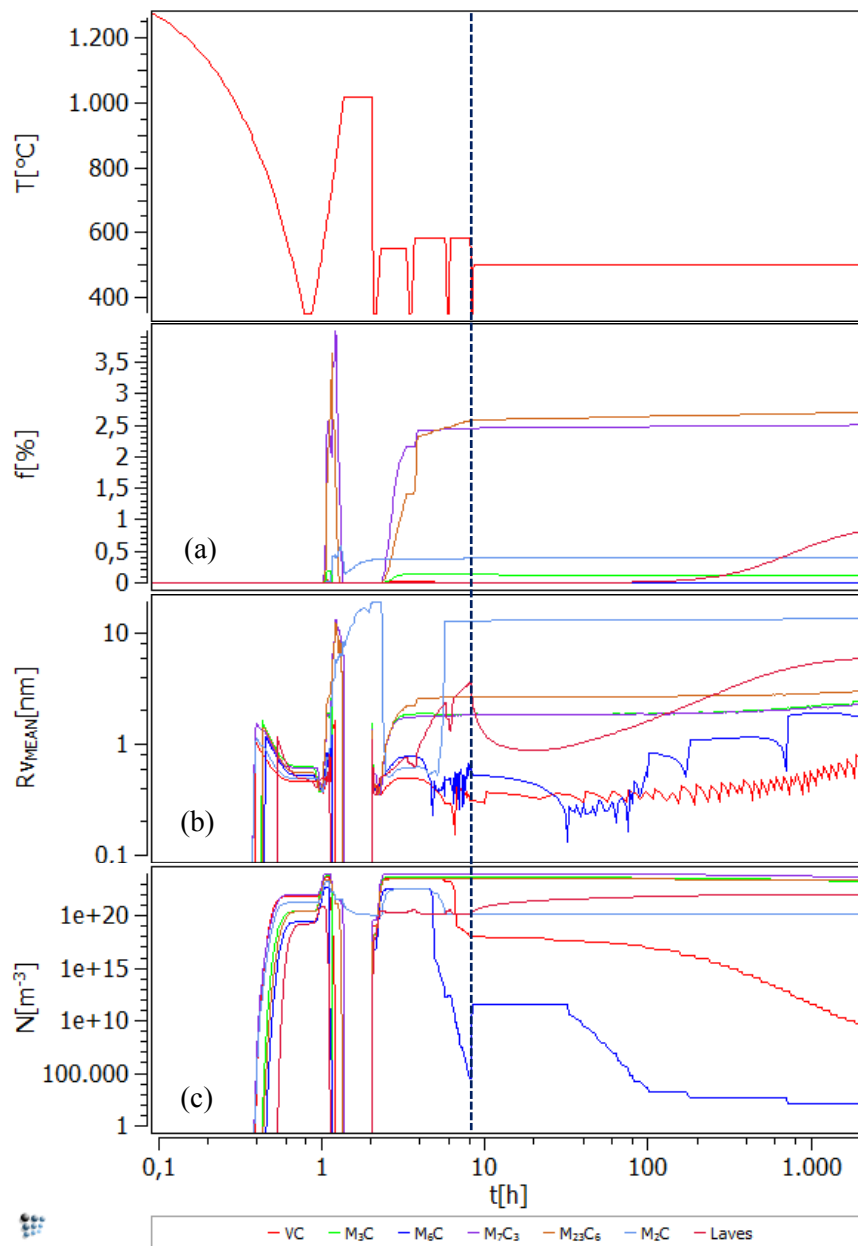


Figure 5.65: (a) Related temporal evolution of volume fractions of the precipitates, (b) corresponding precipitate size evolution and (c) the evolution of the particle number N per volume according to the top shown thermal history with service temperature of 500°C for 2000 hours.

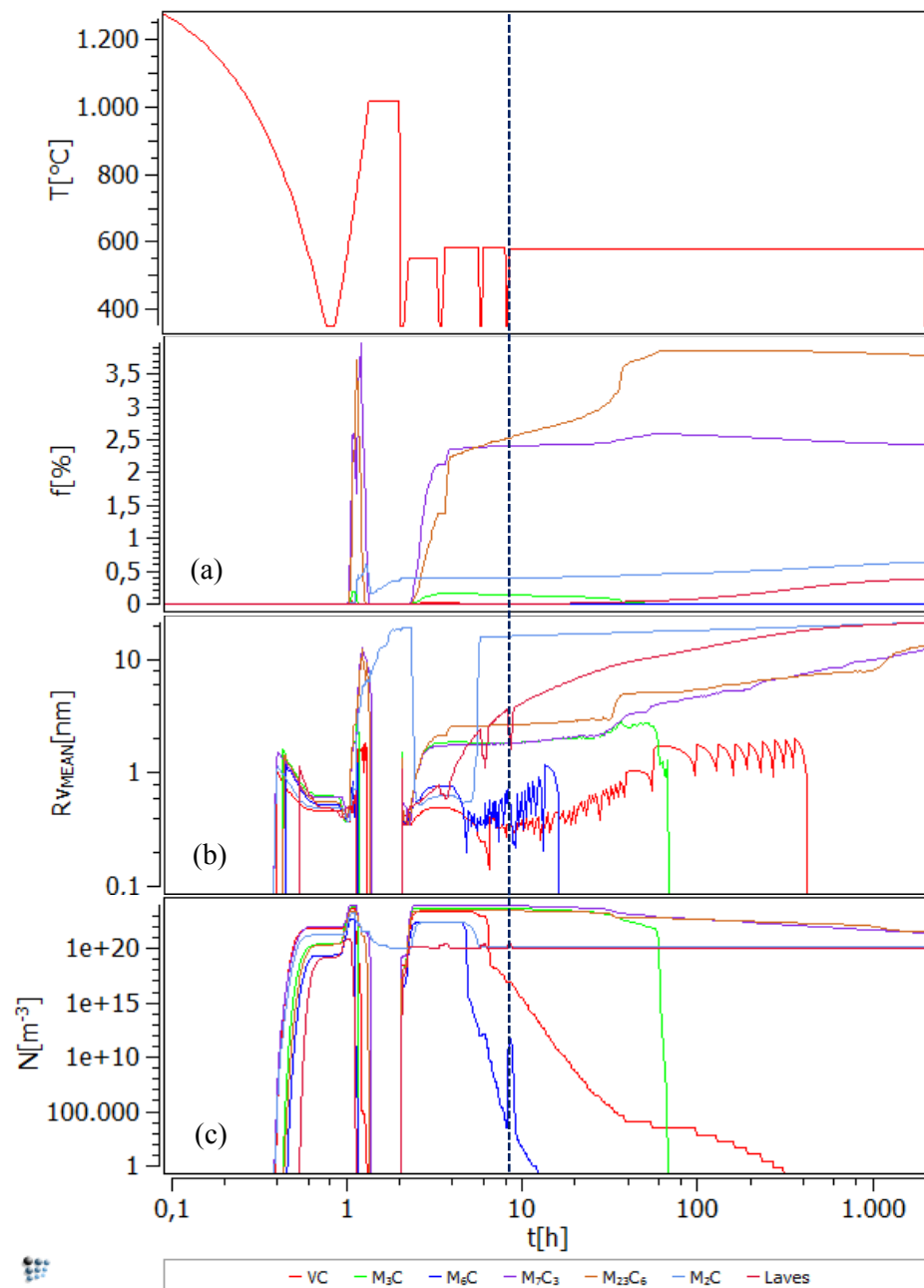


Figure 5.66: (a) Related temporal evolution of volume fractions of the precipitates, (b) corresponding precipitate size evolution and (c) the evolution of the particle number N per volume according to the top shown thermal history with service temperature of 580°C for 2000 hours.

The lasting diffusion and coarsening mechanisms, which occur in the material are clearly recognizable at a simulated service temperature of 580°C, see Fig. 5.66. At 500°C the kinetic is much slower, but the microstructure doesn't stay constant at all.

In Tab. 5.22 the results from the MatCalc simulations are compared with the experimental observations via the total volume fraction of the experimentally observed precipitates. More than 90% of the detected precipitates are chromium-carbides, partly substituted by molybdenum.

Table 5.22: Thermo-mechanical loading history with the related dislocation density as well as the calculated and measured volume fraction of the whole precipitation.

Material	Nr.	Load σ^+/σ^- [MPa]	Cycles to rupture [-]	T [°C]	Duration [h]	ρ [10^{15}m^{-2}]	f_v [%] MatCalc	f_v [%] TEM
W300	A5	-	-	-	--	2.3	5.8	1.95
	A13	922/836	776	500	72.72	2.1	5.9	2.28
	A14	836/749	111	580	15.06	2.8	6.5	2.26
	B15	721/865	857	500	80.06	2.5	5.4	1.08
W400	F3	749/980	1656	500	162.5	-	5.3	1.57

5.3.4 Dislocation density evolution during service

As afore mentioned, in the dislocation density evolution model described in chapter 4.2.2 on page 39-41, the total dislocation density is subdivided into three dislocation classes, namely mobile-, ρ_m , static-, ρ_s , and boundary dislocation density, ρ_b . The evolution of all three dislocation classes as well as the total dislocation density for the specific load case of 400MPa at 580°C is depicted in Fig. 5.67.

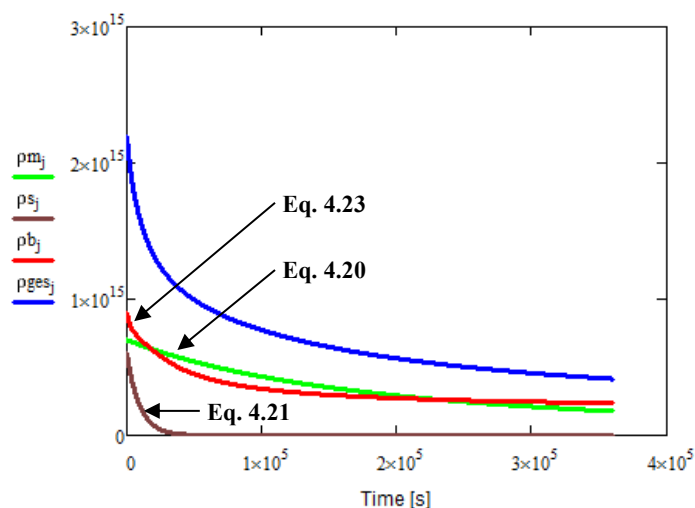


Figure 5.67: Dislocation density [m^{-2}] evolution calculation of all three mentioned dislocation classes (ρ_m , ρ_s , ρ_b) as well the total dislocation density, ρ_{tot} , for a considered creep loading history of 400MPa at 580°C, duration 100 hours. In this observation the initial total dislocation density was found to be $2.3 \cdot 10^{15} \text{m}^{-2}$.

In Fig. 5.67 the equations referring to each dislocation class are indicated.

Remarkable is the fast decrease of the dislocation density at the start of the load as well as the beginning formation of a quasi-stable dislocation substructure. The macroscopic inelastic strain due to dislocation glide as compared with the FE-simulations and experiments can be calculated with the proposed model additionally. In Fig. 5.68 the strain output obtained from the dislocation density model for 500°C and 580°C, respectively, is demonstrated.

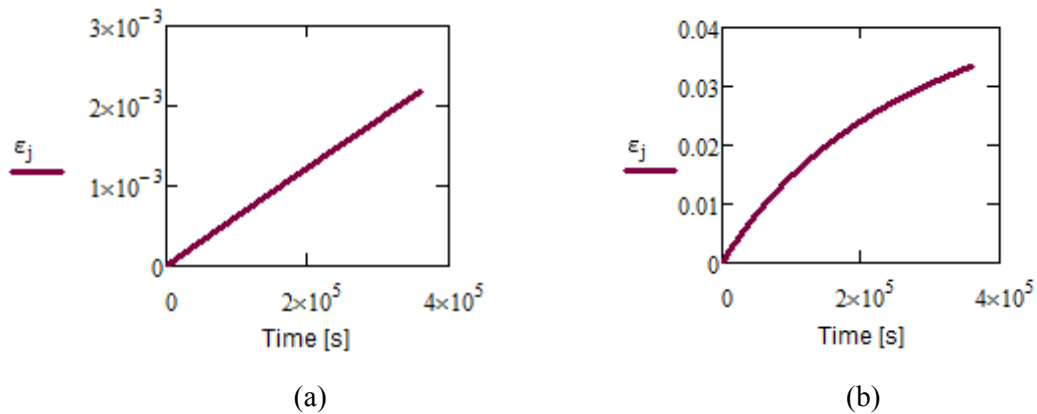


Figure 5.68: Inelastic strain evolution for a considered creep loading history of 400MPa at (a) 500°C and (b) 580°C, duration 100 hours.

The difference of a factor around 15 can be explained by the easier dislocation glide at the higher temperature. In Fig. 5.69 the subgrain size evolution according to the same conditions as in Fig. 5.68 is shown. The initial value for the subgrain size evolution calculation is 200nm, which is related to the experimentally observed martensitic lath width. Again, according to the simulation, a faster coarsening of the substructure at 580°C can be observed.

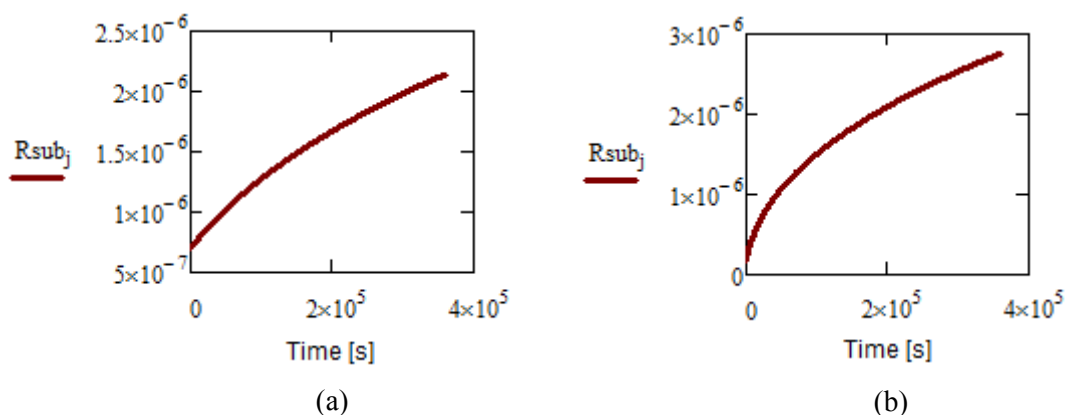


Figure 5.69: Subgrain size evolution for a considered creep loading history of 400MPa at (a) 500°C and (b) 580°C, duration 100 hours.

The highest uncertainty was to account for a reasonable dislocation density distribution among mobile, static and boundary dislocation densities. In Fig. 5.68, one possible solution is mentioned with the related macroscopic inelastic strain.

To demonstrate the dislocation structure evolution at different temperatures, Fig. 5.70 shows the dislocation density evolution for all considered classes of dislocations at 500°C and 580°C at 400 MPa for the early loading stage. The faster rearrangement and recovery processes are responsible for the significant change at 580°C in comparison with the slower evolution at 500°C.

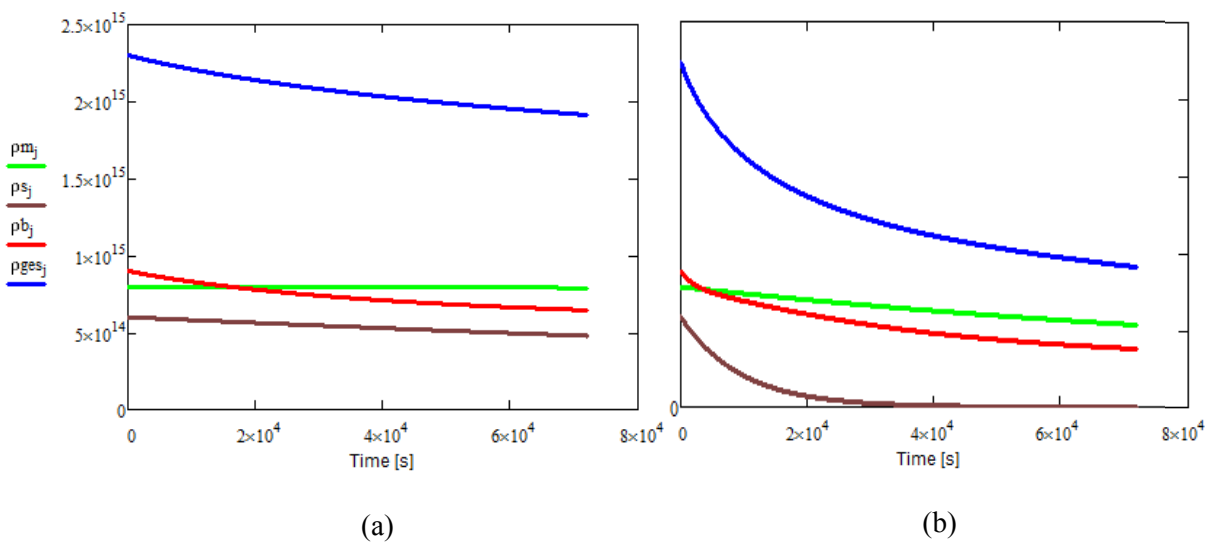


Figure 5.70: (a) Dislocation density evolution calculation of all mentioned dislocation classes (ρ_m , ρ_s , ρ_b) as well the total dislocation density, ρ_{tot} for a representative loading history of 400MPa at (a) 500°C and (b) 580°C, duration 20h. The initial total dislocation density as experimentally determined with the XRD method indicates the initial sum of ρ_m , ρ_s and ρ_b .

It is shown that after reaching a quasi-stable dislocation substructure, the temporal increase of the plastic strain reaches a constant value, comparable with the secondary creep range. Subsequent dislocation density measurements with the XRD method came to the conclusion of an overall decrease in dislocation density during longer service, which also means softening of the material, of around 0.3 to $0.7 \times 10^{15} \text{ m}^{-2}$ depending on service time. The observed finer precipitate size and -distribution in the W400 tool material as well as its high homogeneity due to vacuum melting and remelting, is responsible for significant longer service durations compared to the W300 tool material. A fine and homogeneous precipitation in the matrix inhibits dislocation motion more effectively, which generates higher strength values due to the interaction processes of the dislocations with the precipitates. Thus, a slightly slower evolution of the dislocation kinetics can be observed through a higher amount of obstacles.

6. Discussion

The discussion section is divided into three main topics, first the experimental and FE-simulation of the extrusion process, second the microstructure evolution simulation during heat treatment and service with the thermo-kinetic software MatCalc as well as the characterization of the microstructure and third the dislocation density evolution model results in comparison to the elastic-viscoplastic Chaboche model results.

At the beginning of the discussion section, the overall workflow, which was followed in the thesis is described in Fig. 6.1. There are three main topics going top-down, namely the industrial process, which was meant to describe, characterize and predict, the second topic is the phenomenological workflow, which includes experiments, FE-simulation, damage and lifetime calculation and third, the physical approach, where all the microstructural phenomena are described by physical based laws and functions, with which a comparative cross-check value, namely the inelastic strain can be calculated.

All three columns are influenced by the material boundary conditions as well as by the process boundary conditions. The model outputs of both the phenomenological and the physical approach are also included in Fig. 6.1.

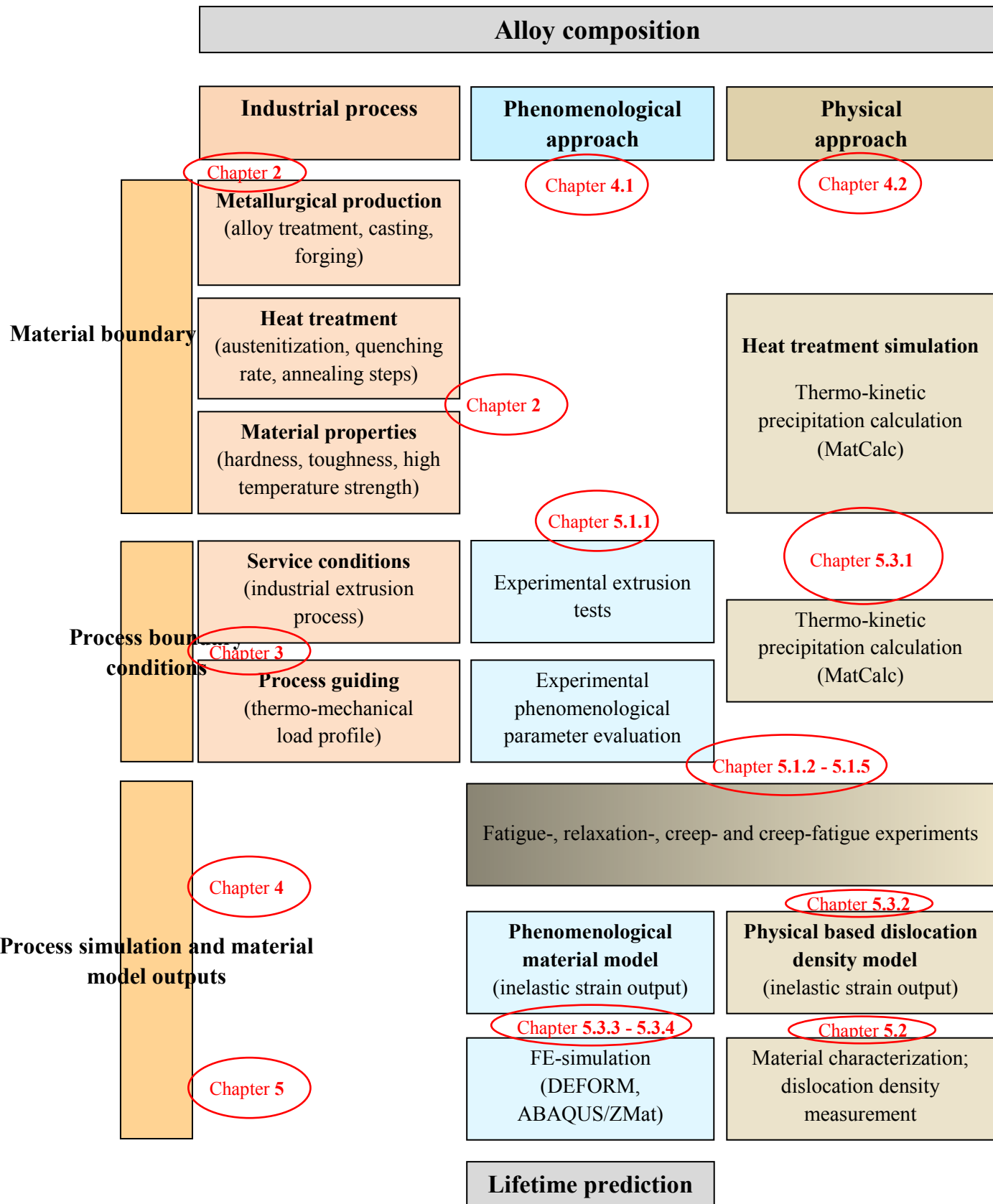


Figure 6.1: Schematic industrial production process and service description with related phenomenological and physical based modelling workflow and related chapters.

6.1 Experimental and FE-Simulation of the extrusion process

The experimental miniature extrusion process simulations, which were performed to validate the experimental boundary conditions during an extrusion process showed a reliable agreement with the simulations, see Fig. 6.2.

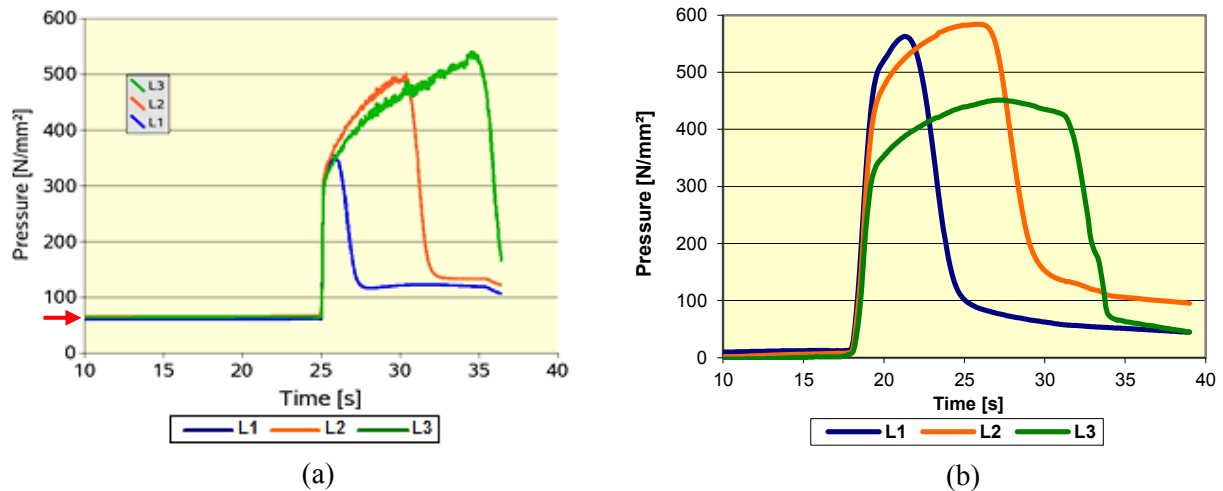


Figure 6.2: (a) Simulation of the pressure distribution in the liner during a copper extrusion process and (b) measured pressure distribution at the tool's surface, with 900°C initial billet temperature.

The simulated pressure values of around 70 MPa (Fig. 6.2 (a), indicated with a red arrow) at the beginning of the billet loading period have no extrusion process influenced meaning, they are residual stress values which may occurred in the liner due to the shrink-fitting process. The stress peak loading, which suddenly occurs at the tool's surface when the ram passes the actual considered level, was additionally found in the simulation and experimentally validated. Despite the experimental measurement system was not very sensitive in recording small and quick changes in the loading, fair success was achieved during some measurements, see Fig. 6.3.

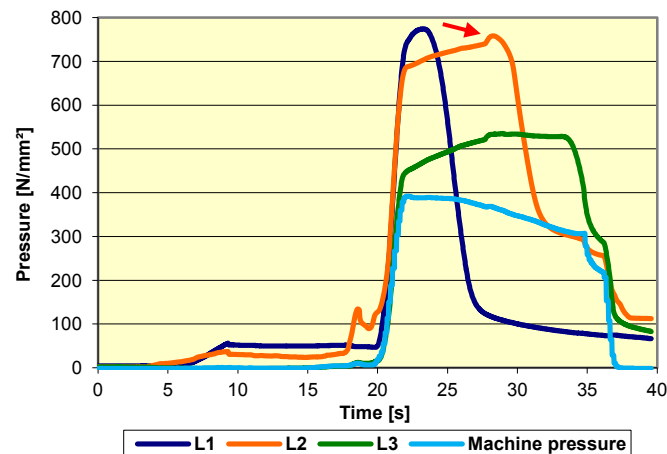


Figure 6.3: The sudden stress increase, which occurs when the ram is passing the considered liner area is marked with a red arrow, which was observed during experimental copper extrusion at 850°C billet and 500°C liner temperature, cycle 1.

The simulations and experimental findings regarding tool loading during copper and aluminium extrusion processes were taken into account to physically simulate the thermo-mechanical loading history during service. The outcome of the experimental program were data about the cyclic lifetime due to various process guidance, fatigue, creep and creep-fatigue data and, regarding the microstructure model, valuable information about the microstructure evolution.

6.2 Microstructure evolution simulation and experimental characterization

MatCalc simulation and experimental investigation

The heat treatment was simulated with the thermo-kinetic software MatCalc to understand the microstructure evolution processes as well as to assess for an optimum initial microstructure. A fully martensitic structure can be obtained through rapid quenching ($\lambda \sim 0.6$) from austenitization temperature (Fig. 6.4), whereas mostly bainitic matrix structure will develop when cooling slower ($\lambda \sim 15$, Fig. 6.5). The deviation from the experimentally detected precipitates volume fraction to the MatCalc simulation results can be explained by two main logical errors in the experimental observation. Firstly, the whole volume of the TEM specimen is taken into account, but not every precipitate inside the considered volume was found, since it was not possible to account for precipitate sizes smaller than about 5 nm. Whereas, as predicted in the simulation, high numbers of precipitates, which were ascertained to be smaller than 2.5 nm concerning the mean radius, were taken into account. Secondly, even bigger sized precipitates could not be clearly detected at locations where the TEM-specimen was relatively thick.

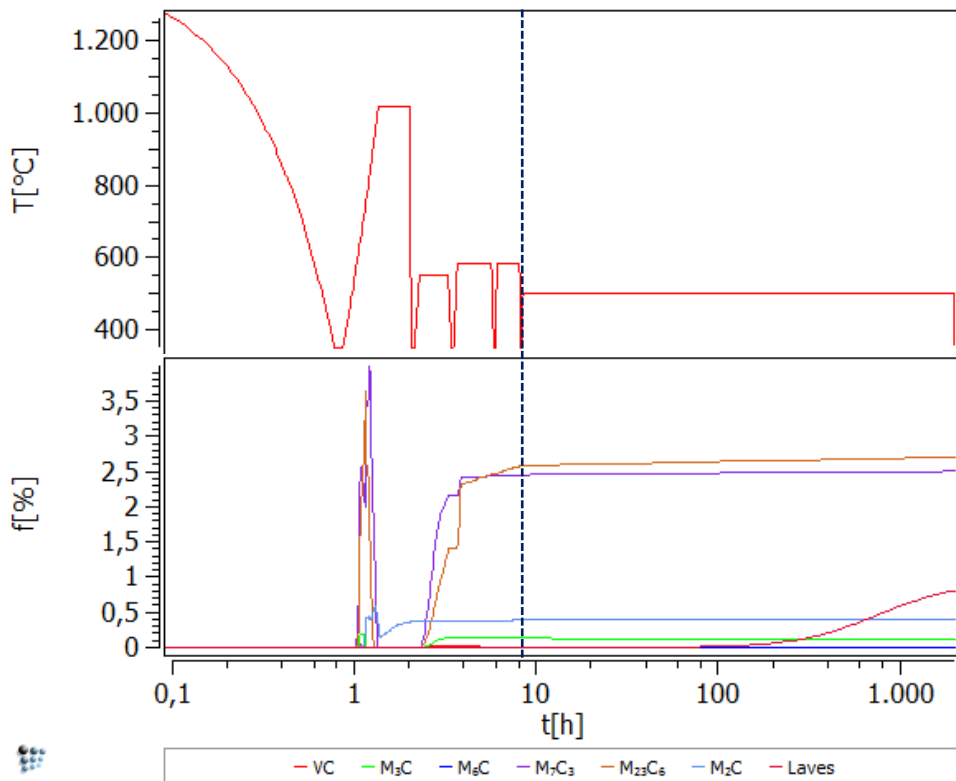


Figure 6.4: Evolution of precipitate's volume fraction in martensitic W300 during 500°C service temperature. The dashed horizontal line marks the state after completed heat treatment.

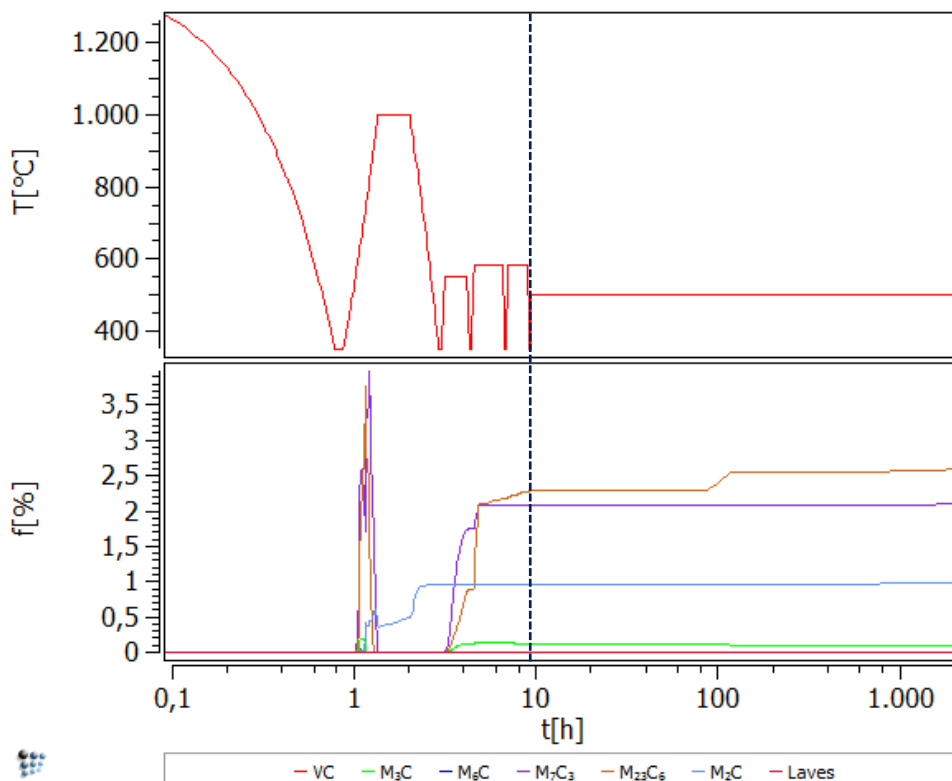


Figure 6.5: Evolution of precipitate's volume fraction in W300 with bainitic matrix during 500°C service temperature.

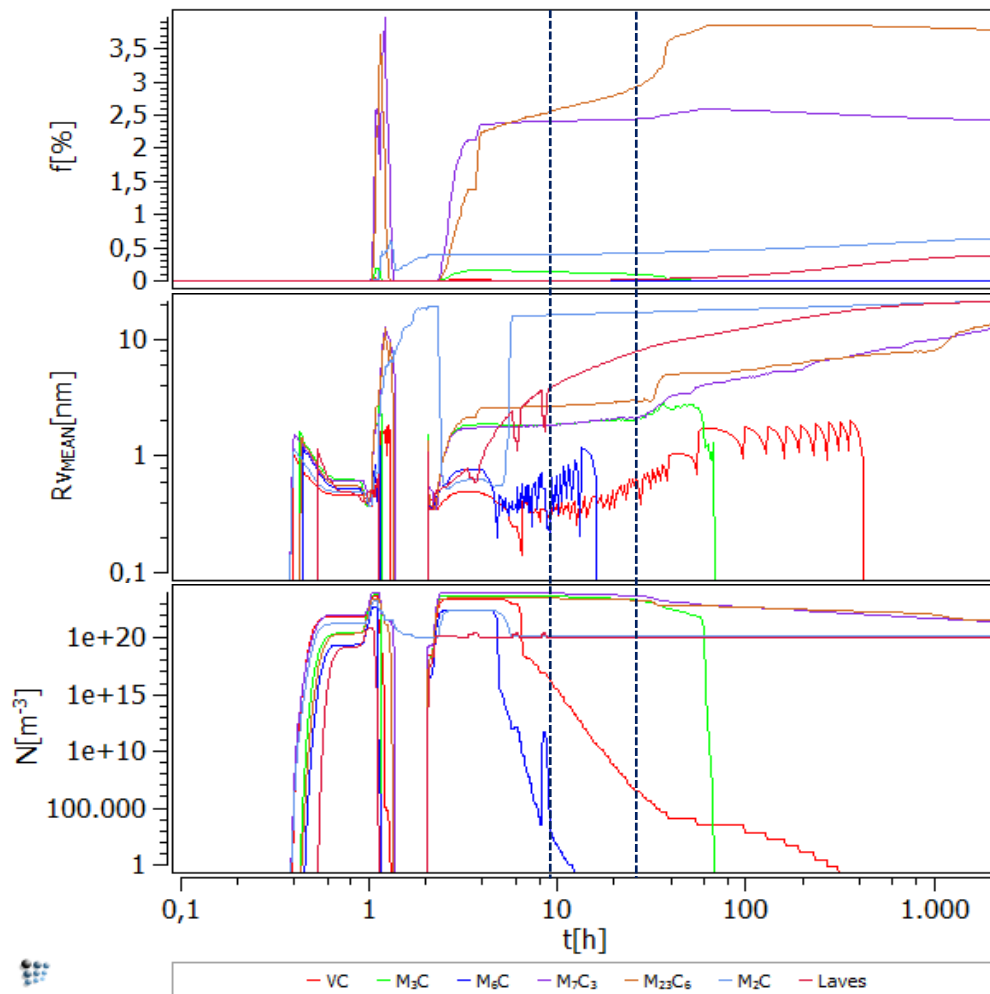


Figure 6.6: Evolution of precipitate's volume fraction, mean particle radii and number density in W300 with martensitic matrix during 580°C service temperature.

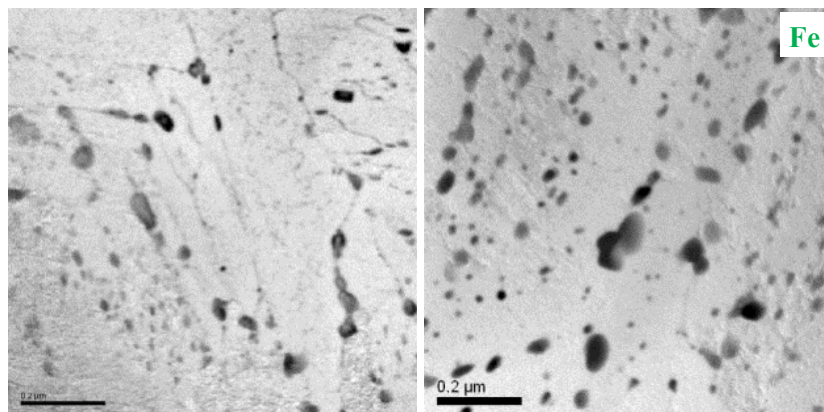


Figure 6.7: Microstructure after completed heat treatment (left) and after additional service for 15.1 h at 580°C. In the MatCalc calculation a slight increase of size, a decrease in number density and dissolution of small precipitate populations was observed. The states are marked with the two dashed lines in Fig. 6.6.

As shown in Fig. 6.6, a coarsening of the microstructure can be observed, i.e. during ongoing service the particle radii increase, whereas the number densities decrease at approximately constant volume. The same calculation was performed for a W400 material, see Fig. 6.8.

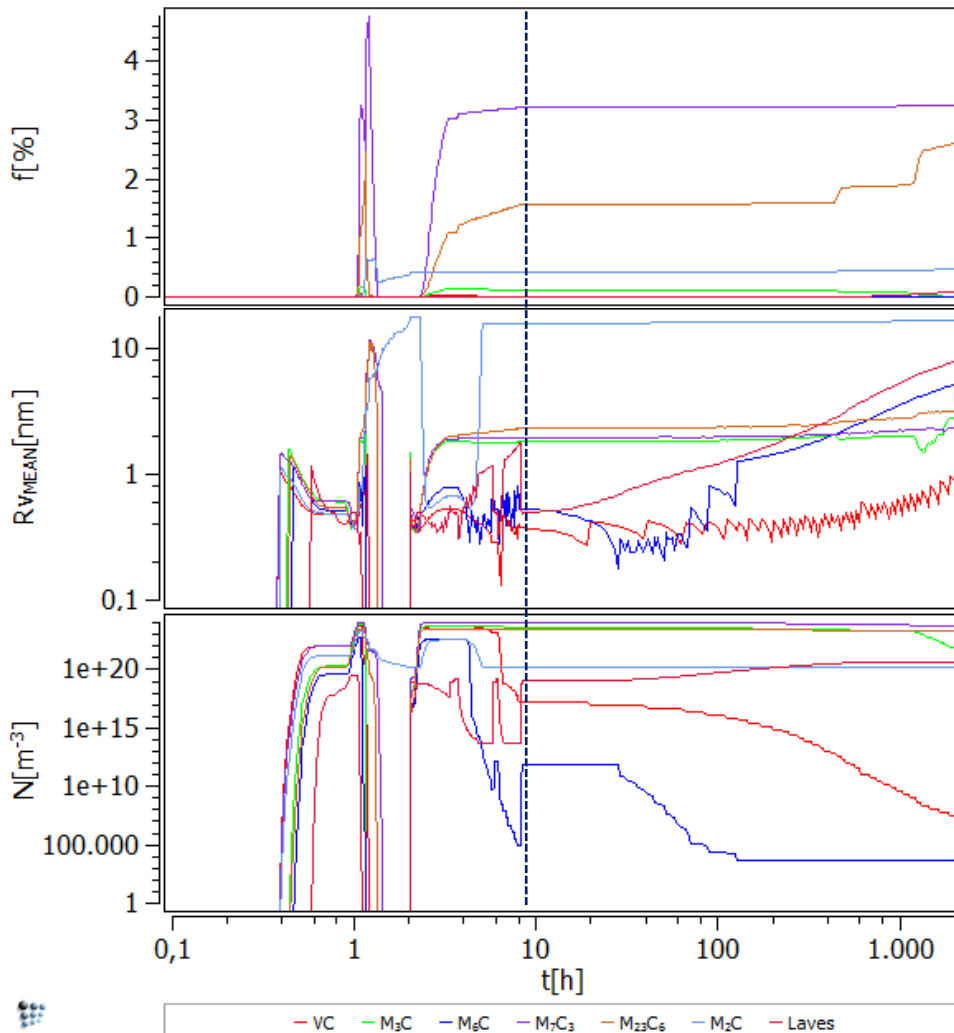


Figure 6.8: Evolution of precipitate's volume fraction, mean particle radii and number density in W400 with martensitic matrix. Similar to W300, the microstructural stability is maintained for long time at 500°C service temperature.

The main precipitates in the W400 are similar to the Cr-rich carbides in the W300, with a little smaller size. The zigzag line when describing the mean radii of some particles derives from numerical instabilities, however a clear trend, either increasing or decreasing can be recognized. The findings from the simulation were used as input data for the dislocation density evolution model.

Since many precipitates, especially the numerous small ones are impossible to detect, a certain deviation from measured to calculated values arises. To account for the precipitation state of the different thermo-mechanically loaded specimen, which are mentioned in Tab. 5.20, a valuable comparison can be generated to show the impact of time-dependent high temperature cyclic fatigue and creep. Fig. 6.9 shows the virgin state after heat treatment.

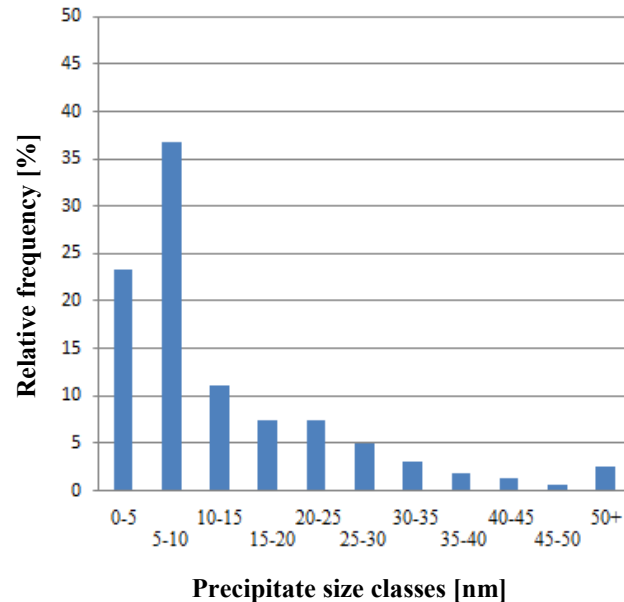


Figure 6.9: Relative frequency of precipitate size classes in the initial state after heat treatment, detected via TEM analysis (A5).

In comparison to the specimens after certain thermo-mechanical loading, the majority of the detected precipitates are below 10nm radius before service. In Fig. 6.10 (a, b) the precipitate distribution of the same W300 with martensitic matrix structure after creep-fatigue loading conditions are depicted. In Fig 6.10 (c, d) the size distribution of bainitic W300 and martensitic W400 after creep-fatigue loading are shown.

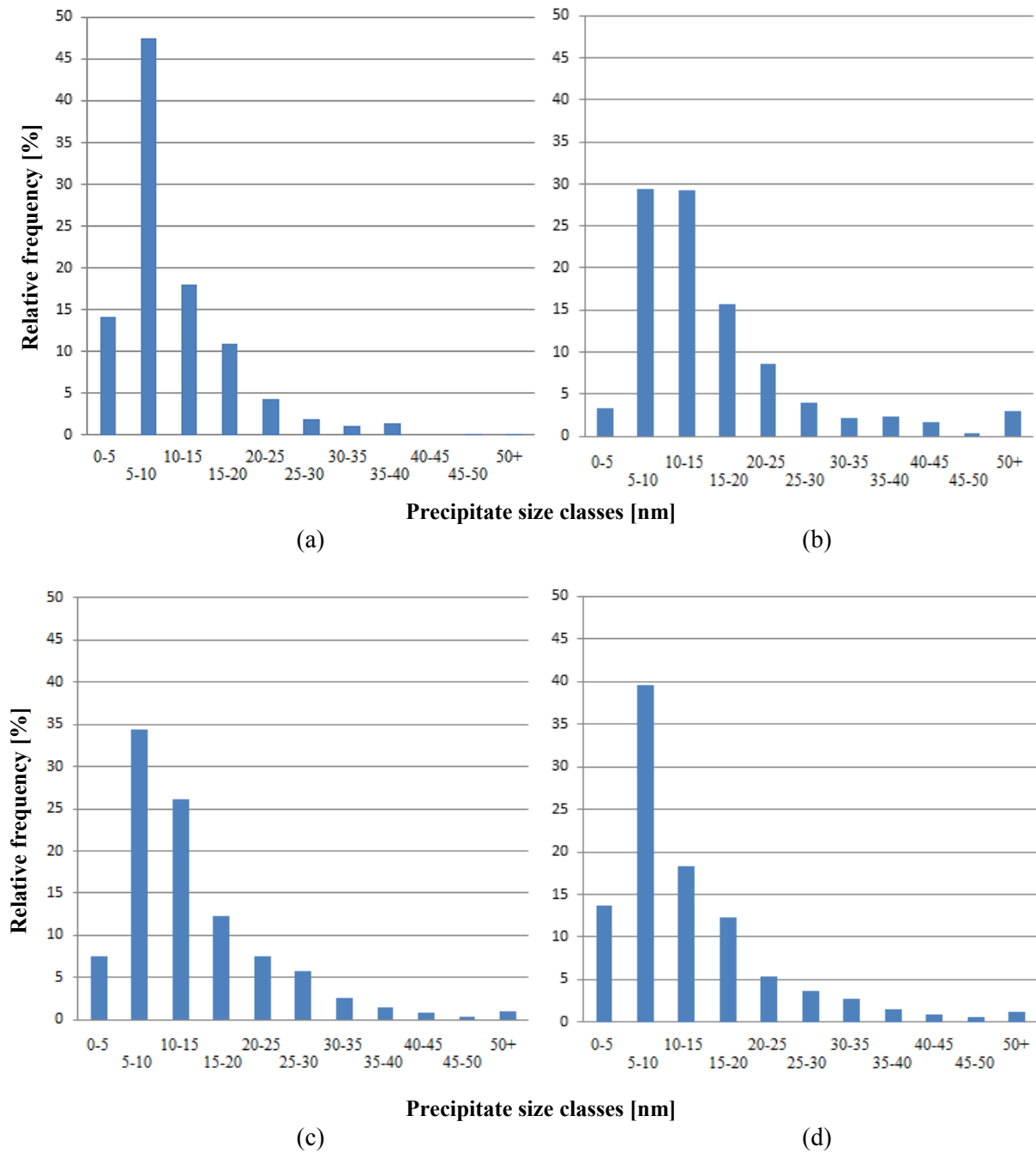


Figure 6.10: Relative frequency of precipitate size classes after creep-fatigue loading at (a) 500°C/73h (A13), (b) 580°C/15h (A14), (c) 500°C/80h (B15), (d) 500°C/162 (F3). A shift to higher radii after thermo-mechanical loading could be detected, compare with Fig. 6.9.

A shift to higher size classes after thermo-mechanical loading was clearly observed when comparing Fig. 6.9 with Fig. 6.10 (b). At thermal loads near the annealing temperature, the microstructure is not stable. Fig. 6.10 (c) shows the precipitate distribution of a creep-fatigue loaded W300 with bainitic matrix structure and in Fig. 6.10 (d) the precipitate distribution of a W400 with martensitic matrix structure for the same creep-fatigue loading conditions, but after double time is demonstrated. The principle longer lifetime of the W400 can also be justified through a higher homogeneity and finer microstructural configuration.

Dislocation density evolution model and inelastic strain output comparison

The results from the dislocation density evolution model were able to deliver a value for the macroscopic inelastic strain. Since the inelastic strain is a result of dislocation dynamics, the model is limited to a certain extent. When damage occurs, the dislocation density evolution model is not capable to account for the absolute inelastic strain, which is then a summation of dislocation glide, pore formation, micro crack and cavity initiation as well as grain boundary sliding at relatively high stresses and temperatures. In Fig. 6.11, the dislocation density output and a realistic short term creep curve is compared and the deviation is schematically shown in principle.

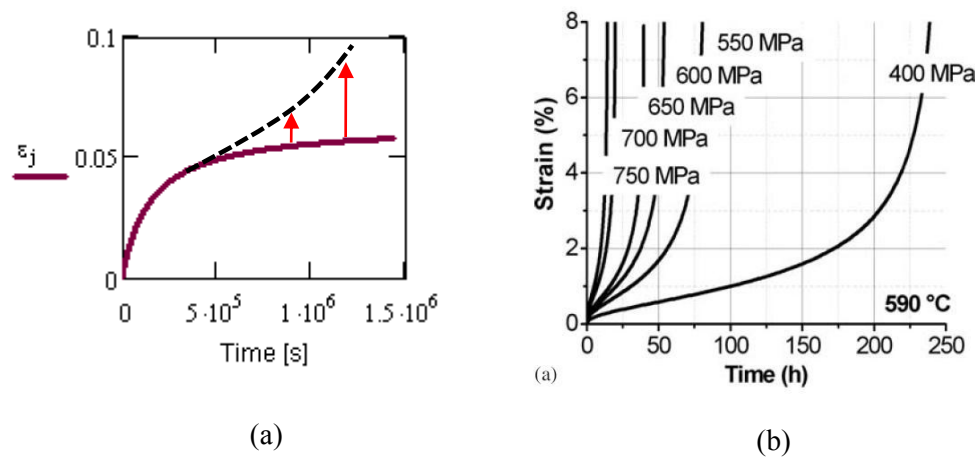


Figure 6.11: Macroscopic inelastic strain (a) as calculated by dislocation motion at 590°C and 600 MPa and (b) experimental trends [57].

The results for the dislocation density measurements varied in the range of maximum 40% difference from peak values to the lowest amounts during long time experimental testing. However in literature [58, 59], a decrease in dislocation density of around 500% or more was found. Since dislocation density measurements are not easy to perform, the found values reflected at least the right trend.

The resulting inelastic strain output was compared with the phenomenological elastic-viscoplastic Chaboche-type model result, as described in Fig. 6.12 to validate the dislocation density model.

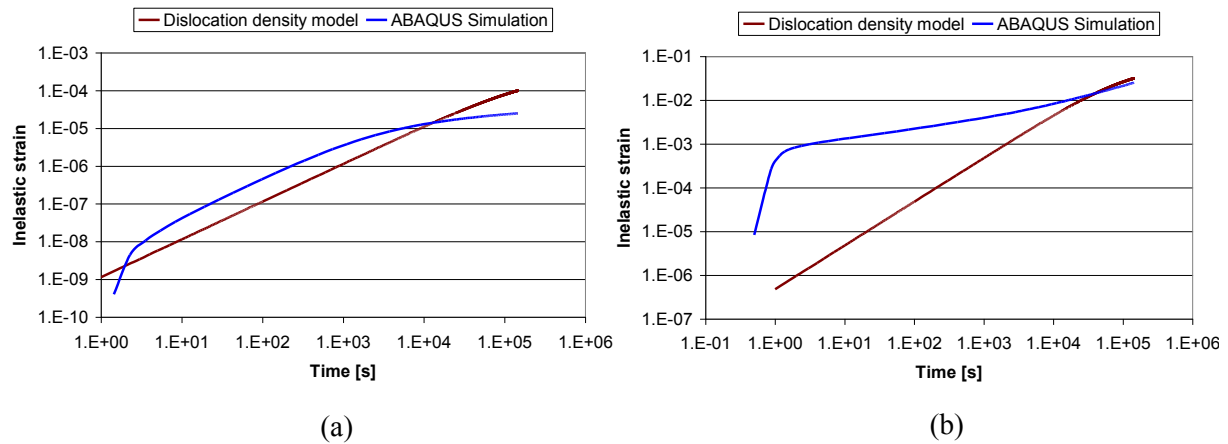


Figure 6.12: Comparison of the calculated as well as FE-simulated inelastic strains for 370MPa at 500°C (a) and 750MPa at 570°C (b) [60]

When explicitly comparing the resulting temporal accumulated strain output from the constitutive elastic-viscoplastic chaboche model with the dislocation density evolution model output at 580°C and 400MPa in Fig. 6.13, it shows a similar progress as in Fig. 6.12.

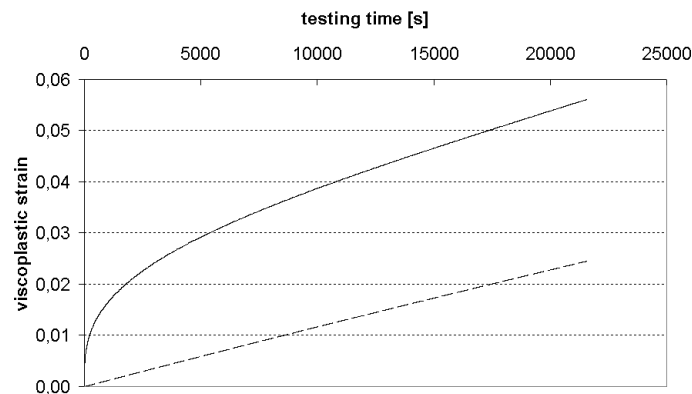


Figure 6.13: Calculated accumulated viscoplastic strain [-] vs. inelastic strain trend due to dislocation glide (dashed line) for creep load at 580°C and 400MPa [61].

The explanation for the gap lies in the fact that the constitutive model reacts much faster at the initial load stage as the dislocation density model, which is based on rate equations and shows a more continuous evolution. The correctness of both models can be ascertained for advanced loading stages, when both results fit better together, see Fig. 6.12 (b). For the occurrence of the fast reacting constitutive model compare also Fig. 5.62 (b) on page 91, which is related to higher damage accumulation at the beginning and constant damage evolution after a few cycles.

Creep-fatigue tests, softening and crack phenomena

During advancing service duration, cyclic material softening takes place, which was clearly observed in the creep-fatigue measurements, see green lines in Fig. 6.14. When accounting for the quantity of relaxation during holding time in compression, a significant higher relaxation part was observed during progressive testing, see diverging red lines in Fig. 6.14.

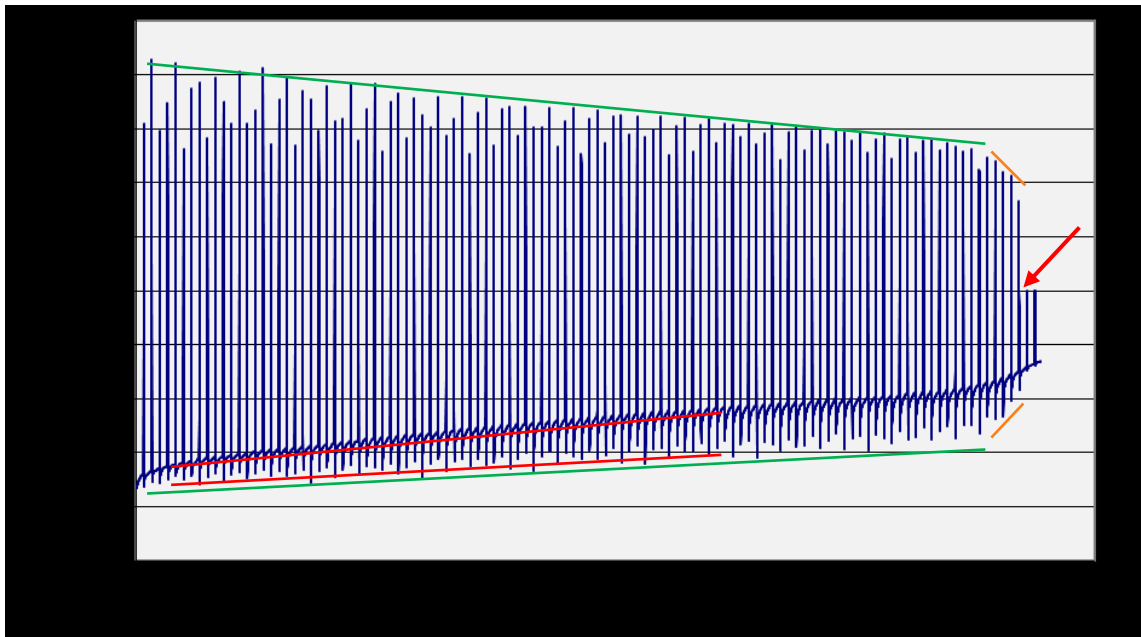


Figure 6.14: Measured stress reaction during creep fatigue testing. The cyclic softening is clearly recognizable. The failure is indicated by the red arrow.

The orange lines mark severe damage with macro cracks and instable crack propagation until the specimen fails. The moment of failure can be clearly identified at that point where no tensile force is carried any more by the specimen, see red arrow in Fig. 6.14. The softening and relaxation can occur due to three main phenomena: first, due to a coarsening as well as a dissolution of small precipitates, which inhibits dislocations from gliding during their presence; second due to activated glide planes with reversible easy glide of dislocations, i.e. reversible plastic deformation and third due to recovery processes, which decrease the dislocation density.

The fracture zone was investigated in detail to define the dominant failure mechanism for each loading case. The crack propagation during creep-fatigue experiments mainly took place transgranularly, whereas during pure creep, the damage initiation occurred along prior austenitic grain boundaries. The macroscopic fracture surface investigations are shown in Fig. 6.15.

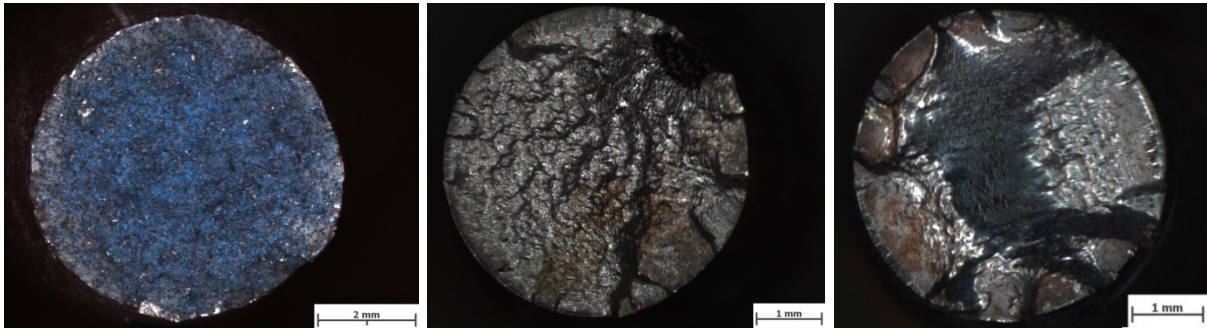


Figure 6.15: (a) Creep fracture (500°C/600MPa, B31), (b) fatigue fracture (540°C/970 cycles, A10) and (c) creep-fatigue (580°C/111 cycles, A14).

In Fig. 6.16 the crack propagation during creep-fatigue and pure creep load is demonstrated.

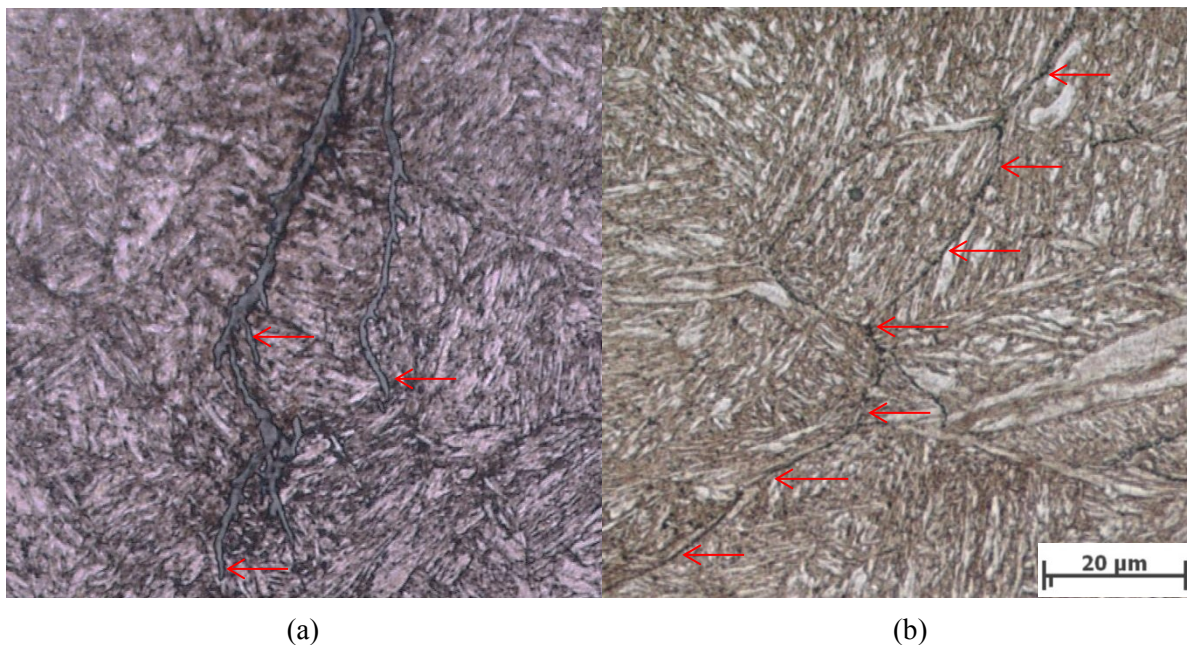


Figure 6.16: (a) Transgranular crack propagation during creep-fatigue testing ($R = -1$, $\Delta\varepsilon = 1.2\%$ and a hold time = 300s) of W300 at 500°C and 776 cycles to rupture and (b) intergranular crack propagation along prior austenitic grain boundaries during creep testing at 500°C and 600MPa.

With knowledge of the crack propagation mechanisms, on the one hand improvements in the microstructure can be applied to counteract specific damage mechanisms in some degree and on the other hand, the process guidance can be additionally optimised. An even more homogeneously and finer distributed microstructure in the W400 lead to significant longer service durations than the W300 tool material. This fact was also verified when calculating the lifetime of W300 and W400 tools during aluminium extrusion [49], which resulted in a three times longer service life of the W400 die.

7. Summary and Outlook

A comprehensive modelling approach was applied to account for the influence of the chemical composition and heat treatment, the microstructure evolution and process conditions onto the service lifetime prediction of tool steels for hot extrusion.

Extrusion application to produce long products in various shapes and geometries is an economic industrial production route. Since this industrial production process causes high thermal and mechanical loads, appropriate tool material selection is essential. Various heat treatments of the tool material as well as several service-near application tests were considered in this work to account for the main influence factors on the tool materials lifetime. Therefore, tests to physically simulate the thermo-mechanical service loading history were performed. The thermo-mechanical test program consisted of three main testing conditions, first creep tests to account for pure time-dependent damage, second fatigue tests to identify the influence of fatigue phenomena onto the lifetime of the tool material and third creep-fatigue tests to simulate extrusion process near service loading conditions.

The extrusion process was simulated in DEFORM with an axisymmetric FE-model. The boundary conditions, namely temperature and stress acting onto the surface of the tools were transmitted to ABAQUS to account for the inelastic strains, which evolve during the cyclic service conditions. These inelastic strains are calculated with an implemented constitutive elastic-viscoplastic model, which is based on empiric material parameters, which have to be experimentally evaluated for every single material condition and temperature dependency. A damage model was added to calculate the service lifetime as number of cycles to failure. For variable chemical compositions, different heat treatments or other service conditions, the empiric parameters have to be exactly determined by costly experiments for each case.

The proposed alternative methodology in this work to account for accumulated inelastic strains due to thermo-mechanical loading is to consider microstructural phenomena, which can be explained physically. Therefore a physically based microstructure modelling approach was introduced, which is able to directly account for inelastic strain results for variable process and material conditions. Such a model approach is more flexible when considering different alloys or heat treatments, i.e. it is adjustable to different material conditions. This can be an advantage when accounting for variabilities in the chemical composition or heat treatment within the agreed specification or norm.

The physical based microstructure modelling approach was realized by introducing a dislocation density evolution model in MathCad with respect to the precipitate structure evolution, which was calculated with the thermo-kinetic software MatCalc. The inelastic strain output of both, the phenomenological model and the physical based model was validated successfully, however some gaps, especially at initial loading states, were observed.

Referring to the experimental test results and simulations to predict the service lifetime of the tool material as a function of heat treatment and loading condition, the longer lifetime of W400 in comparison to W300, both X38CrMoV5-1, despite small alloying differences mainly in the contents of Si and V, lies in the metallurgical production route: The W400 tool material exhibits a higher homogeneity due to a vacuum remelting procedure. Comparing the lifetime results with physical experiments and simulation, a concordance is visible.

Considering further industrial extrusion applications the physical based model approach is valid to determine the microstructure, i.e. precipitation state, dislocation density as well as substructure and to estimate the inelastic strain accumulation as a function of microstructure change and loading history, which can be directly taken into account to estimate the service life, i.e. the number of cycles to failure. Since the proposed physical based model is only valid for bcc lattice structured tool materials, an extension to fcc austenitic tool materials could be taken into consideration. The proposed model is suitable to describe creep phenomena and was adapted to creep-fatigue in this work. The mechanism of dislocation motion is acting by shear stress and the model works at every point in time when there is an applied stress. For this reason, dislocation density evolution due to pure annealing can also be calculated, but it is necessary to account for residual thermal or mechanical stresses in the component, which already exist.

8. References

- [1] F. Krumphals: "On modelling the local damage evolution in hot work tool steels", *Masters Thesis*, Montanuniversität Leoben, Austria, 2007.
- [2] G. Roberts, G. Kraus and R. Kennedy: "Tool Steels 5th ed.", *ASM International, Metals Park Ohio*, 1998.
- [3] J. Davies: "Tools Materials", *ASM International, ASM Speciality Handbook, Material Park Ohio*, pp. 251, 1995.
- [4] F. Pickering: "The Properties of Tool Steels for Mould and Die Applications", *Tool Materials for Molds and Dies, Proceedings of an international Conference*, pp. 1-32, 1987.
- [5] J. Mayerhofer: "Werkstoffkunde der Stähle" - Part: Hochlegierte Stähle, 1998.
- [6] M. Tercelj, A. Smolej, P. Fajfar and R. Turk: "Laboratory Assesment of Wear on nitrided Surfaces of Dies for Hot Extrusion of Aluminium", *Tribol. int.*, 40 pp. 374-384, 2007.
- [7] J. Bergström and J. Sjöström: "Microstructural Stability and Strength of chromium martensitic hot-work Tool Steels", *Tech. rep.*, 2003.
- [8] F. Roters, D. Raabe and G. Gottstein: "Work Hardening in Heterogeneous Alloys - A Microstructural Approach based on Three Internal State Variables", *Acta Materialia*, 40 pp. 4181-4189, 2000.
- [9] B. Reichert, Y. Estrin and H. Schuster: "Implementation of Precipitation and Ripening of Second-Phase Particels in the Constitutive Modelling of Creep", *Scripta mater.*, 38 pp. 1463-1468, 1998.
- [10] J Hirth and J. Lothe: "Theory of Dislocations", *Krieger Publishing Company*, Malbar, Florida, 1992.
- [11] E. Arzt and M. Ashby: "Threshold Stress in Materials Containing Dispersed Particles", *Scripta Metallurgica*, 16 pp. 1285-1290, 1982.
- [12] V. Vitek: "Theory of the Core Structures of Dislocations in BCC-Metals", *Crystal Lattice Defects*, 5 pp. 1-34, 1974.
- [13] A. Argon and S. Takeuchi: "Internal Stress in Power-Law Creep", *Acta Metallurgica*, 29 pp. 1877-1884, 1981.
- [14] N. Ghoniem, J. Matthews and R. Amodeo: "A Dislocation Model for Creep in Engineering Materials", *Res Mechanica*, 29 pp. 179-219, 1990.

- [15] F. Garofalo: "Fundamentals of Creep and Creep-Rupture in Metals", *The MacMillan Company*, 1965.
- [16] F. Humphreys: "A New Analysis of Recovery, Recrystallisation and Grain Growth", *Materials Science and Technology*, 15 pp. 37-44, 1999.
- [17] J. Verhoeven: "Fundamentals of Physical Metallurgy", *John Wiley and Sons, New York, first edition*, 1975.
- [18] R. Sandström: "Subgrain Growth occurring by Boundary Migration", *Acta Metallurgica* 25 pp. 905-911, 1977.
- [19] A. Orlova, K. Miclicka and F. Dobes: "Choice of Evolution Equation for Internal Stress in Creep", *Materials Science and Engineering*, A194 pp. 9-16, 1965.
- [20] R. Honeycombe: "The Plastic Deformation of Metals", *Edward Arnold, London, second edition*, 1982.
- [21] G. Wassermann: *Praktikum der Metallkunde und Werkstoffprüfung*, Springer, Berlin, Heidelberg, New York, 1965.
- [22] P. Weinert: Modellierung des Kriechens von ferritisch/martensitischen 9-12% Cr-Stählen auf mikrostruktureller Basis, *Ph.D thesis*, Technische Universität Graz, 2001.
- [23] G. Gottstein and A. Argon: "Dislocation Theory of Steady State Deformation and its Approach in Creep and Dynamic Tests", *Acta Metallurgica*, 35 pp. 1261-1271, 1987.
- [24] A. Cocks and M. Ashby: "On Creep Fracture by Void Growth", *Progress in Materials Science*, 27 pp. 189-244, 1982.
- [25] M. Ashby and D. Jones: "An Introduction to Properties, Applications and Design", *Elsevier Butterworth-Heinemann*, 2005.
- [26] C. Sommitsch, T. Wlanis and V. Wieser: "Modelling of Creep-Fatigue in Extrusion Dies", *Tech. rep.*, Chair of Metal Forming, Böhler Edelstahl GmbH, 2006.
- [27] C. Sommitsch, R. Sievert, T. Wlanis, B. Günther and V. Wieser: "Modelling of Creep-Fatigue in Containers during Aluminium and Copper Extrusion", *J. Comput. Mat. Sci.* 39 pp. 55-64, 2007.
- [28] R. Teteruk: "Modellierung der Lebensdauer bei thermomechanischer Ermüdungsbeanspruchung unter Berücksichtigung der relevanten Schädigungsmechanismen", *PhD thesis*, Universität Siegen, 2001.
- [29] R. Rie and R. Schmidt: "Low-Cycle Fatigue unter besonderer Berücksichtigung der Temperatur und des Umgebungsmediums", *Ermüdungsverhalten metallischer Werkstoffe*, pp. 379-419, 1985.

- [30] R. Ohtani: "Substance of Creep-Fatigue Interaction Examined from the Point of View of a Crack Propagation Mechanics", *Proc. Second Int. Conf. on Low Cycle Fatigue and Elasto-Plastic Behaviour of Materials*, Elsevier, London pp. 211-222, 1988.
- [31] H. Riedel: Fracture at High Temperatures, *Springer-Verlag* Berlin Heidelberg New York, 1987.
- [32] H. Schitoglu: "Thermo-mechanical Fatigue Life Prediction Models", *Advances in Fatigue Lifetime Predictive Techniques, ASTM STP 1122* pp. 47-76, 1992.
- [33] J. Martin: Micromechanics in Particle Hardened Alloys, *Cambridge Solid State Science Series*, Cambridge University Press, 1980.
- [33] K.-S. Cheong, M. Smilie and D. Knowles: "Predicting Fatigue Crack Initiation Through Image-Based Micromechanical Modeling", *Acta Materialia*, 55 pp. 1757-1768, 2007.
- [34] J. Friedel: Dislocations, *Pergamon Press*, London, New York, Paris, 1967.
- [35] A. Seeger and H. Bross: "Physik", *J. Phys. Chem. Sol.* 16 p. 253, 1956.
- [37] G. Gottstein: Physikalische Grundlagen der Materialkunde, *Springer-Verlag* Berlin Heidelberg New York, 2001.
- [38] N. Yeh and E. Krempl: "An Incremental Life Prediction Law for Multiaxial Creep-Fatigue Interaction and Thermo-mechanical Loading", *Advances in Multiaxial Fatigue, ASTM STP 1191* pp. 107-119, 1993.
- [39] R. Danzer: Lebensdauerprognose hochfester metallischer Werkstoffe im Bereich hoher Temperaturen, *Gebrüder Bornträger*, Berlin-Stuttgart, 1988.
- [40] D. Dendl: Reibwertermittlung beim Aluminium-Strangpressen mittels Spike-Test, *Projektarbeit*, Montanuniversität Leoben 2008.
- [41] J. Zauner: Ausscheidungskinetik von Karbiden in einem Warmarbeitsstahl, *Diplomarbeit*, Montanuniversität Leoben 2008.
- [42] A. J. Gubbens, O.L. Krivanek: "Applications of a post-column imaging filter in biology and materials science", *Ultramicroscopy*, 51(1-4) pp. 146-159, 1993.
- [43] A. Berger, J. Mayer, H. Kohl: "Detection limits in elemental distribution images produced by energy filtering TEM: Case study of grain boundaries in Si₃N₄", *Ultramicroscopy* 55(1), pp. 101-112, 1994.
- [44] F. Hofer et al.: "Quantitative analysis of EFTEM elemental distribution images" *Ultramicroscopy* 67(1-4) pp. 83-103, 1997.

- [45] B. Sonderegger: "Modifications of stereological correction methods for precipitate parameters using transmission microscopy", *Ultramicroscopy* 106(10) pp. 941-950, 2006.
- [46] E. Schafler, M. Zehetbauer, A. Borbely, T. Ungar: "Dislocation densities and internal stresses in large strain cold worked pure iron", *Materials Science and Engineering: A* 234–236 pp 445-448, 1997.
- [47] N. Yeh and E. Krempl: "An Incremental Life Prediction Law for Multiaxial Creep-Fatigue Interaction and Thermo-mechanical Loading", *Advances in Multiaxial Fatigue, ASTM STP 1191* pp. 107–119, 1993.
- [48] V. Wieser, C. Sommitsch, K. Haberfellner, P. Lehofer: "New Developments in Design and Production of Container assemblies", *ET'04 –Proceedings of the 8th International Aluminium Extrusion Technology Seminar*, Kissimmee, Florida, 2004.
- [49] C. Sommitsch, R. Sievert, T. Wlanis , C. Redl : "Lifetime evaluation of two different hot work tool steels in aluminium extrusion", *Comp. Mat. Sci.* 43 (1), pp. 82 – 91, 2008.
- [50] J. LeMaitre and J. Chaboche: *Mechanique de Materiaux Solides*, Dunod, Paris, 1985.
- [51] J. Chaboche: "Cyclic Viscoplastic Constitutive Equations, Part I: A Thermodynamically Consistent Formulation", *Journal of Applied Mechanics* 60 pp. 813–821, 1993.
- [52] J.L. Chaboche, G. Cailletaud: "Integration methods for complex plastic constitutive equations", *Computer Methods in Applied Mechanics and Engineering* 133, Issues 1–2, , pp. 125-155, 15 June 1996.
- [53] B. Günther and R. Sievert: "Bestimmung der Materialparameterwerte des viskoplastischen Chaboche-Modells und einer zeitlich inkrementellen Lebensdauerregel für die Hochtemperatur-Ermüdung des Werkstoffs Böhler W400 in dem Temperaturbereich von 470-590°C, *Tech. rep.*, BAM-V.2 05/02, 2005.
- [54] J. Svoboda, F.D. Fischer, P. Fratzl, E. Kozeschnik: "Modelling of kinetics in multi-component multi-phase systems with spherical precipitates: I: Theory" *Materials Science and Engineering: A* 385, Issues 1–2, pp. 166-174, 2004.
- [55] F. Krumphals, B. Reggiani, L. Donati, T. Wlanis, C. Sommitsch: "Deformation behaviour of a ferritic hot-work tool steel with respect to the microstructure", *Comp. Mat. Sci.* 52, pp. 40 – 4, 2012.
- [56] V. Velay, „Cyclic behaviour modelling and lifetime assessment of martensitic hot work tool steels“, *PhD thesis* (in French), Ecole Nationale Supérieure des Mines de Paris, 2003.

-
- [57] H. Wurmbauer, H. Leitner, M. Panzenböck, C. Scheu, H. Clemens, “Short-term creep behaviour of a Cr Mo V hot-work tool steel”, *Int. J. Mat. Res (formerly Z. Metallkd.)* 100, pp. 1066-1073, 2009
- [58] H. Wurmbauer, H. Leitner, M. Panzenböck, C. Scheu, H. Clemens :“Short term Creep Behaviour of an X 37 Cr Mo V 5-1 Hot-work Tool Steel with almost Bainitic and fully Martensitic Microstructures”, *Steel research international* 7, pp. 569 – 575, 2010.
- [59] J. Pesicka, R. Kutzel, A. Dronhofer, G. Eggeler, “The evolution of dislocation density during heat treatment and creep of tempered martensite ferritic steels”, *Acta Mater.* 51, pp. 4847-4862, 2003.
- [60] F. Krumphals, T. Wlanis, C. Sommitsch, I. Holzer, B. Sonderegger, V. Wieser: “Modelling of microstructure evolution in hot work tool steels during service”, *Computer methods in materials science = Informatyka w technologii materiałów* 9, pp. 228 – 233, 2009.
- [61] F. Krumphals, T. Wlanis, R. Sievert, V. Wieser, C. Sommitsch, “Damage analysis of extrusion tools made from the austenitic hot work tool steel Böhler W750”, *Comp. Mat. Sci.* 50, pp. 1250-1255, 2011

9. Appendix

Appendix A

The investigations, which are shown in Appendix A belong to chapter 5.2.2.

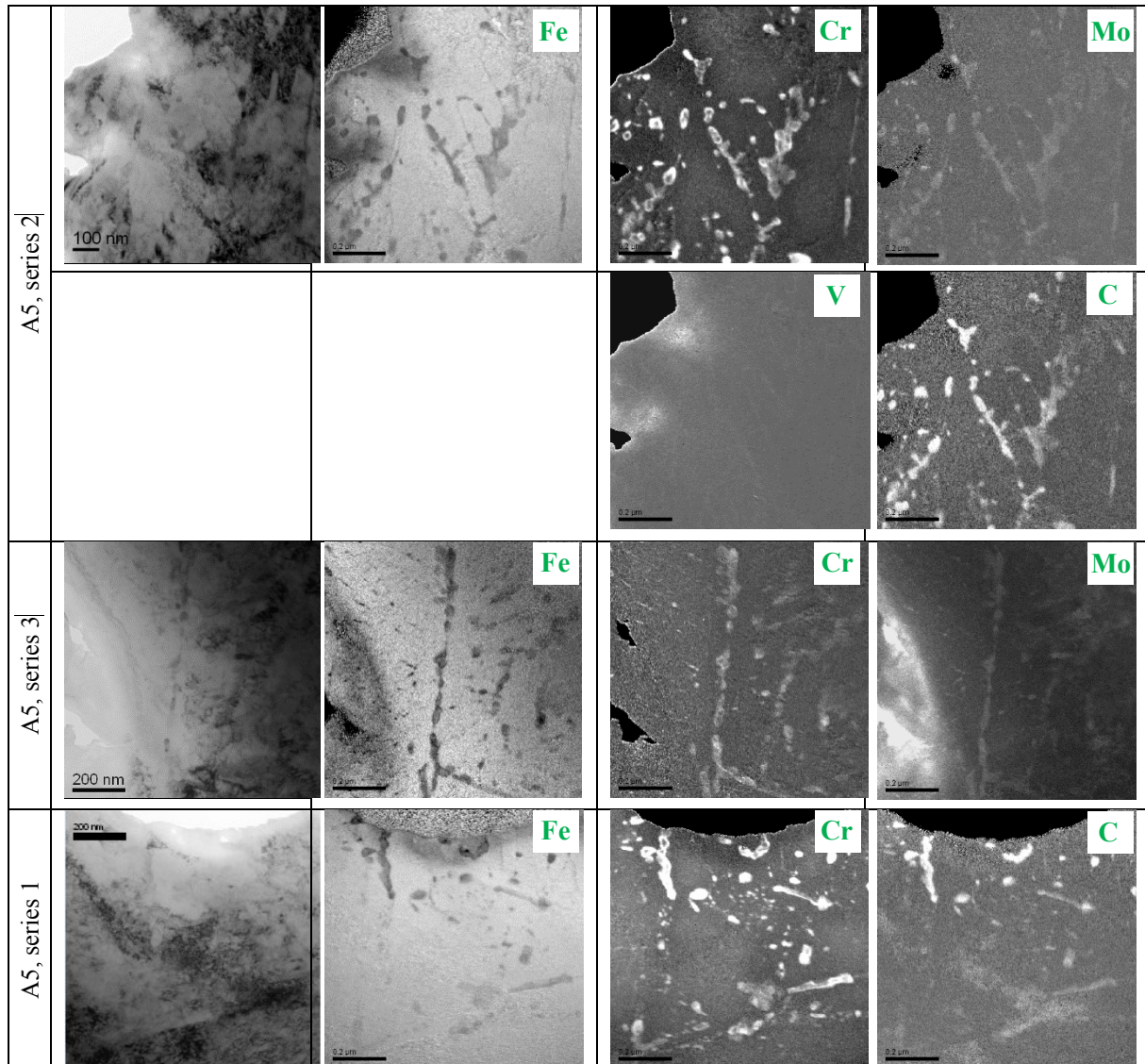


Figure 9.1: Additional TEM investigations of heat treated W300. A tempered martensitic matrix structure with high amounts of small chromium rich carbides was observed.

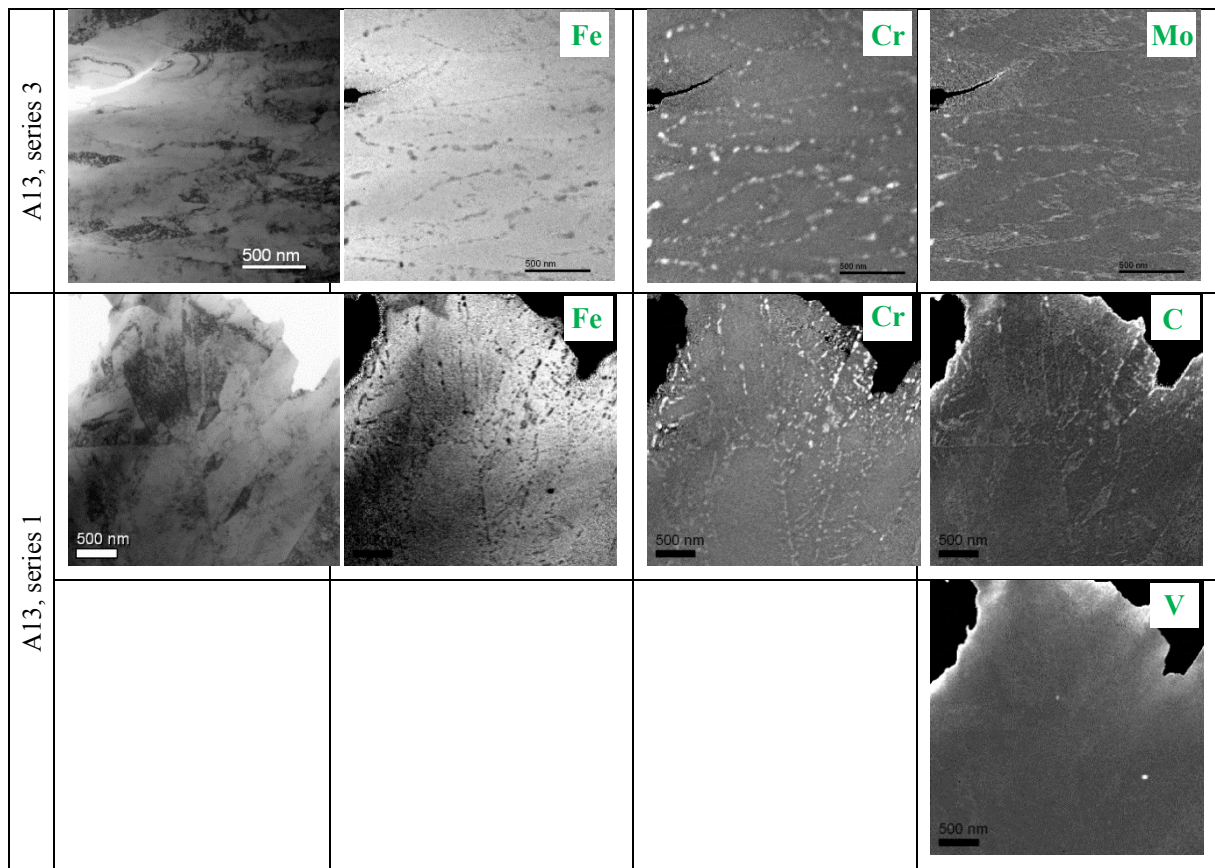


Figure 9.2: Additional TEM investigations of a tempered W300 martensitic matrix structure, creep-fatigue loaded for 72.3 h at 500°C.

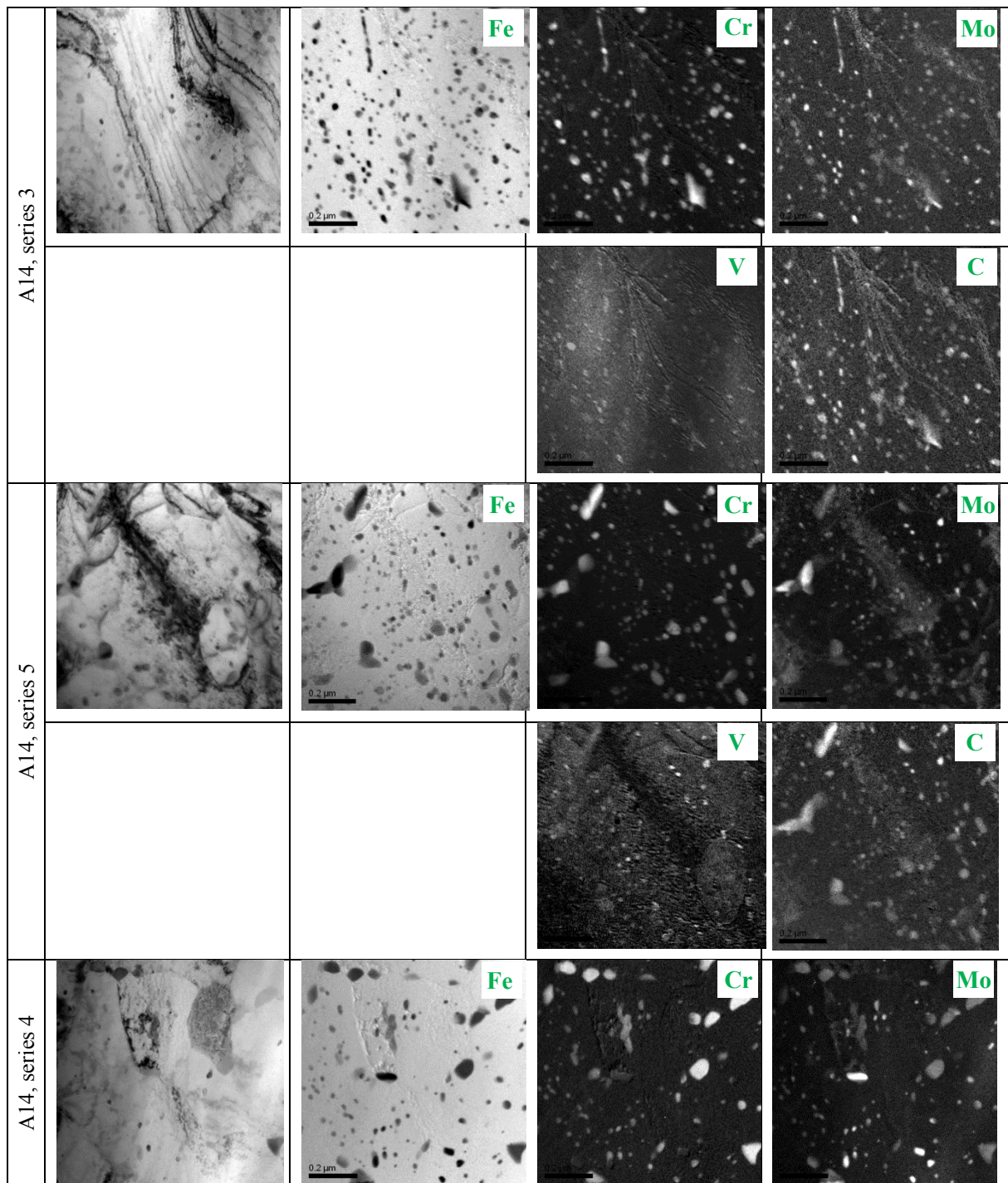


Figure 9.3: Additional TEM investigations of a tempered W300 martensitic matrix structure, creep-fatigue loaded for 15.1 h at 580°C. Again the dominant precipitates are chromium rich carbides.

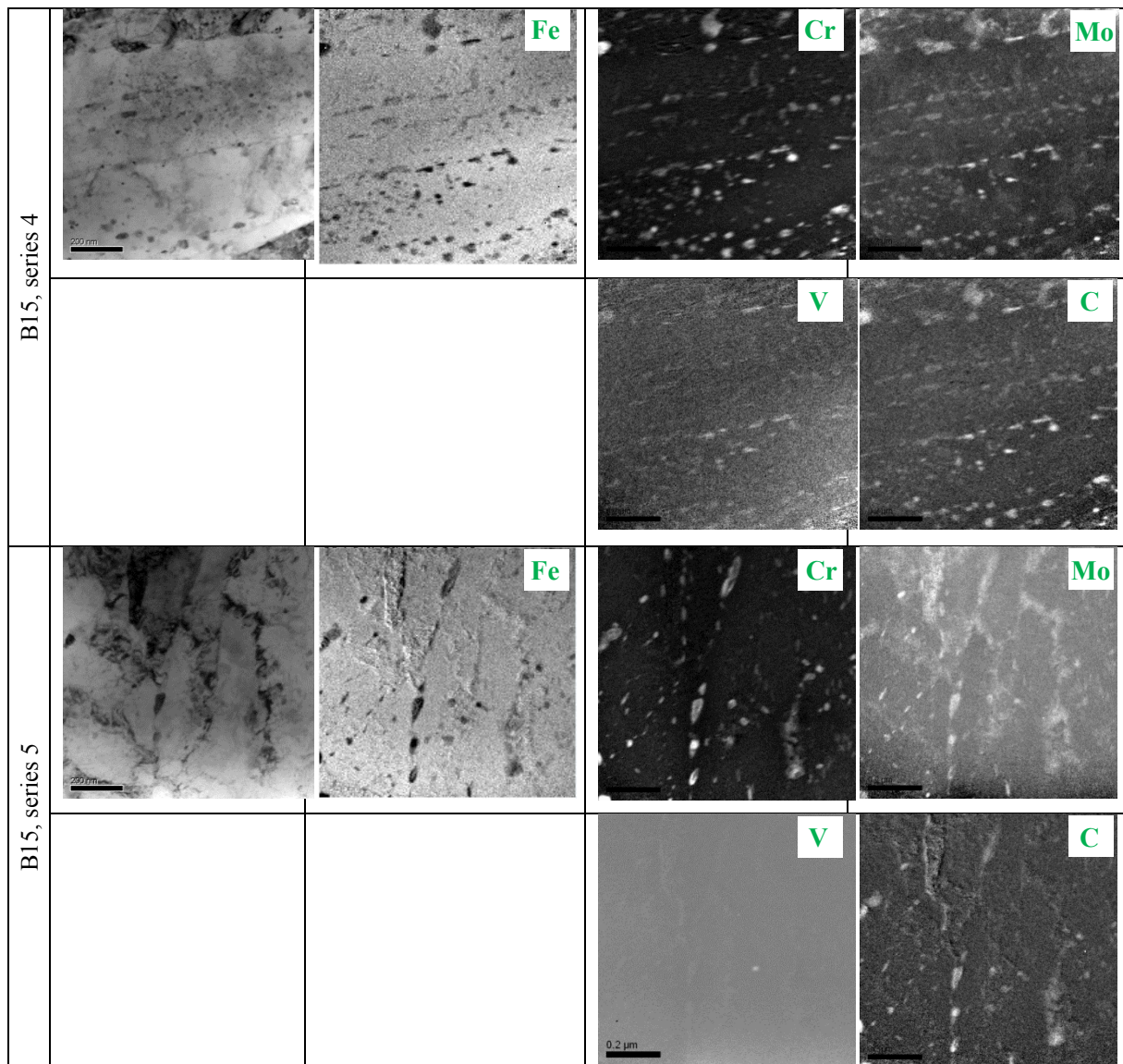


Figure 9.4: Additional TEM investigations of a tempered bainitic matrix structure, creep-fatigue loaded for 15.1 h at 500°C. The dominant precipitates are chromium rich carbides with traces of molybdenum.

Appendix B

The content of Appendix B is the detailed coding of the extended dislocation density evolution model, which was used in this work.

Dislocation density evolution calculation based on the model according to Ghoniem et al.

(Ghoniem et al., "A Dislocation Model for Creep in Engineering Materials", *Res Mechanica*, 29:179-219, 1990)

An adapted model based on the model according to Ghoniem et al. is applied to describe the microstructure, i.e. dislocation density evolution through a system of coupled differential equations.

Constants

$\nu \equiv 10^{13}$	(Debye) Frequency [s^{-1}]
$Q \equiv 4.005441155 \cdot 10^{-19}$	Aktivation energie [J] (1eV = $1.602176462 \cdot 10^{-19}$ J)
$k \equiv 1.3806504 \cdot 10^{-23}$	Boltzmann constant [JK^{-1}]
$b \equiv 2.866 \cdot 10^{-10}$	Burgers vector [m]
$\beta \equiv 6$	Parameter (knitting out process) [1]
$\Omega \equiv 1.149404032 \cdot 10^{-29}$	Atomic volume ($\frac{4}{3} \cdot (0.14 \cdot 10^{-9})^3 \cdot \pi$) [m^3]
$\eta\nu \equiv 1$	Transferparameter [1]
$Kc \equiv 0.0$	Constant [1]
$\zeta \equiv 0.00$	Annihilation parameter (at SGB) [1]
$hsg \equiv 5 \cdot 10^{-8}$	Dislocation distance in subgrain [m]
$\delta \equiv 1 \cdot 10^{-7}$	Dynamic annihilation distance [m]
$\lambda \equiv 2.1 \cdot 10^{-8}$	Jump width [m]
$D_{vp} \equiv 3.05 \cdot 10^{-10}$	Vacancy diffusion through "Pipe" [m^2s^{-1}]
$D_{vl} \equiv 3.05 \cdot 10^{-6}$	Vacancy diffusion through "Lattice" [m^2s^{-1}]
$\Delta V\alpha \equiv 0.5\Omega$	Factor for volume of relaxation (i.A. -0.5 bis 1.2) [m^3]
$L\alpha$	Parameter determining the dimension of the elastic interaction between a dislocation and a defect [$MPa m^4 J^{-1}$]

$D_s = 1.542 \times 10^{-22}$ Diffusion coefficient [m^2s^{-1}]

$\nu \equiv 0.3$ Poisson's ratio [1]

$G = 67.6910^9$ Shear modulus [Pa]

Adjustable induced parameters with initial conditions (start values)

T Process temperature [K]
 tau Acting shear stress [MPa]
 M_{sg} Subgrain mobility [ms^{-1}]
 p_{sg} Driving force [J]
 γ_{sg} Surface energy of subgrain boundary [J]
 N_{vp} Number of precipitates per volume [m^{-3}]
 r_p Particle radius [m]

Variables

i Control variable
 t Time [s]
 dt Time step size [s^{-1}]
 f Number of steps

Initial microstructure

$\rho_{m_0} := 0.3 \cdot 10^{15}$ Initial density of mobile dislocations [m^{-2}]
 $\rho_{s_0} := 0.7 \cdot 10^{15}$ Initial density of static dislocations [m^{-2}]
 $\rho_{b_0} := 1.3 \cdot 10^{15}$ Initial density of boundary dislocations [m^{-2}]
 $R_{\text{sub}_0} := 1 \cdot 10^{-7}$ Initial subgrain radius [m]
 v_{cm_0} Climb velocity of mobile dislocations [ms^{-1}]
 v_{cs_0} Climb velocity of static dislocations [ms^{-1}]

Precipitate classes:

Mean radius [m] Number density [m⁻³]

$$rp1 \equiv 6 \cdot 10^{-9} \quad Nvp1 \equiv 3 \cdot 10^{20}$$

$$rp2 \equiv 150 \cdot 10^{-9} \quad Nvp2 \equiv 3 \cdot 10^{18}$$

$$rp3 \equiv 5 \cdot 10^{-9} \quad Nvp3 \equiv 8 \cdot 10^{15}$$

$$rp4 \equiv 5 \cdot 10^{-9} \quad Nvp4 \equiv 7 \cdot 10^{17}$$

$$rp5 \equiv 8 \cdot 10^{-9} \quad Nvp5 \equiv 2 \cdot 10^{20}$$

$$rp6 \equiv 2 \cdot 10^{-9} \quad Nvp6 \equiv 1 \cdot 10^{20}$$

Explicit calculation steps for parameters in the loop are mentioned below:

- Total dislocation density

$$\rho_{ges0} := \rho m_0 + \rho s_0 + \rho b_0$$

- Misorientation, dislocation distance (hb) in the subgrain

$$\theta_1 := 0.17453292$$

$$\theta := 0.00698131 \quad hb := \frac{b}{\theta_1}$$

- Activation volume and activation energy

$$\Delta V\alpha := 0.5 \cdot 1.149404032 \cdot 10^{-29}$$

$$E_0 := \frac{Gb}{4\pi \cdot (1 - \nu)}$$

- Diffusion path length

$$L\alpha := \frac{(1 + \nu)Gb \cdot |\Delta V\alpha|}{3\pi \cdot (1 - \nu) \cdot k \cdot \text{temp}}$$

- Mobility of subgrain boundary

$$M_{sg} := \frac{2\pi \cdot \eta v \cdot Ds \cdot \Omega}{b \cdot k \cdot \text{temp}} + \frac{2\pi b \cdot Dvp \cdot \Omega}{hb^2 \cdot k \cdot \text{temp}}$$

- Climb velocity through pipe diffusion

Lattice constant a_g :

$$a_g := 0.2866510^{-9}$$

$$\Delta W_s := 1.2 \left(1.602176462 \cdot 10^{-19} \right)$$

$$L_p := \sqrt{2} \cdot a_g \cdot e^{\frac{\Delta W_s}{2 \cdot k \cdot \text{temp}}}$$

$$j_p := \frac{2 \cdot \pi \cdot D_{vp} \cdot \text{Load} \cdot \Omega}{b \cdot L_p \cdot k \cdot \text{temp}}$$

$$v_{cpx} := \frac{j_p \cdot b^2}{L_p}$$

- Climb velocity through lattice diffusion

$$L_{\alpha v} := \frac{(1 + \nu_u) \cdot G \cdot b \cdot |-0.5 \Omega|}{3 \cdot \pi \cdot (1 - \nu_u) \cdot k \cdot \text{temp}}$$

$$L_{\alpha i} := \frac{(1 + \nu_u) \cdot G \cdot b \cdot |1.2 \Omega|}{3 \cdot \pi \cdot (1 - \nu_u) \cdot k \cdot \text{temp}}$$

$$v_{clx} := \frac{2 \cdot \pi \cdot \eta_v \cdot D_s \cdot \Omega}{\left[1 - \eta_v \cdot \ln \left[\left(\frac{\rho_{ges_0}}{\rho_{ges_0}} \right)^2 \cdot L_{\alpha v} \right] \right]} \cdot \text{Load} \cdot b \cdot k \cdot \text{temp}$$

- Total contribution of climb velocity for pipe diffusion and lattice diffusion, $v_{cx} = v_{cpx} + v_{clx}$:

$$v_{cx} := \frac{j_p \cdot b^2}{L_p} + \frac{2 \cdot \pi \cdot \eta_v \cdot D_s \cdot \Omega}{\left[1 - \eta_v \cdot \ln \left[\left(\frac{\rho_{ges_0}}{\rho_{ges_0}} \right)^2 \cdot L_{\alpha v} \right] \right]} \cdot \text{Load} \cdot b \cdot k \cdot \text{temp}$$

Loop indices:

Maximum step number: $f := 360000$

Steps: $i := 1..f$

Time step range: $dt = 1 \cdot 10^0$

Temperature: $temp = 773.1$

Reduction for graphic display:

$j := 10, 20..f$

$n := 10$

Loop start:

$\rho m_i := 0$	$\rho s_i := 0$	$\rho b_i := 0$	$R_{sub_i} := 0$	$\rho ges_i := 0$
$\tau_{i_1} := 0$	$v_i := 0$	$vcm_i := 0$	$vcs_i := 0$	$\varepsilon_i := 0$
$\gamma sg_i := 0$	$psg_i := 0$	$T_i := 0$	$\lambda_i := 0$	$vc_i := 0$

In the following the program loop with coupled differential equations to calculate the evolution of mobile, ρ_m , static, ρ_s and boundary, ρ_b , dislocation density as well as the mean subgrain radius R_{sub} and the resulting macroscopic strain ε , which are the most important output parameters, is depicted. Driving forces and further microstructure parameters such as γ_{sg} , p_{sg} , v_{cm} , v_{cs} , ρ_{ges} , λ , v and vc are additionally defined as output parameters to account for a reliable control of the microstructure evolution model.

$(\rho_m, \rho_s, \rho_b, R_{sub}, \varepsilon, \tau, v, \gamma_{sg}, p_{sg}, v_{cm}, v_{cs}, \rho_{ges}, \lambda, vc) :=$

```

for i ∈ 1..f
  tau_i ←  $\frac{Load}{2} - konst \cdot G \cdot b \cdot \sqrt{\rho_{ges}_i}$ 
  T_i ← temp
  v_i ←  $a1 \cdot \exp\left(\frac{-Q}{k \cdot T_i}\right) \cdot \tau_i \cdot \frac{\Omega}{k \cdot T_i}$ 
  Lp_i ←  $\sqrt{2} \cdot ag \cdot e^{\frac{\Delta W_s}{2 \cdot k \cdot T_i}}$ 
  jp_i ←  $\frac{2 \cdot \pi \cdot Dvp \cdot \tau_i \cdot \Omega}{b \cdot Lp_i \cdot k \cdot T_i}$ 
  vcp_i ←  $\frac{jp_i \cdot b^2}{Lp_i}$ 
  Lcv_i ←  $\frac{(1 + nu) \cdot G \cdot b \cdot |-0.5 \cdot \Omega|}{3 \cdot \pi \cdot (1 - nu) \cdot k \cdot T_i}$ 
  Lcd_i ←  $\frac{(1 + nu) \cdot G \cdot b \cdot |1.2 \cdot \Omega|}{3 \cdot \pi \cdot (1 - nu) \cdot k \cdot T_i}$ 
  vcl_i ←  $\frac{2 \cdot \pi \cdot \eta v \cdot Ds \cdot \Omega}{\left(1 - \eta v \cdot \ln\left(\frac{1}{\sqrt{\rho_{ges}_{i-1}}}\right) \cdot Lcv_i\right)} \cdot \tau_i \cdot b \cdot k \cdot T_i$ 
  vc_i ← vcp_i + vcl_i
  gamma_sg_i ←  $\frac{G \cdot b^2}{3} \cdot \rho_{b_{i-1}} \cdot R_{sub_{i-1}}$ 
  p_sg_i ←  $\frac{4}{3} \cdot G \cdot b^2 \cdot \rho_{b_{i-1}}$ 
  d_rho_m_i ←  $v_i \cdot (\rho_{m_{i-1}})^{0.5} + \frac{\beta \cdot R_{sub_{i-1}}}{hsg^2} \cdot v_i - 8 \cdot vc_i \cdot (\rho_{m_{i-1}})^{1.5} - \delta \cdot (\rho_{m_{i-1}} + \rho_{s_{i-1}}) \cdot v_i$ 
  rho_m_i ← rho_m_{i-1} + d_rho_m_i \cdot dt
  d_rho_s_i ←  $\frac{\rho_{m_{i-1}}}{2 \cdot R_{sub_{i-1}}} \cdot v_i - 8 \cdot \frac{\rho_{s_{i-1}}}{hsg} \cdot vc_i - \delta \cdot \rho_{s_{i-1}} \cdot \rho_{m_{i-1}} \cdot v_i$ 
  rho_s_i ← rho_s_{i-1} + d_rho_s_i \cdot dt

```

$$\begin{aligned}
dpb_i &\leftarrow 8 \cdot (1 - 2 \cdot C) \cdot \frac{\rho s_{i-1}}{hsg} \cdot vc_i - \frac{\rho b_{i-1} \cdot Msg}{Rsub_{i-1}} \left[psg_i - 2 \cdot \pi \cdot (rp1^2 \cdot Nvp1 + rp2^2 \cdot Nvp2 + rp3^2 \cdot Nvp3 + rp4^2 \cdot Nvp4 + rp5^2 \cdot Nvp5 + rp6^2 \cdot Nvp6) \cdot \gamma s g_i \right] \\
\rho b_i &\leftarrow \rho b_{i-1} + dpb_i \cdot dt \\
dRsub_i &\leftarrow Msg \cdot \left[psg_i - 2 \cdot \pi \cdot (rp1^2 \cdot Nvp1 + rp2^2 \cdot Nvp2 + rp3^2 \cdot Nvp3 + rp4^2 \cdot Nvp4 + rp5^2 \cdot Nvp5 + rp6^2 \cdot Nvp6) \cdot \gamma s g_i \right] \\
&\quad - G \cdot \eta v \cdot Kc \cdot Rsub_{i-1} \cdot \left[(\rho m_{i-1} + \rho s_{i-1})^{0.5} - \frac{Kc}{2 \cdot Rsub_{i-1}} \right] \cdot \frac{\Omega \cdot Ds}{k \cdot T_i} \\
Rsub_i &\leftarrow Rsub_{i-1} + dRsub_i \cdot dt \\
d\varepsilon_i &\leftarrow a2 \cdot \frac{1}{M} \cdot \rho m_i \cdot v_i \cdot b \\
\varepsilon_i &\leftarrow \varepsilon_{i-1} + d\varepsilon_i \cdot dt \\
\rho ges_i &\leftarrow \rho m_{i-1} + d\rho m_i \cdot dt + \rho s_{i-1} + d\rho s_i \cdot dt + \rho b_{i-1} + d\rho b_i \cdot dt \\
\lambda_i &\leftarrow \frac{1}{\sqrt{\rho m_{i-1} + d\rho m_i \cdot dt + \rho s_{i-1} + d\rho s_i \cdot dt + \rho b_{i-1} + d\rho b_i \cdot dt}} \\
j &\leftarrow \frac{i}{n} \\
\tau_j &\leftarrow \tau_i \text{ if } \text{mod}(i, n) = 1 \\
\tau &
\end{aligned}$$

Appendix C

Appendix C contains the material parameters for the elastic-viscoplastic Chaboche model for Böhler W300 ISOBLOC grade and W750, which were determined at the Bundesanstalt für Materialprüfung (BAM) in Berlin.

Table 9.1: Values of the material parameters for the elastic–viscoplastic Chaboche model determined for the hot work tool steel Böhler W300 in the range 470 - 590°C.

T [°C]	470	500	530	560	590
E [MPa]	178 400.	175 250.	172 100.	158 700.	154 300.
K_0 [MPa s ^{1/n}]	785.	891.5	998.	1045.	1185.
n	8.	8.	8.	8.	8.
k [MPa]	293.	159.	25.	25.	0.
Q [MPa]	85.	100.	115.	135.	1.
b	1000.	1000.	1000.	1000.	(1000.)
f [MPa s ⁻¹]	0.002	0.00215	0.0023	0.0046	(0.01)
s	1.	0.7	0.4	1.2	(1.)
g [MPa s ^{-(1-1/n)}]	0.	0.0013	0.0026	0.0049	0.007
z	(0.4)	0.4	0.4	0.4	0.4
K [MPa s ^{1/n}]	100.	100.	100.	100.	100.
a_1 [MPa]	308.	312.	316.	200.	212.
c_1	3800.	3650.	3500.	5000.	1600.
a_2 [MPa]	286.	310.5	335.	138.	150.
c_2	285.	315.5	346.	226.	260.
d_1 [MPa s ⁻¹]	4.2	4.6	5.	8.3	0.037
m_1	15.	14.75	14.5	7.4	1.2
d_2 [MPa s ⁻¹]	4.2	4.6	5.	8.3	6.5
m_2	15.	14.75	14.5	7.4	3.7
m_l	6.	5.3	4.9	3.8	1.8
A [MPa]	1105.	1007.	867.	755.	678.
n_l	1.	0.64	0.25	0.04	0.001

Table 9.2: Values of the material parameters for the elastic–viscoplastic Chaboche model determined for the hot work tool steel Böhler W750 in the range 650 - 850°C.

T [°C]	650	700	750	800	850
E [MPa]	155000.	148000.	140000.	138000.	130000.
K_0 [MPa s ^{1/n}]	100.	200.	850.	1020.	636.
n	5.	5.	5.	5.	4.
k [MPa]	170.	100.	82.	0.	0.
Q_R [MPa]	170.	150.	60.	35.	0.01
b_R	2200.	2200.	490.	100.	(100.)
f [MPa s ⁻¹]	0.02	0.5	0.001	0.0009	(0.)
q	8.2	4.	4.	0.4	(0.4)
Q_S [MPa]	0.	0.	82.	0.	0.
b_S	(0.)	(0.)	110.	(110.)	(110.)
K_1 [MPa s ^{1/n}]	100.	200.	850.	705.	636.
b_K	(0.)	(0.)	(0.)	100.	(100.)
K_2 [MPa s ^{1/n}]	(99.)	(100.)	100.	100.	(100.)
g [MPa s ^{-(1-1/n)}]	0.	0.	0.0018	0.00395	0.
z	(0.4)	(0.4)	0.4	0.4	(0.4)
a_1 [MPa]	311.	295.	237.	178.	47.
c_1	6500.	7000.	6500.	5500.	550.
φ_∞	0.3	0.45	0.24	0.18	(1.)
ω	2500.	3000.	4500.	3000.	(3000.)
a_2 [MPa]	277.	200.	220.	35.	45.
c_2	100.	300.	4.	10.	10.
d_1 [MPa s ⁻¹]	2.5	13.	24.	38.	10.
m_1	3.8	7.8	7.9	7.8	5.5
d_2 [MPa s ⁻¹]	40.	45.	24.	38.	10.
m_2	1.7	1.5	7.9	7.8	5.5
m_l	6.8	6.	3.7	5.2	3.5
A [MPa]	542.	460.	429.	292.5	163.
n_l	0.75	0.53	0.38	0.32	0.31